Nuclear matter from chiral effective field theory

Kernmaterie basierend auf chiraler effektiver Feldtheorie
Zur Erlangung des Grades eines Doktors der Naturwissenschaften (Dr. rer. nat.)
genehmigte Dissertation von Christian Drischler aus Rüsselsheim
Tag der Einreichung: 17.10.2017, Tag der Prüfung: 15.11.2017
Darmstadt 2017 — D 17

1. Gutachten: Prof. Ph.D. Achim Schwenk
2. Gutachten: Prof. Dr. Jens Braun

TECHNISCHE
UNIVERSITÄT
DARMSTADT

Fachbereich Physik
Institut für Kernphysik
Theoriezentrum

Nuclear matter from chiral effective field theory
Kernmaterie basierend auf chiraler effektiver Feldtheorie

Genehmigte Dissertation von Christian Drischler aus Rüsselsheim

1. Gutachten: Prof. Ph.D. Achim Schwenk
2. Gutachten: Prof. Dr. Jens Braun

Tag der Einreichung: 17.10.2017
Tag der Prüfung: 15.11.2017

Darmstadt 2017 — D 17

Bitte zitieren Sie dieses Dokument als:
URN: urn:nbn:de:tuda-tuprints-69845
URL: http://tuprints.ulb.tu-darmstadt.de/id/eprint/6984

Abstract

Nuclear matter is an ideal theoretical system that provides key insights into the physics of different length scales. While recent ab initio calculations of medium-mass to heavy nuclei have demonstrated that realistic saturation properties in infinite matter are crucial for reproducing experimental binding energies and charge radii, the nuclear-matter equation of state allows tight constraints on key quantities of neutron stars. In the present thesis we take advantage of both aspects.

Chiral effective field theory (EFT) with pion and nucleon degrees of freedom has become the modern low-energy approach to nuclear forces based on the symmetries of quantum chromodynamics, the fundamental theory of strong interactions. The systematic chiral expansion enables improvable calculations associated with theoretical uncertainty estimates. In recent years, chiral many-body forces were derived up to high orders, allowing consistent calculations including all many-body contributions at next-to-next-to-next-to-leading order (N^3LO). Many further advances have driven the construction of novel chiral potentials with different regularization schemes.

Here, we develop advanced methods for microscopic calculations of the equation of state of homogeneous nuclear matter with arbitrary proton-to-neutron ratio at zero temperature. Specifically, we push the limits of many-body perturbation theory (MBPT) considerations to high orders in the chiral and in the many-body expansion. To address the challenging inclusion of three-body forces, we introduce a new partial-wave method for normal ordering that generalizes the treatment of these contributions. We show improved predictions for the neutron-matter equation of state with consistent N^3LO nucleon-nucleon (NN) plus three-nucleon (3N) potentials using MBPT up to third order and self-consistent Green's function theory. The latter also provides nonperturbative benchmarks for the many-body convergence. In addition, we extend the normal-ordering method to finite temperatures.

Calculations of asymmetric matter require in addition reliable fit values for the low-energy couplings that contribute to the 3N forces. This was not the case for N^3LO calculations. We present a novel Monte-Carlo framework for perturbative calculations with two-, three-, and four-nucleon interactions, which, including automatic code generation, allows to compute successive orders in MBPT as well as chiral EFT in an efficient way. The performance is such that it can be used for optimizing next-generation chiral potentials with respect to saturation properties. As a first step in this direction, we study nuclear matter based on chiral low-momentum interactions, exhibiting a very good many-body convergence up to fourth order. We then explore new chiral interactions up to N^3LO, where simultaneous fits to the triton and to saturation properties can be achieved with natural 3N low-energy couplings.

We perform a comprehensive Weinberg eigenvalue analysis of a representative set of modern local, semilocal, and nonlocal chiral NN potentials. Our detailed comparison of Weinberg eigenvalues provides various insights into idiosyncrasies of chiral potentials for different orders and partial waves. We demonstrate that a direct comparison of numerical cutoff values of different interactions is in general misleading due to the different analytic form of regulators. This shows that Weinberg eigenvalues also can be used as a helpful monitoring scheme when constructing new interactions.

Furthermore, we present solutions of the BCS gap equation in the channels ${}^1S_0$ and ${}^3P_2$—${}^3F_2$ in neutron matter. Our studies are based on nonlocal NN plus 3N interactions up to N^3LO as well as the aforementioned local and semilocal chiral NN interactions up to N^2LO and N^4LO, respectively. In particular, we investigate the impact of N^3LO 3N forces on pairing gaps and also derive uncertainty estimates by taking into account results at different orders in the chiral expansion. In addition, different methods for obtaining self-consistent solutions of the gap equation are discussed. Besides the widely-used quasilinear method we demonstrate that the modified Broyden method is well applicable and exhibits a robust convergence behavior.

Zusammenfassung

Kernmaterie ist ein ideales, theoretisches System, das zentrale Einblicke in die Physik verschiedener Längenskalen gewährt. Während ab initio Rechnungen von mittelschweren bis schweren Kerne vor kurzem gezeigt haben, dass realistische Saturierungseigenschaften in unendlicher Materie für die experimentalen Bindungsenergien und Kernradien wichtig sind, erlaubt die Zustandsgleichung von Kernmaterie starke Einschränkungen von Schlüsselgrößen für Neutronensternen. In der vorliegenden Dissertation machen wir uns beide Aspekte zu nutze.

Die chirale effektive Feldtheorie (EFT), mit Pionen und Nukleonen als Freiheitsgraden, wurde zum modernen, niederenergetischen Zugang zu Kernkräften, basierend auf den Symmetrien der Quantenchromodynamik, der fundamentalen Theorie der Starken Wechselwirkung. Die systematische, chirale Entwicklung ermöglicht verbesserbare Rechnungen mit theoretischen Unsicherheitsabschätzungen. In den letzten Jahren wurden chirale Vielteilchenkräfte bis in hohe Ordnungen ausgearbeitet. Konsistente Rechnungen mit allen Vielteilchenbeiträgen auf der sogenannten „next-to-next-to-next-to-leading order“ (N^3LO) sind daher möglich. Viele weitere Fortschritte führten zu der Entwicklung von neuen chiralen Potentialen innerhalb verschiedener Regularisierungschemen.

Wir entwickeln fortgeschrittene Methoden für mikroskopische Berechnungen der Zustandsgleichung von homogener Kernmaterie mit beliebigem Proton-zu-Neutron-Verhältnis am Temperatur-Nullpunkt. Im Speziellen setzen wir die Maßstäbe für Vielteilchen-störungstheoretische Ansätze zu hohen Ordnungen in der chiralen und der Vielteilchen-Entwicklung. Um die schwierige Einbindung von Dreinukleon-Kräften zu ermöglichen, führen wir eine neue Partialwellen-Methode für die Normalordnung ein, welche die Behandlung dieser Beiträge verallgemeinert. Wir treffen verbesserte Vorhersagen für die Zustandsgleichung von Neutronenmaterie mit konsistenten N^3LO Nukleon-Nukleon- (NN) plus Dreinukleon- (3N) Potentialen bis zur dritten Ordnung in der Vielteilchenstörungstheorie und in der Methode der selbstkonsistenten Greens-Funktionen. Letztere erlaubt nichtperturbative Vergleichsrechnungen zum Bestimmen der Vielteilchenkonvergenz. Wir erweitern außerdem die Methode zur Normalordnung zu endlichen Temperaturen.

Berechnungen von asymmetrischer Materie setzen zusätzlich zuverlässige Fitwerte für die Niederenergiekopplungen, die zu den 3N Kräften beitragen, voraus. Das war bisher nicht der Fall für N^3LO Rechnungen. Wir zeigen ein neues Monte-Carlo Framework für perturbative Rechnungen mit Zwei-, Drei- und Viernukleonen-Wechselwirkungen, das es auf effiziente Weise erlaubt (zusammen mit dem automatischen Generieren von Quellcode), verschiedene Ordnungen in der Störungstheorie als auch in der chiralen EFT zu berechnen. Die Leistungsfähigkeit der Methode ist so angelegt, dass sie zur Optimierung von neuen chiralen Potentialen im Sinne von Saturierungseigenschaften benutzt werden kann. Als einen ersten Schritt in diese Richtung, studieren wir Kernmaterie basierend auf evolvierten chiralen Wechselwirkungen, welche eine sehr gute Vielteilchenkonvergenz bis zur vierten Ordnung aufweisen. Wir untersuchen dann neue chirale Wechselwirkungen bis zur N^3LO, wobei simultane Fits an das Triton und an Saturierungseigenschaften mit natürlichen 3N-Niederenergiekopplungen erzielt werden können.

Wir führen eine umfassende Weinberg-Eigenwert-Analyse mit einer repräsentativen Menge von modernen lokalen, semilokalen und nichtlokalen chiralen NN-Wechselwirkungen durch. Unsere detaillierten Vergleiche anhand von Weinberg-Eigenwerten gewähren verschiedenste Einblicke in die Eigenheiten von chiralen Potentialen für verschiedene Ordnungen und Partialwellen. Wie zeigen, dass ein direkter Vergleich von numerischen Cutoff-Werten für verschiedene Wechselwirkungen, aufgrund der unterschiedlichen analytischen Form von Regulatoren, täuschen kann. Das zeigt, Weinberg-Eigenwerte können auch als nützliche Hilfsmittel beim Erstellen von neuen Wechselwirkungen dienen.

Wir präsentieren weiterhin Lösungen der BCS-Gleichung der Energielücke in den Kanälen ${}^1S_0$ und ${}^3P_2$–${}^3F_2$ in Neutronenmaterie. Unsere Studien basieren sowohl auf nichtlokalen NN- plus 3N-Wechselwirkungen bis zur N^{3}LO, als auch auf den zuvor genannten lokalen und semilokalen chiralen NN-Wechselwirkungen bis zur N^{2}LO beziehungsweise bis zur N^{4}LO. Im Speziellen untersuchen wir den Einfluss von N^{3}LO 3N-Kräften auf die Energielücke und leiten Unsicherheitsabschätzungen her, in dem wir Ergebnisse auf verschiedenen Ordnungen der chiralen Entwicklung berücksichtigen. Zusätzlich werden verschiedene Methoden zum Lösen der BCS-Gleichung der Energielücke diskutiert. Neben einer oft benutzten quasilinearen Methode, zeigen wir, dass die modifizierte Broyden-Methode gut anwendbar ist und ein robustes Konvergenzverhalten aufweist.

Contents

1 Introduction 7

1 Introduction

1.1 Motivation

Nuclear matter is an ideal environment for testing nuclear forces with important consequences for finite nuclei as well as nuclear astrophysics in general [1]. The equation of state allows the prediction of key quantities relevant for neutron stars and their formation in core-collapse supernovae [2, 3]. Being able to interconnect the microscopic length scales of nuclei with the macroscopic scales of neutron stars [4] makes studies of the equation of state of nuclear matter very exciting.

Pioneered by Steven Weinberg and others in the early 1990's chiral effective field theory (EFT) nowadays has become the standard approach to nuclear forces at low-energy scales [5, 6], where momenta are of the order of the pion mass $Q \sim m_\pi$, i.e., lower than the breakdown scale $\Lambda_b \sim 500\,\mathrm{MeV}$ of the theory. Chiral EFT provides a systematic and improvable expansion in powers of $Q/\Lambda_b \sim 1/3$ based on the symmetries of the fundamental theory of strong interactions, quantum chromodynamics (QCD). The dominant implementation of chiral EFT considers nucleons and pions as degrees of freedom and a hierarchy of many-body forces specified by Weinberg power counting in which nucleon-nucleon interactions provide the most important contributions. Not explicitly resolved high-energy physics (such as Δ-excitations) is captured in low-energy constants (LECs) fit to experimental data.

In recent years, significant progress has been made in deriving chiral forces to high orders (see Ref. [7] for a recent review). While consistent nucleon-nucleon (NN), three- (3N), and four-nucleon (4N) forces can in principle be applied, state-of-the-art calculations are still at $\mathrm{N^2LO}$ or based on inconsistent $\mathrm{N^3LO}$ NN plus $\mathrm{N^2LO}$ 3N forces [1]. Apart from computational aspects, this is due to the lack of reliable fit values at $\mathrm{N^3LO}$ for the two 3N LECs that contribute to the $\mathrm{N^2LO}$ 3N forces. All other many-body contributions are predicted by pion-pion, pion-nucleon, and nucleon-nucleon physics. Meanwhile, the NN interactions have been worked out order-by-order up to $\mathrm{N^4LO}$ [8–11] and even partly at $\mathrm{N^5LO}$ [12].

Chiral interactions require moreover an ultraviolet regularization scheme associated with a cutoff scale, or possibly different scales in separate many-body sectors [9]. The broad freedom in choosing the functional form of the regulator has resulted in various new families of chiral NN potentials with conceptionally different regulators schemes: either in momentum [8, 11, 13–15] or coordinate space [16, 17], but also a mixed approach [9, 10] has been introduced recently. Although the regulator choice should be arbitrary, in practice, the actual form can have important consequences at a given order in the chiral expansion, referred to as regulator artifacts [18].

In addition to the development of new fit procedures, e.g., simultaneously optimizing NN plus 3N forces [13, 14], uncertainty quantification using statistical methods [15] (such as Bayesian analyses [19–21]) has started to obtain attention in recent years. All of these new potentials combined with further advances in the many-body frameworks, renormalization group techniques, and the continuously increasing computational resources eventually led nuclear physics to an era of precision.

Microscopic predictions of finite nuclei are the central goals of nuclear-structure studies [1]. The left panel in Fig. 1 compares ground-state energies and charge radii of several nuclei as obtained in ab initio calculations (dark-gray symbols) with experimental data (horizontal lines) [14]. In theory, the general issue is that many interactions overbind medium-mass to heavy nuclei and underestimate their radii [14, 15, 24]. Therefore, Ref. [14] included also heavier nuclei in the optimization protocol of the potential called $\mathrm{NNLO_{sat}}$. The agreement with experiment is manifested by the red diamonds in Fig. 1 (see also Refs. [4, 25, 26]). Nuclear-matter calculations moreover showed that $\mathrm{NNLO_{sat}}$ has at same time realistic saturation properties, especially, the saturation density is within the empirically-known range [14]. Saturation refers here to the empirical fact that both, the density as well as the binding energy of heavy

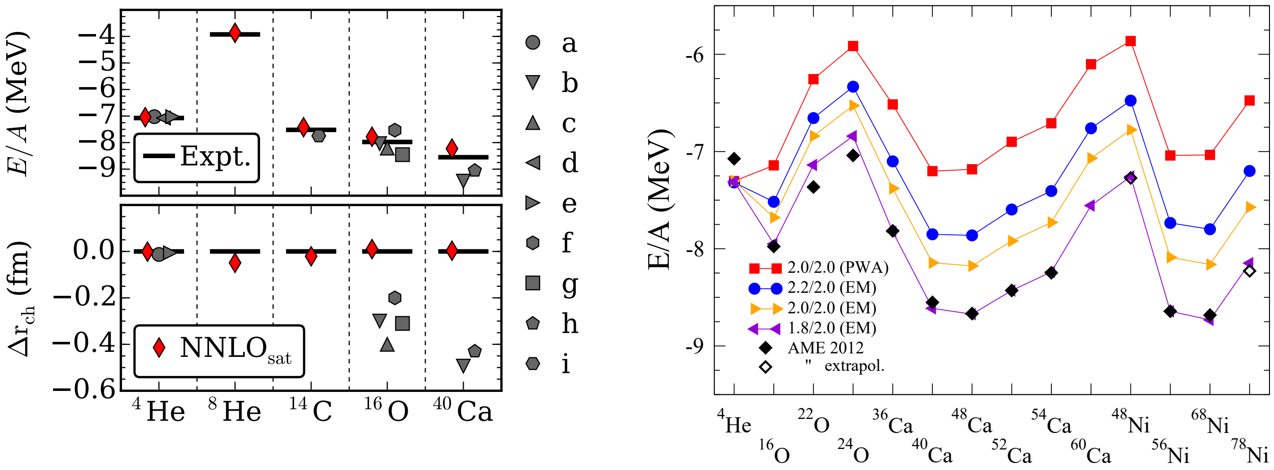

Figure 1: Left: Ground-state energy per particle E/A (upper row) and computed charge radii relative to experiment Δr_{ch} (lower row) for selected nuclei based on chiral Hamiltonians (symbols). The experimental results are depicted by horizontal lines. The figure has been taken from Ref. [14]. Right: Ground-state energy per particle E/A up to heavier nuclei calculated in IM-SRG (extrapolated for ^{48,78}Ni) based on four chiral Hamiltonians used in this work (colored symbols). Experimental data [22] is depicted by black symbols. The figure has been taken from Ref. [23]

nuclei are approximately constant. This gives evidence that reproducing binding energies, charge radii, and saturation properties should be considered on an equal footing.

Using the ab initio in-medium similarity renormalization group (IM-SRG), Ref. [23] recently studied binding energies (as well as charge radii) also for heavier systems based on four established chiral NN plus 3N Hamiltonians [27] used in this work. The results are shown in the right panel of Fig. 1. It is important to stress that the 3N forces were only fit to few-body data. Even though these interactions reproduce few-body data with same accuracy the situation can be different for medium-mass nuclei. To be specific, only the Hamiltonian "1.8/2.0" (purple symbols) agrees with experimental energies (black symbols), whereas the others follow the same trend but are shifted up to $\sim 1.5\,\mathrm{MeV}$ per particle [23]. The charge radii show a similar systematic behavior [23]. Qualitatively, these observations could be related to the Coester-like band of the corresponding saturation points, which we have calculated in Ref. [28]. These findings [23] indeed suggest that saturation properties are important for the accurate description of finite nuclei [14, 23, 29, 30]. Moreover they underline that saturation properties (e.g., from perturbative calculations) can be used as a guidance tool for constraining fits of next-generation chiral interactions. This required, however, a better understanding of the many-body convergence [31, 32] as well as the development of a novel efficient framework to be feasible in practice [32].

Homogeneous nuclear matter represents the theoretical testbed for benchmarking saturation properties. It is an idealized system obtained by extrapolating (heavy) nuclei to infinite mass number A and disregarding Coulomb interactions. Figure 2 depicts schematically the energy per particle $E/A(\beta, n)$ of nuclear matter as a function of the total nucleon density $n = n_p + n_n$. Here, n_p labels the proton and n_n the neutron density. To measure the neutron excess of the system the asymmetry parameter $\beta = 1 - 2x$ can be introduced, or likewise the proton fraction $x = n_p/n$. Neutron matter (cyan line) is unbound and represents the neutron-rich extreme ($\beta = 1$) in Fig. 2. Adding protons ($0 < \beta \leqslant 1$) lowers the energy per particle for (isospin-)asymmetry matter (green line) until bound (isospin-)symmetric nuclear matter (brown line) with equal nucleon densities ($\beta = 0$) is obtained. The energy difference between neutron and symmetric matter,

$$S(n) = \frac{E}{A}(\beta = 1, n) - \frac{E}{A}(\beta = 0, n) \tag{1.1}$$

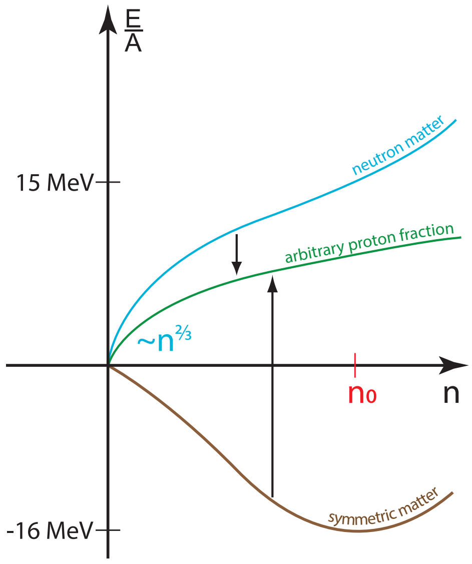

Figure 2: Illustration of the energy per particle $E/A(\beta, n)$ of nuclear matter as a function of the asymmetry β and the total nucleon density n: neutron matter ($\beta = 1$, cyan line), isospin-asymmetric matter ($0 < \beta \leqslant 1$, green line), and isospin-symmetric matter ($\beta = 0$, brown line). At nuclear saturation density $n_0 \simeq 0.16\,\text{fm}^{-3}$, $E/A(\beta = 0, n)$ has a minimum with respect to density and asymmetry.

is called (nuclear) symmetry energy. We empirically know that the energy per particle in symmetric matter has a minimum with respect to n at so-called saturation density n_0, which is associated with the saturation energy $E/A(\beta = 0, n_0) = -a_V$. The latter corresponds to the volume term in the Bethe-Weizsäcker mass formula [33] in absence of Coulomb interactions. Since symmetric matter minimizes in addition the energy with respect to β, one usually expands $E/A(\beta, n)$ in a Taylor series about $\beta = 0$ (see, e.g., Refs. [34, 35]),

$$\frac{E}{A}(\beta, n) = \frac{E}{A}(\beta = 0, n) + \beta^2 E_{\text{sym}}(n) + \mathcal{O}\left(\beta^4\right), \tag{1.2}$$

where we have neglected higher-order corrections in $\beta^{4,6,\dots}$ to good approximation [36] such that $E_{\text{sym}}(n) \simeq S(n)$. However, Refs. [35, 37] showed that these contributions should be investigated further. Only even powers in β contribute due to (approximate) isospin symmetry. Expanding also the density dependence of the coefficients in Eq. (1.2) about n_0,

$$\frac{E}{A}(\beta = 0, n) = -a_V + \frac{K}{18}\left(\frac{n - n_0}{n_0}\right)^2 + \dots, \qquad \text{and} \qquad E_{\text{sym}}(n) = S_v + \frac{L}{3}\left(\frac{n - n_0}{n_0}\right) + \dots, \tag{1.3}$$

imposes the incompressibility K, the slope parameter L of the symmetry energy, and the symmetry energy at saturation density $S_v = E_{\text{sym}}(n_0)$. Within these truncations, only a few parameters, i.e., $n_0 \simeq 0.16\,\text{fm}^{-3}$ (or $\rho_0 \simeq 2.7 \cdot 10^{14}\,\text{g}\,\text{cm}^{-3}$), $a_V \simeq 16\,\text{MeV}$ [38], $K \simeq 240\,\text{MeV}$ [39], $S_v \simeq 32\,\text{MeV}$, and $L \simeq 55\,\text{MeV}$ [40], parametrize the nuclear-matter equation of state. Reproducing empirical ranges is a key benchmark for nuclear interactions. Figure 3 summarizes experimental constraints on the $S_v - L$ correlation, which overlap in the rather small white area. Nevertheless, the strikingly wide ranges from different extractions indicate that especially L is not well constrained. In fact, the most precise constraints are due to the neutron-matter calculations by Hebeler *et al.* [41–43] based on many-body perturbation theory (MBPT) and chiral NN plus 3N interactions, and from quantum Monte Carlo calculations by Gandolfi *et al.* [44] for Hamiltonians adjusted to a fiducial S_v range. Additional constraints are therefore crucial [40, 45], e.g.,

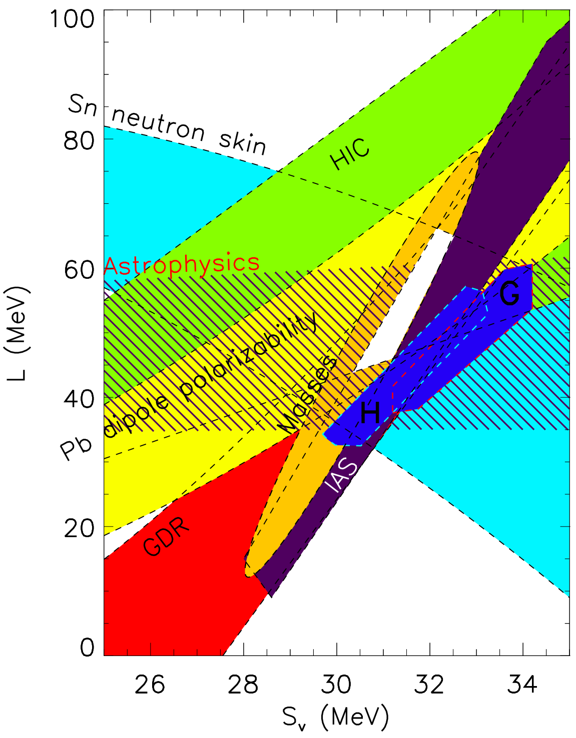

Figure 3: Several experimental constraints on the symmetry energy S_v at saturation density and its slope parameter L: from nuclear masses [49], from analyses of isobaric analog states (IAS) [50], from the neutron skin thickness of tin (Sn) isotopes [51], from heavy-ion collisions (HIC) [52], from the dipole polarizability of ^{208}Pb [53, 54], from giant dipole resonances (GDR) [55], and from modeling $M-R$ relations ("astrophysics") [56]. In addition, the two blue regions depict theoretical constraints from neutron-matter calculations by Hebeler *et al.* (H) [41, 42] and Gandolfi *et al.* (G) [44]. The figure has been taken from Ref. [56] (see also Ref. [57]).

from measurements of ^{48}Ca nuclei [46, 47] that can also be reached in ab initio calculations [4]. On the theory side, this requires, in particular, an improved treatment of 3N forces in many-body calculations [28], reliable fit values for the 3N LECs at N^{3}LO [32], and studies of asymmetric matter [28, 36, 37, 48].

Neutron stars [2, 58] are fascinating stellar objects. With masses of $M \sim 1.5\,M_\odot$ (solar masses) and radii of $R \sim 12\,\mathrm{km}$, for instance, they are one of the densest forms of matter in the observable universe [59]. Constraining the neutron-star equation of state as well as the $M-R$ relation is thus a frontier in astrophysics [3, 60–64]. Two observations already demonstrated that their maximum mass is at least $\sim 2\,M_\odot$ [58, 65], whereas precise radius measurements have not been achieved yet [3]. Taking advantage of the lower maximum mass limit, nuclear-matter calculations based on chiral interactions lead to tight constraints [41, 42]. This is remarkable because typical central densities in neutron stars of several times saturation density exceed the low-energy region of chiral EFT. Therefore, large extrapolations in density are necessary to obtain the $M-R$ relation as solution of the Tolman-Oppenheimer-Volkoff (TOV) equations. Causality and observational data are key constraints to rule out unphysical equations of state [42].

Interestingly, Ref. [66] found an empirical correlation between R and the pressure $p(n)$ of neutron-star matter, as indicated in Fig. 4 for several equations of state. The typical proton fraction $x \sim 5$ % in

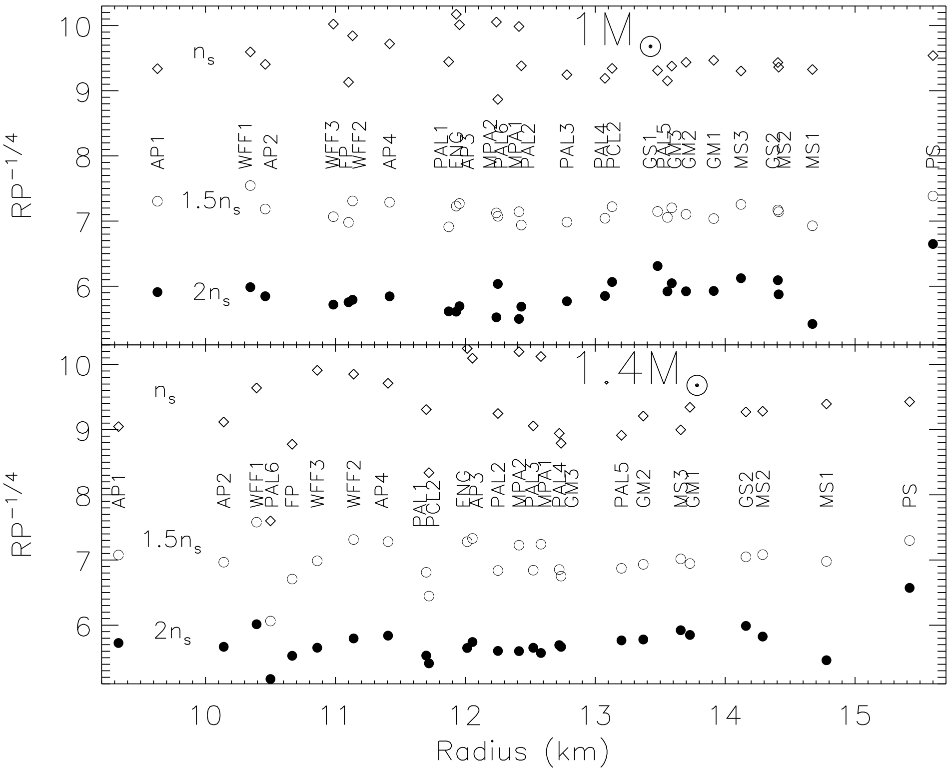

Figure 4: Empirical relation between pressure $p(n)$ and neutron-star radius R for several equations of state. The upper (lower) panel plots the approximate constant $Rp^{-1/4}$ given a $1.0\,M_\odot$ ($1.4\,M_\odot$) neutron star and the densities $n = n_0$, $1.5\,n_0$, as well as $2\,n_0$ (symbols). The figure has been taken from Ref. [66]. Note that the updated analysis in Ref. [57] also accounts for the observation of the first $2\,M_\odot$ neutron star by Demorest *et al.* [65].

β-equilibrated matter is rather small. At saturation density, for a $1.4\,M_\odot$ neutron star, the (updated) empirical correlation reads [57]

$$R(n_0,\, 1.4\,M_\odot) = (9.52 \pm 0.49) \left(\frac{p(n_0)}{1\,\mathrm{MeV\,fm^{-3}}} \right)^{\frac{1}{4}} \mathrm{km}\,, \tag{1.4}$$

where $p(n_0) = n_0^2\, \partial_n E/A(\beta \sim 0.9,\, n)|_{n=n_0}$ is mainly given by L. In consequence, radius predictions (for a given mass) are sensitive to uncertainties in this quantity, consistent to the narrow ranges in Fig. 3 from neutron-matter calculations and the corresponding constraints in Refs. [41, 42]. Using the empirical correlation (1.4) combined with tightly-constrained S_v and L, we also obtained a narrow range for the radius of $1.4\,M_\odot$ neutron star, $11.1\,\mathrm{km} \leqslant R_{1.4\,M_\odot} \leqslant 12.7\,\mathrm{km}$ [4], which underlines that pinning down the symmetry energy and its density dependence is highly-relevant for astrophysical applications.

The present thesis addresses all of these exciting physics challenges. We initiate detailed asymmetric-matter studies using novel methods in order to extent previous state-of-the-art MBPT calculations to high orders in the chiral as well as the many-body expansion. To this end, we also focus on the improved treatment of 3N forces, particularly at N^{3}LO, while making them accessible in general nuclear-matter considerations. We present several applications after assessing the many-body convergence. This naturally leads us to the construction of chiral Hamiltonians involving all many-body forces at N^{3}LO with realistic saturation properties. For tight astrophysical predictions, we perform for the first time neutron- and symmetric-matter calculations up to fourth order in MBPT, enabled by the development of an efficient

Monte-Carlo framework. Further, we provide quantitative insights into recent potentials within different regularization schemes. This paves the way for guiding optimizations of next-generation chiral potentials in terms of empirical saturation properties and triggers ab initio studies of finite nuclei based on these interactions.

We organize the thesis as follows. In Secs. 1.2 and 1.3, we briefly introduce chiral EFT and set the stage for our improved nuclear-matter calculations. Section 2 reviews the operatorial definitions of the chiral many-body forces which are relevant for all of our calculations. In this section, we also discuss the details of the recent local, semilocal, and nonlocal chiral NN potentials, developed by Gezerlis, Tews *et al.* (2013 [16, 17]), Epelbaum, Krebs, and Meißner (2015) [9, 10], Entem, Machleidt, and Nosyk (2017) [11] as well as Carlsson, Ekström *et al.* (2016) [15], respectively.

In Sec. 3, we perform a comprehensive Weinberg eigenvalue analysis based on this representative set of NN potentials. Our detailed comparison in terms of Weinberg eigenvalues provides crucial insights into their idiosyncrasies for different orders and partial waves.

We develop in Sec. 4 an improved normal-ordering framework that allows to include general 3N interactions in nuclear-matter calculations, starting from a plane-wave partial-wave-decomposed form. We then make use of this method and include for the first time N^{3}LO 3N interactions in MBPT up to third order and in self-consistent Green's function (SCGF) theory. Using these two complementary many-body frameworks, we provide improved predictions for the equation of state of neutron matter at zero temperature and also analyze systematically the many-body convergence for different chiral EFT interactions. Furthermore, the normal-ordering framework is extended to finite temperatures.

We present in Sec. 5 an efficient Monte-Carlo framework for perturbative calculations of nuclear matter based on NN, 3N, and 4N interactions. The method enables the incorporation of all many-body contributions in a straightforward and transparent way. After first fourth-order calculations with chiral low-momentum interactions, we explore new chiral interactions up to N^{3}LO.

In Sec. 6, we discuss solutions of the BCS gap equation in the channels $^1S_0$ and $^3P_2-^3F_2$ in neutron matter based on the mentioned local and semilocal chiral NN interactions. In addition, we investigate for the first time the impact of N^{3}LO 3N forces on pairing gaps and derive uncertainty estimates by taking into account results at different orders in the chiral expansion. We also discuss different methods for obtaining self-consistent solutions of the gap equation, including the first application of the modified Broyden method to the BCS gap equation.

Finally, we conclude and give an outlook in Sec. 7.

Throughout the thesis we use natural units, i.e., $\hbar = c = \hbar c = k_B = 1$.

1.2 Chiral effective field theory

Nuclear interactions derived within chiral EFT are central for the present thesis. Starting with QCD we briefly review in this section the theoretical basics of chiral-symmetry breaking and its consequences for chiral EFT. We also introduce the hierarchy of chiral forces as well as theoretical uncertainty estimates based on the expected scaling behavior of chiral EFT. Comprehensive introductions can be found in Refs. [5–7, 67–70].

1.2.1 Quantum chromodynamics and chiral symmetry

The fundamental theory of strong interactions is quantum chromodynamics (QCD) [71]. It describes hadrons as composite particles made of elementary spin-$\frac{1}{2}$ quarks which interact via gluon exchanges. There are in total six known quark flavors as summarized in Table 1 including their charge, isospin, and approximate mass. In addition, (anti)quarks carry color charge, (anti)red, (anti)green, or (anti)blue, corresponding to the additive color model RGB, whereas gluons carry both, a color and an anticolor. The additional degree of freedom is introduced because isolated quarks have not been observed: they are confined to color-neutral hadrons. At high temperatures and/or high densities deconfinement sets in, forming a so-called quark-gluon plasma or a color-superconductor. Color-neutral hadrons consist of two quarks with color and anticolor (meson) or three different colors (baryon), but also exotic pentaquarks [72] and tetraquarks [73, 74] have been discovered recently at the Large Hadron Collider (LHC).

An important property of QCD is that the strong coupling strength [75],

$$\alpha_s(Q) = \frac{6\pi}{33 - 2N_f} \log^{-1}\left[\frac{Q}{\Lambda_{\text{QCD}}}\right], \tag{1.5}$$

depends significantly on the momentum scale Q (see also Ref. [76]). It is therefore called running coupling. In Eq. (1.5) $\Lambda_{\text{QCD}} \sim 200$ MeV denotes the characteristic scale of QCD and N_f is the number of active flavors. With increasing energy α_s goes to zero such that QCD is perturbative at high-energy scales [77]. This is called asymptotic freedom [78, 79] and its discovery was recognized by a Nobel prize to Gross, Politzer, and Wilczek in 2004. However, at low-energy scales QCD is strongly nonperturbative (i.e., $\alpha_s \gtrsim 1$), which makes direct applications to finite nuclei or nuclear matter very involved, if currently feasible at all. A promising approach to address these challenges is lattice QCD [80]: the space-time is discretized on a four-dimensional grid of finite volume, where quarks sit on the lattice points and gluons on the links between them. Observables are calculated from correlation functions after computing high-dimensional path integrals using Monte-Carlo integration. These extremely-demanding calculations are limited by computational resources. Effective field theories, nevertheless, can be used to extrapolate lattice results to the continuum limit and to physical quark masses. Vice versa, constraining LECs by lattice QCD would allow exciting first-principles studies of nuclear matter as well as finite nuclei (see also Ref. [81]).

As preparation for chiral effective field theory, we discuss in the following the symmetries of QCD for the three lightest quark flavors (based on Refs. [6, 83]). The QCD Lagrangian is given by

$$\mathscr{L}_{\text{QCD}} = \sum_{f=u,d,s} \left(\bar{q}_f i \not{D} q_f - m_f \bar{q}_f q_f\right) - \frac{1}{2} \text{Tr}\, G_{\mu\nu} G^{\mu\nu}, \tag{1.6}$$

with $\not{D} = \gamma^\mu D_\mu$, the covariant derivative $D_\mu = \partial_\mu + i g_s A_\mu$, the strong coupling constant g_s associated with $\alpha_s = g_s^2/(4\pi)$, the quark fields q_f as well as masses m_f, the gluon fields A_μ, and the gluon field strength $G_{\mu\nu}$. Let us first consider the chiral limit of vanishing quark masses, $m_f \to 0$. Introducing left- and

Table 1: Properties of the six quarks (for details see Ref. [82]). Up, down, and strange quarks are much lighter than the others. For example, the quark content of protons and neutrons is (uud) and (udd), respectively.

flavor (f)	charge in e	isospin	mass (m_f) in MeV
up	$+\frac{2}{3}$	$+\frac{1}{2}$	≈ 2
down	$-\frac{1}{3}$	$-\frac{1}{2}$	≈ 5
strange	$-\frac{1}{3}$	–	≈ 96
charm	$+\frac{2}{3}$	–	≈ 1280
bottom	$-\frac{1}{3}$	–	≈ 4180
top	$+\frac{2}{3}$	–	≈ 173000

right-handed quark fields $q_{L,i} = 1/2(1-\gamma_5)q_i$ and $q_{R,i} = 1/2(1+\gamma_5)q_i$, respectively, the Lagrangian (1.6) reads

$$\mathscr{L}^0_{\mathrm{QCD}} = \sum_{f=u,d,s} \left[\bar{q}_{L,f}\, i\not{D}\, q_{L,f} + \bar{q}_{R,f}\, i\not{D}\, q_{R,f}\right] - \frac{1}{2}\mathrm{Tr}\; G_{\mu\nu}G^{\mu\nu}\,, \tag{1.7}$$

which has a global $\mathrm{U}(3)_L \times \mathrm{U}(3)_R$ symmetry in flavor space, i.e., Eq. (1.7) is invariant under rotations of left- and right-handed quarks by independent unitary matrices. This group can also be written as $\mathrm{SU}(3)_L \times \mathrm{SU}(3)_R \times \mathrm{U}(1)_A \times \mathrm{U}(1)_V$. The vector symmetry $\mathrm{U}(1)_V$ corresponds to the baryon number (an exact symmetry also for nonzero quark masses), whereas the axial symmetry $\mathrm{U}(1)_A$ is broken by the axial anomaly. Further, chiral symmetry $\mathrm{SU}(3)_L \times \mathrm{SU}(3)_R$ allows independent rotations of left- and right-handed quarks in terms of SU(3) matrices. For nonzero quark masses, however, it is explicitly broken due to the mass term in the Lagrangian (1.6),

$$\sum_f m_f\, \bar{q}_f q_f = \sum_f \bar{q}_{R,f}\, m_f\, q_{L,f} + \mathrm{h.c.}\,. \tag{1.8}$$

Assuming equal but nonzero quark masses $\mathrm{SU}(3)_L \times \mathrm{SU}(3)_R$ reduces to its subgroup $\mathrm{SU}(3)_V$. As can be seen in Table 1 the mass difference of up and down quarks is indeed small, leading to approximate isospin symmetry $\mathrm{SU}(2)_V \subset \mathrm{SU}(3)_V$. Chiral symmetry is in addition spontaneously broken, even in the chiral limit, as indicated by the absence of parity doublets in nature. For instance, the ρ-meson ($J^P = 1^-$) and its partner the a_1-meson ($J^P = 1^+$) have the same quantum numbers except for parity but fairly different masses. Isospin symmetry, on the other hand, is approximately observed by comparable masses of the three charged states ρ^0 and $\rho^\pm$ [6]. A spontaneously-broken continuous symmetry gives rise to a so-called Goldstone boson for each generator [84]. These particles are massless in case the broken symmetry was exact. Since chiral symmetry is also explicitly broken we therefore deal with so-called pseudo-Goldstone bosons that have finite mass: pions, kaons, and the η-meson. Pions are the lightest because of they have no strange-quark content.

1.2.2 Hierarchy of chiral many-body forces

Chiral effective field theory (EFT) was pioneered by Steven Weinberg in a series of publications in the early 1990's [85–87] (see also Ref. [88]) and has become since then the modern approach to nuclear forces [5, 6]. It considers nucleons as well as pions as the relevant degrees of freedom at the low-energy scales of nuclear physics, where the fundamental quarks and gluons are not resolved. Different choices may be efficient as well (or even more efficient) depending on the energy scale of interest, e.g., below the pion mass, also pions are integrated out, called pion-less EFT [89] (see Ref. [90] for a recent application). Another example is Δ-full EFT that is expected to improve the convergence of chiral EFT by using nucleons, pions, and Δ-resonances as degrees of freedom [5, 6]. Hence, EFTs inherently predict their own breakdown. For chiral EFT, the breakdown scale roughly corresponds to the mass of heavier mesons, in particular, the ρ-mesons: $\Lambda_b \sim 500\,\mathrm{MeV} < m_\rho$ is a more conservative value [9]. Above the breakdown scale additional degrees of freedom have to be added to the theory. Although not treated explicitly those contributions are still encoded in LECs fit experimental data. Using these effective degrees of freedom, one determines the most general Lagrangian, $\mathscr{L}_{\mathrm{EFT}} = \mathscr{L}_{\pi\pi} + \mathscr{L}_{\pi\mathrm{N}} + \mathscr{L}_{\mathrm{NN}} + \ldots$, consistent with the exact and broken symmetries of QCD [88]. Note that this connection to the fundamental theory distinguishes chiral EFT from phenomenological approaches (e.g., Refs. [91–93]). In the Lagrangian, $\mathscr{L}_{\pi\pi}$ contains the dynamics between pions, $\mathscr{L}_{\pi\mathrm{N}}$ the pion-nucleon interactions, and $\mathscr{L}_{\mathrm{NN}}$ the nucleon-nucleon contact interactions, while the ellipsis accounts for contributions with two or more nucleons and pions, or A-nucleon contact interactions [6]. The infinitely many terms of the effective Lagrangian can be organized in powers of the expansion parameter, i.e., Q^ν with

$$Q(p) = \max\left(\frac{p}{\Lambda_b}, \frac{m_\pi}{\Lambda_b}\right) . \tag{1.9}$$

Equation (1.9) is the ratio of a typical nucleon momentum p or the pion mass m_π (soft scale) and Λ_b (hard scale). The value $Q(p) \sim 1/3$ suggests that higher-order terms are sufficiently less important, if the coefficients of the expansion (including the LECs) are of natural size. In analogy to the multipole expansion in electrodynamics, the idea is to successively work out different orders Q^ν until the desired accuracy is obtained. This can be done because only finite number of terms and LECs contributes at each order (see below), being crucial for the predictive power of chiral EFT. Furthermore, the systematic expansion naturally allows to estimate the neglected contributions in form of theoretical uncertainties (see Sec. 1.2.3). One derives, practically, nuclear forces in a diagrammatic representation based on the effective Lagrangian at a given order. To associated these diagrams with their corresponding order ν a power-counting scheme is required. Weinberg power counting [85, 86] is based on dimensional analysis and obtains for a diagram involving N nucleons [5, 6]

$$\nu = -2 + 2N + 2(L - C) + \sum_i \Delta_i \,, \qquad \text{with} \qquad \Delta_i = d_i + \frac{n_i}{2} - 2 \geqslant 0\,, \tag{1.10}$$

Here, L specifies the number of loops and C denotes the number of separately connected pieces. The sum goes over all vertices i, where d_i represents the number of derivatives or pion mass insertions and n_i is the number of nucleon fields. Based on the power counting (1.10) Fig. 5 depicts the hierarchy of chiral forces up to N^{4}LO. The orders $\nu = 0, 2, 3, \ldots$ are referred to as leading order (LO), next-to-leading order (NLO), next-to-next-to-leading order (N^{2}LO), respectively, and so on. Notice that $\nu = 1$ is forbidden due to parity as well as time-reversal invariance [6].

We give in the following a brief overview of the chiral forces up to N^{4}LO based on Refs. [6, 7]. Section 2 is then dedicated to a detailed discussion including the operatorial expressions relevant for our work, antisymmetrization, and regularization. One expects the dominant contributions in the chiral expansion from LO NN forces. They are given by momentum-independent (i.e., S-wave) contact interactions plus the long-range 1π-exchange potential. Nucleons (pions) are depicted in Fig. 5 by solid (dashes) lines. At NLO, momentum-dependent contacts (up to P-waves) as well as the 2π exchange for the intermediate-range attraction start contributing. Many-body forces are suppressed, $V_{\mathrm{NN}} \gg V_{3\mathrm{N}} \gg V_{4\mathrm{N}} \ldots$, specifically, the first nonvanishing 3N forces appear at N^{2}LO in three topologies (orange-shaded). The 3N 2π exchange is governed by the LECs $c_{1,3,4}$, similar to the 2π exchange in the NN forces at this order. Different determini-

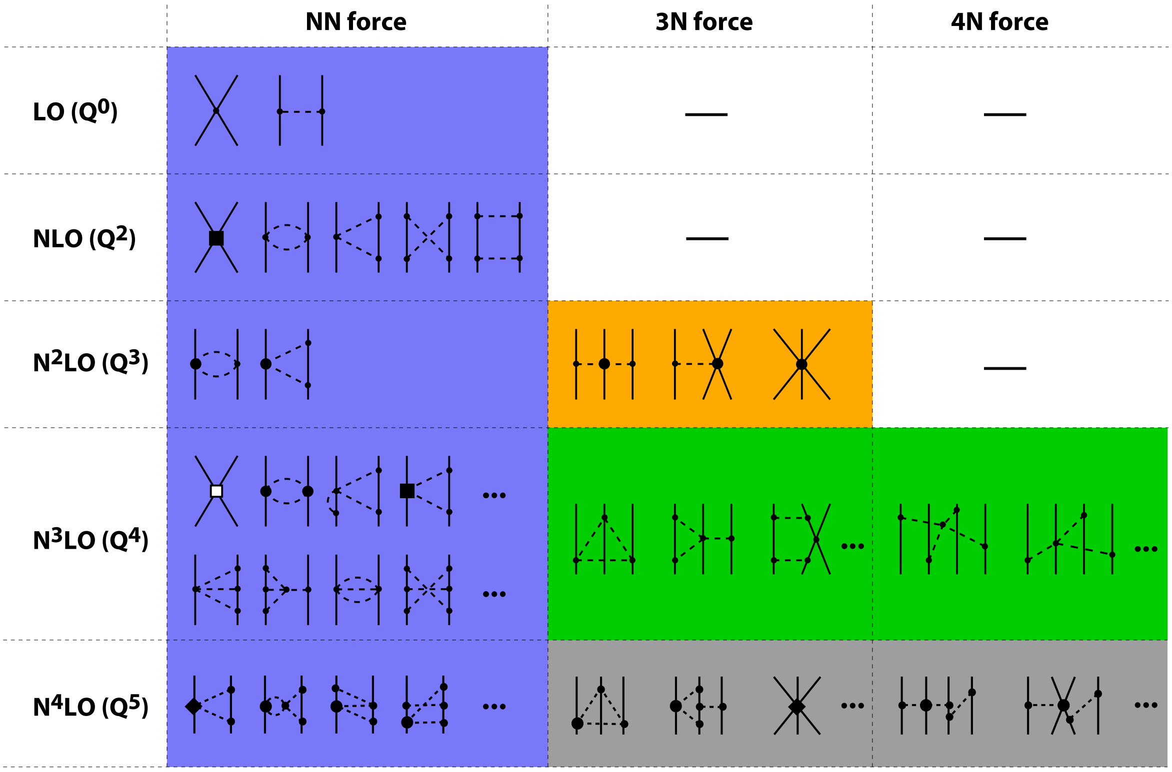

Figure 5: Hierarchy of chiral nuclear forces up to N^{4}LO. The diagrams are organized according to Weinberg power counting (1.10). Dashed lines denote pions, solid lines denote nucleons. Solid dots, filled circles, filled rectangles, filled diamonds, and open rectangles depict vertices with $\Delta_i = 0, 1, 2, 3, 4$, respectively. Blue-, orange-, and green-shaded diagrams are available for calculations, whereas the others (gray-shaded) are currently under development (3N forces) or have not been worked out yet (4N forces). The figure has been modified from Ref. [94], see also Refs. [6, 69].

ations of these show significant deviations of the order of 30 % but agree within the uncertainties [70]. Additionally, the 3N LECs c_D and c_E emerge from the 1π-exchange-contact and the pure 3N contact interaction, respectively, which can be fit to few-body observables. There are no additional contacts due to N^{2}LO NN forces. At N^{3}LO, one has subleading 3N interactions as well as the first nonvanishing 4N forces (green-shaded). Both are free of unknown parameters. Moreover, contact interactions (up to *D*-waves), 2π exchanges, and the appearance of 3π exchanges in the NN forces complete this order. At N^{4}LO, further corrections to these pion exchanges occur. The derivation of the 3N interactions at this order is currently ongoing [95, 96], while the 4N forces have not been worked out yet (gray-shaded). During the course of the thesis we study NN forces up to N^{4}LO and perform nuclear-matter calculations with consistent many-body contributions up to N^{3}LO.

1.2.3 Theoretical uncertainties

As discussed in the previous section, the EFT framework allows to estimate theoretical uncertainties for an observable $X(p)$ at a given momentum scale p [9]. In this work, $X(p)$ corresponds to the energy per particle of nuclear matter as well as the pairing gap, associated with the Fermi momentum (or its average). Uncertainties arise in chiral EFT from several sources [9], e.g., from the truncation of the chiral expansion [9, 15, 19, 97], or from the determination of πN and contact LECs [15, 21, 98–100]. The cited references already indicate that nowadays advanced statistical techniques are being used to study theoretical uncertainties in more detail. We refer the reader to Ref. [20] for a comprehensive recipe for uncertainty quantification using Bayesian methods [101]. The employed framework to calculate the observable leads to additional uncertainties. These will be addressed in Sec. 1.3.1 for many-body perturbation theory.

Cutoff variation in the regulator function (see Sec. 2.1.1) measures the sensitivity to neglected contact interactions and thus systematic uncertainties due to the truncation of the chiral expansion. However, the residual cutoff dependence can be quite misleading as the example in Ref. [9] demonstrates. Regarding NN forces, contacts appear only at even orders, so cutoff variation probes similarly N^{3}LO short-range physics at both, NLO and N^{2}LO. The uncertainty attached to the observable at NLO (or likewise N^{3}LO) consequently will likely be underestimated. Furthermore, the range of applicable cutoff values excludes in practice too high momenta, whereas for low-momentum scales finite-cutoff effects distort extractions of realistic uncertainties.

A new uncertainty estimate has recently been proposed in Refs. [9, 10] and applied to few-body calculations [102–105] as well as to nuclear matter [32, 106]. The corresponding statistical interpretation is provided in Ref. [19] in terms of Bayesian uncertainty quantification. Instead of cutoff variations at fixed chiral order, the new approach considers results for $X := X(p)$ at different orders while keeping cutoff values constant. This allows to assess the order-by-order convergence of the chiral expansion related to that observable. As we will report in Sec. 2.1.1, there are several complete sets of NN potentials available by now (e.g., from LO up to N^{4}LO) that can be studied accordingly. To be specific, the prediction is given by the telescoping series $X^{(\nu)} = \sum_{i=0}^{\nu} \mathrm{d}X^{(i)}$ at chiral order $\nu = 0, 2, 3, \ldots$, where

$$\mathrm{d}X^{(i)} = \begin{cases} X^{(0)} & i = 0\,, \\ X^{(2)} - X^{(0)} & i = 2\,, \\ X^{(i)} - X^{(i-1)} & i \geqslant 3\,, \end{cases} \tag{1.11}$$

are the individual corrections from each order (see also Ref. [102]). Assuming the expected scaling in powers of the expansion parameter (1.9), i.e., $\mathrm{d}X^{(i)} = \mathcal{O}(Q^i X^{(0)})$, Refs. [9, 10] defined the theoretical uncertainty as

$$\delta X^{(\nu)} = \begin{cases} Q^2 \left|X^{(0)}\right| & \nu = 0\,, \\ \max\limits_{2 \leqslant j \leqslant \nu} \left(Q^{\nu+1} \left|X^{(0)}\right|, Q^{\nu+1-j} \left|\mathrm{d}X^{(j)}\right|\right) & \nu \geqslant 2\,. \end{cases} \tag{1.12}$$

That is, the range $X^{(\nu)} \pm \delta X^{(\nu)}$ specifies a band for the prediction. To furthermore ensure a systematic rate of convergence within the uncertainty estimate the additional constraint

$$\delta X^{(\nu)} \geqslant \max_{j,k} \left(\left|X^{(j \geqslant \nu)} - X^{(k \geqslant \nu)}\right|\right) \tag{1.13}$$

was imposed which accounts for higher-order results. Notice that the above discussion is based on consistent calculations at each order, however, it should be modified for $\nu \geqslant 3$ if many-body contributions are neglected. In these cases, Ref. [102] avoids Eq. (1.13) and adopts in place of Eq. (1.12) the constraints

$$\delta X^{(\nu)} = \max\left(Q^{\nu+1} \left|X^{(0)}\right|, Q^{\nu-1} \left|\mathrm{d}X^{(2)}\right|, Q^{\nu-2} \left|\mathrm{d}X^{(3)}\right|\right), \tag{1.14a}$$

$$\delta X^{(2)} \geqslant Q\, \delta X^{(0)}\,, \text{ and} \tag{1.14b}$$

$$\delta X^{(\nu \geqslant 3)} \geqslant Q\, \delta X^{(\nu-1)}\,. \tag{1.14c}$$

1.3 Infinite nuclear matter

From the perspective of infinite nuclear matter, we discuss in this section MBPT and the relationship to other nonperturbative methods. In particular, we elaborate on the inclusion of 3N contributions beyond Hartree-Fock using normal ordering. Furthermore, we provide all energy relations in MBPT that are relevant for our improved matter calculations.

1.3.1 Many-body perturbation theory

Perturbation theory is a well-known framework in physics and at the heart of the present thesis. In particular, we are interested MBPT for infinite matter [18, 27, 28, 31, 32, 37, 48, 107–113] but the same concept also applies to finite nuclei [114, 115], see Refs. [116, 117] for recent applications. To familiarize ourselves with notations, we briefly introduce the formalism at zero temperature, and refer to the standard literature [118–121] for extensive discussions.

For now, we consider the generic nuclear Hamiltonian,

$$H = T + V = H_0 + \lambda H_1 \,, \tag{1.15}$$

where T denotes the kinetic energy operator, V contains the interactions, and λ is the expansion parameter. To apply perturbation theory, we have partitioned Eq. (1.15) in an unperturbed part H_0 and a (small) perturbation λH_1. Then, perturbation theory solves, if it converges, the Schrödinger equation of the many-body system,

$$(H_0 + \lambda H_1) \left|\Psi_i\right\rangle = E_i \left|\Psi_i\right\rangle \,, \quad \text{with } i \geqslant 0 \,, \tag{1.16}$$

in terms of a perturbation expansion about the unperturbed system, i.e., $E_i = \sum_{n=0}^{\infty} \lambda^n E_i^{(n)}$ and similarly for the eigenstates $|\Psi_i\rangle$. It is more likely an approximation in practice since the series has to be truncated at a given finite order. We focus here on ground states, hence, $i = 0$ in Eq. (1.16). The coefficients $E_{i=0}^{(n)}$ are order-by-order determined by the known solutions of the unperturbed Schrödinger equation $H_0 \left|\Phi_i\right\rangle = E_i^{(0)} \left|\Phi_i\right\rangle$, as discussed in the following. More strictly, this corresponds to the *diagonal case* of perturbation theory, allowing simplifications, while generally it is only required that $|\Phi_0\rangle$ denotes an eigenstate in the arbitrary orthonormal basis $|\Phi_{i\geqslant 0}\rangle$ [119]. Multiplying the Schrödinger equation (1.16) from left by $\langle\Phi_0|$ and using the intermediate normalization $\langle\Phi_0|\Psi_0\rangle = 1$ leads to

$$\Delta E := E_0 - E_0^{(0)} = \langle\Phi_0|\lambda H_1|\Psi_0\rangle \,. \tag{1.17}$$

It remains to derive an expression that relates $|\Psi_0\rangle$ with the known $|\Phi_0\rangle$. To this end, we define the projection operator onto the unperturbed ground state $P = |\Phi_0\rangle\langle\Phi_0|$ and its complement $Q = 1 - P$, such that we obtain

$$|\Psi_0\rangle = (P + Q)\left|\Psi_0\right\rangle = |\Phi_0\rangle + Q\left|\Psi_0\right\rangle \,. \tag{1.18}$$

In infinite nuclear matter $|\Phi_0\rangle$ represents the free Fermi sea, whereas $|\Phi_{i\geqslant 1}\rangle$ includes excitations of particles and holes with respect to this ground state (see also the discussion in Sec. 1.3.3). Adding a term $\zeta\left|\Psi_0\right\rangle$ on both sides of the Eq. (1.16) as well as multiplying by Q results in,

$$Q\left|\Psi_0\right\rangle = \frac{Q}{\zeta - H_0}\left(\lambda H_1 - E_0 + \zeta\right)\left|\Psi_0\right\rangle \,, \tag{1.19}$$

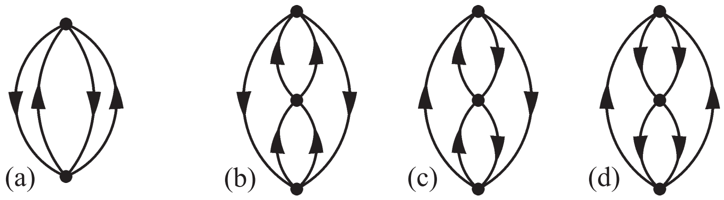

Figure 6: Hugenholtz diagrams for NN forces at second (a) and third order (b–d). Particles (holes) are indicated by up (down) arrows. The dots correspond to antisymmetrized interaction vertices. At third order, one has contributions from particle-particle (b), particle-hole (c), and hole-hole excitations (d). The figure has been modified from Ref. [122].

which is iterated in Eq. (1.18) to read

$$|\Psi_0\rangle = |\Phi_0\rangle + \frac{Q}{\zeta - H_0}(\lambda H_1 - E_0 + \zeta)\,|\Psi_0\rangle = \sum_{n=0}^{\infty}\left(\frac{Q}{\zeta - H_0}(\lambda H_1 - E_0 + \zeta)\right)^n |\Phi_0\rangle \,. \tag{1.20}$$

We employ Rayleigh-Schrödinger perturbation theory, i.e., $\zeta := E_0^{(0)}$, and evaluate Eq. (1.17)

$$\Delta E = E_0 - E_0^{(0)} = \sum_{n=0}^{\infty} \langle\Phi_0|\, \lambda H_1 \left(R_0 \left(\lambda H_1 - \Delta E\right)\right)^n |\Phi_0\rangle \,, \quad \text{with} \quad R_0 = \frac{Q}{E_0^{(0)} - H_0} = \sum_{k\neq 0} \frac{|\Phi_k\rangle\,\langle\Phi_k|}{E_0^{(0)} - E_k^{(0)}} \,. \tag{1.21}$$

Furthermore, we expand in a perturbation series, $\Delta E = \sum_{n=1}^{\infty} \lambda^n E_0^{(n)}$. Organizing the terms in powers of $\lambda \to 1$ determines the desired coefficients of the expansion, here given up to fourth order [118],

$$E_0^{(0)} = \langle\Phi_0|H_0|\Phi_0\rangle \,, \qquad E_0^{(1)} = \langle\Phi_0|H_1|\Phi_0\rangle \,, \tag{1.22a}$$

$$E_0^{(2)} = \langle\Phi_0|H_1 R_0 H_1|\Phi_0\rangle \,, \qquad E_0^{(3)} = \langle\Phi_0|H_1 R_0 (H_1 - E_0^{(1)}) R_0 H_1|\Phi_0\rangle \,, \tag{1.22b}$$

$$\begin{aligned} E_0^{(4)} &= \langle\Phi_0|H_1 R_0 (H_1 - E_0^{(1)}) R_0 (H_1 - E_0^{(1)}) R_0 H_1|\Phi_0\rangle \\ &\quad - E_0^{(2)} \langle\Phi_0|H_1 R_0^2 H_1|\Phi_0\rangle \,. \end{aligned} \tag{1.22c}$$

The presented analytic derivation of perturbation theory comes along with an equivalent pictorial approach, so-called diagrammatic perturbation theory, which is conceptionally similar to Feynman techniques. One draws all possible (e.g., Hugenholtz) diagrams with n vertices (dots) and connects them by continuous lines, following remarkable simple rules [120, 122]. Because of Goldstone's linked-diagram theorem [123] only connected diagrams contribute to the expansion. The explicit cancellation of size-inconsistent terms (see also Ref. [124]) related to unlinked diagrams transforms Rayleigh-Schrödinger perturbation theory to MBPT [118, 125]. In practice, the diagrammatic approach is more convienient and thus typically the method of choice, especially, regarding automation on a computer [122, 126–128]. Rules to translate diagrams to analytic expressions are given in the cited literature.

It is however a nontrivial assumption that the perturbation series convergences at a useful rate. The efficiency of MBPT clearly depends on the underlying interaction as well as the chosen partition in Eq. (1.15). To quantify the *perturbativeness* of recent NN potentials in free space, we make use of Weinberg eigenvalues in Sec. 3 as a powerful diagnostic tool. Additionally, in Sec. 4.3 we benchmark the neutron-matter equation of state involving NN plus 3N interactions up to N^{3}LO order-by-order to a nonperturbative method, where calculations using two partitions serve as a many-body uncertainty.

One has for NN interactions 1, 3, 39, … Hugenholtz diagram(s) at second, third, fourth order, respectively, and so on [122, 129]. Figure 6 shows these at second and third order; for the fourth-order diagrams we refer to Ref. [130]. Below, we summarize the underlying analytic expressions up to fourth order, as this is the highest order considered in the present thesis. They are expressed in the particle-hole formalism, where only the particle (hole) states created above (below) the Fermi surface are considered (see, e.g., Ref. [118]). For brevity we define $E_{\text{NN}}^{(n)} := E_0^{(n)}$. In the following Sec. 1.3.2, we will discuss normal-ordering and the inclusion of many-body forces at and beyond the Hartree-Fock level.

Energy relations up to second order

The energy contributions up to second order based on antisymmetrized NN interactions $\mathscr{A}_{12} V_{\text{NN}}$ are given by the following expressions (see also Refs. [43, 118, 119])

$$\frac{T}{V} = + \sum_i \langle i | T | i \rangle \,, \tag{1.23}$$

$$\frac{E_{\text{NN}}^{(1)}}{V} = + \frac{1}{2} \sum_{ij} \langle ij | \mathscr{A}_{12} V_{\text{NN}} | ij \rangle \,, \tag{1.24}$$

$$\frac{E_{\text{NN}}^{(2)}}{V} = + \frac{1}{4} \sum_{\substack{ij\\ab}} \frac{\langle ij | \mathscr{A}_{12} V_{\text{NN}} | ab \rangle \, \langle ab | \mathscr{A}_{12} V_{\text{NN}} | ij \rangle}{D_{ijab}} \,. \tag{1.25}$$

Equation (1.25) is associated with diagram (a) in Fig. 6. We use the short-hand notation for the single-particle states $|i\rangle = |\mathbf{k}_i \sigma_i \tau_i\rangle$, having the momentum $\mathbf{k}_i$, the spin and isospin projections $\sigma_i = \pm\frac{1}{2}$ and $\tau_i = \pm\frac{1}{2}$, respectively. Furthermore, particles are labeled by a, b, … and holes by i, j, …, so the sums transform into, e.g.,

$$\sum_a \longrightarrow \sum_{\sigma_a \tau_a} \int \frac{\mathrm{d}\mathbf{k}_a}{(2\pi)^3} \left(1 - n_{\mathbf{k}_a}^{\tau_a}\right) , \qquad \text{and} \qquad \sum_i \longrightarrow \sum_{\sigma_i \tau_i} \int \frac{\mathrm{d}\mathbf{k}_i}{(2\pi)^3} n_{\mathbf{k}_i}^{\tau_i} \,, \tag{1.26}$$

where $n_{\mathbf{k}_i}^{\tau_i}$ is the Heaviside step function. Intermediate states beyond first order are weighted in terms of the single-particle energies,

$$D_{ijk\ldots abc\ldots} = \varepsilon_{\mathbf{k}_i} + \varepsilon_{\mathbf{k}_j} + \varepsilon_{\mathbf{k}_k} + \ldots - \varepsilon_{\mathbf{k}_a} - \varepsilon_{\mathbf{k}_b} - \varepsilon_{\mathbf{k}_c} - \ldots \,. \tag{1.27}$$

The trivial partition in Eq. (1.15), $H_0 = T$ and $H_1 = V$, corresponds to the free spectrum with $\varepsilon_{\mathbf{k}_i} = \mathbf{k}_i^2/(2m)$, whereas $H_0 = T + V_{\text{HF}}$ and $H_1 = V - V_{\text{HF}}$ adds first-order self-energy corrections to the kinetic energy, called Hartree-Fock spectrum. Due to translational invariance, both, the kinetic-energy operator T and the Hartree-Fock potential V_{HF} are diagonal in the plane-wave basis (see also Ref. [121]). We have thus the second-quantized Fock operator $H_0 = \sum_{ij} f_{ij} \, a_j^\dagger a_i$ with $f_{ij} = \delta_{ij} \, \varepsilon_i$ and the single-particle energies

$$\varepsilon_i = \frac{\mathbf{k}_i^2}{2m} + \sum_j \langle ij \,|\, \mathscr{A}_{12} V_{\text{NN}} \,|\, ij \rangle \,. \tag{1.28}$$

In our calculations, we average Eq. (1.28) over spin as well as isospin quantum numbers. The two employed spectra lead to the same Hartree-Fock energy, i.e., the sum of all zero- and first-order terms. Adding 3N contributions to Eq. (1.28) will be addressed in Sec. 1.3.2.

For completeness, we note that there is an additional single-excitation diagram at second order, which is anomalous due to momentum conservation. It cancels using a Hartree-Fock spectrum [118].

Energy relations at third order

One has in total three diagrams at third order when using a Hartree-Fock spectrum, depicted by (b–d) in Fig. 6. This results from a fine cancellation of several diagrams driven by the Hartree-Fock Hamiltonian. In a free spectrum, however, eleven additional (partly anomalous) terms arise [118]. We therefore consider solely Hartree-Fock single-particle energies beyond second order. Specifically, one has then contributions from hole-hole, particle-hole, and particle-particle excitations with respect to the Hartree-Fock reference state. These correspond to the following expressions, respectively, (see also Refs. [112, 118, 119])

$$\frac{E_1^{(3)}}{V} = +\frac{1}{8} \sum_{\substack{ijkl\\ab}} \frac{\langle ij|\mathscr{A}_{12}V_{\mathrm{NN}}|ab\rangle \, \langle kl|\mathscr{A}_{12}V_{\mathrm{NN}}|ij\rangle \, \langle ab|\mathscr{A}_{12}V_{\mathrm{NN}}|kl\rangle}{D_{ijab}D_{klab}} \,, \tag{1.29a}$$

$$\frac{E_2^{(3)}}{V} = + \sum_{\substack{ijk\\abc}} \frac{\langle ij|\mathscr{A}_{12}V_{\mathrm{NN}}|ab\rangle \, \langle ak|\mathscr{A}_{12}V_{\mathrm{NN}}|ic\rangle \, \langle bc|\mathscr{A}_{12}V_{\mathrm{NN}}|jk\rangle}{D_{ijab}D_{jkbc}} \,, \tag{1.29b}$$

$$\frac{E_3^{(3)}}{V} = +\frac{1}{8} \sum_{\substack{ij\\abcd}} \frac{\langle ij|\mathscr{A}_{12}V_{\mathrm{NN}}|ab\rangle \, \langle ab|\mathscr{A}_{12}V_{\mathrm{NN}}|cd\rangle \, \langle cd|\mathscr{A}_{12}V_{\mathrm{NN}}|ij\rangle}{D_{ijab}D_{ijcd}} \,. \tag{1.29c}$$

Time reversal (exchanging holes and particles) relates the hole-hole and particle-particle terms, unfortunately, without reducing the number of diagrams to be computed. In total, the third-order contribution is given by

$$\frac{E_{\mathrm{NN}}^{(3)}}{V} = \left.\frac{E_1^{(3)}}{V}\right|_{\mathrm{hh}} + \left.\frac{E_2^{(3)}}{V}\right|_{\mathrm{ph}} + \left.\frac{E_3^{(3)}}{V}\right|_{\mathrm{pp}} . \tag{1.30}$$

Energy relations at fourth order: an overview

The fourth order consists of 39 linked diagrams when using a Hartree-Fock spectrum [118, 122]. They are categorized according to the level of excitations obtained after the second interaction with respect to the Fermi sea [131]. One has thus 4 single-, 12 double-, 16 triple-, and 7 quadruple-excitation diagrams, hence, the total energy of all fourth-order terms is given by

$$\frac{E_{\mathrm{NN}}^{(4)}}{V} = \sum_{i=1}^{4} \left.\frac{E_i^{(4)}}{V}\right|_{\mathrm{single}} + \sum_{i=5}^{16} \left.\frac{E_i^{(4)}}{V}\right|_{\mathrm{double}} + \sum_{i=17}^{32} \left.\frac{E_i^{(4)}}{V}\right|_{\mathrm{triple}} + \sum_{i=33}^{39} \left.\frac{E_i^{(4)}}{V}\right|_{\mathrm{quadruple}} . \tag{1.31}$$

The sum of all contributions is order-by-order real in perturbation theory because the nuclear Hamiltonian is hermitian. This is also the case for each individual term up to third order. However, starting at fourth order we encounter complex-conjugated pairs of diagrams, which in total are again real [130]. Exploiting momentum conservation, in addition, reduces the number of diagrams to be computed to effectively 24. In the following, we carefully provide the complete set of energy expressions (including time-reversed pairs) as preparation for Sec. 5. These are more familiar in quantum chemistry but have not been studied to the best of our knowledge in infinite-matter calculations.

Energy relations at fourth order: single excitations

There are four contributions having single excitations after the second interaction [130, 131]:

$$\frac{E_1^{(4)}}{V} = +\frac{1}{4} \sum_{\substack{abcde\\ijk}} \frac{\langle ij|\mathscr{A}_{12}V_{\mathrm{NN}}|ab\rangle \langle ab|\mathscr{A}_{12}V_{\mathrm{NN}}|cj\rangle \langle ck|\mathscr{A}_{12}V_{\mathrm{NN}}|de\rangle \langle de|\mathscr{A}_{12}V_{\mathrm{NN}}|ik\rangle}{D_{ijab}D_{ic}D_{ikde}}\,, \tag{1.32a}$$

$$\frac{E_2^{(4)}}{V} = -\frac{1}{4} \sum_{\substack{abcd\\ijkl}} \frac{\langle ij|\mathscr{A}_{12}V_{\mathrm{NN}}|ab\rangle \langle ab|\mathscr{A}_{12}V_{\mathrm{NN}}|cj\rangle \langle kl|\mathscr{A}_{12}V_{\mathrm{NN}}|id\rangle \langle cd|\mathscr{A}_{12}V_{\mathrm{NN}}|kl\rangle}{D_{ijab}D_{ic}D_{klcd}}\,, \tag{1.32b}$$

$$\frac{E_3^{(4)}}{V} = -\frac{1}{4} \sum_{\substack{abcd\\ijkl}} \frac{\langle ij|\mathscr{A}_{12}V_{\mathrm{NN}}|ab\rangle \langle kb|\mathscr{A}_{12}V_{\mathrm{NN}}|ij\rangle \langle al|\mathscr{A}_{12}V_{\mathrm{NN}}|cd\rangle \langle cd|\mathscr{A}_{12}V_{\mathrm{NN}}|kl\rangle}{D_{ijab}D_{ka}D_{klcd}}\,, \tag{1.32c}$$

$$\frac{E_4^{(4)}}{V} = +\frac{1}{4} \sum_{\substack{abc\\ijklm}} \frac{\langle ij|\mathscr{A}_{12}V_{\mathrm{NN}}|ab\rangle \langle kb|\mathscr{A}_{12}V_{\mathrm{NN}}|ij\rangle \langle lm|\mathscr{A}_{12}V_{\mathrm{NN}}|kc\rangle \langle ac|\mathscr{A}_{12}V_{\mathrm{NN}}|lm\rangle}{D_{ijab}D_{ka}D_{lmac}}\,, \tag{1.32d}$$

Note that these (anomalous) diagrams do not contribute at zero temperature because of momentum conservation or chancel in a Hartree-Fock spectrum. The diagrams labeled by (2, 3) are related via complex conjugation.

Energy relations at fourth order: double excitations

There are twelve contributions having double excitations after the second interaction [130, 131]:

$$\frac{E_5^{(4)}}{V} = +\frac{1}{16} \sum_{\substack{abcdef\\ij}} \frac{\langle ij|\mathscr{A}_{12}V_{\mathrm{NN}}|ab\rangle \langle ab|\mathscr{A}_{12}V_{\mathrm{NN}}|cd\rangle \langle cd|\mathscr{A}_{12}V_{\mathrm{NN}}|ef\rangle \langle ef|\mathscr{A}_{12}V_{\mathrm{NN}}|ij\rangle}{D_{ijab}D_{ijcd}D_{ijef}}\,, \tag{1.33a}$$

$$\frac{E_6^{(4)}}{V} = +\frac{1}{16} \sum_{\substack{abcd\\ijkl}} \frac{\langle ij|\mathscr{A}_{12}V_{\mathrm{NN}}|ab\rangle \langle ab|\mathscr{A}_{12}V_{\mathrm{NN}}|cd\rangle \langle kl|\mathscr{A}_{12}V_{\mathrm{NN}}|ij\rangle \langle cd|\mathscr{A}_{12}V_{\mathrm{NN}}|kl\rangle}{D_{ijab}D_{ijcd}D_{klcd}}\,, \tag{1.33b}$$

$$\frac{E_7^{(4)}}{V} = +\frac{1}{16} \sum_{\substack{abcd\\ijkl}} \frac{\langle ij|\mathscr{A}_{12}V_{\mathrm{NN}}|ab\rangle \langle kl|\mathscr{A}_{12}V_{\mathrm{NN}}|ij\rangle \langle ab|\mathscr{A}_{12}V_{\mathrm{NN}}|cd\rangle \langle cd|\mathscr{A}_{12}V_{\mathrm{NN}}|kl\rangle}{D_{ijab}D_{klab}D_{klcd}}\,, \tag{1.33c}$$

$$\frac{E_8^{(4)}}{V} = +\frac{1}{16} \sum_{\substack{ab\\ijklmn}} \frac{\langle ij|\mathscr{A}_{12}V_{\mathrm{NN}}|ab\rangle \langle kl|\mathscr{A}_{12}V_{\mathrm{NN}}|ij\rangle \langle mn|\mathscr{A}_{12}V_{\mathrm{NN}}|kl\rangle \langle ab|\mathscr{A}_{12}V_{\mathrm{NN}}|mn\rangle}{D_{ijab}D_{klab}D_{mnab}}\,, \tag{1.33d}$$

$$\frac{E_9^{(4)}}{V} = -\frac{1}{2} \sum_{\substack{abcde\\ijk}} \frac{\langle ij|\mathscr{A}_{12}V_{\mathrm{NN}}|ab\rangle \langle ab|\mathscr{A}_{12}V_{\mathrm{NN}}|cd\rangle \langle kd|\mathscr{A}_{12}V_{\mathrm{NN}}|ie\rangle \langle ce|\mathscr{A}_{12}V_{\mathrm{NN}}|kj\rangle}{D_{ijab}D_{ijcd}D_{jkce}}\,, \tag{1.33e}$$

$$\frac{E_{10}^{(4)}}{V} = -\frac{1}{2} \sum_{\substack{abcde\\ijk}} \frac{\langle ij|\mathscr{A}_{12}V_{\mathrm{NN}}|ab\rangle \langle kb|\mathscr{A}_{12}V_{\mathrm{NN}}|ic\rangle \langle ac|\mathscr{A}_{12}V_{\mathrm{NN}}|de\rangle \langle de|\mathscr{A}_{12}V_{\mathrm{NN}}|kj\rangle}{D_{ijab}D_{jkac}D_{jkde}}\,, \tag{1.33f}$$

$$\frac{E_{11}^{(4)}}{V} = -\frac{1}{2} \sum_{\substack{abc\\ijklm}} \frac{\langle ij|\mathscr{A}_{12}V_{\mathrm{NN}}|ab\rangle \langle kl|\mathscr{A}_{12}V_{\mathrm{NN}}|ij\rangle \langle am|\mathscr{A}_{12}V_{\mathrm{NN}}|cl\rangle \langle cb|\mathscr{A}_{12}V_{\mathrm{NN}}|km\rangle}{D_{ijab}D_{klab}D_{kmbc}}\,, \tag{1.33g}$$

$$\frac{E^{(4)}_{12}}{V} = -\frac{1}{2} \sum_{\substack{abc\\ijklm}} \frac{\langle ij|\mathscr{A}_{12}V_{\mathrm{NN}}|ab\rangle \langle ak|\mathscr{A}_{12}V_{\mathrm{NN}}|cj\rangle \langle lm|\mathscr{A}_{12}V_{\mathrm{NN}}|ik\rangle \langle cb|\mathscr{A}_{12}V_{\mathrm{NN}}|lm\rangle}{D_{ijab}D_{ikbc}D_{lmbc}}, \tag{1.33h}$$

$$\frac{E^{(4)}_{13}}{V} = +\sum_{\substack{abcd\\ijkl}} \frac{\langle ij|\mathscr{A}_{12}V_{\mathrm{NN}}|ab\rangle \langle ak|\mathscr{A}_{12}V_{\mathrm{NN}}|cj\rangle \langle cl|\mathscr{A}_{12}V_{\mathrm{NN}}|dk\rangle \langle db|\mathscr{A}_{12}V_{\mathrm{NN}}|il\rangle}{D_{ijab}D_{ikbc}D_{ilbd}}, \tag{1.33i}$$

$$\frac{E^{(4)}_{14}}{V} = -\sum_{\substack{abcd\\ijkl}} \frac{\langle ij|\mathscr{A}_{12}V_{\mathrm{NN}}|ab\rangle \langle kb|\mathscr{A}_{12}V_{\mathrm{NN}}|cj\rangle \langle cl|\mathscr{A}_{12}V_{\mathrm{NN}}|id\rangle \langle ad|\mathscr{A}_{12}V_{\mathrm{NN}}|kl\rangle}{D_{ijab}D_{ikac}D_{klad}}, \tag{1.33j}$$

$$\frac{E^{(4)}_{15}}{V} = -\sum_{\substack{abcd\\ijkl}} \frac{\langle ij|\mathscr{A}_{12}V_{\mathrm{NN}}|ab\rangle \langle kb|\mathscr{A}_{12}V_{\mathrm{NN}}|cj\rangle \langle al|\mathscr{A}_{12}V_{\mathrm{NN}}|kd\rangle \langle cd|\mathscr{A}_{12}V_{\mathrm{NN}}|il\rangle}{D_{ijab}D_{ikac}D_{ilcd}}, \tag{1.33k}$$

$$\frac{E^{(4)}_{16}}{V} = +\sum_{\substack{abcd\\ijkl}} \frac{\langle ij|\mathscr{A}_{12}V_{\mathrm{NN}}|ab\rangle \langle kb|\mathscr{A}_{12}V_{\mathrm{NN}}|ic\rangle \langle al|\mathscr{A}_{12}V_{\mathrm{NN}}|dj\rangle \langle dc|\mathscr{A}_{12}V_{\mathrm{NN}}|kl\rangle}{D_{ijab}D_{jkac}D_{klcd}}, \tag{1.33l}$$

The complex-conjugation pairs are labeled by (6, 7), (9, 10), and (11, 12).

Energy relations at fourth order: triple excitations

There are sixteen contributions having triple excitations after the second interaction [130, 131]:

$$\frac{E^{(4)}_{17}}{V} = -\frac{1}{2} \sum_{\substack{abcde\\ijk}} \frac{\langle ij|\mathscr{A}_{12}V_{\mathrm{NN}}|ab\rangle \langle ak|\mathscr{A}_{12}V_{\mathrm{NN}}|cd\rangle \langle cb|\mathscr{A}_{12}V_{\mathrm{NN}}|ek\rangle \langle ed|\mathscr{A}_{12}V_{\mathrm{NN}}|ij\rangle}{D_{ijab}D_{ijkbcd}D_{ijde}}, \tag{1.34a}$$

$$\frac{E^{(4)}_{18}}{V} = -\frac{1}{2} \sum_{\substack{abcde\\ijk}} \frac{\langle ij|\mathscr{A}_{12}V_{\mathrm{NN}}|ab\rangle \langle ak|\mathscr{A}_{12}V_{\mathrm{NN}}|cd\rangle \langle cd|\mathscr{A}_{12}V_{\mathrm{NN}}|ej\rangle \langle eb|\mathscr{A}_{12}V_{\mathrm{NN}}|ik\rangle}{D_{ijab}D_{ijkbcd}D_{ikbe}}, \tag{1.34b}$$

$$\frac{E^{(4)}_{19}}{V} = -\frac{1}{2} \sum_{\substack{abc\\ijklm}} \frac{\langle ij|\mathscr{A}_{12}V_{\mathrm{NN}}|ab\rangle \langle kl|\mathscr{A}_{12}V_{\mathrm{NN}}|ic\rangle \langle mb|\mathscr{A}_{12}V_{\mathrm{NN}}|kl\rangle \langle ac|\mathscr{A}_{12}V_{\mathrm{NN}}|mj\rangle}{D_{ijab}D_{jklabc}D_{jmac}}, \tag{1.34c}$$

$$\frac{E^{(4)}_{20}}{V} = -\frac{1}{2} \sum_{\substack{abc\\ijklm}} \frac{\langle ij|\mathscr{A}_{12}V_{\mathrm{NN}}|ab\rangle \langle kl|\mathscr{A}_{12}V_{\mathrm{NN}}|ic\rangle \langle mc|\mathscr{A}_{12}V_{\mathrm{NN}}|kj\rangle \langle ab|\mathscr{A}_{12}V_{\mathrm{NN}}|ml\rangle}{D_{ijab}D_{jklabc}D_{mlab}}, \tag{1.34d}$$

$$\frac{E^{(4)}_{21}}{V} = +\sum_{\substack{abcde\\ijk}} \frac{\langle ij|\mathscr{A}_{12}V_{\mathrm{NN}}|ab\rangle \langle ak|\mathscr{A}_{12}V_{\mathrm{NN}}|cd\rangle \langle cb|\mathscr{A}_{12}V_{\mathrm{NN}}|ej\rangle \langle ed|\mathscr{A}_{12}V_{\mathrm{NN}}|ik\rangle}{D_{ijab}D_{ijkbcd}D_{ikde}}, \tag{1.34e}$$

$$\frac{E^{(4)}_{22}}{V} = +\frac{1}{4} \sum_{\substack{abcde\\ijk}} \frac{\langle ij|\mathscr{A}_{12}V_{\mathrm{NN}}|ab\rangle \langle ak|\mathscr{A}_{12}V_{\mathrm{NN}}|cd\rangle \langle cd|\mathscr{A}_{12}V_{\mathrm{NN}}|ek\rangle \langle eb|\mathscr{A}_{12}V_{\mathrm{NN}}|ij\rangle}{D_{ijab}D_{ijkbcd}D_{ijbe}}, \tag{1.34f}$$

$$\frac{E^{(4)}_{23}}{V} = +\frac{1}{4} \sum_{\substack{abc\\ijklm}} \frac{\langle ij|\mathscr{A}_{12}V_{\mathrm{NN}}|ab\rangle \langle kl|\mathscr{A}_{12}V_{\mathrm{NN}}|ic\rangle \langle mc|\mathscr{A}_{12}V_{\mathrm{NN}}|kl\rangle \langle ab|\mathscr{A}_{12}V_{\mathrm{NN}}|mj\rangle}{D_{ijab}D_{jklabc}D_{jmab}}, \tag{1.34g}$$

$$\frac{E^{(4)}_{24}}{V} = + \sum_{\substack{abc\\ijklm}} \frac{\langle ij|\mathscr{A}_{12}V_{\mathrm{NN}}|ab\rangle \langle kl|\mathscr{A}_{12}V_{\mathrm{NN}}|ic\rangle \langle mb|\mathscr{A}_{12}V_{\mathrm{NN}}|kj\rangle \langle ac|\mathscr{A}_{12}V_{\mathrm{NN}}|ml\rangle}{D_{ijab}D_{jklabc}D_{lmac}}, \tag{1.34h}$$

$$\frac{E^{(4)}_{25}}{V} = -\frac{1}{4} \sum_{\substack{abcd\\ijkl}} \frac{\langle ij|\mathscr{A}_{12}V_{\mathrm{NN}}|ab\rangle \langle ak|\mathscr{A}_{12}V_{\mathrm{NN}}|cd\rangle \langle lb|\mathscr{A}_{12}V_{\mathrm{NN}}|ij\rangle \langle cd|\mathscr{A}_{12}V_{\mathrm{NN}}|lk\rangle}{D_{ijab}D_{ijkbcd}D_{klcd}}, \tag{1.34i}$$

$$\frac{E^{(4)}_{26}}{V} = - \sum_{\substack{abcd\\ijkl}} \frac{\langle ij|\mathscr{A}_{12}V_{\mathrm{NN}}|ab\rangle \langle ak|\mathscr{A}_{12}V_{\mathrm{NN}}|cd\rangle \langle ld|\mathscr{A}_{12}V_{\mathrm{NN}}|ik\rangle \langle cb|\mathscr{A}_{12}V_{\mathrm{NN}}|lj\rangle}{D_{ijab}D_{ijkbcd}D_{jlbc}}, \tag{1.34j}$$

$$\frac{E^{(4)}_{27}}{V} = - \sum_{\substack{abcd\\ijkl}} \frac{\langle ij|\mathscr{A}_{12}V_{\mathrm{NN}}|ab\rangle \langle kl|\mathscr{A}_{12}V_{\mathrm{NN}}|ic\rangle \langle ac|\mathscr{A}_{12}V_{\mathrm{NN}}|dl\rangle \langle db|\mathscr{A}_{12}V_{\mathrm{NN}}|kj\rangle}{D_{ijab}D_{jklabc}D_{jkbd}}, \tag{1.34k}$$

$$\frac{E^{(4)}_{28}}{V} = -\frac{1}{4} \sum_{\substack{abcd\\ijkl}} \frac{\langle ij|\mathscr{A}_{12}V_{\mathrm{NN}}|ab\rangle \langle kl|\mathscr{A}_{12}V_{\mathrm{NN}}|ic\rangle \langle ab|\mathscr{A}_{12}V_{\mathrm{NN}}|dj\rangle \langle dc|\mathscr{A}_{12}V_{\mathrm{NN}}|kl\rangle}{D_{ijab}D_{jklabc}D_{klcd}}, \tag{1.34l}$$

$$\frac{E^{(4)}_{29}}{V} = +\frac{1}{2} \sum_{\substack{abcd\\ijkl}} \frac{\langle ij|\mathscr{A}_{12}V_{\mathrm{NN}}|ab\rangle \langle ak|\mathscr{A}_{12}V_{\mathrm{NN}}|cd\rangle \langle lb|\mathscr{A}_{12}V_{\mathrm{NN}}|ik\rangle \langle cd|\mathscr{A}_{12}V_{\mathrm{NN}}|lj\rangle}{D_{ijab}D_{ijkbcd}D_{jlcd}}, \tag{1.34m}$$

$$\frac{E^{(4)}_{30}}{V} = +\frac{1}{2} \sum_{\substack{abcd\\ijkl}} \frac{\langle ij|\mathscr{A}_{12}V_{\mathrm{NN}}|ab\rangle \langle kl|\mathscr{A}_{12}V_{\mathrm{NN}}|ic\rangle \langle ab|\mathscr{A}_{12}V_{\mathrm{NN}}|dl\rangle \langle dc|\mathscr{A}_{12}V_{\mathrm{NN}}|kj\rangle}{D_{ijab}D_{jklabc}D_{jkcd}}, \tag{1.34n}$$

$$\frac{E^{(4)}_{31}}{V} = +\frac{1}{2} \sum_{\substack{abcd\\ijkl}} \frac{\langle ij|\mathscr{A}_{12}V_{\mathrm{NN}}|ab\rangle \langle kl|\mathscr{A}_{12}V_{\mathrm{NN}}|ic\rangle \langle ac|\mathscr{A}_{12}V_{\mathrm{NN}}|dj\rangle \langle db|\mathscr{A}_{12}V_{\mathrm{NN}}|kl\rangle}{D_{ijab}D_{jklabc}D_{klbd}}, \tag{1.34o}$$

$$\frac{E^{(4)}_{32}}{V} = +\frac{1}{2} \sum_{\substack{abcd\\ijkl}} \frac{\langle ij|\mathscr{A}_{12}V_{\mathrm{NN}}|ab\rangle \langle ak|\mathscr{A}_{12}V_{\mathrm{NN}}|cd\rangle \langle ld|\mathscr{A}_{12}V_{\mathrm{NN}}|ij\rangle \langle cb|\mathscr{A}_{12}V_{\mathrm{NN}}|lk\rangle}{D_{ijab}D_{ijkbcd}D_{klbc}}. \tag{1.34p}$$

Note that the (anomalous) diagrams with index 25 and 28 do not contribute at zero temperature because of momentum conservation or chancel in a Hartree-Fock spectrum. The complex-conjugation pairs are labeled by (25, 28), (26, 27), (29, 30), and (31, 32).

Energy relations at fourth order: quadruple excitations

There are seven contributions having quadruple excitations after the second interaction [130, 131]:

$$\frac{E^{(4)}_{33}}{V} = + \sum_{\substack{abcd\\ijkl}} \frac{\langle ij|\mathscr{A}_{12}V_{\mathrm{NN}}|ab\rangle \langle kl|\mathscr{A}_{12}V_{\mathrm{NN}}|cd\rangle \langle cb|\mathscr{A}_{12}V_{\mathrm{NN}}|il\rangle \langle ad|\mathscr{A}_{12}V_{\mathrm{NN}}|kj\rangle}{D_{ijab}D_{ijklabcd}D_{jkad}}, \tag{1.35a}$$

$$\frac{E^{(4)}_{34}}{V} = +\frac{1}{16} \sum_{\substack{abcd\\ijkl}} \frac{\langle ij|\mathscr{A}_{12}V_{\mathrm{NN}}|ab\rangle \langle kl|\mathscr{A}_{12}V_{\mathrm{NN}}|cd\rangle \langle cd|\mathscr{A}_{12}V_{\mathrm{NN}}|ij\rangle \langle ab|\mathscr{A}_{12}V_{\mathrm{NN}}|kl\rangle}{D_{ijab}D_{ijklabcd}D_{klab}}, \tag{1.35b}$$

$$\frac{E^{(4)}_{35}}{V} = +\frac{1}{16} \sum_{\substack{abcd\\ijkl}} \frac{\langle ij|\mathscr{A}_{12}V_{\mathrm{NN}}|ab\rangle \langle kl|\mathscr{A}_{12}V_{\mathrm{NN}}|cd\rangle \langle ab|\mathscr{A}_{12}V_{\mathrm{NN}}|kl\rangle \langle cd|\mathscr{A}_{12}V_{\mathrm{NN}}|ij\rangle}{D_{ijab}D_{ijklabcd}D_{ijcd}}, \tag{1.35c}$$

$$\frac{E^{(4)}_{36}}{V} = -\frac{1}{4} \sum_{\substack{abcd\\ ijkl}} \frac{\langle ij|\mathscr{A}_{12}V_{\mathrm{NN}}|ab\rangle \, \langle kl|\mathscr{A}_{12}V_{\mathrm{NN}}|cd\rangle \, \langle cb|\mathscr{A}_{12}V_{\mathrm{NN}}|ij\rangle \, \langle ad|\mathscr{A}_{12}V_{\mathrm{NN}}|kl\rangle}{D_{ijab}D_{ijklabcd}D_{klad}} \,, \tag{1.35d}$$

$$\frac{E^{(4)}_{37}}{V} = -\frac{1}{4} \sum_{\substack{abcd\\ ijkl}} \frac{\langle ij|\mathscr{A}_{12}V_{\mathrm{NN}}|ab\rangle \, \langle kl|\mathscr{A}_{12}V_{\mathrm{NN}}|cd\rangle \, \langle ad|\mathscr{A}_{12}V_{\mathrm{NN}}|kl\rangle \, \langle cb|\mathscr{A}_{12}V_{\mathrm{NN}}|ij\rangle}{D_{ijab}D_{ijklabcd}D_{ijbc}} \,, \tag{1.35e}$$

$$\frac{E^{(4)}_{38}}{V} = -\frac{1}{4} \sum_{\substack{abcd\\ ijkl}} \frac{\langle ij|\mathscr{A}_{12}V_{\mathrm{NN}}|ab\rangle \, \langle kl|\mathscr{A}_{12}V_{\mathrm{NN}}|cd\rangle \, \langle cd|\mathscr{A}_{12}V_{\mathrm{NN}}|il\rangle \, \langle ab|\mathscr{A}_{12}V_{\mathrm{NN}}|kj\rangle}{D_{ijab}D_{ijklabcd}D_{jkab}} \,, \tag{1.35f}$$

$$\frac{E^{(4)}_{39}}{V} = -\frac{1}{4} \sum_{\substack{abcd\\ ijkl}} \frac{\langle ij|\mathscr{A}_{12}V_{\mathrm{NN}}|ab\rangle \, \langle kl|\mathscr{A}_{12}V_{\mathrm{NN}}|cd\rangle \, \langle ab|\mathscr{A}_{12}V_{\mathrm{NN}}|kj\rangle \, \langle cd|\mathscr{A}_{12}V_{\mathrm{NN}}|il\rangle}{D_{ijab}D_{ijklabcd}D_{ilcd}} \,. \tag{1.35g}$$

These expressions can be cast into the following forms

$$\frac{E^{(4)}_{40}}{V} = \frac{1}{2}\left(\frac{E^{(4)}_{33}}{V} + \frac{E^{(4)}_{33}}{V}\right), \qquad \frac{E^{(4)}_{41}}{V} = \frac{E^{(4)}_{34}}{V} + \frac{E^{(4)}_{35}}{V} \,, \tag{1.36a}$$

$$\frac{E^{(4)}_{42}}{V} = \frac{E^{(4)}_{36}}{V} + \frac{E^{(4)}_{37}}{V} \,, \qquad \frac{E^{(4)}_{43}}{V} = \frac{E^{(4)}_{38}}{V} + \frac{E^{(4)}_{39}}{V} \,, \tag{1.36b}$$

where the energy denominator in $E^{(4)}_{40}$ is simplified compared to $E^{(4)}_{33}$ and only the contributions with index 40, 41, 42, and 43 have to be evaluated (four instead of seven). The corresponding analytic expressions read [131]

$$\frac{E^{(4)}_{40}}{V} = +\frac{1}{2} \sum_{\substack{abcd\\ ijkl}} \frac{\langle ij|\mathscr{A}_{12}V_{\mathrm{NN}}|ab\rangle \, \langle kl|\mathscr{A}_{12}V_{\mathrm{NN}}|cd\rangle \, \langle cb|\mathscr{A}_{12}V_{\mathrm{NN}}|il\rangle \, \langle ad|\mathscr{A}_{12}V_{\mathrm{NN}}|kj\rangle}{D_{ijab}D_{ilbc}D_{jkad}} \,, \tag{1.37a}$$

$$\frac{E^{(4)}_{41}}{V} = +\frac{1}{16} \sum_{\substack{abcd\\ ijkl}} \frac{\langle ij|\mathscr{A}_{12}V_{\mathrm{NN}}|ab\rangle \, \langle kl|\mathscr{A}_{12}V_{\mathrm{NN}}|cd\rangle \, \langle cd|\mathscr{A}_{12}V_{\mathrm{NN}}|ij\rangle \, \langle ab|\mathscr{A}_{12}V_{\mathrm{NN}}|kl\rangle}{D_{ijab}D_{ijcd}D_{klab}} \,, \tag{1.37b}$$

$$\frac{E^{(4)}_{42}}{V} = -\frac{1}{4} \sum_{\substack{abcd\\ ijkl}} \frac{\langle ij|\mathscr{A}_{12}V_{\mathrm{NN}}|ab\rangle \, \langle kl|\mathscr{A}_{12}V_{\mathrm{NN}}|cd\rangle \, \langle cb|\mathscr{A}_{12}V_{\mathrm{NN}}|ij\rangle \, \langle ad|\mathscr{A}_{12}V_{\mathrm{NN}}|kl\rangle}{D_{ijab}D_{ijbc}D_{klad}} \,, \tag{1.37c}$$

$$\frac{E^{(4)}_{43}}{V} = -\frac{1}{4} \sum_{\substack{abcd\\ ijkl}} \frac{\langle ij|\mathscr{A}_{12}V_{\mathrm{NN}}|ab\rangle \, \langle kl|\mathscr{A}_{12}V_{\mathrm{NN}}|cd\rangle \, \langle cd|\mathscr{A}_{12}V_{\mathrm{NN}}|il\rangle \, \langle ab|\mathscr{A}_{12}V_{\mathrm{NN}}|kj\rangle}{D_{ijab}D_{jkab}D_{ilcd}} \,. \tag{1.37d}$$

One proves the relations (1.36) by rewriting the sum of two denominators [131], e.g.,

$$\delta_1^{-1} + \delta_2^{-1} = \left(D_{ijab}D_{ijcd}D_{klab}\right)^{-1} \,, \tag{1.38a}$$

$$\delta_1 = D_{ijab}D_{ijklabcd}D_{ijcd} \,, \tag{1.38b}$$

$$\delta_2 = D_{ijab}D_{ijklabcd}D_{klab} \,, \tag{1.38c}$$

combined with the permutation symmetries of $D_{ijk\ldots abc\ldots}$ and, for $E^{(4)}_{40}$, one needs to interchange the tuples: $(i,\, j)$, $(k,\, l)$, $(a,\, b)$, and $(c,\, d)$.

1.3.2 Normal ordering with 3N forces

In this section, we extend the discussion of MBPT to include 3N forces. Their analytic definition up to N^3LO will be given in Sec. 2.2. Normal ordering is a well-known method to account for dominant 3N contributions in terms of density-dependent effective two-body interactions (see, e.g., Refs. [28, 43, 132–134] for infinite matter and Refs. [24, 117, 135, 136] for nuclear structure). They are obtained by summing one particle over the occupied states of a finite-density reference state. However, we also consider here the computationally more involved residual 3N term of the normal-ordered Hamiltonian [137]. The new Monte-Carlo framework in Sec. 5 is well-suited for including this (and other) frequently neglected contributions.

In second quantization, the general nuclear Hamiltonian with antisymmetrized NN and 3N interactions,

$$\begin{aligned} H = \sum_{12} T_{12} a_1^\dagger a_2 + \frac{1}{(2!)^2} \sum_{1234} \langle 12|\mathscr{A}_{12} V_{12}|34\rangle\, a_1^\dagger a_2^\dagger a_4 a_3 \\ + \frac{1}{(3!)^2} \sum_{123456} \langle 123|\mathscr{A}_{123} V_{123}|456\rangle\, a_1^\dagger a_2^\dagger a_3^\dagger a_6 a_5 a_4\,, \end{aligned} \tag{1.39}$$

is inherently normal ordered with respect to the vacuum state $|0\rangle$. That means, creation operators $a_i^\dagger$ are located on the left-hand side of annihilation operators a_i, so the vacuum expectation value vanishes by construction, i.e., $\langle 0|a^{(\dagger)}|0\rangle = 0$. However, this is just a specific choice and, in fact, it is usually more convenient to consider likewise a finite-density reference state. As discussed in Sec. 1.3.1, in infinite matter it is natural to work with the Fermi sea in which all single-particle states $|i\rangle = |\mathbf{k}_i \sigma_i \tau_i\rangle$ are filled up to the Fermi momentum k_F,

$$|\Phi\rangle := \prod_{i=1}^{k_i<k_\mathrm{F}} a_i^\dagger\, |0\rangle\ . \tag{1.40}$$

Using Wick's theorem one can rearrange strings of creation and annihilation operators such that $\langle\Phi|N\left[a_1^\dagger a_2^\dagger a_4 a_3\right]|\Phi\rangle = 0$, where $N[\,\cdot\,]$ is the normal-ordered form [138]. Specifically, the theorem states that a string of operators

$$ABCD\ldots = N[ABCD\ldots] + \sum_{\text{single}} N[\wick{\c A \c B} CD\ldots] + \sum_{\text{double}} N[\wick{\c1 A \c2 B \c2 C \c1 D}\ldots] + \ldots\,, \tag{1.41}$$

is equal to sums over all possible normal-ordered contractions: no contraction, single and double contractions and so on. A *contraction* is formally defined by the expectation value of two operators with the reference state,

$$\wick{\c A \c B} := \langle\Phi|AB|\Phi\rangle\ . \tag{1.42}$$

For the Fermi sea, this leads to the relations

$$\wick{\c a_i \c a_j} = \wick{\c a_i^\dagger \c a_j^\dagger} = 0\,, \qquad \wick{\c a_i \c a_j^\dagger} = \delta_{ij}(1-n_j)\,, \qquad \text{and} \qquad \wick{\c a_i^\dagger \c a_j} = \delta_{ij} n_j\,, \tag{1.43}$$

in terms of the Heaviside step function $n_j = \Theta(k_{\mathrm{F},j} - |\mathbf{k}_j|)$ at zero temperature. Wick's theorem transforms the general Hamiltonian (1.39) *exactly* to [125, 139]

$$\begin{aligned} H = E^{(\mathrm{HF})} &+ \sum_{12} f_{12} N[a_1^\dagger a_2] + \frac{1}{(2!)^2} \sum_{1234} \langle 12|\overline{V}^{\mathrm{as}}_{3\mathrm{N}}|34\rangle\, N[a_1^\dagger a_2^\dagger a_4 a_3] \\ &+ \frac{1}{(3!)^2} \sum_{123456} \langle 123|\mathscr{A}_{123} V_{123}|456\rangle\, N[a_1^\dagger a_2^\dagger a_3^\dagger a_6 a_5 a_4]\,, \end{aligned} \tag{1.44}$$

with the normal-ordered zero-, one-, and two-body term defined by,

$$\begin{aligned} E^{(\mathrm{HF})} &= \langle \Phi | H | \Phi \rangle \\ &= \sum_1 T_{11} n_1 + \frac{1}{2!} \sum_{12} \langle 12|\mathscr{A}_{12} V_{12}|12\rangle\, n_1 n_2 + \frac{1}{3!} \sum_{123} \langle 123|\mathscr{A}_{123} V_{123}|123\rangle\, n_1 n_2 n_3\,, \end{aligned} \tag{1.45a}$$

$$f_{12} = T_{12} + \sum_i \langle 1i|\mathscr{A}_{12} V_{12}|2i\rangle\, n_i + \frac{1}{2} \sum_{ij} \langle 1ij|\mathscr{A}_{123} V_{123}|2ij\rangle\, n_i n_j\,, \tag{1.45b}$$

$$\langle 12|\overline{V}^{\mathrm{as}}_{3\mathrm{N}}|34\rangle = \langle 12|\mathscr{A}_{12} V_{12}|34\rangle + \zeta \sum_i \langle 12i|\mathscr{A}_{123} V_{123}|34i\rangle\, n_i\,. \tag{1.45c}$$

Several comments are in order. Equation (1.45c) can be interpreted as a density-dependent (effective) two-body interaction. It contains the usual NN potential as well as a term in which one particle of the initial 3N forces is summed over the occupied states of the reference state. When applied to an NN framework it will automatically take care of (in fact, dominant) 3N contributions at a given density.

Dealing with these effective potentials requires some care. In the formal definition (1.45c), we have introduced the additional (symmetry) factor ζ for technical reasons. At the level of the Hamiltonian (1.44) $\zeta \equiv 1$ but, practically, it is specific to the type of calculation. In MBPT for infinite nuclear matter, $\zeta = 1$ at all orders except if one uses the effective two-body potential to calculate the Hartree-Fock energy (1.45a). To illustrate this, we write

$$E^{(\mathrm{HF})} = \sum_1 T_{11} n_1 + \frac{1}{2!} \sum_{12} \left[\langle 12|\mathscr{A}_{12} V_{12}|12\rangle + \frac{1}{3} \sum_i \langle 12i|\mathscr{A}_{123} V_{123}|12i\rangle\, n_i \right] n_1 n_2\,, \tag{1.46}$$

and identify $\zeta = 1/3$ in comparison to Eq. (1.45c). Obviously, the diagonal one-body term (1.45b) sets $\zeta = 1/2$ in the Fock operator when adding first-order self-energy corrections (from both, NN and 3N forces) to the kinetic energy, see Eq. (1.28). A detailed discussion of symmetry factors regarding the Hartree-Fock spectrum as well as solving the BCS gap equation (see Sec. 6) is given in App. A.

In Fig. 7, we show the diagrams in MBPT up to second order. The ones depicted in the first row sum up to the total Hartree-Fock energy density (1.45a),

$$\frac{E^{(\mathrm{HF})}}{V} = \frac{T^{(0)}}{V} + \frac{E^{(1)}_{\mathrm{NN}}}{V} + \frac{E^{(1)}_{3\mathrm{N}}}{V} \equiv \frac{T^{(0)}}{V} + \frac{E^{(1)}_{\mathrm{NN}+\overline{3\mathrm{N}}}}{V}\,, \tag{1.47}$$

corresponding to Eqs. (1.23), (1.24), and

$$\frac{E^{(1)}_{3\mathrm{N}}}{V} = +\frac{1}{6} \sum_{ijk} \langle ijk|\mathscr{A}_{123} V_{3\mathrm{N}}|ijk\rangle\,. \tag{1.48}$$

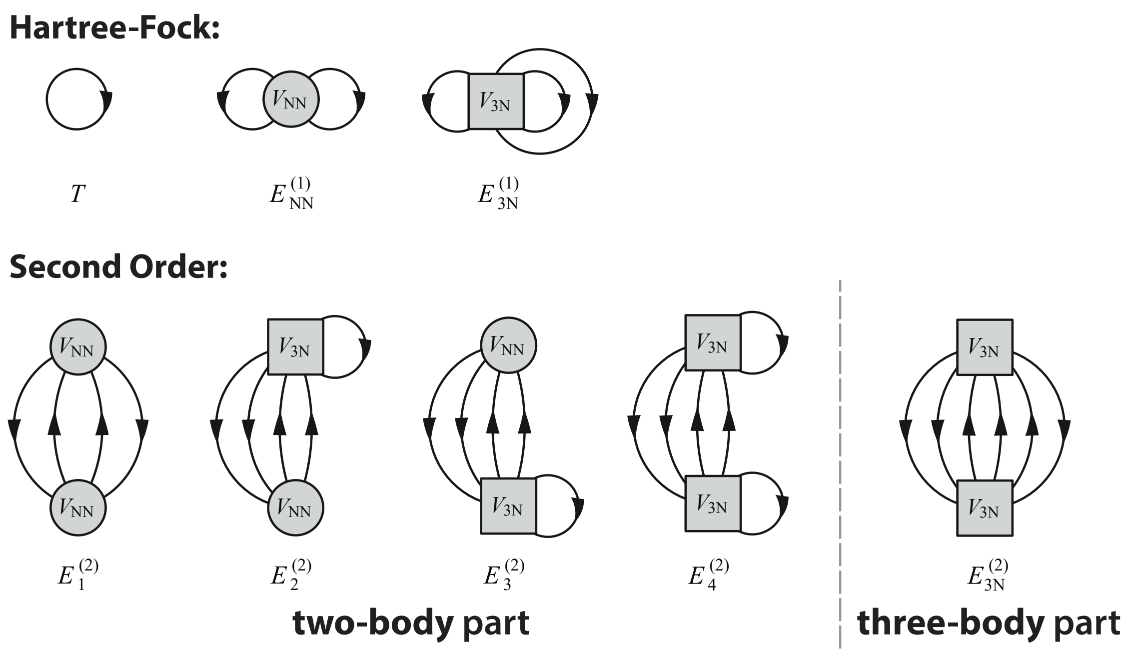

Figure 7: Diagrams in MBPT up to second order with vertices from NN and 3N forces. First row: kinetic energy plus the different Hartree-Fock energies. Second row: diagrams from the normal-ordered two- and three-body part of the Hamiltonian (1.44). Note that $E^{(2)}_{3N}$ cannot be addressed using effective two-body potentials. The figure has been modified from Ref. [43].

As indicated by the second equality in Eq. (1.47) the NN and 3N contributions may be calculated either separately or at once using the NN Hartree-Fock relation (1.24) combined with the effective NN potential (1.45c) and the appropriate symmetry factor (see above). Note that some of our N^{3}LO calculations will moreover add the 4N Hartree-Fock energy,

$$\frac{E^{(1)}_{4N}}{V} = +\frac{1}{24}\sum_{ijkl} \langle ijkl|\mathscr{A}_{1234} V_{4N}|ijkl\rangle \ . \tag{1.49}$$

The effective two-body interaction (1.45c) at second order generates the four diagrams $E^{(2)}_{1\ldots 4}$, associated with the normal-ordered two-body part of the Hamiltonian (1.44). We refer to them by NN+$\overline{3N}$, $\overline{3N}$+NN, and $\overline{3N}$-$\overline{3N}$, respectively, according to the involved interactions: $\overline{3N}$ labels the normal-ordered vertex. Note that $E^{(2)}_2$ and $E^{(2)}_3$ are equivalent. On the other hand, the last diagram in Fig. 7 with

$$\frac{E^{(2)}_{3N}}{V} = +\frac{1}{36}\sum_{\substack{ijk\\abc}} \frac{\langle ijk|\mathscr{A}_{123} V_{3N}|abc\rangle \, \langle abc|\mathscr{A}_{123} V_{3N}|ijk\rangle}{D_{ijkabc}} , \tag{1.50}$$

addresses the residual normal-ordered 3N part of the Hamiltonian. Since it cannot be considered by means of effective two-body potentials it is frequently neglected in infinite-matter calculations (see, e.g., Refs. [27, 140, 141] or Sec. 4). In total, we have at second order

$$\frac{E^{(2)}}{V} = \frac{E^{(\mathrm{HF})}}{V} + \frac{E^{(2)}_{\mathrm{NN}+\overline{3\mathrm{N}}}}{V} + \frac{E^{(2)}_{3N}}{V} , \tag{1.51}$$

where $E^{(2)}_{\mathrm{NN}+\overline{3\mathrm{N}}}$ refers to the second-order term (1.25) combined with the effective potential (1.45c). At higher orders, we neglect residual 3N contributions (see discussion in Sec. 5.4).

More general, the effective potential (1.45c) divides each diagram at order N_{ord} into $2^{N_{\mathrm{ord}}}$ subsequent terms. We evaluate them separately in order to monitor the normal-ordering process. At third order, one has thus $3 \cdot 2^3 = 24$ diagrams which are added to the total energy

$$\frac{E^{(3)}}{V} = \frac{E^{(2)}}{V} + \frac{E^{(3)}_{\mathrm{NN}+\overline{3\mathrm{N}}}}{V} \,. \tag{1.52}$$

Similarly, $E^{(3)}_{\mathrm{NN}+\overline{3\mathrm{N}}}$ refers to the third-order term (1.30) combined with the effective potential (1.45c).

At fourth order, we consider, if at all, only NN contributions because of the significant amount of subsequent diagrams as a consequence of normal ordering:

$$\frac{E^{(4)}}{V} = \frac{E^{(3)}}{V} + \frac{E^{(4)}_{\mathrm{NN}}}{V} \,. \tag{1.53}$$

In practice, we are interested in the energy per particle rather than the energy density. Dividing E/V by the total density of nucleons n gives the desired expression, with

$$n = n_p + n_n = 2 \int \frac{\mathrm{d}\mathbf{k}}{(2\pi)^3} \left[n^p_{\mathbf{k}} + n^n_{\mathbf{k}} \right] = \frac{k^3_{\mathrm{F},p}}{3\pi^2} + \frac{k^3_{\mathrm{F},n}}{3\pi^2} \,. \tag{1.54}$$

1.3.3 Other approaches

Besides MBPT, the nuclear-matter equation of state has been studied within different approaches, such as coupled-cluster theory [13, 14, 137, 142], self-consistent Green's function method [31, 134, 143, 144], and quantum Monte Carlo [16, 17, 44, 103, 145, 146]. In this section, we briefly introduce these nonperturbative methods. A broad overview of recent applications to nuclear matter as well as finite nuclei can be found in Ref. [1]. Similar to Sec. 1.3.1 we concentrate here on ground-state energies.

Coupled-cluster (CC) theory is well-established in nuclear physics and quantum chemistry (see Refs. [124, 125] for reviews). It starts from expanding the true ground-state wave function of a system about a reference state (e.g., the Fermi sea) in the basis of n-particle-n-hole excitations [125], i.e.,

$$|\Psi_0\rangle = |\Phi_0\rangle + \sum_{\substack{a\\i}} C^a_i \, |\Phi^a_i\rangle + \frac{1}{(2!)^2} \sum_{\substack{ab\\ij}} C^{ab}_{ij} \, |\Phi^{ab}_{ij}\rangle + \frac{1}{(3!)^2} \sum_{\substack{abc\\ijk}} C^{abc}_{ijk} \, |\Phi^{abc}_{ijk}\rangle + \ldots \equiv \left(1 + \sum_{n=1}^{\infty} \mathscr{C}_n \right) |\Phi_0\rangle \,, \tag{1.55}$$

where $|\Phi^{a_1 \ldots a_n}_{i_1 \ldots i_n}\rangle := a^\dagger_{a_1} \ldots a^\dagger_{a_n} a_{i_n} \ldots a_{i_1} \, |\Phi_0\rangle$ is the corresponding excited state with amplitude $C^{a_1 \ldots a_n}_{i_1 \ldots i_n}$ in intermediate normalization (for notation see Sec. 1.3.2) and $\mathscr{C}_n$ denotes the excitation operator with $\mathscr{C}_n \, |\Phi_0\rangle \propto |\Phi^{a_1 \ldots a_n}_{i_1 \ldots i_n}\rangle$. This picture also applies to MBPT, in which the order-by-order corrections are given by summations over multiple-excited intermediate states. However, in contrast to MBPT, coupled-cluster theory inherently considers (some of) these states up to all orders, making it a nonperturbative method.

The fundamental concept to achieve this is rather simple: one expresses the basis expansion (1.55) as an exponential function, $|\Psi_0\rangle = e^T |\Phi_0\rangle$, using the (connected) cluster operator [125],

$$T = \sum_{n=1}^{\infty} T_n \,, \qquad \text{with} \qquad T_n = \frac{1}{(n!)^2} \sum_{\substack{i_1,\dots,i_n \\ a_1,\dots,a_n}} t^{a_1\dots a_n}_{i_1\dots i_n} \, a^\dagger_{a_1} \dots a^\dagger_{a_n} a_{i_n} \dots a_{i_1} \,, \tag{1.56}$$

that generates all possible particle-hole excitations. In finite systems, T is naturally truncated by the total particle number. One readily sees that the exponential ansatz and Eq. (1.55) are equivalent; the first three coefficients read [125],

$$\mathscr{C}_1 = T_1 \,, \qquad \mathscr{C}_2 = T_2 + \frac{1}{2} T_1^2 \,, \qquad \mathscr{C}_3 = T_3 + T_1 T_2 + \frac{1}{3!} T_1^3 \,. \tag{1.57}$$

Notice that T_1^2 already results in doubly-excited states. To determine the unknown amplitudes $t^{a_1\dots a_n}_{i_1\dots i_n}$ in Eq. (1.56), one multiplies the Schrödinger equation from left by $\langle \Phi_0 | e^{-T}$ or by each (possible) excited state, such that the so-called coupled-cluster equations are projected out [125],

$$E_0 = \left\langle \Phi_0 \middle| \overline{H} \middle| \Phi_0 \right\rangle \,, \qquad \text{and} \qquad 0 = \left\langle \Phi^{a_1\dots a_n}_{i_1\dots i_n} \middle| \overline{H} \middle| \Phi_0 \right\rangle \,. \tag{1.58}$$

with the similarity-transformed Hamiltonian $\overline{H} = e^{-T} H e^{T}$. The second equation, a set of nonlinear equations, is usually evaluated in terms of the Baker-Campbell-Hausdorff formula, normal-orderered operators, as well as Goldstone's linked-diagram theorem. Having determined the unknown cluster amplitudes it remains to calculate the expectation value for the ground-state energy in Eq. (1.58). At this stage, the Schrödinger equation has been solved *exactly*. In practice, however, approximations are needed to keep the method computationally tractable. Prominently, the cluster operator (1.56) is truncated to single or single and double excitations only, referred to as CCS and CCSD, respectively, whereas CCSD(T) approximates also contributions from triply-excited states (see Refs. [124, 137]). Furthermore, infinite matter is typically modeled by a finite number of particles in a box [137, 142].

For a historical overview of nuclear-matter studies within coupled-cluster theory, we refer the reader to Ref. [124] and emphasize here more recent advances based on chiral interactions. Specifically, in Refs. [13, 142], the energy per particle of neutron and symmetric matter has been studied using CCD in the particle-particle and hole-hole ladder approximation. Note that CCSD becomes CCD for infinite matter [137, 142] since single excitations with respect to the Hartree-Fock reference state vanish, similar to the discussion in Sec. 1.3.1. As pointed out in Ref. [142], also the method of self-consistent Green's function (SCGF) in Ref. [144] employed the ladder approximation. However, while CCD uses only Hartree-Fock single-particle energies, SCGF self-consistently solves for off-shell self-energies but requires extrapolations from finite temperatures due to pairing instabilities. In Sec. 4.3, we will apply the SCGF method of Ref. [144] in order to assess the convergence of MBPT.

In addition to normal-ordered 3N forces, Refs. [147, 148] extended coupled-cluster theory to also work with the residual 3N term in Eq. (1.44). The impact of these contributions together with correlations beyond particle-particle and hole-hole ladders, has been investigated in Refs. [14, 137] using CCD(T). In symmetric matter, they found sizable contributions from both. To improve current state-of-the-art MBPT calculations along these lines, we have developed the Monte Carlo framework in Sec. 5.

The term quantum Monte Carlo (QMC) spans a wide range of stochastic methods (see Refs. [149–151] for reviews). We focus here on one specific class related to diffusion Monte-Carlo (DMC), which projects out the lowest eigenstate of the Hamiltonian that has nonzero overlap with a given trial wave function $|\Psi_T\rangle$. Another approach will be discussed at the end of Sec. 5.3. In the following, we assume $\langle \Psi_0 | \Psi_T \rangle \neq 0$

such that the ground state $|\Psi_0\rangle$ is obtained. Let us consider the propagation of the trial state in imaginary time $\tau = i \cdot t$,

$$\begin{aligned} |\Psi_T(\tau)\rangle = e^{-(H-E_T)\tau}\,|\Psi_T\rangle &= \sum_{i=0}^{\infty} \langle\Psi_i|\Psi_T\rangle\, e^{-(E_i-E_T)\tau}\,|\Psi_i\rangle\;, \\ &= e^{(E_T-E_0)\tau}\Bigg[\,\langle\Psi_0|\Psi_T\rangle\;|\Psi_0\rangle + \sum_{i\neq 0}^{\infty} \langle\Psi_i|\Psi_T\rangle\, e^{-(E_i-E_0)\tau}\,|\Psi_i\rangle\,\Bigg], \end{aligned} \tag{1.59}$$

where we measure energies relative to E_T and treat τ as a real variable. Formally, we have expanded $|\Psi_T\rangle = |\Psi_T(\tau=0)\rangle$ in terms of the eigenstates of the Hamiltonian $|\Psi_{i\geqslant 0}\rangle$ in order to apply the eigenvalue relation for the energies E_i. Knowing that $E_0 < E_1 < \ldots$ we get in the limit of infinite imaginary time both, the (unnormalized) ground-state wave function as well as the corresponding energy,

$$\lim_{\tau\to\infty} |\Psi_T(\tau)\rangle = e^{(E_T-E_0)\tau}\,\langle\Psi_0|\Psi_T\rangle\;|\Psi_0\rangle\;, \qquad \text{and thus} \qquad E_0 = \lim_{\tau\to\infty} \frac{\langle\Psi_T(\tau)|H|\Psi_T(\tau)\rangle}{\langle\Psi_T(\tau)|\Psi_T(\tau)\rangle}\,. \tag{1.60}$$

To this end, one considers in practice the imaginary-time Schrödinger equation in coordinate space,

$$-\partial_\tau \Psi(\mathbf{R},\tau) = -\frac{1}{2m}\nabla^2_{\mathbf{R}}\Psi(\mathbf{R},\tau) + (V(\mathbf{R},\tau) - E_T)\,\Psi(\mathbf{R},\tau)\,, \tag{1.61}$$

as a diffusion equation for a density $\Psi(\mathbf{R},\tau)$ of discrete random walkers, subject to Brownian motion due to the kinetic term and to fluctuations in the population governed by $V(\mathbf{R},\tau) - E_T$ in Eq. (1.61). Here, **R** contains the spatial coordinates of all particles including their spin and isospin quantum numbers, while the interaction has to be local to obtain low-variance results. During the imaginary-time propagation, for instance, one adjusts E_T to regulate the number of random walkers until eventually equilibrium settles in. The projection onto the ground-state wave function is then completed and DMC has solved the many-body Schrödinger equation (in principle) *exactly*. However, sampling fermionic wave functions by random walkers as described above is nontrivial because they are not of definite sign due to antisymmetry. This is still an unsolved issue referred to as the Fermion sign problem [149]. When using fixed-node or constrained-path approximations, one makes an ansatz for the nodal surface and separates the propagation of random walkers to regions where the wave function is of one sign. Obviously, this requires good estimates of the true ground-state wave function, whereas in practice the projected ground-state energy will scatter for different initial guesses. Furthermore, QMC calculations are computationally expensive and thus limited in particle number, in particular, due to the spin-isospin dependence of the nuclear interaction. A related method is called auxiliary-diffusion Monte Carlo (AFDMC) which improves the scaling behavior by introducing additional auxiliary fields (for details see Ref. [150]). Recently, Refs. [16, 17, 146] constructed local chiral potentials up to N^{2}LO, which enabled for the first time QMC calculations with interactions derived within chiral EFT [16, 17, 81, 103–105, 146, 152]. The results of these studies also provide the first nonperturbative validations of MBPT for neutron matter. Promising, however, approximate AFDMC calculations of symmetric (and even asymmetric) matter can be found in Refs. [145, 153] based on phenomenological NN interactions.

Figure 8 compiles the energy per particle in neutron matter up to saturation density as obtained in different many-body frameworks [1]; see in addition Ref. [155]. All calculations in the left panel are based on the N^{3}LO NN potential EM 500 MeV [154] plus individual 3N contributions, where the uncertainty bands are dominated by (the same) c_i variation in the N^{2}LO 3N forces; in MBPT [42] (region between red-dashed lines), in the SCGF method [141] (region between yellow lines) including leading 3N forces, and combined with all 3N and 4N interactions up to N^{3}LO [108, 140] (cyan band). Evolving the NN potential to $\Lambda = 2\,\mathrm{fm}^{-1}$ combined with bare N^{2}LO 3N forces [42, 43] leads to the magenta band. In

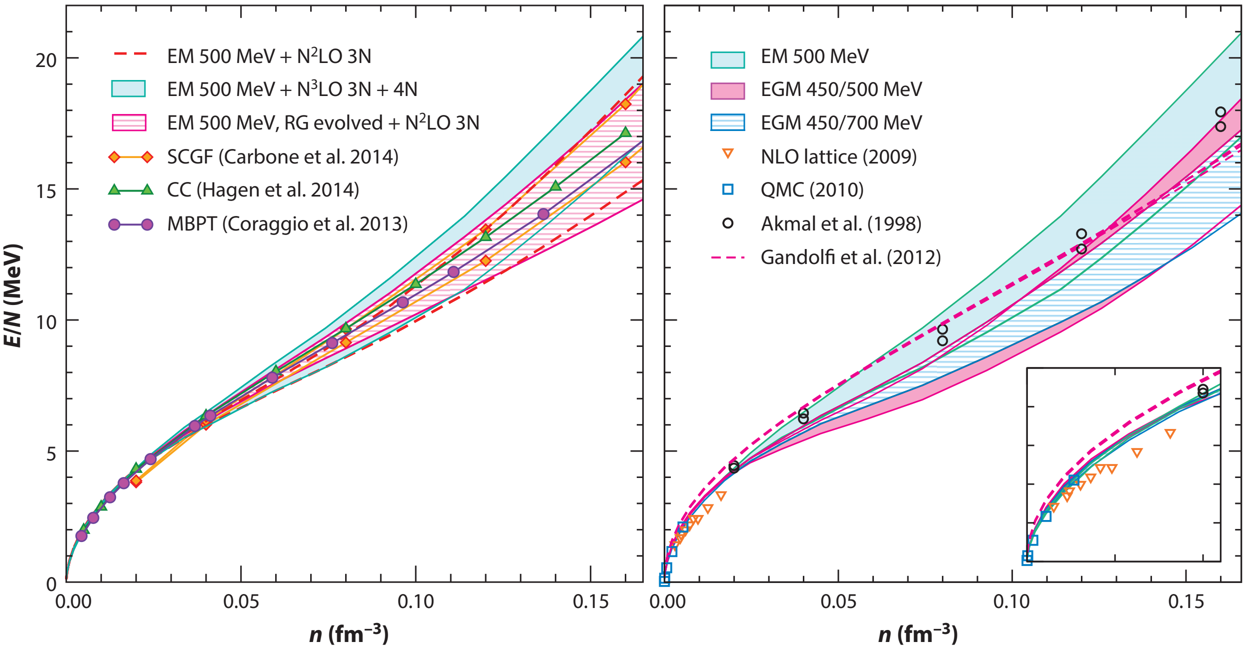

Figure 8: Various calculations of the energy per particle of neutron matter. All calculations in the left panel are based on the N^{3}LO NN potential EM 500 MeV [154] combined with individual 3N forces. The figure has been taken from Ref. [1]. See the main text for details.

comparison, the results in CC theory [137] and MBPT [107] are depicted by the green and purple line, respectively. Notice that all calculations lay in the union of the magenta and cyan band, except for the lowest-density point of the SCGF method (presumably due to the extrapolation to zero temperature).

In the right panel of Fig. 8 we show bands including all many-body forces at N^{3}LO based on the NN potentials of Refs. [67, 154]. The cyan, magenta, and blue band accounts for the many-body uncertainty, the variation in the LECs c_i, and the different 3N as well as 4N cutoffs (for details see Refs. [108, 140]). Furthermore, there are low-density results from NLO lattice [156] and QMC [157] (magnified in the inset), whereas up saturation density from variational calculations [158] (Akmal *et al.*) and AFDMC [44] (Gandolfi *et al.*) based on phenomenological NN plus 3N potentials. For more details we refer to Ref. [1].

The overall agreement between different many-body frameworks and Hamiltonians is quite remarkable, which demonstrates that the neutron-matter equation of state is tightly constrained at these densities. As we will see in the present thesis, this is different in symmetric matter (see also Ref. [14]).

1.3.4 Similarity renormalization group

Renormalization-group (RG) methods play a key role in softening nuclear interactions and thus improving the convergence of many-body frameworks which are based on basis expansions. In this thesis, we are in particular interested in making MBPT for infinite matter more efficient (or applicable at all) within the limited orders we can calculate. We discuss here briefly the similarity renormalization group (SRG) [159–161] as preparation for our calculations. A review on low-momentum interactions in general and the wide range of applications in nuclear physics can be found in Ref. [139], including the alternative $V_{\mathrm{low}\,k}$ approach. We will monitor the SRG-evolution using Weinberg eigenvalues and partial-wave matrix elements of the interactions in Sec. 3.3.

The left panel of Fig. 9 exemplarily shows a contour plot of the phenomenological NN potential Argonne v_{18} [92] in the $^1S_0$ channel as a function of the initial and final relative momenta of two nucleons

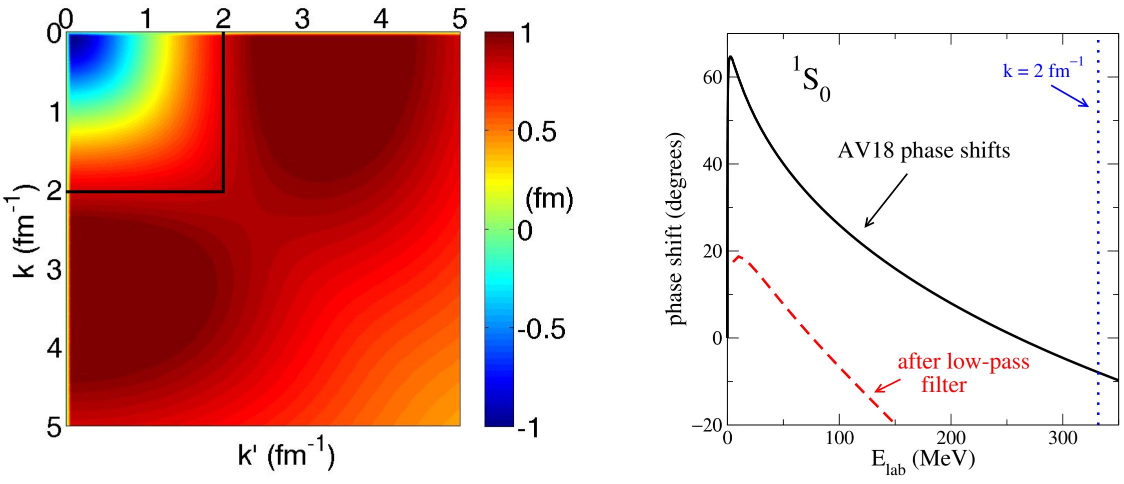

Figure 9: Contour plot of the phenomenological NN potential Argonne v_{18} [92] in momentum space in the $^1S_0$ channel (left panel). The black box indicates a naive approach to decouple low from high momenta by chopping all matrix elements above $\Lambda = 2\,\text{fm}^{-1}$. Only the phase shifts of the initial potential (black line) reproduce experimental extractions, whereas the low-pass filter (black box) renders the potential useless [162] (right panel). The figures have been modified from Ref. [139].

k and k', respectively. In the following, we define $k \lesssim 2\,\text{fm}^{-1}$ as low momenta [162], corresponding to $E_{\text{lab}} \lesssim 330\,\text{MeV}$. Notice the large low-to-high-momentum couplings in Fig. 9 (dark-red regions), which can be traced back to the strong repulsive core, i.e., short-range correlations. From our discussion in Sec. 1.3.1, it is evident that second- and higher-order corrections in MBPT will be enhanced due to these large offdiagonal matrix elements. One might naively think that the decoupling can be achieved by simply imposing a regulator function (i.e., a low-pass filter) which chops all components above the momentum scale $\Lambda = 2\,\text{fm}^{-1}$, as depicted by the black box. The right panel of Fig. 9, however, reveals that this renders the potential useless at all scales (even for momenta below Λ) since it does not reproduce phase shifts anymore. These high-momentum couplings inherently contribute to low-energy observables due to intermediate-state summations [139].

Preserving observables such as scattering phase shifts to all energies the decoupling can safely be realized in terms of unitary transformations U (i.e., $U^\dagger U = 1$), as shown here for the evaluation of an energy expectation value [162]

$$E_0 = \langle \Psi_0 | H | \Psi_0 \rangle = \langle \Psi_0 | U^\dagger\, U H U^\dagger\, U | \Psi_0 \rangle = \langle \tilde{\Psi}_0 | \tilde{H} | \tilde{\Psi}_0 \rangle \, . \tag{1.62}$$

Both, the Hamiltonian $\tilde{H} = U\,H\,U^\dagger$ and the wave function $|\tilde{\Psi}\rangle = U\,|\Psi_0\rangle$ are transformed while E_0 remains invariant. The SRG however transforms an initial Hamiltonian $H = T_{\text{rel}} + V$ in a series of infinitesimal steps to

$$H_s = U(s)\,H\,U^\dagger(s) = T_{\text{rel}} + V_s \, , \tag{1.63}$$

where s labels the flow parameter and T_{rel} is the relative kinetic-energy operator, chosen to be invariant. Taking the first derivative with respect to s results in the flow equation, which describes the SRG evolution [163],

$$\frac{\mathrm{d}H_s}{\mathrm{d}s} = [\eta(s), H_s] \, , \qquad \text{with} \qquad \eta(s) = \frac{\mathrm{d}U(s)}{\mathrm{d}s} U^\dagger(s) = -\eta^\dagger(s) \, . \tag{1.64}$$

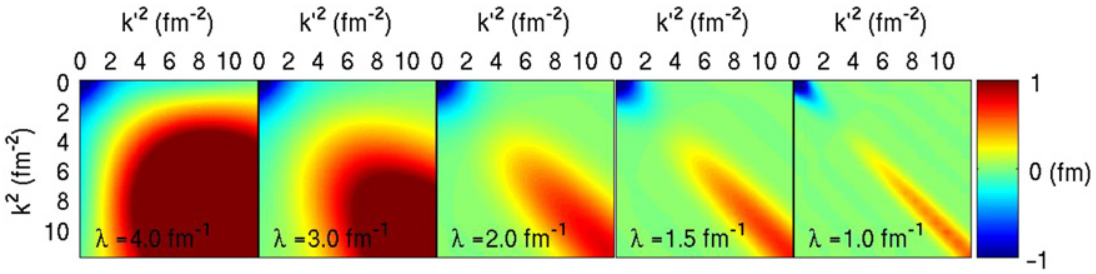

Figure 10: Contour plot in momentum space of the initial N^{3}LO NN potential EM 600 MeV [154] in the $^1S_0$ channel evolved from left to right towards lower SRG resolution scales $\lambda = s^{-1/4}$, as annotated. The figure has been taken from Ref. [139].

The anti-Hermitian operator $\eta(s) = [G_s, H_s]$ generates the transformation and can be expressed as a commutator of a Hermitian operator G_s and H_s. For the frequent choice $G_s = T_{\text{rel}}$ the evolved potential V_s in a given partial-wave channel is determined by [163]

$$\frac{\mathrm{d}V_s(k, k')}{\mathrm{d}s} = -(k^2 - k'^2)^2 V_s(k, k') + \frac{2}{\pi} \int_0^\infty \mathrm{d}q\, q^2 (k^2 + k'^2 - 2q^2) V_s(k, q) V_s(q, k') \,. \tag{1.65}$$

In the region far away from the diagonal the first term dominates, so the analytic solution reads [163]

$$V_s(k, k') = V_{s=0}(k, k')\, e^{-(k^2 - k'^2)^2 s} \,. \tag{1.66}$$

Equation (1.66) readily shows that the Hamiltonian is driven towards the band-diagonal form (for the block-diagonal approach see Ref. [164]) and that $\lambda = s^{-1/4}$ in units of fm^{-1} measures the band width. Figure 10 depicts the SRG evolution in momentum space based on the initial N^{3}LO NN potential EM 600 MeV [154] in the $^1S_0$ channel. From left to right, the resolution scale λ is lowered and the green colored regions indicate that offdiagonal matrix elements successively have been suppressed. Evolved to low-resolution scales one observes a universal behavior among nuclear potentials due to the common long-range 1π exchange and the reproduction of low-energy NN observables [139]. The SRG transformation was first applied to NN interactions in Ref. [163].

In general, RG transformations induce many-body forces even if they are not present in the initial Hamiltonian. That means, many-body observables such as the triton binding energy will depend on λ (see, e.g., Fig. 1 in Ref. [165]), unless all induced forces are properly included. These residual scale dependences contribute then to the theoretical uncertainties of the calculation. For first studies of neutron matter using consistently-evolved NN and 3N forces we refer the reader to Refs. [166, 167].

2 Nuclear forces from chiral effective field theory

Chiral nuclear forces are the microscopic input to all calculations of this thesis. Following up the formal introduction in Sec. 1.2.2, we discuss here the operatorial expressions for NN, 3N, as well as 4N forces up to N^{3}LO in Weinberg power counting and conclude with achievements beyond N^{3}LO (see also Fig. 5). This is currently the highest order at which state-of-the-art calculations involving consistent many-body contributions can be realized. The new Monte-Carlo framework presented in Sec. 5 directly implements the analytic expressions shown in this section. Furthermore, we compare properties of recent chiral NN interactions with emphasis on the different regularization schemes.

We refer the reader to Refs. [5–7, 67–70] and the references therein for comprehensive reviews on chiral interactions. Numerical values for physical constants are provided in Refs. [168, 169].

2.1 Nucleon-nucleon interactions

In recent years, significant progress has been made in developing new nuclear potentials derived within chiral EFT. This includes the development of novel advanced fitting frameworks [14, 15], the exploration of new regularization schemes [9, 10], the explicit inclusion of Δ-resonances [29, 170, 171], and the derivation of more systematic theoretical uncertainties estimates [9, 10]. In addition to local chiral interactions, now available up to N^{2}LO [16, 17], nonlocal potentials were systematically (i.e., order-by-order) constructed up to N^{4}LO [8–11], even considering selected 2π- and 3π-exchange contributions at N^{5}LO [12].

Chiral EFT describes long- and short-range physics differently. The former is predicted by multiple exchanges of the Goldstone bosons of (spontaneous) chiral-symmetry breaking, the pions, combined with data from pion-nucleon (πN) scattering, whereas the latter cannot be resolved explicitly and is thus encoded in terms of LECs to be fitted to experimental data. Specifically, one has the chiral expansion for the total NN interaction

$$V_{\mathrm{NN}} = V_{\mathrm{cont}} + \sum_{n=1}^{\infty} V_{n\pi}\,, \qquad \text{with} \qquad V_{\mathrm{cont}} = \sum_{\nu=0,2,4,\ldots}^{\infty} V_{\mathrm{cont}}^{(\nu)}\,, \qquad \text{and} \qquad V_{n\pi} = \sum_{\substack{\nu=2n-2\\ \nu\neq 1}}^{\infty} V_{n\pi}^{(\nu)}\,. \tag{2.1}$$

The subscripts denote either contact terms or pion exchanges, and ν is the order in the chiral expansion defined in Eq. (1.10). Although the analytic form (to full extent) is rather involved at the orders we consider here, the interaction (2.1) contains only a few operator structures,

$$\begin{aligned} V_{\mathrm{NN}} = \mathcal{V}_C\,\mathbb{1} + \mathcal{V}_S\,\boldsymbol{\sigma}_1\cdot\boldsymbol{\sigma}_2 + \mathcal{V}_T\,\boldsymbol{\sigma}_1\cdot\mathbf{q}\,\boldsymbol{\sigma}_2\cdot\mathbf{q} + \mathcal{V}_{T,k}\,\boldsymbol{\sigma}_1\cdot\mathbf{k}\,\boldsymbol{\sigma}_2\cdot\mathbf{k} \\ + \mathcal{V}_{LS}\,(-i)\,\mathbf{S}\cdot(\mathbf{q}\times\mathbf{k}) + \mathcal{V}_{\sigma L}\,\boldsymbol{\sigma}_1\cdot(\mathbf{q}\times\mathbf{k})\,\boldsymbol{\sigma}_2\cdot(\mathbf{q}\times\mathbf{k})\,, \end{aligned} \tag{2.2}$$

with the total spin $\mathbf{S} = (\boldsymbol{\sigma}_1 + \boldsymbol{\sigma}_2)/2$ as well as with

$$\mathbf{q} = \mathbf{p}' - \mathbf{p}\,, \qquad \mathbf{k} = \frac{\mathbf{p}' + \mathbf{p}}{2}\,, \qquad \mathbf{p}' = \frac{\mathbf{p}_1' - \mathbf{p}_2'}{2}\,, \qquad \text{and} \qquad \mathbf{p} = \frac{\mathbf{p}_1 - \mathbf{p}_2}{2}\,, \tag{2.3}$$

defined by the initial and final single-particle momenta $\mathbf{p}_i$ and $\mathbf{p}_i'$, respectively. That is the momentum transfer, the momentum transfer in the exchange channel, the final and the initial relative momentum. Galilean invariance prevents the total momentum $\mathbf{P} = \mathbf{p}_1 + \mathbf{p}_2$ (conserved) from appearing in Eq. (2.2). The scalar functions $\mathcal{V}_i := \mathcal{V}_i(\mathbf{p}, \mathbf{p}')$ subdivide into two terms, proportional to $\mathbb{1}$ or $\boldsymbol{\tau}_1\cdot\boldsymbol{\tau}_2$, both having long- and short-range contributions in general. For nonlocal potentials, it is however practice to exploit Fierz ambiguities from antisymmetrization (see below) in order to pick an isospin-independent contact-operator basis [67]. As a result, we deal with

$$\mathcal{V}_i = V_i^{(\mathrm{cont})} + [V_i + \boldsymbol{\tau}_1 \cdot \boldsymbol{\tau}_2 \, W_i] \, , \tag{2.4}$$

where the scalar functions $V_i^{(\mathrm{cont})}$ and V_i, W_i express contacts and pion exchanges, respectively. The latter are local (i.e., depend solely on $\mathbf{q}$), disregarding relativistic corrections [9]. In Refs. [16, 17], this freedom in choosing a suitable basis for short-range physics was key for constructing local chiral potentials.

Following Refs. [8, 9, 67], we now discuss order-by-order the analytic expressions of chiral NN forces. Each scalar function is expanded separately, as indicated by an additional superscript. Not explicitly defined terms do not contribute to keep the presentation brief. One should be aware of the fact that the notation in Eq. (2.2) follows the convention by Entem, Machleidt [6, 8]. Regarding the spin-orbit operator, Epelbaum *et al.* [9, 67] factorize $-1/2$ into the scalar functions V_{LS}, W_{LS} and separate $V_{LS}^{(\mathrm{cont})}$ with a minus sign. Obviously, these formal redefinitions do not affect the overall potential. For the 2π-exchange contributions, it is convenient to introduce the abbreviations

$$w = \sqrt{q^2 + 4m_\pi^2}\, , \qquad \tilde{w} = \sqrt{q^2 + 2m_\pi^2}\, , \qquad \text{and} \qquad s = \sqrt{\tilde{\Lambda}^2 - 4m_\pi^2}\, , \tag{2.5}$$

where $\tilde{\Lambda}$ is the cutoff scale associated with the spectral-function regularization (SFR) of the loop diagrams [172, 173]. The corresponding expressions used in dimensional regularization (DR) are obtained by taking the limit $\tilde{\Lambda} \to \infty$. Two (regularized) loop functions appear in the definitions:

$$L(q;\, \tilde{\Lambda}) = \frac{w}{2q} \ln \frac{\tilde{\Lambda}^2 w^2 + q^2 s^2 + 2\tilde{\Lambda} q w s}{4m_\pi^2(\tilde{\Lambda}^2 + q^2)}\, , \qquad \text{with} \qquad L(q) = \lim_{\tilde{\Lambda}\to\infty} L(q;\, \tilde{\Lambda}) = \frac{w}{q} \ln \frac{w+q}{2m_\pi}\, , \tag{2.6}$$

$$A(q;\, \tilde{\Lambda}) = \frac{1}{2q} \arctan \frac{q(\tilde{\Lambda} - 2m_\pi)}{q^2 + 2\tilde{\Lambda} m_\pi}\, , \qquad \text{with} \qquad A(q) = \lim_{\tilde{\Lambda}\to\infty} A(q;\, \tilde{\Lambda}) = \frac{1}{2q} \arctan \frac{q}{2m_\pi}\, . \tag{2.7}$$

At leading-order (LO, $\nu = 0$), the NN forces consist of momentum-independent contact interactions as well as the 1π-exchange potential,

$$W_T^{(0)}(q;\, m_\pi) = -\frac{g_A^2}{4f_\pi^2} \frac{1}{q^2 + m_\pi^2}\, , \tag{2.8}$$

with the axial coupling constant $g_A = 1.267$, the average pion mass $m_\pi = (2\, m_{\pi^\pm} + m_{\pi^0})/3$, and the pion decay constant f_π. Instead of Eq. (2.8), one uses (e.g., in Refs. [8, 9]) the corresponding charge-dependent expressions

$$V_T^{(0,pp)}(q) = V_T^{(0,nn)}(q) = W_T^{(0)}(q;\, m_{\pi^0})\, , \tag{2.9a}$$

$$V_T^{(0,np)}(q;\, T) = -W_T^{(0)}(q;\, m_{\pi^0}) + 2\,(-1)^{T+1}\, W_T^{(0)}(q;\, m_{\pi^\pm})\, , \tag{2.9b}$$

to account for the different pion masses $m_{\pi^\pm} \neq m_{\pi^0}$. Note that $\boldsymbol{\tau}_1 \cdot \boldsymbol{\tau}_2$ has been written in terms of the total isospin $T = 0, 1$. As mentioned above, one has the freedom to arbitrarily choose two of the four possible contact operators $\mathbb{1}$, $\boldsymbol{\sigma}_1 \cdot \boldsymbol{\sigma}_2$, $\boldsymbol{\tau}_1 \cdot \boldsymbol{\tau}_2$, and $\boldsymbol{\sigma}_1 \cdot \boldsymbol{\sigma}_2\, \boldsymbol{\tau}_1 \cdot \boldsymbol{\tau}_2$ since only two physical S-waves exist. The other two (linear-dependent) operator terms are generated through antisymmetrization [67]. In practice, one usually takes the first two terms (see also the original work in Refs. [85, 86]),

$$V_C^{(0,\mathrm{cont})} = C_S^{(m_T)}\, , \qquad V_S^{(0,\mathrm{cont})} = C_T^{(m_T)}\, , \tag{2.10}$$

proportional to C_S and C_T, respectively. Arguing with the two large S-wave scattering lengths and (approximately) Wigner symmetry, one expects C_T to be small. Beyond LO, the two LECs in Eq. (2.10) get charge-dependent as indicated by the superscript $m_T = nn, pp, np$.

At next-to-leading order (NLO, $\nu = 2$), 2π exchanges enter and, similar to the ambiguities at LO, one has the freedom to choose seven out of 14 allowed contact operators in total which are proportional to $C_{1\ldots7}$,

$$V_C^{(2,\,\mathrm{cont})} = C_1\,q^2 + C_2\,k^2\,, \qquad V_S^{(2,\,\mathrm{cont})} = C_3\,q^2 + C_4\,k^2\,, \qquad V_{LS}^{(2,\,\mathrm{cont})} = C_5\,, \tag{2.11a}$$

$$V_T^{(2,\,\mathrm{cont})} = C_6\,, \qquad V_{T,k}^{(2,\,\mathrm{cont})} = C_7\,. \tag{2.11b}$$

The axial coupling constant g_A in the 1π exchange (2.8) is modified due to the Goldberger-Treiman discrepancy [174],

$$g_{\pi N} = \frac{g_A m}{f_\pi}\left(1 - \frac{2m_\pi^2 \bar{d}_{18}}{g_A} + \ldots\right), \tag{2.12}$$

with $m = 2m_p m_n/(m_p + m_n)$ being the nucleon mass. This correction can be considered by replacing $g_A \to g_A - 2d_{18}m_\pi^2$. The LEC $\bar{d}_{18}$ originates from the πN Lagrangian and the ellipsis indicates higher-order terms. With $g_A = 1.267$ and the empirical value for $g_{\pi N} \simeq 13.65$ [6] one gets $\bar{d}_{18} \sim -1\ \mathrm{GeV}^{-2}$. Typically, the discrepancy (2.12) is taken care of by using a larger overall value for $g_A = 1.29$ (see Refs. [6, 67, 172, 173, 175] for detailed discussions).

For the 2π-exchange contribution, one has the parameter-free expressions [176]

$$W_C^{(2)}(q) = -\frac{L(q;\,\tilde{\Lambda})}{384\pi^2 f_\pi^4}\left[4m_\pi^2(5g_A^4 - 4g_A^2 - 1) + q^2(23g_A^4 - 10g_A^2 - 1) + \frac{48g_A^4 m_\pi^4}{w^2}\right], \tag{2.13}$$

$$V_T^{(2)}(q) = -\frac{1}{q^2}V_S^{(2)} = -\frac{3g_A^4}{64\pi^2 f_\pi^4}\,L(q;\,\tilde{\Lambda})\,. \tag{2.14}$$

At next-to-next-to-leading order (N^{2}LO, $\nu = 3$), no additional contact terms appear. The contributions to the subleading 2π exchange read [176]

$$V_C^{(3)}(q) = -\frac{3g_A^2}{16\pi f_\pi^4}\left[2m_\pi^2(2c_1 - c_3) - c_3 q^2\right]\tilde{w}^2 A(q;\,\tilde{\Lambda})\,, \tag{2.15}$$

$$W_T^{(3)}(q) = -\frac{1}{q^2}W_S^{(3)} = -\frac{g_A^2}{32\pi f_\pi^4}\,c_4 w^2 A(q;\,\tilde{\Lambda})\,. \tag{2.16}$$

Internal excitations of Δ-resonances with energies $m_\Delta - m \approx 300\,\mathrm{MeV} < \Lambda_b$ are not explicitly resolved within chiral EFT [5, 6]. They are however mimicked by larger values for the LECs $c_{3,4}$, known as resonance saturation [177, 178], whereas the Δ-full description is expected to improve the convergence of the chiral expansion [70].

At next-to-next-to-next-to-leading order (N^{3}LO, $\nu = 4$), one has 15 additional LECs $D_{1\ldots15}$ (chosen out of 30 allowed terms),

$$V_C^{(4,\,\mathrm{cont})} = D_1\,q^4 + D_2\,k^4 + D_3\,q^2k^2 + D_4\,(\mathbf{q}\times\mathbf{k})^2\,, \qquad V_T^{(4,\,\mathrm{cont})} = D_{11}\,q^2 + D_{12}\,k^2\,, \tag{2.17a}$$

$$V_S^{(4,\,\mathrm{cont})} = D_5\,q^4 + D_6\,k^2 + D_7\,q^2\,k^2 + D_8\,(\mathbf{q}\times\mathbf{k})^2\,, \qquad V_{T,k}^{(4,\,\mathrm{cont})} = D_{13}\,q^2 + D_{14}\,k^2\,, \tag{2.17b}$$

$$V_{LS}^{(4,\,\mathrm{cont})} = D_9\,q^2 + D_{10}\,k^2\,, \qquad V_{\sigma L}^{(4,\,\mathrm{cont})} = D_{15}\,. \tag{2.17c}$$

Notice that Lagrange's identity yields $(\mathbf{q}\times\mathbf{k})^2 = p^2 p'^2\left(1-z^2\right)$ with $z=\cos\theta_{\mathbf{pp}'}$.

The 2π-exchange contribution can be separated into two groups. Specifically, the first group has the closed analytic form [179],

$$V_C^{(4;a)}(q) = \frac{3}{16\pi^2 g_\pi^4}\left\{\left[\frac{c_2}{6}w^2 + c_3\tilde{w}^2 - 4c_1 m_\pi^2\right]^2 + \frac{c_2^2}{45}w^4\right\} L(q;\,\tilde{\Lambda})\,, \tag{2.18}$$

$$W_T^{(4;a)}(q) = -\frac{1}{q^2}W_S^{(4;a)}(q) = \frac{c_4^2}{96\pi^2 f_\pi^4}w^2\, L(q;\,\tilde{\Lambda})\,, \tag{2.19}$$

while the second group involves integrals,

$$V_{C,S}^{(4;b)}(q) = -\frac{2q^6}{\pi}\int_{2m_\pi}^{\tilde{\Lambda}} \mathrm{d}\mu \frac{\rho_{C,S}^{(4)}(\mu)}{\mu^5(\mu^2+q^2)}\,, \qquad V_T^{(4;b)}(q) = \frac{2q^4}{\pi}\int_{2m_\pi}^{\tilde{\Lambda}} \mathrm{d}\mu \frac{\rho_T^{(4)}(\mu)}{\mu^3(\mu^2+q^2)}\,, \tag{2.20a}$$

$$W_{C,S}^{(4;b)}(q) = -\frac{2q^6}{\pi}\int_{2m_\pi}^{\tilde{\Lambda}} \mathrm{d}\mu \frac{\eta_{C,S}^{(4)}(\mu)}{\mu^5(\mu^2+q^2)}\,, \qquad W_T^{(4;b)}(q) = \frac{2q^4}{\pi}\int_{2m_\pi}^{\tilde{\Lambda}} \mathrm{d}\mu \frac{\eta_T^{(4)}(\mu)}{\mu^3(\mu^2+q^2)}\,, \tag{2.20b}$$

over the spectral functions [9, 179],

$$\rho_C^{(4)}(\mu) = -\frac{3g_A^4 t^2}{\pi\mu(4f_\pi)^6}\left((m_\pi^2 - 2\mu^2)\left[2m_\pi - \frac{t^2}{2\mu}\ln\frac{\mu+2m_\pi}{\mu-2m_\pi}\right] - 4g_A^2 m_\pi t^2\right)\,, \tag{2.21}$$

$$\eta_S^{(4)}(\mu) = \mu^2\eta_T^{(4)}(\mu) = -\frac{4g_A^4 r^2}{\pi(4f_\pi)^6}\left\{-r^2\ln\frac{\mu+2m_\pi}{\mu-2m_\pi} + (1+2g_A^2)\mu m_\pi\right\}\,, \tag{2.22}$$

$$\rho_S^{(4)}(\mu) = \mu^2\rho_T^{(4)}(\mu) = -\left\{\frac{g_A^2 r^3\mu}{8f_\pi^4\pi}(\bar{d}_{14}-\bar{d}_{15}) - \frac{2g_A^6\mu r^3}{(8\pi f_\pi^2)^3}\left[\frac{1}{9} - J_1 + J_2\right]\right\}\,, \tag{2.23}$$

$$\begin{aligned}
\eta_C^{(4)}(\mu) = \Bigg\{ & \frac{rt^2}{24f_\pi^4\mu\pi}\left[2(g_A^2-1)r^2 - 3g_A^2t^2\right](\bar{d}_1+\bar{d}_2) \\
& + \frac{r^3}{60f_\pi^4\mu\pi}\left[6(g_A^2-1)r^2 - 5g_A^2t^2\right]\bar{d}_3 - \frac{rm_\pi^2}{6f_\pi^4\mu\pi}\left[2(g_A^2-1)r^2 - 3g_A^2t^2\right]\bar{d}_5 \\
& - \frac{1}{92160f_\pi^6\mu^2\pi^3}\Big[-320\left(1+2g_A^2\right)^2 m_\pi^6 + 240(1+6g_A^2+8g_A^4)m_\pi^4\mu^2 \\
& - 60g_A^2(8+15g_A^2)m_\pi^2\mu^4 + \left(-4+29g_A^2+122g_A^4+3g_A^6\right)\mu^6\Big]\ln\frac{2r+\mu}{2m_\pi} \\
& - \frac{r}{2700\mu(8\pi f_\pi^2)^3}\Big[-16\left(171+2g_A^2(1+g_A^2)(327+49g_A^2)\right)m_\pi^4 \\
& + 4\left(-73+1748g_A^2+2549g_A^4+726g_A^6\right)m_\pi^2\mu^2 \\
& - \left(-64+389g_A^2+1782g_A^4+1093g_A^6\right)\mu^4\Big] \\
& + \frac{2r}{3\mu(8\pi f_\pi^2)^3}\left[g_A^6t^4J_1 - 2g_A^4(2g_A^2-1)r^2t^2J_2\right]\Bigg\}\,,
\end{aligned} \tag{2.24}$$

which depend on the LECs $\bar{d}_1+\bar{d}_2$, $\bar{d}_3$, $\bar{d}_5$, as well as $\bar{d}_{14}-\bar{d}_{15}$ (see Ref. [174]). Here, we introduced the short-hand notation

$$r = \frac{1}{2}\sqrt{\mu^2-4m_\pi^2}\,, \qquad t = \sqrt{\mu^2-2m_\pi^2}\,, \tag{2.25}$$

and the dimensionless functions [9]

$$J_1(\mu) = \int_0^1 \mathrm{d}x \left\{ \frac{m_\pi^2}{r^2x^2} - \left(1 + \frac{m_\pi^2}{r^2x^2}\right)^{3/2} \ln \frac{rx + \sqrt{m_\pi^2 + r^2x^2}}{m_\pi} \right\}, \tag{2.26}$$

$$J_2(\mu) = \int_0^1 \mathrm{d}x\, x^2 \left\{ \frac{m_\pi^2}{r^2x^2} - \left(1 + \frac{m_\pi^2}{r^2x^2}\right)^{3/2} \ln \frac{rx + \sqrt{m_\pi^2 + r^2x^2}}{m_\pi} \right\}. \tag{2.27}$$

In addition, there are the relativistic corrections to the NLO diagrams [8, 9],

$$V_C^{(4;c)} = \frac{3g_A^4}{128\pi f_\pi^4 m} \left[\frac{m_\pi^5}{2w^2} + \tilde{w}^2 (q^2 - m_\pi^2) A(q;\, \tilde{\Lambda}) \right], \tag{2.28}$$

$$W_C^{(4;c)} = \frac{g_A^2}{64\pi f_\pi^4 m} \left\{ \frac{3g_A^2 m_\pi^5}{2\omega^2} + \left[g_A^2 (3m_\pi^2 + 2q^2) - \tilde{w}^2 \right] \tilde{w}^2 A(q;\, \tilde{\Lambda}) \right\}, \tag{2.29}$$

$$V_T^{(4;c)} = -\frac{1}{q^2} V_S^{(4;c)} = \frac{3g_A^4}{256\pi f_\pi^4 m} (5m_\pi^2 + 2q^2) A(q;\, \tilde{\Lambda}), \tag{2.30}$$

$$W_T^{(4;c)} = -\frac{1}{q^2} W_S^{(4;c)} = \frac{g_A^2}{128\pi f_\pi^4 m} \left[g_A^2 (3m_\pi^2 + q^2) - w^2 \right] A(q;\, \tilde{\Lambda}), \tag{2.31}$$

$$V_{LS}^{(4;c)} = \frac{3g_A^4}{32\pi f_\pi^4 m} \tilde{w}^2 A(q;\, \tilde{\Lambda}), \tag{2.32}$$

$$W_{LS}^{(4;c)} = \frac{g_A^2 (1 - g_A^2)}{32\pi f_\pi^4 m} w^2 A(q;\, \tilde{\Lambda}). \tag{2.33}$$

Note that Refs. [8, 9] employ in fact the same relativistic corrections at this order, although they are written as a sum of two contributions in Ref. [9]. The more traditional N^{3}LO potentials by Epelbaum, Glöckle, and Meißner (EGM) [67] do not consider the additional terms δV_i and δW_i as they are defined in Ref. [9].

In summary, the 2π-exchange contributions at N^{3}LO are given by

$$V_i^{(4)} = V_i^{(4;a)} + V_i^{(4;b)} + V_i^{(4;c)}, \qquad \text{and} \qquad W_i^{(4)} = W_i^{(4;a)} + W_i^{(4;b)} + W_i^{(4;c)}. \tag{2.34}$$

The leading 3π-exchange potential appears at N^{3}LO but its contribution is found to be negligible [180, 181] and therefore usually neglected [6, 9, 11].

At next-to-next-to-next-to-next-to-leading order (N^{4}LO, $\nu = 5$), the analytic expressions for the 2π and 3π exchanges are in general very involved [7]. They can be found in Ref. [8], including additional relativistic corrections. The contributions from the subleading 3π exchange (see also Ref. [182]) have been included only in Refs. [8, 11]. In the $^1S_0$ channel, Ref. [10] considers the isospin-breaking LECs $C^{pp}_{^1S_0} \neq C^{np}_{^1S_0}$.

At next-to-next-to-next-to-next-to-next-to-leading order (N^{5}LO, $\nu = 6$), one has further corrections to the 2π- and 3π-exchange potential, while the effect of leading 4π exchanges is expected to be negligible [12]. As reported in Ref. [12], their contribution to the periphal phase shifts is significantly smaller compared to N^{4}LO, which might indicate that the chiral expansion for NN forces tends to converge. In addition, 26 new contact terms contribute (up to F-waves) such that the total number of NN contact LECs at this order reads 50 [12]. Constructing a complete N^{5}LO NN potential is currently work in progress (see Ref. [7]).

Concluding this section, we multiply the NN potential (2.1) by the antisymmetrizer $\mathscr{A}_{12} = 1 - P_{12}$, where P_{12} denotes the transposition operator, and by the regulator functions f_R in order to render loop diagrams convergent,

$$V_{\mathrm{NN}}^{\mathrm{as}} = f_R^{(A=2)}(p;\, \Lambda_{\mathrm{NN}})\, \mathscr{A}_{12}\, V_{\mathrm{NN}}\, f_R^{(A=2)}(p';\, \Lambda_{\mathrm{NN}})\,. \tag{2.35}$$

We discuss different regularization schemes in Sec. 2.1.1 and study how they impact the perturbativeness of the potentials in Sec. 3. For our infinite-matter calculations, however, we employ here the nonlocal regulator with integer exponent n (e.g., similar to Refs. [11, 15, 67, 154]),

$$f_R^{(A=2)}(p;\, \Lambda_{\mathrm{NN}}) = \exp\left[-\left(\frac{p}{\Lambda_{\mathrm{NN}}}\right)^n\right]. \tag{2.36}$$

Regarding the implementation in Sec. 5, we note that Eq. (2.35) is combined with the relativistic scattering T-matrix equation, which reduces to the usual nonrelativistic expression when replacing $V_{\mathrm{NN}}^{\mathrm{as}} \to h(p')\, V_{\mathrm{NN}}^{\mathrm{as}}\, (\mathbf{g}(\mathbf{p}), \mathbf{g}(\mathbf{p}'))\, h(p)$ [6]. In Refs. [6, 15], the minimal-relativity prescription of Ref. [183],

$$h(p) = \sqrt{\frac{m}{\sqrt{p^2 + m^2}}}\,, \qquad \mathbf{g}(\mathbf{p}) = \mathbf{p}\,, \tag{2.37}$$

applies, while Ref. [67] considers the so-called Kamada-Glöckle transform [184],

$$h(p) = \sqrt{\left(1 + \frac{p^2}{2m^2}\right)\sqrt{1 + \frac{p^2}{4m^2}}}\,, \qquad \mathbf{g}(\mathbf{p}) = \mathbf{p}\sqrt{1 + \frac{p^2}{4m^2}}\,. \tag{2.38}$$

2.1.1 Regularization schemes

We briefly summarize properties of recent chiral NN interactions [188] to prepare for diagnosing them using the Weinberg eigenvalue analysis in Sec. 3 and for studying the BCS pairing gaps in Sec. 6. Particularly, we focus on three sets of potentials, commonly referred to as local, nonlocal, and semilocal, which are characterized by different regularization schemes to separate the long-distance from the short-distance physics. To be specific, we consider the local potentials of Refs. [16, 17] by Gezerlis, Tews *et al.* (GT+), the semilocal potentials of Refs. [9, 10] by Epelbaum, Krebs, and Meißner (EKM), the nonlocal potentials of Ref. [15] by Carlsson, Ekström *et al.* (sim), and the nonlocal potentials of Ref. [11] by Entem, Machleidt, and Nosyk (EMN). Table 2 summarizes properties of these potentials including the specific form of the employed regulators as well as the available orders in the chiral expansion, the πN LECs, the 2π regularization, and the fitting protocols. For more detailed information, we refer the reader to the given references.

Local interactions use regulators that only depend on the momentum transfer $\mathbf{q} = \mathbf{p}' - \mathbf{p}$ in momentum space or on the relative distance $\mathbf{r}$ in coordinate space, respectively. The development of the local GT+ interactions in Refs. [16, 17] opened new ways for using nuclear interactions derived within chiral EFT in QMC calculations [103, 104, 146, 152]. The benefits of locally regularizing long-range physics such as the pion-exchange interactions are discussed in Ref. [9]. These include the conservation of the analytical structure of the T-matrix close to the pion threshold and the fact that SFR is not needed in this regularization approach (see also Ref. [17]). Note that DR has been applied in Ref. [9]. On the other hand, for the short-range couplings the local regularization leads to a mixing of different partial-wave channels due to the dependence of $\mathbf{q}$ on $z = \cos\theta_{\mathbf{pp}'}$. As a consequence, S-wave short-range contact interactions generally induce nonvanishing contributions in higher partial waves after regularization [17], whereas for nonlocal regulators, which only depend on the magnitudes of the relative momenta p and

Table 2: Short- and long-range regulators for the local, semilocal, and nonlocal potentials of Refs. [9–11, 15–17] with $\widetilde{r} \equiv r/R_0$ and $\widetilde{p} \equiv p/\Lambda_{\mathrm{NN}}$ in the second and third columns, where $\alpha = (\pi\Gamma(3/4)R_0^3)^{-1}$ is a normalization constant and ν is the order in the chiral expansion defined in Eq. (1.10). For the EMN potentials, the regulator exponent $n_2 = 2$ is applied to the pion exchanges and $n_2 = 4$ for 1π exchange beyond NLO. The highest available chiral order and the cutoff ranges are given in the fifth column, while the determination of the πN LECs, the 2π regularization and the fitting protocol are given in the second-to-last and the last columns, respectively. SFR and DR denote spectral-function and dimensional regularization, whereas PWA stands for partial-wave analysis.

	regulator functions		regulator exponent(s)	chiral order/ cutoff range	πN/ 2π regularization	fitting protocol
	short (contact)	long (pion exchanges)				
local						
GT+ [16, 17]	$\alpha e^{-\widetilde{r}^n}$	$1 - e^{-\widetilde{r}^n}$	$n = 4$	up to N^{2}LO $R_0 = (0.9 - 1.2)$ fm	fixed values from Ref. [67] SFR	Nijmegen PWA [185]
semilocal						
EKM [9, 10]	$e^{-\widetilde{p}^{n_1}} e^{-\widetilde{p}'^{n_1}}$	$\left(1 - e^{-\widetilde{r}^2}\right)^{n_2}$	$n_1 = 2$ $n_2 = 6$	up to N^{4}LO $R_0 = (0.8 - 1.2)$ fm $\Lambda_{\mathrm{NN}} \approx (493 - 329)$ MeV	fixed values [9] DR	Nijmegen PWA [185]
nonlocal						
sim [15]	$e^{-\widetilde{p}^{2n}} e^{-\widetilde{p}'^{2n}}$	$e^{-\widetilde{p}^{2n}} e^{-\widetilde{p}'^{2n}}$	$n = 3$	up to N^{2}LO $\Lambda_{\mathrm{NN}} = (450 - 600)$ MeV	fitting parameter in simultaneous fit SFR	fits to NN, πN, and few-body systems ^{2,3}H,^{3}He
EMN [11]	$e^{-\widetilde{p}^{2n_1}} e^{-\widetilde{p}'^{2n_1}}$	$e^{-\widetilde{p}^{2n_2}} e^{-\widetilde{p}'^{2n_2}}$	$n_1 > \nu/2$ $n_2 = 2\ (4)$	up to N^{4}LO $\Lambda_{\mathrm{NN}} = (450 - 550)$ MeV	fixed values from Ref. [186] SFR	NN data from 1955–2016 [187]

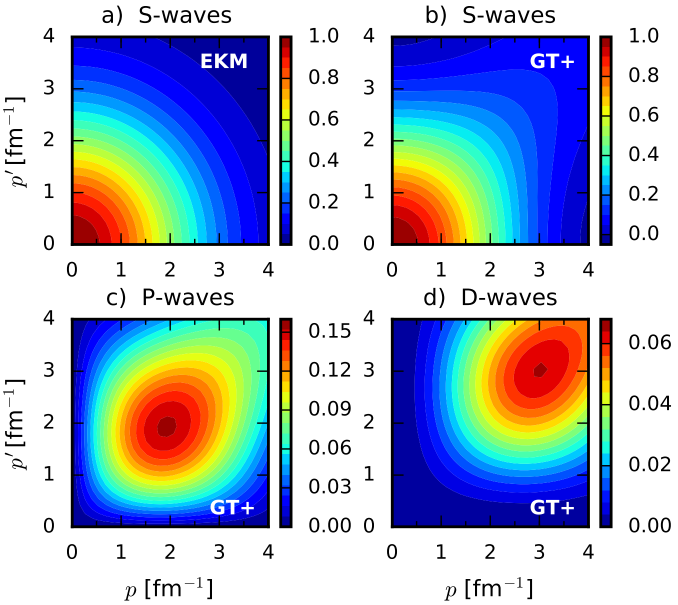

Figure 11: Contour plot in momentum space for the short-range regulator of the EKM and GT+ potentials with $R_0^{\mathrm{EKM}} = 0.8$ fm and $R_0^{\mathrm{GT+}} = 1.2$ fm, respectively. The nonlocal EKM regulator, which is independent of the angular momentum, is plotted for $\Lambda_{\mathrm{NN}} = 493$ MeV (a) assuming Eq. (2.39), while the local GT+ regulator, which depends on the partial wave, is shown in the S-, P-, and D-waves (b, c, d, respectively). We find good agreement in the S-waves for this cutoff combination, where a least-squares minimization reveals that the regulators are most comparable for $R_0^{\mathrm{EKM}} = 0.85$ fm.

p', such short-range interactions remain restricted to only S-waves. This leads in particular to technical simplifications since different partial-wave channels can be fitted independently.

The semilocal EKM interactions [9, 10] combine the conceptual advantages of locally regularized long-range interactions with technical benefits of nonlocal short-range interactions. In practice, the regularization of the long-range parts is formulated in coordinate space and is characterized by a cutoff scale R_0, whereas the short-range regularization is performed in momentum space involving a cutoff scale Λ_{NN}. Physically, it is a natural assumption that these two scales should be related. In Ref. [9], a mapping between the two scales,

$$\Lambda_{\mathrm{NN}}(R_0) = \frac{2}{R_0}\,, \tag{2.39}$$

was motivated by considering Fourier transforms of Gaussians. For the local GT+ potentials, a mapping between momentum and coordinate space was suggested in Ref. [17] which relates the integral over the Fourier-transformed short-range regulator (see Table 2)

$$f_{\mathrm{local}}(q^2, R_0) = \int \mathrm{d}\mathbf{r}\; \alpha\, e^{-(r/R_0)^4} e^{-i\mathbf{q}\cdot\mathbf{r}}\,, \tag{2.40}$$

with the integral over a sharp momentum cutoff:

$$\int \mathrm{d}\mathbf{q}\, f_{\mathrm{local}}(q^2, R_0) = \int \mathrm{d}\mathbf{q}\, \Theta\,(\Lambda_{\mathrm{NN}} - |\mathbf{q}|)\,. \tag{2.41}$$

Table 3: Distance r^* where the long-range regulator function takes the value $f_{\text{long}}(r^*, R_0) = 1/2$ for the GT+ (middle column) and EKM (right column) case, see Table 2. Results are shown for a cutoff range of $R_0 = (0.8 - 1.2)$ fm. We find again best agreement for the cutoff combination $R_0^{\text{GT+}} = 1.2$ fm and $R_0^{\text{EKM}} = 0.8$ fm.

R_0 [fm]	$r^*_{\text{GT+}}$ [fm]	r^*_{EKM} [fm]
0.8	0.73	1.19
0.9	0.82	1.34
1.0	0.91	1.49
1.1	1.00	1.64
1.2	1.10	1.79

Obviously, there is no universal way to relate R_0 and Λ_{NN}. We obtain quite different numerical values from Eqs. (2.39) and (2.41): for $R_0 = 0.8$ fm, we get $\Lambda_{\text{NN}} = 493$ MeV and 614 MeV, whereas for $R_0 = 1.2$ fm, $\Lambda_{\text{NN}} = 329$ MeV and 409 MeV, respectively. In Fig. 11 we show a contour plot of the nonlocal short-range regulator with $R_0^{\text{EKM}} = 0.8$ fm ($\Lambda_{\text{NN}} = 493$ MeV) in the S-wave (a) and $f_{\text{local}}(q^2, R_0^{\text{GT+}})$ with $R_0^{\text{GT+}} = 1.2$ fm ($\Lambda_{\text{NN}} = 409$ MeV) in the S-, P-, and D-wave (b, c, d, respectively). We find good agreement in the S-waves for this chosen cutoff combination, with a least-squares minimization indicating best agreement for a semilocal potential with $R_0^{\text{EKM}} = 0.85$ fm. However, we observe in general a quite different behavior for the nonlocal versus the (angular-dependent) local regulator in momentum-space, where the latter does not cut off contributions with $\mathbf{p} = \mathbf{p}'$. Furthermore, the q^2-dependent contacts at NLO and beyond with $p \neq p'$ are cut off much slower by the local regulator. This shows that the comparison of the numerical values of R_0 alone can be quite misleading due to the different regulator forms for different interactions.

We can confirm this observation also for the long-range part of the regulators. In Table 3 we give the distance r^*, where $f_{\text{long}}(r^*, R_0) = 1/2$ for the cutoff range $R_0 = (0.8-1.2)$ fm. Similarly to the short-range part of the regulators, we find good agreement for $R_0^{\text{GT+}} = 1.2$ fm and $R_0^{\text{EKM}} = 0.8$ fm. As shown in Fig. 12, the regulator functions moreover agree well over the entire range of distances. It is therefore natural to expect that the Weinberg eigenvalue analysis will provide similar results for the long-range part for this cutoff combination of these two interactions, which we will focus on in Sec. 3.

2.1.2 Partial-wave decomposition

Projecting the chiral NN forces (2.2) on the Legendre polynomials $P_L(z)$ leads to the set of partial-wave matrix elements in the coupled basis $|(LS)J\rangle$ [67, 189]:

$$\langle (J0)J|V_{\text{NN}}|(J0)J\rangle = 2\pi \int_{-1}^{1} \mathrm{d}z \left\{ \mathcal{V}_C - 3\mathcal{V}_S + p'^2 p^2 (z^2-1)\mathcal{V}_{\sigma L} - q^2 \mathcal{V}_T - k^2 \mathcal{V}_{T,k} \right\} P_J(z)\,, \tag{2.42a}$$

$$\begin{aligned}\langle (J1)J|V_{\text{NN}}|(J1)J\rangle = 2\pi \int_{-1}^{1} \mathrm{d}z \Bigg\{ \Big[& \mathcal{V}_C + \mathcal{V}_S + 2p'pz\mathcal{V}_{LS} - p'^2p^2(1+3z^2)\mathcal{V}_{\sigma L} + 4k^2\mathcal{V}_T + \frac{1}{4}q^2\mathcal{V}_{T,k} \Big] \\ & \times P_J(z) + \left[2p'^2p^2z\mathcal{V}_{\sigma L} - p'p\left(2\mathcal{V}_{\sigma q} - \frac{1}{2}\mathcal{V}_{T,k} + \mathcal{V}_{LS}\right)\right] \left(P_{J^-}(z) + P_{J^+}(z)\right) \Bigg\}\,,\end{aligned} \tag{2.42b}$$

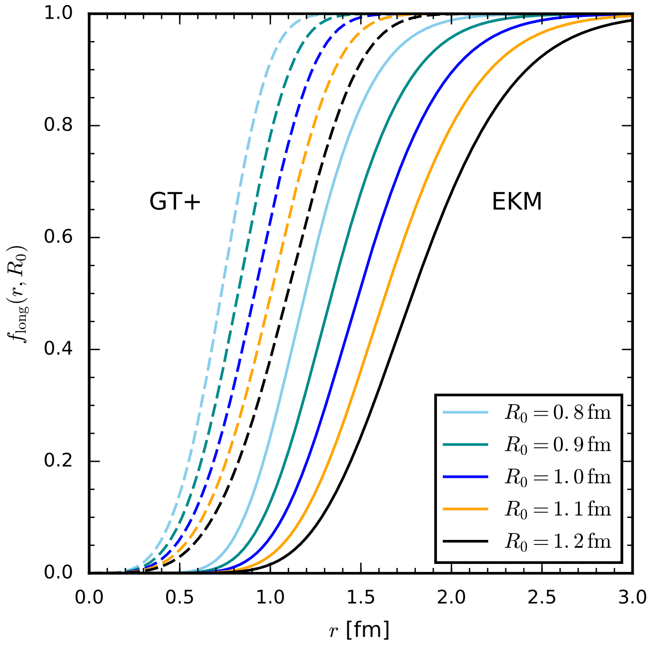

Figure 12: Plot of the long-range regulator functions for the GT+ (dashed lines) and EKM (solid lines) potentials with cutoffs $R_0 = (0.8 - 1.2)$ fm (see Table 2). The regulators corresponding to $R_0^{\mathrm{GT+}} = 1.2$ fm (black-dashed line) and $R_0^{\mathrm{EKM}} = 0.8$ fm (light blue-solid line) lead to best agreement (see also Fig. 11).

$$\begin{aligned}\langle (J^{\pm}1)J|V_{\mathrm{NN}}|(J^{\pm}1)J\rangle = 2\pi \int_{-1}^{1} \mathrm{d}z \, \Bigg\{ p'p \left[-\mathcal{V}_{LS} \pm \frac{2}{2J+1} \left(-p'pz\mathcal{V}_{\sigma L} + \mathcal{V}_T - \frac{1}{4}\mathcal{V}_{T,k} \right) \right] P_J(z) \\ + \Big[\mathcal{V}_C + \mathcal{V}_S + p'pz\mathcal{V}_{LS} + p'^2 p^2 (1-z^2) \mathcal{V}_{\sigma L} \\ \pm \frac{1}{2J+1} \left(2p'^2 p^2 \mathcal{V}_{\sigma L} - (p'^2 + p^2) \left(\mathcal{V}_T + \frac{1}{4}\mathcal{V}_{T,k} \right) \right) \Big] P_{J^{\pm}}(z) \Bigg\} ,\end{aligned} \tag{2.42c}$$

$$\begin{aligned}\langle (J^{\pm}1)J|V_{\mathrm{NN}}|(J^{\mp}1)J\rangle = 2\pi \frac{\sqrt{J(J+1)}}{2J+1} \int_{-1}^{1} \mathrm{d}z \, \Bigg\{ -p'p \, (4\mathcal{V}_T - \mathcal{V}_{T,k}) \, P_J(z) \\ + \left[\mp \frac{2p'^2 p^2}{2J+1} \mathcal{V}_{\sigma L} + p'^2 \left(2\mathcal{V}_T + \frac{1}{2}\mathcal{V}_{T,k} \right) \right] P_{J^{\mp}}(z) \\ + \left[\pm \frac{2p'^2 p^2}{2J+1} \mathcal{V}_{\sigma L} + p^2 \left(2\mathcal{V}_T + \frac{1}{2}\mathcal{V}_{T,k} \right) \right] P_{J^{\pm}}(z) \Bigg\} ,\end{aligned} \tag{2.42d}$$

with $J^{\pm} := J \pm 1$ and the (regularized) scalar functions $\mathcal{V}_i = \mathcal{V}_i(p, p', z)$. The latter include the isospin part of the basis, i.e., $\langle T' m_{T'} | \boldsymbol{\tau}_1 \cdot \boldsymbol{\tau}_2 | T m_T \rangle = \delta_{T,T'} \, \delta_{m_T, m_{T'}} \, (2T(T+1) - 3)$. Notice that the nonlocal regulators in Table 2 have no angular dependence and thus factorize globally. As emphasized in Ref. [67] additional factors may be necessary depending on the definition of the decomposition. When using $|\mathbf{p}\rangle = (4\pi) \sum_{L,M} i^L \, Y_L^{*M}(\theta, \varphi) \, |pLM\rangle$, the overall factor reads $(4\pi)^{-2} i^{L'-L}$ which changes the sign of coupled channels with different $L = J \pm 1$ and $L' = J \mp 1$.

To be able to incorporate also the sim potentials in our (partial-wave) calculations, we evaluate Eqs. (2.42) using the implementation of the scalar functions in Sec. 5.1. The corresponding LECs are tabulated in the supplementary material of Ref. [15]. For the other (bare) potentials, however, we use the external sources codes provided by the respective authors.

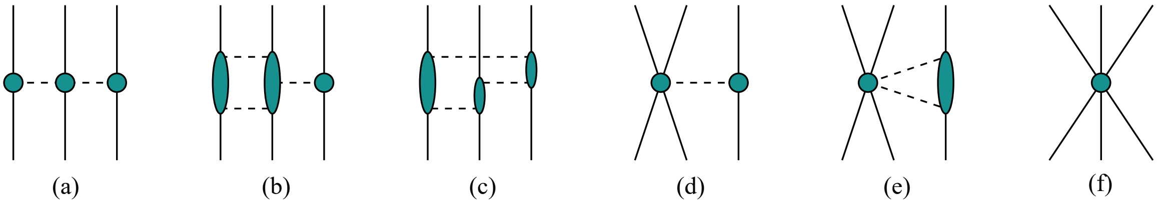

Figure 13: Topologies of the 3N forces at N^{3}LO (or equally N^{4}LO): 2π-exchange (a), 2π-1π (b), pion-ring (c), 1π-contact (d), 2π-contact (e), and pure 3N contact (f). Solid (dashed) lines denote nucleons (pions), whereas the ellipses are the corresponding amplitudes. Relativistic $1/m$ corrections are not shown. The figure has been taken from Refs. [95, 96].

2.2 Three-nucleon interactions

Three-nucleon forces sum up to a vanishing contribution at NLO ($\nu = 2$) [87, 190], so the total contribution up to N^{3}LO ($\nu = 4$) is given by [190–193]

$$V_{3\text{N}} = V_{3\text{N}}^{(\nu=3)} + V_{3\text{N}}^{(\nu=4)} \quad \text{with,} \tag{2.43a}$$
$$V_{3\text{N}}^{(\nu=3)} = V_c^{(2\pi)} + V_D^{(1\pi\text{-cont})} + V_E^{(\text{cont})}, \tag{2.43b}$$
$$V_{3\text{N}}^{(\nu=4)} = V^{(2\pi)} + V^{(1\pi\text{-cont})} + V^{(2\pi\text{-}1\pi)} + V^{(\text{ring})} + V^{(2\pi\text{-cont})} + V^{(1/m)}. \tag{2.43c}$$

The superscripts on the right-hand side correspond to the six 3N topologies depicted by (a)–(f) in Fig. 13 plus relativistic $1/m$ corrections (not shown). We neglect here isospin-breaking corrections [194]. Due antisymmetrization and Fierz ambiguities the leading 3N forces (2.43b) in (a), (d), and (f) can be expressed as [191]

$$V_c^{(2\pi)} = \frac{g_A^2}{8f_\pi^2} \sum_{i\neq j\neq k} \frac{(\boldsymbol{\sigma}_i \cdot \mathbf{q}_i)(\boldsymbol{\sigma}_k \cdot \mathbf{q}_k)}{(q_i^2 + m_\pi^2)(q_k^2 + m_\pi^2)} F_{ijk}\,, \tag{2.44a}$$
$$V_D^{(1\pi\text{-cont})} = -\frac{c_D}{f_\pi^2 \Lambda_\chi} \frac{g_A}{8f_\pi^2} \sum_{i\neq j\neq k} \frac{\boldsymbol{\sigma}_j \cdot \mathbf{q}_j}{q_j^2 + m_\pi^2} (\boldsymbol{\tau}_i \cdot \boldsymbol{\tau}_j)(\boldsymbol{\sigma}_i \cdot \mathbf{q}_j)\,, \tag{2.44b}$$
$$V_E^{(\text{cont})} = \frac{c_E}{f_\pi^4 \Lambda_\chi} \frac{1}{2} \sum_{i\neq j\neq k} \boldsymbol{\tau}_i \cdot \boldsymbol{\tau}_j\,, \tag{2.44c}$$

with the difference of final and initial single-particle momenta $\mathbf{q}_i = \mathbf{p}_i' - \mathbf{p}_i$, the axial coupling constant $g_A = 1.29$ (we use the larger value), the pion mass $m_\pi = 138.04$ MeV, the pion decay constant $f_\pi = 92.4$ MeV, the chiral symmetry breaking scale $\Lambda_\chi = 700$ MeV of the order of m_ρ and with the short-hand notation

$$F_{ijk} := \left[-\frac{4c_1 m_\pi^2}{f_\pi^2} + \frac{2c_3}{f_\pi^2} \mathbf{q}_i \cdot \mathbf{q}_k \right] \boldsymbol{\tau}_i \cdot \boldsymbol{\tau}_k + \frac{c_4}{f_\pi^2} (\boldsymbol{\tau}_i \times \boldsymbol{\tau}_k) \cdot \boldsymbol{\tau}_j \, (\mathbf{q}_i \times \mathbf{q}_k) \cdot \boldsymbol{\sigma}_j\,. \tag{2.45}$$

Notice that the sums in Eqs. (2.44) consider the six permutations of three particle labels. The long-range 2π exchange (2.44a) is already predicted through the NN forces at this order since c_1, c_3, and c_4 also contribute to the subleading 2π exchange in Eqs. (2.15) and (2.16). However, the dimensionless 3N LECs c_D and c_E in Eq. (2.44b) and (2.44c), respectively, which govern the shorter-range physics need to be fit to experimental data, e.g., the binding energies of ^{3}H and ^{4}He or likewise the ^{4}He radius [27, 195]. For discussions related to the impact of Δ-resonances we refer the reader to Refs. [95, 96, 196, 197].

In pure neutron matter, only c_1 and c_3 are in fact relevant for the antisymmetrized 3N forces (2.44) as the following arguments will show [43]. While $V_E^{(\text{cont})}$ is forbidden by the Pauli principle since it is not possible to construct an antisymmetric wave function for three identical nucleons, $V_D^{(1\pi\text{-cont})}$ vanishes due to its simple isospin structure. One has $\boldsymbol{\tau}_i \cdot \boldsymbol{\tau}_j \equiv 1$ and, therefore,

$$V_D^{(1\pi\text{-cont})} \sim \sum_{i\neq j\neq k} \frac{\boldsymbol{\sigma}_j \cdot \mathbf{q}_j}{q_j^2 + m_\pi^2} (\boldsymbol{\sigma}_i \cdot \mathbf{q}_j)\,. \tag{2.46}$$

Fixing $j(\neq i \neq j)$ results in terms like $(\boldsymbol{\sigma}_j \cdot \boldsymbol{q}_j)(\boldsymbol{\sigma}_i + \boldsymbol{\sigma}_k) \cdot \mathbf{q}_j$ which contribute only if the spins of particles i, k couple to $S = 1$ (symmetric spin wave function). These terms are independent of the momenta of i, k, so the momentum part will also be symmetric under particle exchange and, thus, the isospins of i, k would have to couple to $T = 0$ to support an overall antisymmetric wave function. That is in contradiction to pure neutron matter having $T = 1$. Moreover, the term proportional to c_4 in Eq. (2.44a) vanishes due to the isospin triple-product structure. Since the isospin states are orthonormal in $\langle nnn|\epsilon^{\alpha\beta\gamma}\tau_1^\alpha\tau_2^\beta\tau_3^\gamma|nnn\rangle$, the Pauli matrices require $\alpha = \beta = \gamma = z$ for a nonzero matrix element. In that case, however, the Levi-Civita symbol vanishes.

The subleading 3N forces at N^{3}LO have been derived in Refs. [192, 193, 198]. They are free of new LECs and provide more involved operator structures compared to N^{2}LO (see also the discussion in Refs. [95, 96]). Figure 13 depicts the five relevant topologies in (a)–(e) plus the relativistic $1/m$ corrections (not shown) to (a) and (d).

The 2π-exchange potential at N^{3}LO can be split into $V^{(2\pi)} := V_{\delta c}^{(2\pi)} + V_{\text{res}}^{(2\pi)}$. $V_{\delta c}^{(2\pi)}$ just renormalizes the LECs $c_i \longrightarrow c_i + \delta c_i$ in Eq. (2.44a) as follows

$$\delta c_1 = -\frac{g_A^2 m_\pi}{64\pi f_\pi^2} = -0.134\ \text{GeV}^{-1}\,, \qquad \delta c_3 = +\frac{g_A^4 m_\pi}{16\pi f_\pi^2} = +0.891\ \text{GeV}^{-1}\,, \qquad \delta c_4 = -\delta c_3\,. \tag{2.47}$$

Notice that these corrections are given by physical constants [192]. The residual contribution reads

$$\begin{aligned} V_{\text{res}}^{(2\pi)} = \frac{g_A^4}{256\pi f_\pi^6} \sum_{i\neq j\neq k} \frac{\boldsymbol{\sigma}_i \cdot \mathbf{q}_i\, \boldsymbol{\sigma}_k \cdot \mathbf{q}_k}{\left(q_i^2 + m_\pi^2\right)\left(q_k^2 + m_\pi^2\right)} \Big[& \boldsymbol{\tau}_i \cdot \boldsymbol{\tau}_k \left(m_\pi \left(m_\pi^2 + 3q_i^2 + 3q_k^2 + 4\mathbf{q}_i \cdot \mathbf{q}_k \right) \right. \\ & \left. + \left(2m_\pi^2 + q_i^2 + q_k^2 + 2\mathbf{q}_i \cdot \mathbf{q}_k\right)\left(3m_\pi^2 + 3q_i^2 + 3q_k^2 + 4\mathbf{q}_i \cdot \mathbf{q}_k\right) A(q_j) \right) \\ & - \boldsymbol{\tau}_i \times \boldsymbol{\tau}_k \cdot \boldsymbol{\tau}_j\, \mathbf{q}_i \times \mathbf{q}_k \cdot \boldsymbol{\sigma}_j\, \left(m_\pi + \left(4m_\pi^2 + q_i^2 + q_k^2 + 2\mathbf{q}_i \cdot \mathbf{q}_k\right) A(q_j) \right) \Big]\,, \end{aligned} \tag{2.48}$$

where the loop function in dimensional regularization $A(q)$ is already defined in Eq. (2.7).

There are no additional net contributions from the 1π-exchange-contact interaction at N^{3}LO [193], i.e., $V^{(1\pi\text{-cont})} = 0$.

In terms of the eight scalar functions $F_{1\ldots 8}(q)$

$$F_1(q) = -\frac{g_A^6}{256\pi f_\pi^6}\left[\frac{m_\pi}{4m_\pi^2+q^2} + \frac{2m_\pi}{q^2} - \frac{8m_\pi^2+q^2}{q^2}A(q)\right] + \frac{g_A^4}{256\pi f_\pi^6}\left[\frac{m_\pi}{q^2} + \frac{q^2-4m_\pi^2}{q^2}A(q)\right], \tag{2.49}$$

$$F_2(q) = \frac{1}{2}F_6(q) = F_7(q) = -4F_8(q) = \frac{g_A^4}{128\pi f_\pi^6}\left[m_\pi + (q^2+2m_\pi^2)A(q)\right], \tag{2.50}$$

$$F_3(q) = -\frac{g_A^6}{256\pi f_\pi^6}\left[3m_\pi + (8m_\pi^2+3q^2)A(q)\right] + \frac{g_A^4}{256\pi f_\pi^6}\left[m_\pi + (q^2+4m_\pi^2)A(q)\right], \tag{2.51}$$

$$F_4(q) = -\frac{1}{q^2}F_5(q) = -\frac{g_A^6}{128\pi f_\pi^6}A(q), \tag{2.52}$$

the 2π-1π-exchange contribution is

$$\begin{aligned}
V^{(2\pi\text{-}1\pi)} = \sum_{i\neq j\neq k} \frac{\boldsymbol{\sigma}_k\cdot\mathbf{q}_k}{q_k^2+m_\pi^2}\Big[& \boldsymbol{\tau}_i\cdot\boldsymbol{\tau}_k\left(\boldsymbol{\sigma}_j\cdot\mathbf{q}_i\,\mathbf{q}_i\cdot\mathbf{q}_k\,F_1(q_i) + \boldsymbol{\sigma}_j\cdot\mathbf{q}_i\,F_2(q_i) + \boldsymbol{\sigma}_j\cdot\mathbf{q}_k\,F_3(q_i)\right) \\
& + \boldsymbol{\tau}_j\cdot\boldsymbol{\tau}_k\left(\boldsymbol{\sigma}_i\cdot\mathbf{q}_i\,\mathbf{q}_i\cdot\mathbf{q}_k\,F_4(q_i) + \boldsymbol{\sigma}_i\cdot\mathbf{q}_k\,F_5(q_i) + \boldsymbol{\sigma}_j\cdot\mathbf{q}_i\,F_6(q_i) + \boldsymbol{\sigma}_j\cdot\mathbf{q}_k\,F_7(q_i)\right) \\
& + \boldsymbol{\tau}_i\times\boldsymbol{\tau}_j\cdot\boldsymbol{\tau}_k\,\boldsymbol{\sigma}_i\times\boldsymbol{\sigma}_j\cdot\mathbf{q}_i\,F_8(q_i)\Big].
\end{aligned} \tag{2.53}$$

The pion-ring contribution

$$\begin{aligned}
V^{(\text{ring})} = \sum_{i\neq j\neq k} & \boldsymbol{\sigma}_i\cdot\boldsymbol{\sigma}_j\,\boldsymbol{\tau}_j\cdot\boldsymbol{\tau}_k\,R_1 + \boldsymbol{\sigma}_i\cdot\mathbf{q}_i\boldsymbol{\sigma}_j\cdot\mathbf{q}_i\,\boldsymbol{\tau}_j\cdot\boldsymbol{\tau}_k\,R_2 + \boldsymbol{\sigma}_i\cdot\mathbf{q}_i\boldsymbol{\sigma}_j\cdot\mathbf{q}_k\,\boldsymbol{\tau}_j\cdot\boldsymbol{\tau}_k\,R_3 \\
& + \boldsymbol{\sigma}_i\cdot\mathbf{q}_k\boldsymbol{\sigma}_j\cdot\mathbf{q}_i\,\boldsymbol{\tau}_j\cdot\boldsymbol{\tau}_k\,R_4 + \boldsymbol{\sigma}_i\cdot\mathbf{q}_k\boldsymbol{\sigma}_j\cdot\mathbf{q}_k\,\boldsymbol{\tau}_j\cdot\boldsymbol{\tau}_k\,R_5 + \boldsymbol{\tau}_i\cdot\boldsymbol{\tau}_k\,R_6 \\
& + \boldsymbol{\sigma}_i\cdot\mathbf{q}_i\boldsymbol{\sigma}_k\cdot\mathbf{q}_i\,R_7 + \boldsymbol{\sigma}_i\cdot\mathbf{q}_i\boldsymbol{\sigma}_k\cdot\mathbf{q}_k\,R_8 + \boldsymbol{\sigma}_i\cdot\mathbf{q}_k\boldsymbol{\sigma}_k\cdot\mathbf{q}_i\,R_9 \\
& + \boldsymbol{\sigma}_i\cdot\boldsymbol{\sigma}_k\,R_{10} + \mathbf{q}_i\cdot\mathbf{q}_k\times\boldsymbol{\sigma}_j\,\boldsymbol{\tau}_i\cdot\boldsymbol{\tau}_j\times\boldsymbol{\tau}_k\,R_{11} \\
& + \boldsymbol{\tau}_i\cdot\boldsymbol{\tau}_j\,S_1 + \boldsymbol{\sigma}_i\cdot\mathbf{q}_i\boldsymbol{\sigma}_k\cdot\mathbf{q}_i\,\boldsymbol{\tau}_i\cdot\boldsymbol{\tau}_j\,S_2 \\
& + \boldsymbol{\sigma}_i\cdot\mathbf{q}_k\boldsymbol{\sigma}_k\cdot\mathbf{q}_i\,\boldsymbol{\tau}_i\cdot\boldsymbol{\tau}_j\,S_3 + \boldsymbol{\sigma}_i\cdot\mathbf{q}_i\boldsymbol{\sigma}_k\cdot\mathbf{q}_k\,\boldsymbol{\tau}_i\cdot\boldsymbol{\tau}_j\,S_4 \\
& + \boldsymbol{\sigma}_i\cdot\mathbf{q}_k\boldsymbol{\sigma}_k\cdot\mathbf{q}_k\,\boldsymbol{\tau}_i\cdot\boldsymbol{\tau}_j\,S_5 + \boldsymbol{\sigma}_i\cdot\boldsymbol{\sigma}_k\,\boldsymbol{\tau}_i\cdot\boldsymbol{\tau}_j\,S_6 \\
& + \mathbf{q}_i\cdot\mathbf{q}_k\times\boldsymbol{\sigma}_i\,\boldsymbol{\tau}_i\cdot\boldsymbol{\tau}_j\times\boldsymbol{\tau}_k\,S_7,
\end{aligned} \tag{2.54}$$

consists of the so-called ring functions $R_{1\ldots 11} := R_{1\ldots 11}(q_i, q_k, z)$ and $S_{1\ldots 7} := S_{1\ldots 7}(q_i, q_k, z)$ with $z = \cos\theta_{\mathbf{q}_i,\mathbf{q}_k}$. The 18 rather lengthy expressions are defined in the appendix of Ref. [192]. For our implementation in C++ (see Sec. 5.1), we use a *Wolfram* Mathematica notebook provided by Herman Krebs that also corrects several misprints: $R_{6,8,9,10,11}$ missed a factor of 1/2 in Ref. [192] (see also Refs. [108, 140]).

The 2π-contact interaction is proportional to the spin-dependent LO LEC C_T and reads,

$$\begin{aligned}
V^{(2\pi\text{-cont})} = \frac{g_A^4 C_T}{48\pi f_\pi^4}\sum_{i\neq j\neq k}\Big\{ & 2\boldsymbol{\tau}_i\cdot\boldsymbol{\tau}_j\,(\boldsymbol{\sigma}_j\cdot\boldsymbol{\sigma}_k)\Big[3m_\pi - \frac{m_\pi^3}{4m_\pi^2+q_i^2} + 2(2m_\pi^2+q_i^2)A(q_i)\Big] \\
& + 9\Big[(\mathbf{q}_i\cdot\boldsymbol{\sigma}_i)(\mathbf{q}_i\cdot\boldsymbol{\sigma}_j) - q_i^2(\boldsymbol{\sigma}_i\cdot\boldsymbol{\sigma}_j)\Big]A(q_i)\Big\} \\
& - \frac{g_A^2 C_T}{24\pi f_\pi^4}\sum_{i\neq j\neq k}\boldsymbol{\tau}_i\cdot\boldsymbol{\tau}_j\,(\boldsymbol{\sigma}_j\cdot\boldsymbol{\sigma}_k)\Big[m_\pi + (2m_\pi^2+q_i^2)A(q_i)\Big].
\end{aligned} \tag{2.55}$$

Finally, the total relativistic correction has contributions from the 2π-exchange as well as from the 1π-contact topology, $V^{(1/m)} := V^{(2\pi,\,1/m)} + V^{(1\pi\text{-cont},\,1/m)}$. The first term reads

$$V^{(2\pi,\,1/m)} = \frac{g_A^2}{32 m f_\pi^4} \sum_{i \neq j \neq k} \frac{1}{(q_i^2 + m_\pi^2)(q_k^2 + m_\pi^2)} \Big(\boldsymbol{\tau}_i \cdot \boldsymbol{\tau}_k A_{ijk} + [\boldsymbol{\tau}_i \times \boldsymbol{\tau}_j] \cdot \boldsymbol{\tau}_k B_{ijk} \Big) , \tag{2.56}$$

with the nucleon mass m, the short-hand notation

$$A_{ijk} = (\boldsymbol{\sigma}_i \cdot \mathbf{q}_i)(\boldsymbol{\sigma}_k \cdot \mathbf{q}_k)\, a_{ijk} + (\boldsymbol{\sigma}_i \cdot \mathbf{q}_i)(\boldsymbol{\sigma}_k \cdot \mathbf{k}_k)\, c_{ijk} \,, \tag{2.57}$$

$$B_{ijk} = (\boldsymbol{\sigma}_i \cdot \mathbf{q}_i)(\boldsymbol{\sigma}_k \cdot \mathbf{q}_k)\, b_{ijk} + (\boldsymbol{\sigma}_i \cdot \mathbf{q}_i)(\boldsymbol{\sigma}_k \cdot \mathbf{k}_k)\, d_{ijk} \,, \tag{2.58}$$

and with the definitions

$$\begin{aligned} a_{ijk} = {} & -\frac{g_A^2}{q_i^2 + m_\pi^2} \Big[(1 - 2\bar{\beta}_8)(\mathbf{q}_i \cdot \mathbf{q}_k)^2 - 2i [\mathbf{q}_i \times \mathbf{q}_k] \cdot \boldsymbol{\sigma}_j \\ & \times \big((1 - 2\bar{\beta}_8)(\mathbf{q}_i \cdot \mathbf{k}_j) + (1 + 2\bar{\beta}_8)(\mathbf{q}_i \cdot \mathbf{k}_i) \big) \Big] - g_A^2 (2\bar{\beta}_9 - 1) \big(q_i^2 + 2i [\mathbf{q}_i \times \mathbf{k}_j] \cdot \boldsymbol{\sigma}_j \big) \,, \end{aligned} \tag{2.59}$$

$$c_{ijk} = 2i g_A^2 (2\bar{\beta}_9 + 1) [\mathbf{q}_i \times \mathbf{q}_k] \cdot \boldsymbol{\sigma}_j \,, \tag{2.60}$$

$$\begin{aligned} b_{ijk} = {} & -\frac{g_A^2}{q_i^2 + m_\pi^2} \Big[(1 - 2\bar{\beta}_8)\, [\mathbf{q}_i \times \mathbf{q}_k] \cdot \boldsymbol{\sigma}_j\, (\mathbf{q}_i \cdot \mathbf{q}_k) \\ & + 2i (\mathbf{q}_i \cdot \mathbf{q}_k) \big((1 - 2\bar{\beta}_8)(\mathbf{q}_i \cdot \mathbf{k}_j) + (1 + 2\bar{\beta}_8)(\mathbf{q}_i \cdot \mathbf{k}_i) \big) \Big] \\ & + 2i \mathbf{q}_k \cdot (\mathbf{k}_k - \mathbf{k}_j) + 2i g_A^2 (2\bar{\beta}_9 - 1)(\mathbf{q}_i \cdot \mathbf{k}_j) - [\mathbf{q}_i \times \mathbf{q}_k] \cdot \boldsymbol{\sigma}_j \,, \end{aligned} \tag{2.61}$$

$$d_{ijk} = -2i g_A^2 (2\bar{\beta}_9 + 1)(\mathbf{q}_i \cdot \mathbf{q}_k) \,. \tag{2.62}$$

The second contribution is written as

$$V^{(1\pi\text{-cont},\,1/m)} = \frac{g_A^2}{8 m f_\pi^2} \sum_{i \neq j \neq k} \frac{1}{q_i^2 + m_\pi^2} \boldsymbol{\tau}_i \cdot \boldsymbol{\tau}_j \Big((\boldsymbol{\sigma}_i \cdot \mathbf{q}_i)\, f_{ijk} + (\boldsymbol{\sigma}_i \cdot \mathbf{k}_i)\, g_{ijk} \Big) , \tag{2.63}$$

with the following definitions

$$\begin{aligned} f_{ijk} = {} & \frac{1}{q_i^2 + m_\pi^2} \Big[(1 - 2\bar{\beta}_8)(\mathbf{q}_i \cdot \mathbf{q}_k) \Big(C_S (\mathbf{q}_i \cdot \boldsymbol{\sigma}_j) + C_T (\mathbf{q}_i \cdot \boldsymbol{\sigma}_k) \Big) \\ & + 2i C_T \mathbf{q}_i \cdot [\boldsymbol{\sigma}_j \times \boldsymbol{\sigma}_k] \Big((1 - 2\bar{\beta}_8)(\mathbf{q}_i \cdot \mathbf{k}_j) + (1 + 2\bar{\beta}_8)(\mathbf{q}_i \cdot \mathbf{k}_i) \Big) \Big] \\ & + (2\bar{\beta}_9 - 1) \Big[C_S (\mathbf{q}_k \cdot \boldsymbol{\sigma}_j) + C_T (\mathbf{q}_k \cdot \boldsymbol{\sigma}_k) \Big] + 2i C_T (2\bar{\beta}_9 - 1) \mathbf{k}_j \cdot [\boldsymbol{\sigma}_j \times \boldsymbol{\sigma}_k] \,, \end{aligned} \tag{2.64}$$

$$g_{ijk} = -2i C_T (2\bar{\beta}_9 + 1) \mathbf{q}_i \cdot \Big[\boldsymbol{\sigma}_j \times \boldsymbol{\sigma}_k \Big] \,. \tag{2.65}$$

Notice that the relativistic corrections are nonlocal due to the dependence on the momentum transfer in the exchange channel $\mathbf{k}_i = (\mathbf{p}_i + \mathbf{p}_i')/2$. We refer to Table 4 for C_S, C_T of several N^{3}LO NN potentials. The two additional parameters are $\bar{\beta}_8 = -\bar{\beta}_9 = 1/4$ [9].

For completeness, we note that the long- and intermediate-range topologies (a)–(c) at N^{4}LO also have been derived including a general operator basis of local isospin-invariant 3N forces [95, 96, 199] (see moreover Ref. [200]). The short-range contributions are currently work in progress.

Table 4: Spin-independent and spin-dependent NN contact couplings C_S and C_T, respectively, for several N^{3}LO NN potentials.

N^{3}LO NN potential	C_S [fm^2]	$C_T^{(np)}$ [fm^2]
EGM 450/500 MeV [67]	-4.188	-0.453
EGM 450/700 MeV [67]	-4.715	-0.241
EM 500 MeV [6, 154]	-3.905	$+0.218$
EMN 450 MeV [11]	-4.606	-0.004
EMN 500 MeV [11]	-4.791	-0.155
EMN 550 MeV [11]	-4.565	-0.062

Supplementing the formal definition (2.43) chiral forces are antisymmetrized and regularized, i.e.,

$$V_{3N}^{\text{as}} := f_R^{(3)}(\mathbf{p}_1', \mathbf{p}_2', \mathbf{p}_3'; \Lambda_{3N})\,\mathscr{A}_{123} V_{3N} f_R^{(3)}(\mathbf{p}_1, \mathbf{p}_2, \mathbf{p}_3; \Lambda_{3N})\,. \tag{2.66}$$

We apply the 3N antisymmetrizer [191]

$$\mathscr{A}_{123} = 1 - P_{12} - P_{13} - P_{23} + P_{123} + P_{132}\,, \tag{2.67a}$$

$$= (1 + P_{123} + P_{132})(1 - P_{12})\,, \tag{2.67b}$$

where P_{ijk} denotes the operator of the cyclic permutation $(i\ j\ k)$, or symbolically, $(i \to j \to k \to i)$. In practice, it is suitable to convert these into strings of transposition operators, $P_{ijk} = P_{ij}P_{ik} = P_{jk}P_{ij}$, using the identities [201]

$$(1\ 2\ 3\ \dots\ n) \equiv (1\ n)(1\ n-1)\dots(1\ 3)(1\ 2)\,, \tag{2.68}$$

$$\equiv (1\ 2)(2\ 3)\dots(n-1\ n)\,. \tag{2.69}$$

We have factorized the NN antisymmetrizer $\mathscr{A}_{12} = 1 - P_{12}$ (similarly, $\mathscr{A}_{13}$ or $\mathscr{A}_{23}$) in Eq. (2.67b) with regard to normal-ordering in Sec. 4.1. For the 3N regulator, we employ the established nonlocal function of the single-particle momenta [191],

$$f_R^{(A\geqslant 3)}(\mathbf{p}_1, \mathbf{p}_2, \dots, \mathbf{p}_A; \Lambda_{AN}) = \exp\left[-\left(\frac{\sum_{i\leqslant j=1}^{A}(-1+2\delta_{ij})\,\mathbf{p}_i\cdot\mathbf{p}_j}{A\Lambda_{AN}^2}\right)^{n_{\exp}}\right]\,, \tag{2.70}$$

with $A = 3$, cutoff Λ_{AN}, and integer exponent $n_{\exp}$. This particular choice is invariant under interchanging particle labels and thus commutes with the antisymmetrizer. Local regulators have been investigated, e.g., in Refs. [17, 18, 104, 146, 202–204].

Recently, Ref. [205] developed a computationally efficient framework for decomposing 3N interactions in a momentum-space partial-wave basis (see also Refs. [206, 207]) which was applied to calculate the 3N matrix elements at N^{2}LO as well as (for the first time) at N^{3}LO. This denotes a key step toward more consistent studies at N^{3}LO. We make use of this in Sec. 4 and 6.

2.3 Four-nucleon interactions

The first nonvanishing 4N forces appear at N^{3}LO ($\nu = 4$) and have been derived in Refs. [208, 209] using the method of unitary transformation (see also Refs. [200, 210–212]). They are local and free of unknown parameters. More specifically, they depend on the spin-dependent LO NN LEC C_T, the pion mass m_π, the axial coupling $g_A = 1.29$ (we use again the larger value), and the pion decay constant f_π. According to Refs. [208, 209] the net contribution reads

$$V_{4\mathrm{N}} = V_{4\mathrm{N}}^{(\nu=4)} = V^a + V^c + V^e + V^f + V^k + V^l + V^n\,, \tag{2.71}$$

with the analytic expressions for the 3π exchanges

$$\begin{aligned}
V^a = &-\frac{2g_A^6}{(2f_\pi)^6} \sum_{i\neq j\neq k\neq l} \frac{\boldsymbol{\sigma}_i\cdot\mathbf{q}_i\,\boldsymbol{\sigma}_l\cdot\mathbf{q}_l}{[\mathbf{q}_i^2+m_\pi^2][\mathbf{q}_{ij}^2+m_\pi^2]^2[\mathbf{q}_l^2+m_\pi^2]} \\
&\times\Big[(\boldsymbol{\tau}_i\cdot\boldsymbol{\tau}_l\,\boldsymbol{\tau}_j\cdot\boldsymbol{\tau}_k - \boldsymbol{\tau}_i\cdot\boldsymbol{\tau}_k\,\boldsymbol{\tau}_j\cdot\boldsymbol{\tau}_l)\,\mathbf{q}_i\cdot\mathbf{q}_{ij}\,\mathbf{q}_l\cdot\mathbf{q}_{ij} + \boldsymbol{\tau}_i\times\boldsymbol{\tau}_j\cdot\boldsymbol{\tau}_l\,\mathbf{q}_i\cdot\mathbf{q}_{ij}\,\mathbf{q}_{ij}\times\mathbf{q}_l\cdot\boldsymbol{\sigma}_k \\
&\quad+\boldsymbol{\tau}_i\times\boldsymbol{\tau}_k\cdot\boldsymbol{\tau}_l\,\mathbf{q}_l\cdot\mathbf{q}_{ij}\,\mathbf{q}_i\times\mathbf{q}_{ij}\cdot\boldsymbol{\sigma}_j + \boldsymbol{\tau}_i\cdot\boldsymbol{\tau}_l\,\mathbf{q}_{ij}\times\mathbf{q}_i\cdot\boldsymbol{\sigma}_j\,\mathbf{q}_{ij}\times\mathbf{q}_l\cdot\boldsymbol{\sigma}_k\Big]\,,
\end{aligned} \tag{2.72a}$$

$$\begin{aligned}
V^c = &\frac{2g_A^4}{(2f_\pi)^6} \sum_{i\neq j\neq k\neq l} \frac{\boldsymbol{\sigma}_i\cdot\mathbf{q}_i\,\boldsymbol{\sigma}_l\cdot\mathbf{q}_l}{[\mathbf{q}_i^2+m_\pi^2][\mathbf{q}_{ij}^2+m_\pi^2][\mathbf{q}_l^2+m_\pi^2]} \\
&\times\Big[(\boldsymbol{\tau}_i\cdot\boldsymbol{\tau}_l\,\boldsymbol{\tau}_j\cdot\boldsymbol{\tau}_k - \boldsymbol{\tau}_i\cdot\boldsymbol{\tau}_k\,\boldsymbol{\tau}_j\cdot\boldsymbol{\tau}_l)\,\mathbf{q}_{ij}\cdot\mathbf{q}_l + \boldsymbol{\tau}_i\times\boldsymbol{\tau}_j\cdot\boldsymbol{\tau}_l\,\mathbf{q}_{ij}\times\mathbf{q}_l\cdot\boldsymbol{\sigma}_k\Big]\,,
\end{aligned} \tag{2.72b}$$

$$V^e = \frac{g_A^4}{(2f_\pi)^6} \sum_{i\neq j\neq k\neq l} \frac{\boldsymbol{\sigma}_j\cdot\mathbf{q}_j\,\boldsymbol{\sigma}_k\cdot\mathbf{q}_k\,\boldsymbol{\sigma}_l\cdot\mathbf{q}_l}{[\mathbf{q}_j^2+m_\pi^2][\mathbf{q}_k^2+m_\pi^2][\mathbf{q}_l^2+m_\pi^2]}\boldsymbol{\tau}_i\cdot\boldsymbol{\tau}_j\,\boldsymbol{\tau}_k\cdot\boldsymbol{\tau}_l\,\boldsymbol{\sigma}_i\cdot(\mathbf{q}_k+\mathbf{q}_l)\,, \tag{2.72c}$$

the pion-pion interaction

$$V^f = \frac{g_A^4}{2(2f_\pi)^6} \sum_{i\neq j\neq k\neq l} \Big[\big(\mathbf{q}_i+\mathbf{q}_j\big)^2+m_\pi^2\Big] \frac{\boldsymbol{\sigma}_i\cdot\mathbf{q}_i\,\boldsymbol{\sigma}_j\cdot\mathbf{q}_j\,\boldsymbol{\sigma}_k\cdot\mathbf{q}_k\,\boldsymbol{\sigma}_l\cdot\mathbf{q}_l}{[\mathbf{q}_i^2+m_\pi^2][\mathbf{q}_j^2+m_\pi^2][\mathbf{q}_k^2+m_\pi^2][\mathbf{q}_l^2+m_\pi^2]}\boldsymbol{\tau}_i\cdot\boldsymbol{\tau}_j\,\boldsymbol{\tau}_k\cdot\boldsymbol{\tau}_l\,, \tag{2.72d}$$

and the short-range contributions (see Table 4 for the LECs)

$$V^k = 4C_T\frac{g_A^4}{(2f_\pi)^4} \sum_{i\neq j\neq k\neq l} \frac{\boldsymbol{\sigma}_i\cdot\mathbf{q}_i\,\boldsymbol{\sigma}_k\times\boldsymbol{\sigma}_l\cdot\mathbf{q}_{ij}}{[\mathbf{q}_i^2+m_\pi^2][\mathbf{q}_{ij}^2+m_\pi^2]^2}\Big[\boldsymbol{\tau}_i\cdot\boldsymbol{\tau}_k\,\mathbf{q}_i\times\mathbf{q}_{ij}\cdot\boldsymbol{\sigma}_j - \boldsymbol{\tau}_i\times\boldsymbol{\tau}_j\cdot\boldsymbol{\tau}_k\,\mathbf{q}_i\cdot\mathbf{q}_{ij}\Big]\,, \tag{2.72e}$$

$$V^l = 2C_T\frac{g_A^2}{(2f_\pi)^4} \sum_{i\neq j\neq k\neq l} \frac{\boldsymbol{\sigma}_i\cdot\mathbf{q}_i\,\boldsymbol{\sigma}_k\times\boldsymbol{\sigma}_l\cdot\mathbf{q}_{ij}}{[\mathbf{q}_i^2+m_\pi^2][\mathbf{q}_{ij}^2+m_\pi^2]}\,\boldsymbol{\tau}_i\times\boldsymbol{\tau}_j\cdot\boldsymbol{\tau}_k\,, \tag{2.72f}$$

$$V^n = 2C_T^2\frac{g_A^2}{(2f_\pi)^2} \sum_{i\neq j\neq k\neq l} \frac{\boldsymbol{\sigma}_i\times\boldsymbol{\sigma}_j\cdot\mathbf{q}_{ij}\,\boldsymbol{\sigma}_k\times\boldsymbol{\sigma}_l\cdot\mathbf{q}_{ij}}{[\mathbf{q}_{ij}^2+m_\pi^2]^2}\,\boldsymbol{\tau}_j\cdot\boldsymbol{\tau}_k\,. \tag{2.72g}$$

Here, one uses the short-hand notation $\mathbf{q}_{ij} = \mathbf{q}_i + \mathbf{q}_j = -\mathbf{q}_k - \mathbf{q}_l = -\mathbf{q}_{kl}$ with $\mathbf{q}_i = \mathbf{p}_i' - \mathbf{p}_i$ being the difference of final and initial momenta. Note that the overall signs of V^c and V^l were misprinted in Ref. [208] and that the sums consider the 24 permutations of four particle labels. The regularized and antisymmetrized 4N potential is finally given by

$$V_{4\mathrm{N}}^{\mathrm{as}} := f_R^{(4)}(\mathbf{p}_1', \mathbf{p}_2', \mathbf{p}_3', \mathbf{p}_4'; \Lambda_{4\mathrm{N}})\,\mathscr{A}_{1234}V_{4\mathrm{N}}\,f_R^{(4)}(\mathbf{p}_1, \mathbf{p}_2, \mathbf{p}_3, \mathbf{p}_4; \Lambda_{4\mathrm{N}})\,. \tag{2.73}$$

We employ in this thesis the nonlocal regulator (2.70) with $A = 4$ and choose the cutoff $\Lambda_{4\mathrm{N}}$ as well as the exponent n_{exp} equal to the 3N regularization [108, 140]. The antisymmetrizer reads

$$\begin{aligned}\mathscr{A}_{1234} = \mathbb{1} &- P_{34} - P_{23} + P_{234} + P_{243} - P_{24} \\ &- P_{12} + P_{12}P_{34} + P_{123} - P_{1234} - P_{1243} + P_{124} \\ &+ P_{132} - P_{1342} - P_{13} + P_{134} + P_{13}P_{24} - P_{1324} \\ &- P_{1432} + P_{142} + P_{143} - P_{14} - P_{1423} + P_{14}P_{23}\,,\end{aligned} \tag{2.74}$$

where P_{ijk} is known from the antisymmetrizer (2.67a) and, similarly, P_{ijkl} denotes the cyclic permutation operator of four particles $(i\ j\ k\ l)$, or symbolically, $(i \to j \to k \to l \to i)$. Similar to the 3N case, it is suitable in practice to express these as strings of transposition operators using the identities in Eq. (2.68), $P_{ijkl} = P_{ij}P_{ik}P_{il} = P_{kl}P_{jk}P_{ij}$.

3 Weinberg eigenvalue analysis of chiral NN interactions

In this chapter, we present a comprehensive Weinberg eigenvalue analysis of a representative set of modern chiral NN interactions (see Table 2) based on our publication in Ref. [188]. As discussed in Sec. 2.1.1, chiral interactions can be classified according to the regulator implementation, with broad freedom to choose the functional form of the regulator within each category. Our set contains specifically local, semilocal, and nonlocal potentials developed by Gezerlis, Tews *et al.* (2013) [16, 17], Epelbaum, Krebs, and Meißner (2015) [9, 10], and Entem, Machleidt, and Nosyk (2017) [11], as well as Carlsson, Ekström *et al.* (2016) [15]. In principle, these interactions should all be capable of describing the same physical phenomena, but in practice the differences can be important (see also Ref. [18]). Our detailed comparison of Weinberg eigenvalues provides various insights into their idiosyncrasies for different orders and partial waves. It could be used, moreover, as a helpful monitoring scheme when constructing next-generation interactions.

3.1 Weinberg eigenvalue analysis

The Weinberg eigenvalue analysis is a versatile diagnostic tool to quantify perturbativeness of nuclear interactions and takes a close look on the physics of individual partial-wave channels. By perturbativeness we mean the order-by-order convergence pattern in a perturbative many-body expansion which needs to be distinguished from an order-by-order convergence in the chiral EFT expansion. For NN scattering in free space, this expansion is the Born series. For many-body systems such as infinite matter and finite nuclei, this expansion is MBPT. While in this thesis we are particularly interested in whether MBPT for infinite matter converges and at a practical rate (e.g., at low-enough order to be tractable), the characterization of perturbativeness is of more general concern. Even for nonperturbative many-body methods using a basis expansion (e.g., the self-consistent Green's function method), the computational resources for convergence depend strongly on this property. It is also relevant for identifying or justifying reference states such as Hartree-Fock and for motivating microscopic nuclear density functional theory.

Originally, Weinberg developed this method in the early 1960's [213] (see also Refs. [214–216]) while working to understand bound states in nonrelativistic quantum mechanics (as a warm-up for composite particles in quantum field theory) and how to introduce quasiparticles to cure nonconvergent Born series [213, 217, 218]. More recent applications of the Weinberg analysis [219–221] provide quantitative insights into how RG techniques soften both, the strongly repulsive short-range interaction and the tensor force whereas bound (or nearly bound) states are not affected and thus remain sources of nonperturbativeness. It has been shown in medium, however, that Pauli blocking tames the latter in the particle-particle channel [219] which is manifested by decreasing (attractive) in-medium Weinberg eigenvalues towards saturation density. This is an important result for infinite-matter calculations within MBPT in general, combined with the RG methods. Work is currently in progress to quantify the perturbativeness of chiral NN plus 3N interactions up to N^{3}LO at the normal-ordered two-body level [222], in particular, the ones adopted in the present thesis. Furthermore, in-medium Weinberg analyses have successfully been employed to study pairing phenomena and to extract the BCS energy gap at the Fermi surface (see also Sec. 6) [223–225].

3.1.1 Perturbative convergence and eigenvalue equation

We review briefly the most important aspects of the Weinberg eigenvalue analysis in vacuum and refer to the original work in Ref. [213] as well as to the literature [226, 227] for more detailed discussions.

Motivating the concept, we consider for simplicity the Lippmann-Schwinger equation for the free-space T-matrix in the center-of-mass frame,

$$T(W) = V + V G_0(W) T(W) , \tag{3.1a}$$

$$= \sum_{n=0}^{\infty} V \left(G_0(W) V\right)^n , \tag{3.1b}$$

with the free propagator $G_0(W) = (W - H_0)^{-1}$, the kinetic energy $H_0 = p^2/m$, where m is the averaged nucleon mass, and W is the complex energy. Iteration of the Born series (3.1b) may converge to a self-consistent solution. Due to nonperturbative sources, however, the convergence is by no means guaranteed; e.g., bound states are poles of the T-matrix, which render the expansion naturally divergent. Studying the convergence and efficiency of perturbation theory, Weinberg analyzed the eigenvalues of the operator $G_0(W)V$,

$$G_0(W) V \, |\Psi_\nu(W)\rangle = \eta_\nu(W) \, |\Psi_\nu(W)\rangle . \tag{3.2}$$

The so-called Weinberg eigenvalues $\eta_\nu(W)$ are defined in the complex energy plane cut along the positive real axis, and form a discrete set for any value of W. In the following, we will take $W = E + i\varepsilon$ for positive energies. Making use of the eigenvalue relation (3.2), the Born series expansion (3.1b) is a geometric series which converges if and only if all eigenvalues lie within the unit circle in the complex plane, i.e., $|\eta_\nu(W)| < 1$. The largest eigenvalue sets the rate of convergence, if at all, where overall smaller magnitudes imply faster convergence. As an important result for curing divergent Born series, Weinberg has shown that only a finite number of eigenvalues are located outside the unit circle, $|\eta_\nu(W)| > 1$. In that region, the precise magnitudes of the eigenvalues still have a dramatic impact on the convergence in a nonperturbative many-body method.

We summarize here several definitions as well as selected properties of $\eta_\nu(W)$ relevant for this chapter. Rewriting the eigenvalue relation (3.2) as a modified Schrödinger equation [213],

$$\left(H_0 + \frac{V}{\eta_\nu(W)}\right) |\Psi_\nu(W)\rangle = W \, |\Psi_\nu(W)\rangle , \tag{3.3}$$

allows intuitively a physical interpretation: the eigenvalue is effectively an energy-depending coupling $\eta_\nu^{-1}(W)$ which rescales the interaction. Following the original discussion by Weinberg, real bound states of the potential having $W = E < 0$ (e.g., for the deuteron, $E = -2.223$ MeV) correspond to $\eta_\nu(E) = 1$. The modified Schrödinger equation equals to the physical one in this case. More generally, even though the original potential does not support a bound state with binding energy $E < 0$, a scaled interaction $\eta_\nu^{-1}(E)V$ would have a bound state at E. A purely attractive potential has only positive eigenvalues for $E < 0$. On the other hand, a purely repulsive potential cannot have a bound-state solution of the Schrödinger equation, which naively seems to imply that the modified Schrödinger equation (3.3) has no solutions. However, Eq. (3.3) may have a solution for a sign-flipped interaction $\eta_\nu^{-1}(E)V$ in which the Weinberg eigenvalue is negative. Therefore, it is convention that a positive (negative) eigenvalue is referred to as an attractive (repulsive) eigenvalue.

In the case of positive energies ($E > 0$) for $W = E + i\varepsilon$ with $\varepsilon \to 0$, the modified Schrödinger equation (3.3) has complex energy eigenvalues, leading to complex Weinberg eigenvalues since $\eta_\nu^{-1}(E)V$ cannot be Hermitian anymore. Thus, we obtain complex (real) eigenvalues for positive (negative) energies E. The same definition of attractive and repulsive as before applies to the imaginary part of the eigenvalues for positive energies, which is motivated by analytic continuation from the solution along the negative real axis. In general, both attractive and repulsive eigenvalues occur for a nuclear potential.

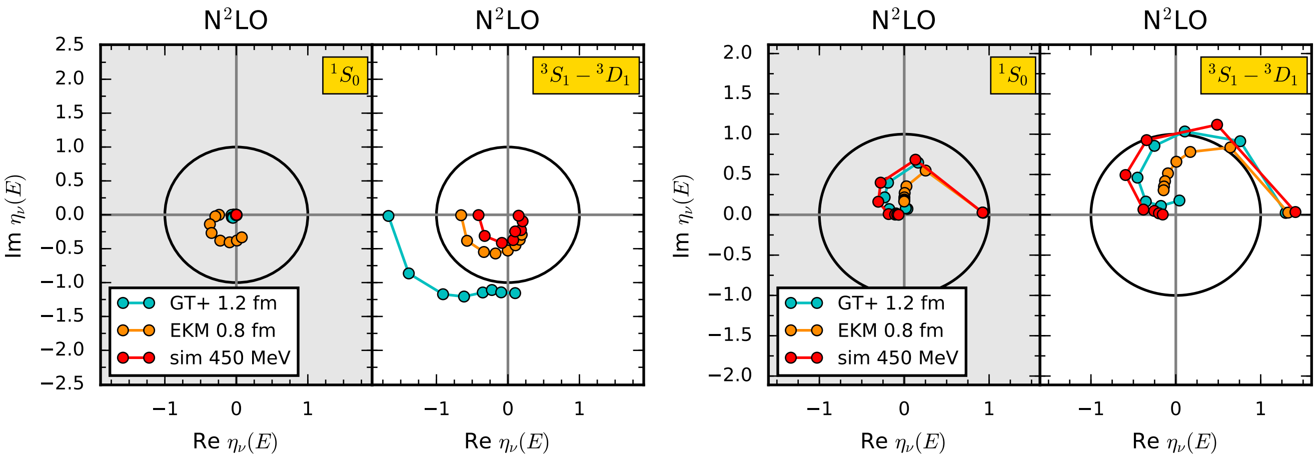

(a) Repulsive eigenvalues (negative imaginary part).

(b) Attractive eigenvalues (positive imaginary part). (Nearly and shallow) bound states close to $E = 0$ are indicated by $\eta \sim 1$.

Figure 14: Weinberg eigenvalues for the N^{2}LO NN potentials GT+ 1.2 fm, EKM 0.8 fm, and sim 450 MeV ($T_{\text{rel}} = 290$ MeV), as trajectories of energy in the complex plane, starting on the real axes and evolving counterclockwise. We show results for energies $E = 0, 25, 66, 100, 150, 200, 250,$ 300 MeV as circles in the $^1S_0$ (left panels) and $^3S_1$—$^3D_1$ channel (right panels), respectively. The nomenclature of the potentials follows Table 2.

We illustrate in Fig. 14 the behavior of repulsive and attractive Weinberg eigenvalues, respectively, in the complex plane for positive energies $E = (0-300)$ MeV in the $^1S_0$ and $^3S_1$—$^3D_1$ channels for a set of three different potentials, by taking the limit $\varepsilon \to 0$ of $\eta_\nu(E + i\varepsilon)$. The trajectories start on the real axis, evolve counterclockwise with increasing energy and eventually vanish in the limit $|W| \to \infty$. Nearly (or shallow) bound states are represented by attractive eigenvalues with magnitudes close to unity for $E = 0$. The deuteron binding energy can be determined by the intersection of the trajectory in the $^3S_1$—$^3D_1$ channel and the unit circle when lowering the energy $E < 0$ as the eigenvalues decrease in magnitude on the real axis. Since the attractive eigenvalues are typically dominated by (nearly or shallow) bound states in the two S-wave channels, we discuss in this chapter mainly repulsive eigenvalues.

3.1.2 Solving the eigenvalue equation

In practice, it is convenient to solve the eigenvalue equation (3.2) in a partial-wave representation because $G_0V(W)$ is block diagonal in the partial-wave quantum numbers $(LS)JT$,

$$\begin{array}{c} \\ ^1S_0 \\ ^3S_1 \\ ^3D_1 \\ ^1P_1 \\ \vdots \end{array} \begin{array}{c} \begin{array}{ccccc} ^1S_0 & ^3S_1 & ^3D_1 & ^1P_1 & \cdots \end{array} \\ \left(\begin{array}{ccccc} \blacksquare & 0 & 0 & 0 & \cdots \\ 0 & \blacksquare & \blacksquare & 0 & \cdots \\ 0 & \blacksquare & \blacksquare & 0 & \cdots \\ 0 & 0 & 0 & \blacksquare & \\ \vdots & \vdots & \vdots & \vdots & \ddots \end{array}\right) \end{array}, \tag{3.4}$$

where L denotes the angular momentum, S the two-body spin, J the total angular momentum, and T the two-body isospin. This allows to separately diagonalize blocks of given S, J, and T (the ■ in Eq. (3.4)),

$$\frac{2}{\pi}\sum_{L,L'}\int \mathrm{d}k'\,\frac{k'^2 m V^{JT}_{LL'S}(k,k')}{k_0^2-k'^2+i\varepsilon}\left\langle k'(L'S)JT\,\middle|\,\Psi_\nu(W)\right\rangle=\eta_\nu(W)\sum_L\langle k(LS)JT\,|\,\Psi_\nu(W)\rangle\,, \tag{3.5}$$

where different L values may be coupled due to the potential ($k_0^2+i\varepsilon=mW$). For coupled channels, we have $L,\, L'=|J\pm 1|$, whereas in uncoupled channels $L=L'$. The main discussion of this chapter is based on the free propagator and on the neutron-proton (np) channel but isospin-symmetry breaking is usually small. Hence, we have dropped the index $m_T=0$ for simplicity.

In the case of negative energies (i.e., purely imaginary k_0) poles do not occur and we can take $\varepsilon=0$. Technically, we then solve the eigenvalue problem on a well-suited Gaussian quadrature momentum grid to ensure numerical convergence. After performing the standard substitution $\int \mathrm{d}p\to\sum_{i=1}^{N_p}$, the left-hand side of the eigenvalue problem (3.5) can be written as a matrix. The basis vectors have a size of N_p ($2N_p$) in uncoupled (coupled) channels.

For the positive energies, however, one has to carefully take into account the pole in Eq. (3.5) at $k=k_0$. In that case, we make use of the Sokhotski-Plemelj theorem for a real, continuous function $f(k)$,

$$\frac{f(k)}{k-(k_0\pm i\varepsilon)}=\mathscr{P}\frac{f(k)}{k-k_0}\pm i\pi\delta(k-k_0)f(k)\,, \tag{3.6}$$

with the Cauchy principal value $\mathscr{P}$, and integrate explicitly over the singularity. Following, e.g., Ref. [183], we convert the principal-value integral into a standard integral by adding

$$-g(k_0)\,\mathscr{P}\int_0^\infty\frac{\mathrm{d}k}{k^2-k_0^2}=0 \tag{3.7}$$

to Eq. (3.5) in order to make the integral well-behaved, i.e.,

$$\mathscr{P}\int_0^\infty \mathrm{d}k\,\frac{g(k)}{k^2-k_0^2}=\int_0^\infty \mathrm{d}k\,\frac{g(k)-g(k_0)}{k^2-k_0^2}\,, \tag{3.8}$$

where we define $f(k)=g(k)/(k+k_0)$. To evaluate numerically the integral on the right-hand side of Eq. (3.8), it is crucial to split the integral at some sufficiently large $p_{\max}>k_0$ such that $f(k)$ is known to vanish for all $p>p_{\max}$. Due to the regularization of the potential, it is usually straightforward to find a suitable value for $p_{\max}$. The advantage of this procedure is that the remaining integral of the form,

$$\int_{p_{\max}}^\infty\frac{\mathrm{d}k}{k^2-k_0^2}=\frac{1}{k_0}\,\mathrm{artanh}\left(\frac{k_0}{p_{\max}}\right)\,, \tag{3.9}$$

no longer has a pole because of $p_{\max}>k_0$, and can be evaluated analytically. We have carefully checked the numerical stability of this method, in particular the subtraction in Eq. (3.8). The subtracted pole as well as the additional constant term in Eq. (3.6) are taken care of by enlarging the basis vector by one for each L component, so the matrix to be diagonalized is of rank N_p+1 ($2N_p+2$) for an uncoupled (coupled) channel.

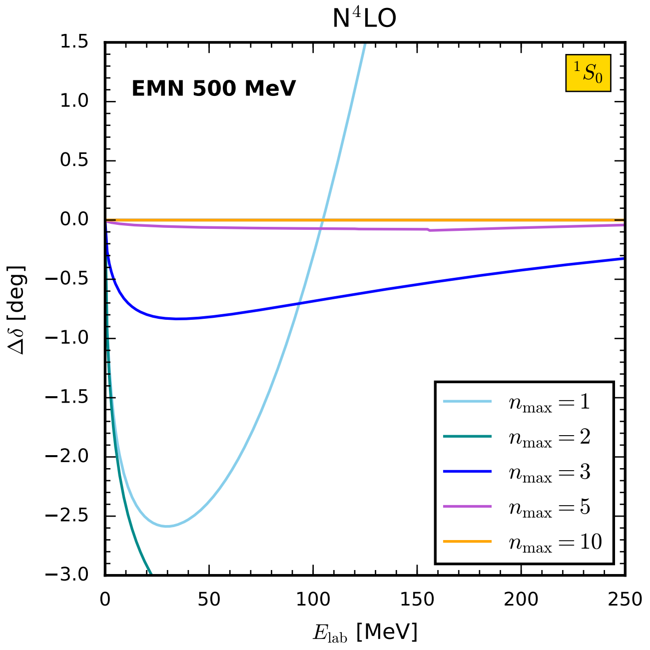

Figure 15: Convergence pattern of $^1S_0$ phase shifts calculated using the largest Weinberg eigenvalues and different truncations $n \leqslant n_{\text{max}}$ in the expansion (3.10). The results as function of $E_{\text{lab}} = 2E$ are based on the potential EMN 500 MeV at N^{4}LO, but the other potentials and channels show a similar behavior. Note that for $n_{\text{max}} = 1$, we restrict the sum to the largest attractive (instead of the overall largest) eigenvalue to avoid a discontinuity that happens because the trajectories of attractive and repulsive eigenvalues are crossing each other.

3.1.3 Connection to phase shifts

We also review an intriguing feature of the Weinberg analysis. Weinberg showed in Section VI of Ref. [213] that the eigenvalues and phase shifts in an uncoupled channel $(LS)JT$ are related by

$$\delta^{JT}_{LS}(E) = \sum_{\nu=1}^{\infty} \delta_\nu(E), \qquad \text{and} \qquad \delta_\nu(E) \equiv -\arg\left(1-\eta_\nu(E+i\varepsilon)\right), \tag{3.10}$$

where the η_ν are solutions to Eq. (3.5) for the uncoupled channel. The $\delta_\nu(E)$ are called elemental phase shifts. For coupled channels, Eq. (3.10) gives the sum of the partial phase shifts, $\delta^{JT}_{L-1S} + \delta^{JT}_{L+1S}$, which is independent of a particular phase-shift convention. Repulsive (attractive) eigenvalues lead to elemental phase shifts $-\pi \leqslant \delta_\nu(E) \leqslant 0$ $(0 \leqslant \delta_\nu(E) \leqslant \pi)$ resulting, as expected for purely repulsive (attractive) interactions, in negative (positive) phase shifts.

Weinberg already observed that Eq. (3.10) usually converges rapidly, taking into account only a few terms. Consequently, there can only be a few eigenvalues with significant magnitudes. We find a similar convergence pattern also for our representative set of modern chiral potentials. In Fig. 15, we show the residuals

$$\Delta\delta^{JT}_{LS}(E) = \sum_{\nu=1}^{n_{\text{max}}} \delta_\nu(E) - \delta^{JT}_{LS}(E), \tag{3.11}$$

evaluated for several truncations n_{max}. The results in Fig. 15 are shown for the EMN 500 MeV potential at N^{4}LO in the $^1S_0$ channel, however, the other potentials and channels discussed in this chapter behave similarly. The reference phase shifts $\delta^{JT}_{LS}(E)$ result from the on-shell T-matrix as obtained in a nonpertur-

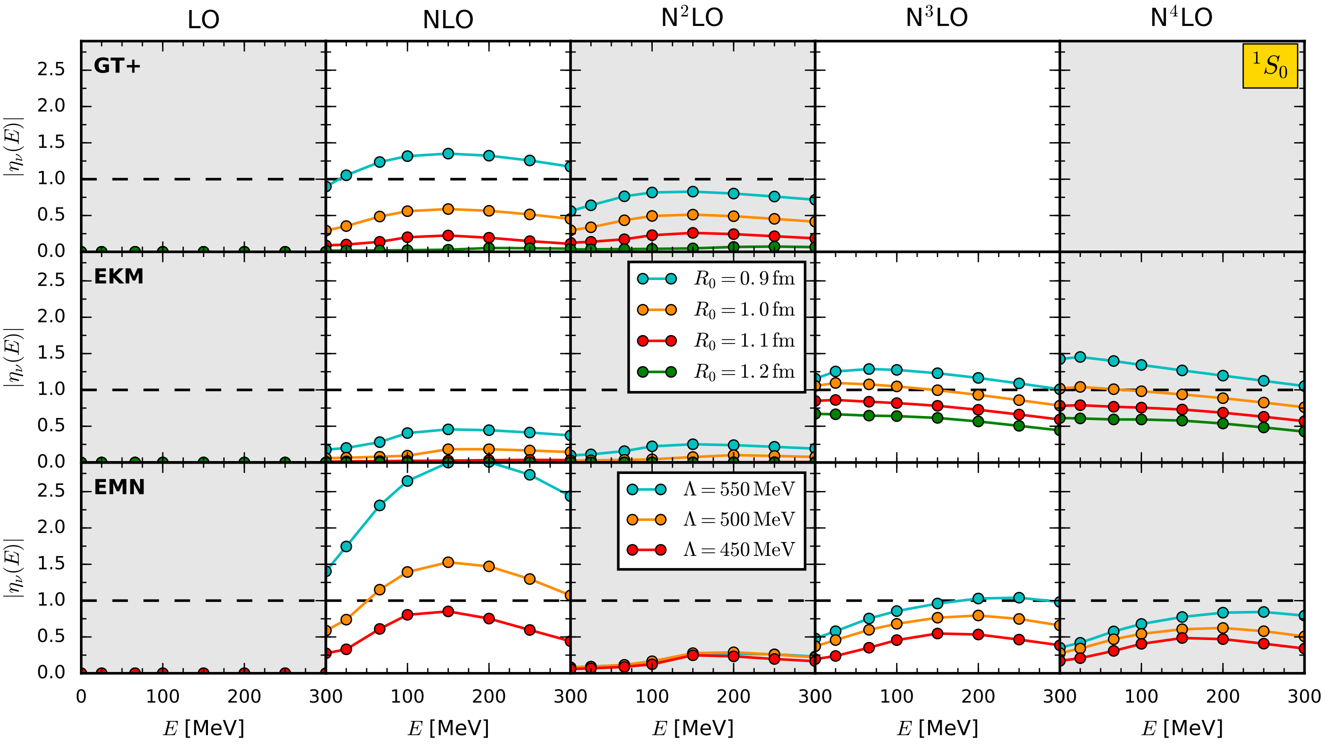

Figure 16: Magnitude of the largest repulsive Weinberg eigenvalues for the GT+ (first row), EKM (middle row), and EMN potentials (bottom row) as function of energy $E = 0, 25, 66, 100, 150, 200, 250, 300$ MeV in the $^1S_0$ channel up to the highest chiral order available, respectively. We show results for coordinate-space cutoffs $R_0 = (0.9-1.2)$ fm for the GT+ and EKM potential, as well as for momentum-space cutoffs $\Lambda = (450-550)$ MeV for the EMN potential.

bative calculation by inverting Eq. (3.1a), i.e., $T(W) = (1 - VG_0(W))^{-1}V$. The converged phase shifts are very well reproduced for $n_{\max} \sim 5-10$.

3.2 Comprehensive study of local, semilocal, and nonlocal interactions

3.2.1 Observations from repulsive and attractive eigenvalues

As mentioned above, we apply here the Weinberg eigenvalue analysis to the recent local, semilocal, and nonlocal chiral NN potentials in different partial waves. We investigate and compare order by order characteristic features of each potential (see also Table 2) and exploit the regulator comparison of Sec. 2.1.1 for the local and semilocal potentials. The repulsive eigenvalues manifest the differences between the various potentials, so we focus our analysis on them, but also illustrate the common trends of attractive eigenvalues. In Sec. 3.3, we revisit the question of whether distinct but phase-shift equivalent initial potentials flow to the same low-momentum form under the SRG.

We start with the $^1S_0$ and coupled $^3S_1$–$^3D_1$ channels, as they are most important for low-energy physics, and then extend the discussion to higher partial waves. In Figs. 16 and 17, we show the magnitude of the S-wave repulsive eigenvalues as function of energy from LO up to highest order available, respectively, for the local GT+, semilocal EKM, and nonlocal EMN potentials in each row with various cutoffs. The black-dotted line denotes where the Born series expansion diverges, corresponding to the unit circle in Figs. 14a and 14b. For the GT+ potential we use the SFR cutoff $\tilde{\Lambda} = 1000$ MeV. From these figures, we observe the following:

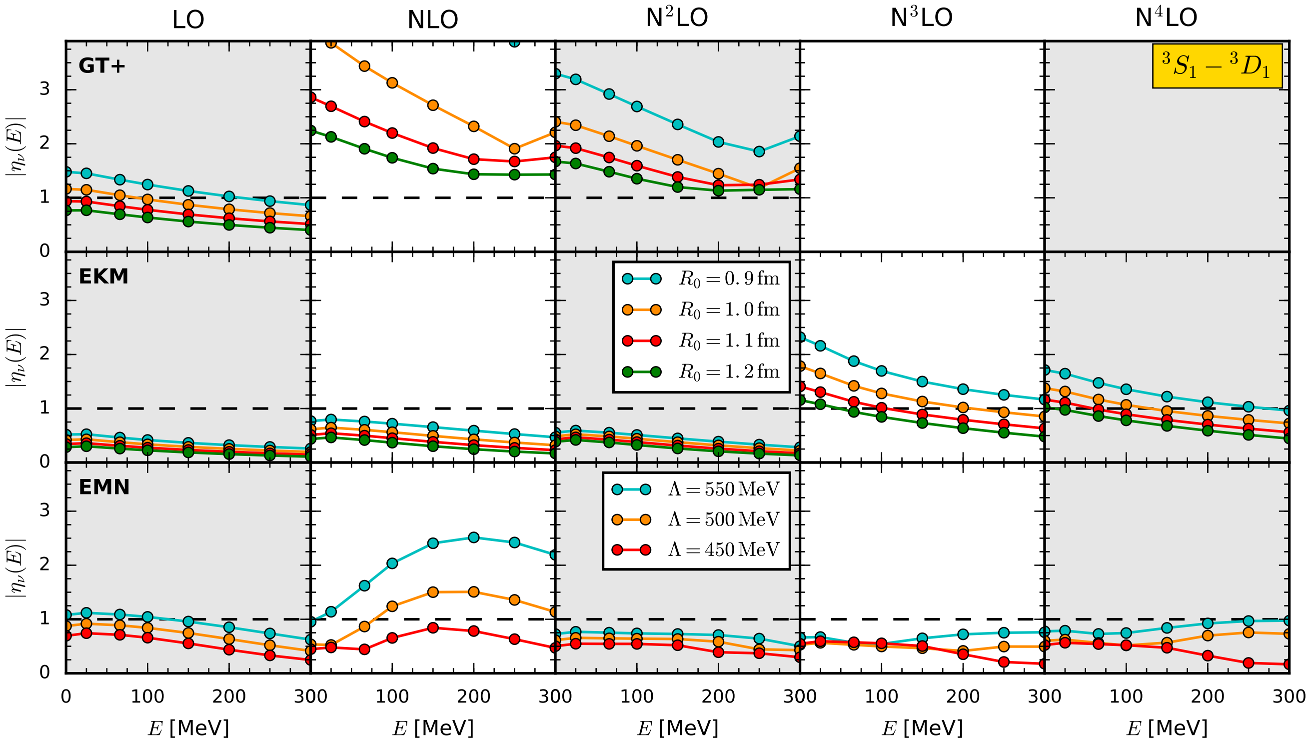

Figure 17: Same as Fig. 16 (largest repulsive eigenvalues) but for the $^3S_1$–$^3D_1$ channel. Notice that the Weinberg eigenvalues are above the scale for the NLO NN potential GT+ 0.9 fm, as we use the same plot range for all panels for better comparison.

- In the $^1S_0$ channel, all three LO potentials are purely attractive and so the repulsive eigenvalues are zero. In contrast, the corresponding eigenvalues in the $^3S_1$–$^3D_1$ channel are nonzero and show significant differences, with the EKM potentials being softer than GT+ and EMN.
- At NLO we find nonvanishing repulsive eigenvalues, large in magnitude for the GT+ potentials and even larger for the EMN potentials in the $^1S_0$ channel. In the $^3S_1$–$^3D_1$ channel, we observe magnitudes up to $|\eta_\nu| = 8$ for the GT+ 0.9 fm potential and up to $|\eta_\nu| = 2.5$ for the EMN 550 MeV potential, while eigenvalues are below one for the EKM potentials in both channels.
- Going from NLO to N^{2}LO leads to reduced eigenvalues uniformly, with EMN in particular changing from nonperturbative for the larger Λ values to perturbative.
- The eigenvalues for the EKM and EMN potentials in the $^1S_0$ channel jump upwards at N^{3}LO and stay equally large in magnitude at N^{4}LO. In the $^3S_1$–$^3D_1$ channel, the eigenvalues for the EKM potentials again increase at N^{3}LO and N^{4}LO, whereas for the EMN potentials we observe essentially no change in magnitude but an increased spread in Λ for higher energies. Enhanced repulsive eigenvalues at N^{3}LO have been discussed in Ref. [220] due to the sub-sub-leading 2π exchange as a new nonperturbative source entering at N^{3}LO. It is interesting to note that these jumps in the eigenvalues are also manifested in the form of large energy changes of the triton binding energy [11, 102] based on these NN interactions [228].

All potentials at all orders get softened for larger coordinate-space cutoffs or smaller momentum-space cutoffs, respectively, resulting in less repulsion and therefore smaller repulsive eigenvalues. In general, the larger eigenvalues of the local GT+ potentials indicate that it is less perturbative than the semilocal or nonlocal potentials. This observation is consistent with past studies of local versus nonlocal one-boson-exchange potentials [229]. However, as discussed in Sec. 2.1.1, a direct comparison of the local

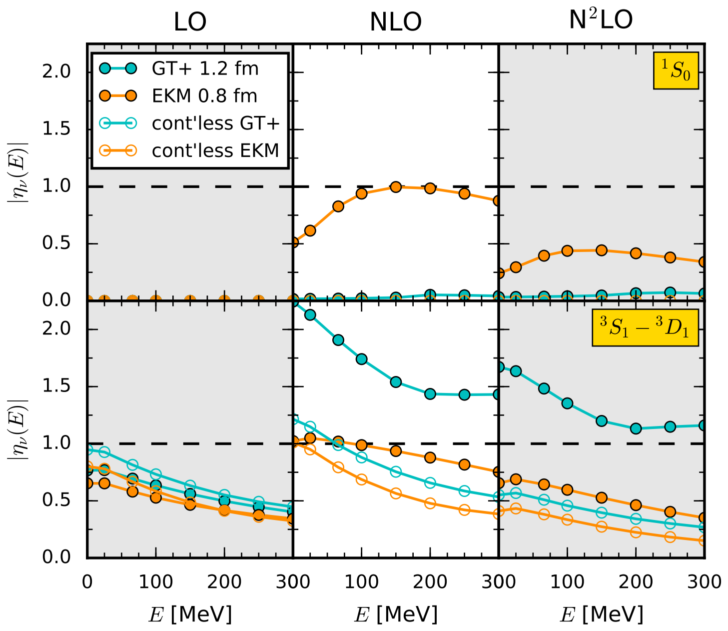

Figure 18: Magnitude of the largest repulsive Weinberg eigenvalues for the GT+ and EKM potentials at LO, NLO, and N^{2}LO for the fixed cutoff combination derived in Sec. 2.1.1. We show results for the full potential (full circles) in contrast to the potential without contacts (open circles) in the $^1S_0$ (upper panel) and $^3S_1-{}^3D_1$ channel (lower panel). The eigenvalues for the contactless potential are in fair agreement for the cutoff combination $R_0^{\text{GT+}} = 1.2$ fm and $R_0^{\text{EKM}} = 0.8$ fm at all orders and in both channels.

GT+ and semilocal EKM potentials with the same regulator parameter R_0 is misleading, because of the differing forms of the regulator functions. We identified comparable cutoff values, but good agreement for eigenvalues of the corresponding full potentials is only seen at LO. In Fig. 18, we compare the full and contactless potentials to shed light on the deviations. In this context, contactless means all contacts up to the given chiral order are set to zero. We find fair agreement for eigenvalues of the contactless potentials in both channels, even at NLO and N^{2}LO. Thus, we conclude that the different inclusion of the momentum-dependent short-range couplings (for local and semilocal or nonlocal) at NLO and beyond lead to the differences in eigenvalues.

We also examine the S-wave repulsive eigenvalues for selected nonlocal sim potentials at N^{2}LO, which are shown in Fig. 19. They are similar to the EKM and EMN results in the $^1S_0$ channel, while in the $^3S_1-{}^3D_1$ channel the eigenvalues show a spread in Λ as for the N^{2}LO EMN potential. In addition, the pattern of energy dependence is different except for the softest cutoff.

Examples of repulsive eigenvalues in the higher partial waves for the EMN and EKM potentials are shown in Figs. 20 and 21, respectively. In most channels there are not significant differences. The increases going from N^{2}LO to N^{3}LO noted for the S-waves are present for the EKM P-waves but without the dramatic jumps. These are only seen for the EMN potential in the ^{3}D$_2$ channel. The energy dependence of the repulsive eigenvalues is generally similar even for different regulators. However, as noted, the sim potential at N^{2}LO shows quite different energy dependence in the $^3S_1-{}^3D_1$ channel as the cutoff increases.

The attractive eigenvalues in the $^1S_0$ and $^3S_1-{}^3D_1$ channel are shown in Figs. 22 and 23, respectively, for the GT+, EKM, and EMN potentials. We find only a minor dependence on the cutoff and nearly the same eigenvalues for all potentials at all chiral orders. This behavior follows because the magnitude of

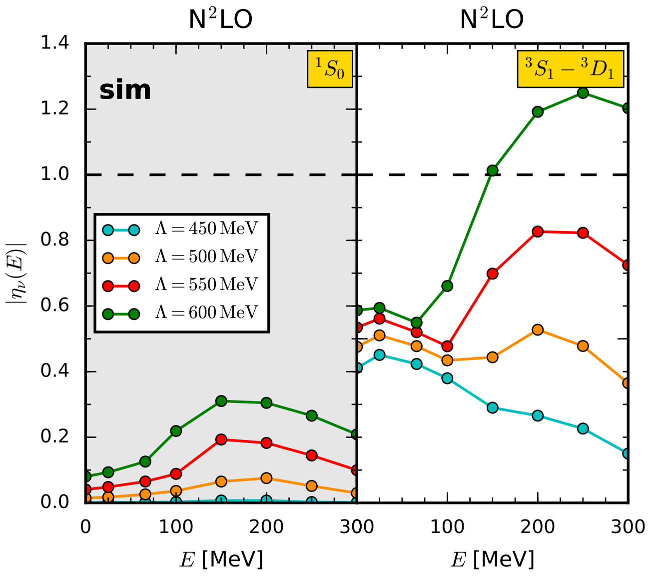

Figure 19: Magnitude of the largest repulsive Weinberg eigenvalues for the sim potentials at N^{2}LO with $T_{\text{rel}} = 290$ MeV and the cutoff range $\Lambda = (450 - 600)$ MeV as function of energy $E = 0$, 25, 66, 100, 150, 200, 250, 300 MeV in the $^1S_0$ (left panel) and $^3S_1$—$^3D_1$ channel (right panel).

the attractive eigenvalues is determined by the shallow or nearly bound state to be close to one at low energies (see also Ref. [220]). The energy dependence for all potentials at all orders and in both channels shows the same fall-off toward perturbative values.

3.2.2 Interpretation and general conclusions

These many observations illustrate how Weinberg eigenvalues may point to subtle issues, e.g., with the fitting procedure, but following up in detail is beyond the scope of this work. Instead, we give examples of more general conclusions from consideration of the eigenvalue systematics:

- For the EKM potential, we traced the increased repulsive eigenvalues at N^{3}LO and N^{4}LO to the new contacts at N^{3}LO. We observe eigenvalues equal to zero for the potential without N^{3}LO contacts in the $^1S_0$ channel, and significantly reduced eigenvalues (below one) in the $^3S_1$—$^3D_1$ channel. We conclude that the main contribution to the change in magnitude is from the contacts at this order.
- The repulsion needed to obtain correct phase shifts at high energies is provided by contact terms, but how this is realized differs between local and nonlocal implementations. For local potentials, the repulsive part is largely built up through the energy-independent LECs, because the q^2-dependent contacts at NLO and beyond are suppressed by at least a factor r^2 in coordinate-space (see also Ref. [17]). These LECs contribute equally at lower energies, leading to enhanced eigenvalues at NLO and beyond. The build-up of the short-range repulsion is visible in Fig. 24 for the N^{2}LO GT+ potential in coordinate-space. In contrast, contact terms for the semilocal and nonlocal potentials at NLO and beyond also depend on the momentum transfer in the exchange channel (i.e., k^2), which allows for momentum dependence, with large (small) repulsion for higher (lower) energies.
- We observed reduced eigenvalues when going from NLO to N^{2}LO. This could be due to the improved description of the mid-range part of the potential as a result of the subleading 2π exchange, entering at N^{2}LO, which requires less fitting into the contact parameters at this order.
- One might have guessed that the enhanced repulsive Weinberg eigenvalues are related to the low- to high-momentum coupling of local regulators. This has been ruled out by adding an additional

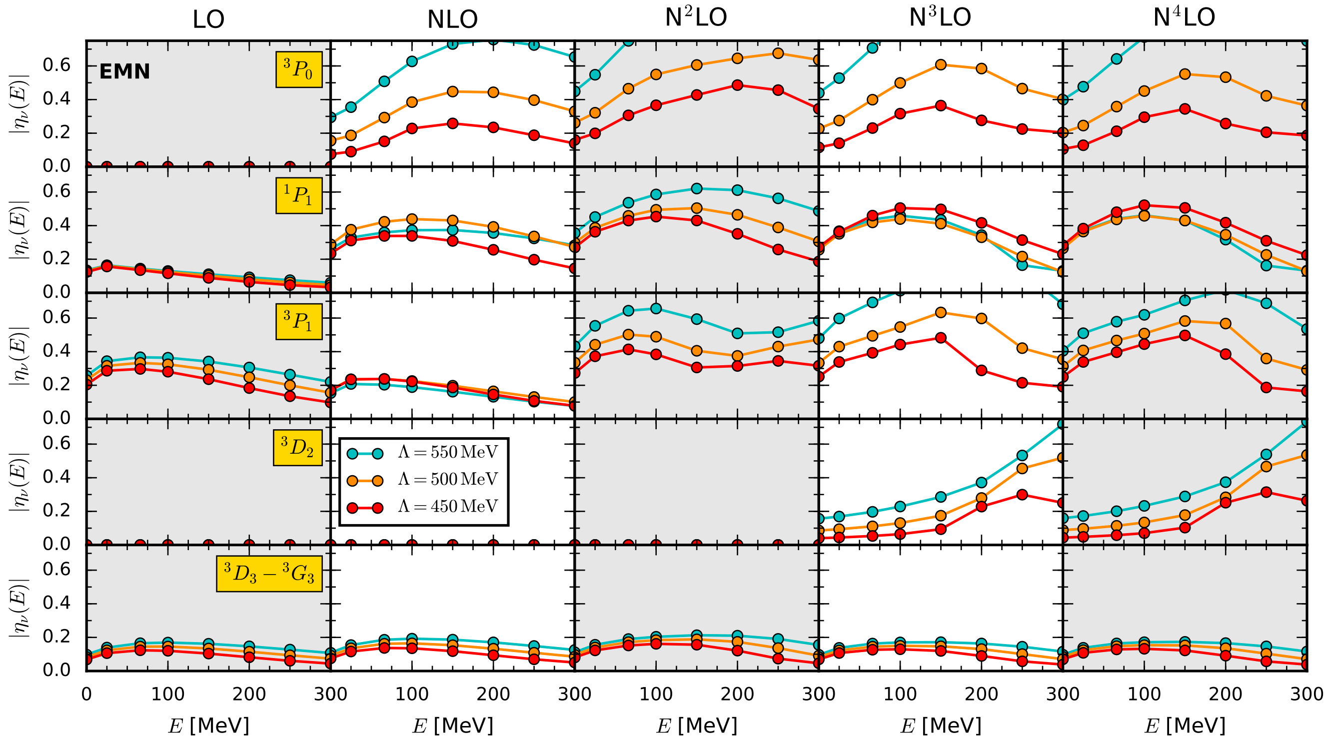

Figure 20: Magnitude of the largest repulsive Weinberg eigenvalues for the EMN potentials up to N^{4}LO as function of energy $E = 0, 25, 66, 100, 150, 200, 250, 300$ MeV in different higher partial waves. We show results for momentum-space cutoffs $\Lambda = (450 - 550)$ MeV. Notice that some eigenvalues are partially above the scale, as we apply the same plot range at all chiral orders and partial waves for better comparison.

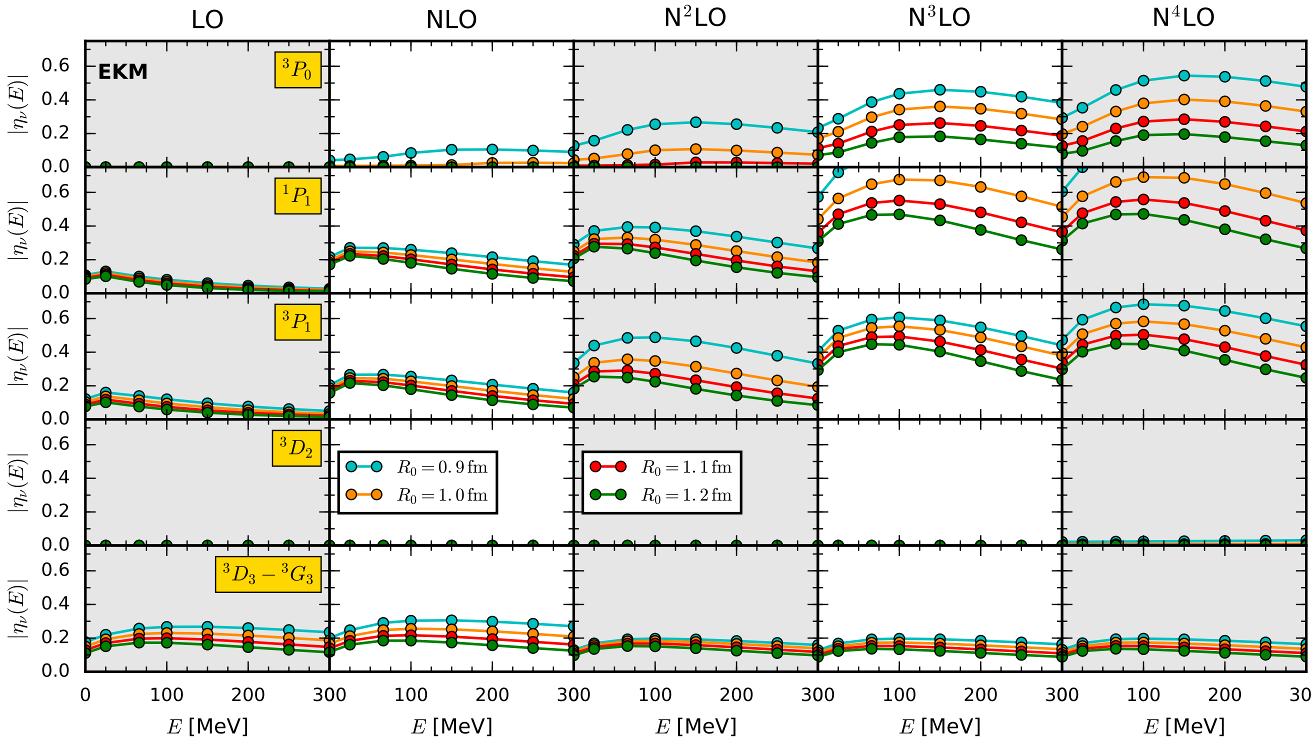

Figure 21: Magnitude of the largest repulsive Weinberg eigenvalues for the EKM potentials up to N^{4}LO as function of energy $E = 0, 25, 66, 100, 150, 200, 250, 300$ MeV in different higher partial waves. We show results for coordinate-space cutoffs $R_0 = (0.9-1.2)$ fm.

sharp cutoff of $\Lambda = (4-5)\ \mathrm{fm}^{-1}$, which leaves the eigenvalues nearly unchanged, showing that they are determined by the contributions below this cutoff.

In general, even when comparing regulators for different potentials can be quite cumbersome, the Weinberg eigenvalue analysis as a diagnostic tool offers the possibility to study the perturbativeness, indicate scheme dependence and possible issues in the fitting procedure, as well as draw conclusions on the regulator impact.

3.3 Evolved potentials and universality

For a given family of potentials, defined with the same regularization scheme and constructed with the same fitting protocol, the repulsive Weinberg eigenvalues reflect the softening of the interaction with progressively smaller (larger) regulator parameters in momentum (coordinate) space. This softening can also be realized through an RG evolution, e.g., via the SRG. In Fig. 25, we show the eigenvalues at zero energy in the $^1S_0$ and $^3S_1-^3D_1$ channel at N^{2}LO for the EKM, EMN, and GT+ potentials, as well as at N^{3}LO for the EKM and EMN potentials as function of the SRG parameter λ. The eigenvalues at large λ, which correspond to the unevolved (initial) potentials, exhibit the dramatic jump in hardness from $^1S_0$ to $^3S_1-^3D_1$ for GT+, and in both channels from N^{2}LO to N^{3}LO for EKM. The jump is much smaller for EMN $^1S_0$ and no change or even a softening is observed for EMN $^3S_1-^3D_1$. With evolution to smaller λ, all potentials are monotonically softened, with even the EKM N^{3}LO and GT+ N^{2}LO $^3S_1-^3D_1$ eigenvalues becoming perturbative for $\lambda < 4\,\mathrm{fm}^{-1}$, and $\lambda < 3.5\,\mathrm{fm}^{-1}$, respectively.

The fine details of the eigenvalue flow mirror the flow of the potential matrix elements. We show in Fig. 26a unevolved and SRG evolved ($\lambda = 2.0\ \mathrm{fm}^{-1}$) matrix elements in the $^1S_0$ channel for the EMN, EKM, and GT+ potentials at N^{2}LO as functions of the momentum. Specifically, we plot $V(p, p' = p)$ in the

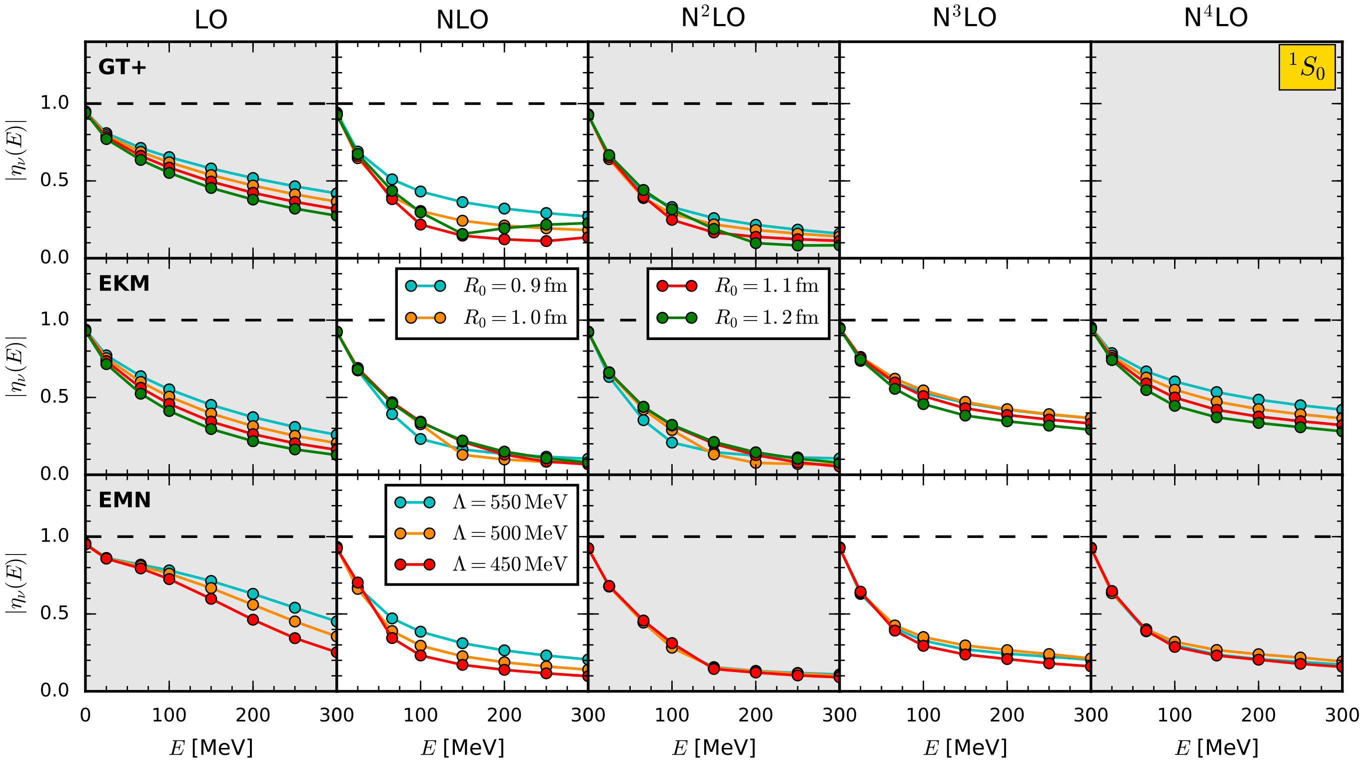

Figure 22: Magnitude of the largest attractive Weinberg eigenvalues for the GT+ (first row), EKM (middle row), and EMN potentials (bottom row), as function of energy $E = 0, 25, 66, 100, 150, 200, 250, 300$ MeV in the $^1S_0$ channel up to highest chiral order available, respectively. We show results for coordinate-space cutoffs $R_0 = (0.9-1.2)$ fm for the GT+ and EKM potentials, as well as for momentum-space cutoffs $\Lambda = (450-550)$ MeV for the EMN potentials.

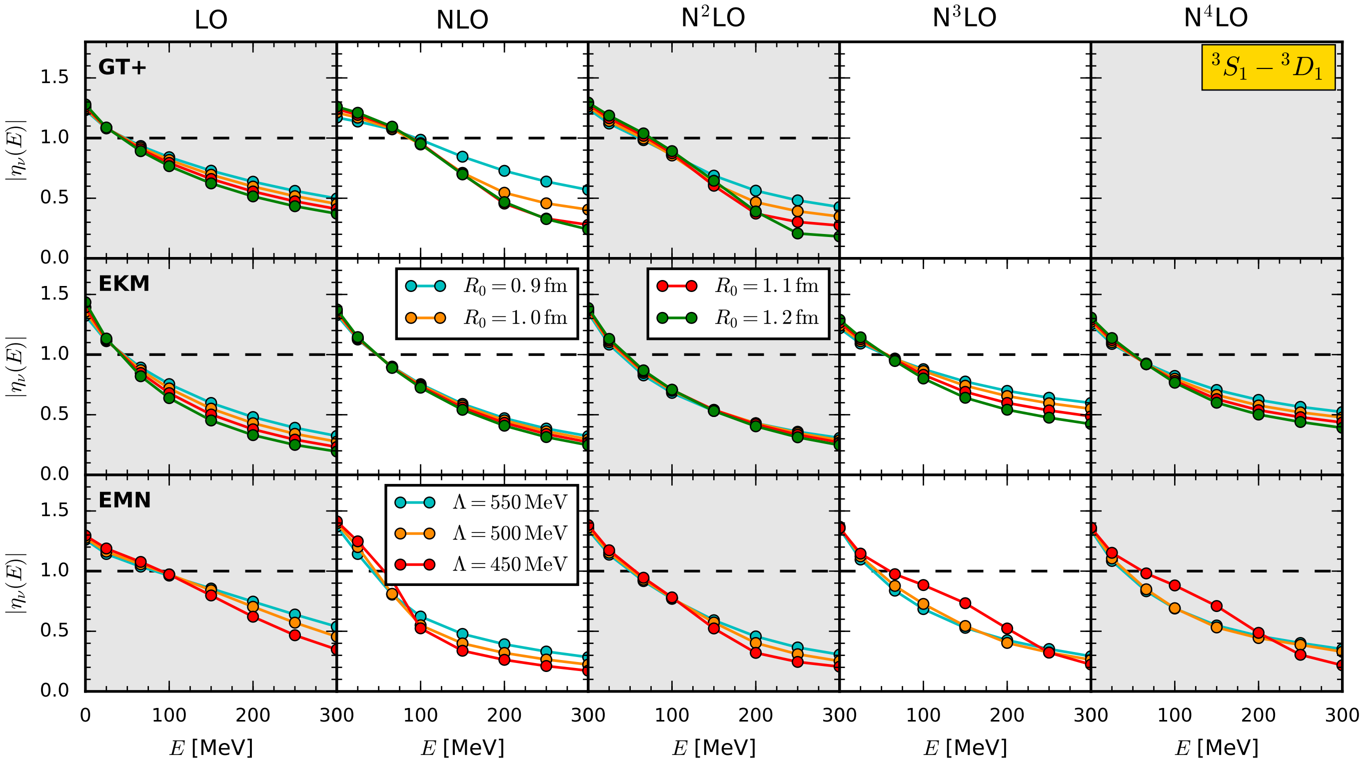

Figure 23: Same as Fig. 22 (largest attractive eigenvalues) but for the $^3S_1$–$^3D_1$ channel.

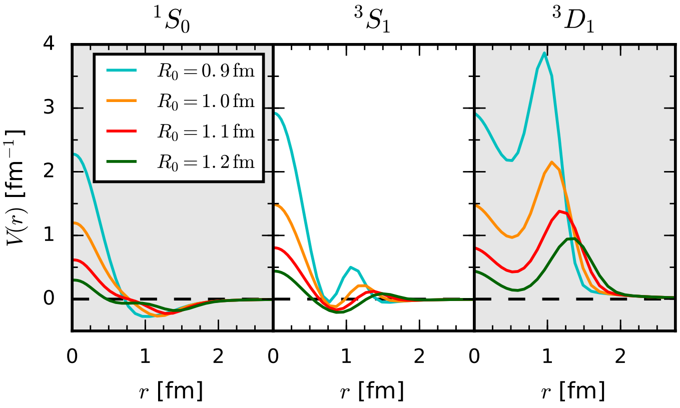

Figure 24: Coordinate-space representation of the GT+ potentials at N^{2}LO for the cutoff range $R_0 = (0.9 - 1.2)$ fm in the $^1S_0$ (left panel), $^3S_1$ (middle panel), and $^3D_1$ (right panel) channel. Note that the limit $r \to 0$ can easily be obtained using Appendix A and Table 1 in Ref. [17].

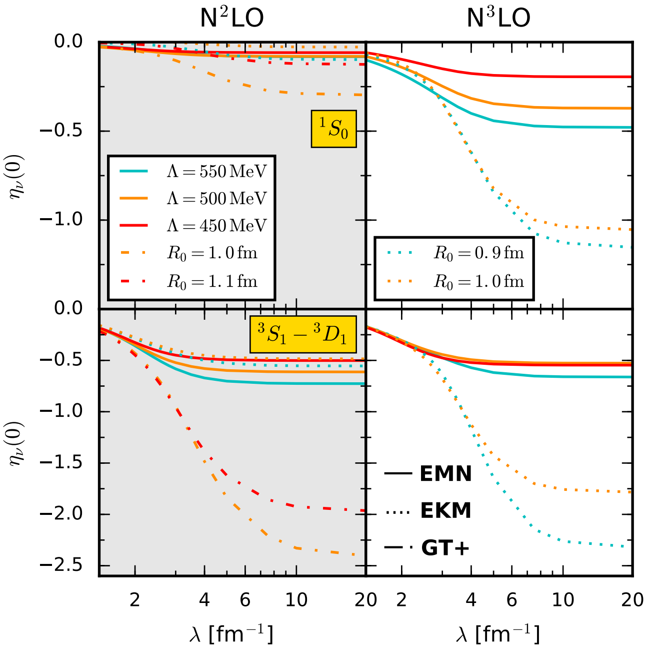

Figure 25: Largest repulsive Weinberg eigenvalues for the N^{2}LO EMN (solid lines), EKM (dotted lines), and GT+ (dash-dotted lines), as well as N^{3}LO EMN (solid lines) and EKM (dotted lines) NN potentials at $E = 0$ MeV as function of the SRG resolution scale λ in the $^1S_0$ (upper panels) and the $^3S_1$–$^3D_1$ channel (lower panels). For small λ, the eigenvalues are in good agreement and exhibit the universality for potentials evolved to low resolution scales.

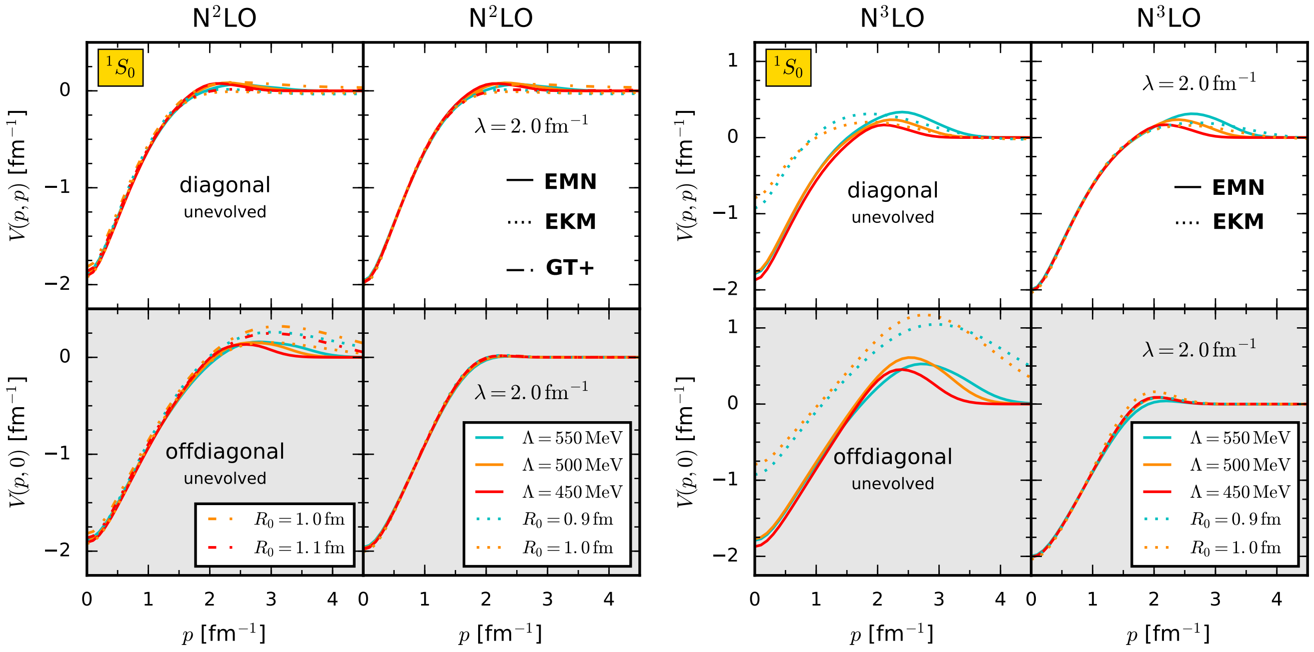

(a) EMN, EKM, and GT+ potentials at N^{2}LO.

(b) EMN and EKM potentials at N^{3}LO.

Figure 26: Diagonal (upper rows) and offdiagonal (lower rows) matrix elements $V(p, p' = p)$ and $V(p, p' = 0)$, respectively, of the unevolved (left columns) and SRG evolved to $\lambda = 2.0\ \mathrm{fm}^{-1}$ (right columns) EMN (solid lines), EKM (dotted lines), and GT+ potentials (dash-dotted lines) in momentum space in the $^1S_0$ channel. For small λ the diagonal elements are again in good agreement.

upper and $V(p, p' = 0)$ in the lower row. Figure 26b depicts similarly the N^{3}LO EMN and EKM potentials. At N^{2}LO, the relatively small degree of softening reflects the suppression of off-diagonal matrix elements, and all couplings are quantitatively close for $\lambda = 2\,\mathrm{fm}^{-1}$. At N^{3}LO, both diagonal and off-diagonal matrix elements exhibit a flow toward universal potentials for momenta below λ.

4 Neutron-matter equation of state based on chiral NN and 3N interactions up to N^{3}LO

We have developed a new normal-ordering framework to systematically include general 3N forces in calculations of asymmetric nuclear matter [28, 230]. It enables us to extend previous studies, e.g., in Refs. [36, 108, 140] to third order in MBPT with consistent contributions from NN and 3N forces up to N^{3}LO as well as to systems with arbitrary isospin asymmetries. Since there were no reliable fits at N^{3}LO for the two unknown 3N LECs c_D and c_E our first applications in Ref. [28] were limited to Hamiltonians with N^{3}LO NN and N^{2}LO 3N forces (see also our results in Ref. [4]).

Taking further advantage of this framework we include here for the first time N^{3}LO 3N interactions in MBPT up to third order and in the method of SCGF [31]. Neutron matter is therefore an ideal laboratory since all contributions are predicted up to N^{3}LO in the chiral expansion. Using these two complementary many-body frameworks, we provide improved predictions for the equation of state of neutron matter at zero temperature and analyze systematically the many-body convergence for different chiral EFT interactions. Referring to our (vacuum) Weinberg eigenvalue analysis in Sec. 3, this is a first step to assess the perturbativeness of the potentials for in-medium calculations. Furthermore, we extend the new framework to finite temperatures. These developments set the stage for improved calculations of neutron-rich matter including estimates of theoretical uncertainties for astrophysical applications once next-generation Hamiltonians are available.

4.1 Improved normal-ordering method

Normal ordering with respect to a reference state is a key step for the practical treatment of 3N forces as effective NN interactions in many-body calculations of matter and nuclei. Following our formal introduction in Sec. 1.3.2, normal ordering in infinite matter involves a summation of one particle over occupied states in the Fermi sphere [43, 133, 231]. For 3N forces this summation can be expressed formally as

$$\overline{V}_{3\text{N}} = \sum_i \langle 12i|V_{3\text{N}}^{\text{as}}|12i\rangle\, n_i = \text{Tr}_{\sigma_3}\text{Tr}_{\tau_3} \int \frac{d\mathbf{k}_3}{(2\pi)^3}\, n_{\mathbf{k}_3}^{\tau_3}\, V_{3\text{N}}^{\text{as}}\,, \tag{4.1}$$

which involves sums over spin and isospin projection quantum numbers σ_3 and τ_3 as well as an integration over all momentum states, weighted by the momentum distribution functions $n_{\mathbf{k}}^{\tau_3}$ for a given neutron n_n and proton density n_p, or likewise, the total density $n = n_p + n_n$ and the proton fraction $x = n_p/n$. In the following, we choose the Fermi–Dirac distribution function at zero temperature, $n_{\mathbf{k}}^{\tau_3} = \Theta(k_{\text{F}}^{\tau_3} - |\mathbf{k}|)$ with $n_i = k_{\text{F},i}^3/(3\pi^2)$, and we assume spin-unpolarized, homogeneous matter. The finite-temperatures extension is subject of Sec. 4.3. We can apply the present framework also to general correlated distributions functions. However, it was shown in infinite matter [141] that the energy per particle is not very sensitive to the particular choice of the reference state for the employed chiral EFT interactions. This indicates that the residual 3N contributions, e.g., from diagram $E_{3\text{N}}^{(2)}$ in Fig. 7, are small such that they can be neglected, particularly, in neutron matter. For including these, we refer to the Monte-Carlo framework developed in Sec. 5 and to the coupled-cluster calculations in Ref. [137]. $V_{3\text{N}}^{\text{as}}$ is the antisymmetrized and regularized 3N interaction (2.66). The effective interaction $\overline{V}_{3\text{N}}$ represents a density-dependent NN interaction that can be combined with contributions from free-space NN interactions via Eq. (1.45c).

As defined in Sec. 2.2 the 3N interaction is the fundamental microscopic input to Eq. (4.1). The momentum dependence of a general translationally invariant 3N interaction can be most efficiently expressed as a function of the Jacobi momenta (see Fig. 27)

$$\mathbf{p} = \frac{\mathbf{k}_1 - \mathbf{k}_2}{2}\,, \quad \mathbf{q} = \frac{2}{3}\left[\mathbf{k}_3 - \frac{1}{2}(\mathbf{k}_1 + \mathbf{k}_2)\right], \tag{4.2}$$

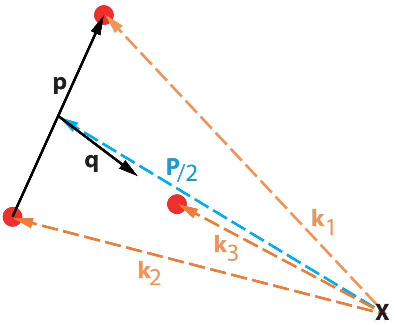

Figure 27: The Jacobi momenta are illustrated as defined in the text. The conserved total three-body momentum $\mathbf{X} = \mathbf{k}_1 + \mathbf{k}_3 + \mathbf{k}_3$ is not shown.

where $\mathbf{k}_i$ are the single-nucleon momenta. In the following, $\mathbf{p}$ and $\mathbf{q}$ ($\mathbf{p}'$ and $\mathbf{q}'$) denote the Jacobi momenta of the initial (final) state: $V_{3\mathrm{N}} = V_{3\mathrm{N}}(\mathbf{p}, \mathbf{q}, \mathbf{p}', \mathbf{q}')$. Hence, it is natural to perform the normal ordering (4.1) in this Jacobi basis. By expressing all single-particle momenta in terms of the Jacobi momenta and the two-body center-of-mass momentum $\mathbf{P} = \mathbf{k}_1 + \mathbf{k}_2 = \mathbf{k}'_1 + \mathbf{k}'_2$ we obtain for Eq. (4.1):

$$\overline{V}_{3\mathrm{N}} = \left(\frac{3}{2}\right)^3 \mathrm{Tr}_{\sigma_3}\mathrm{Tr}_{\tau_3} \int \frac{\mathrm{d}\mathbf{q}}{(2\pi)^3}\, n^{\tau_3}_{(3\mathbf{q}+\mathbf{P})/2}\, V^{\mathrm{as}}_{3\mathrm{N}} \,. \tag{4.3}$$

The calculation of the effective interaction (4.3) is challenging due to the complex structure of general 3N interactions. For the practical treatment of these, it is common to decompose the interactions in a Jj-coupled 3N partial-wave momentum basis of the form [207, 227]:

$$|pq\alpha\rangle := |pq;[(LS)J\,(ls)\,j]\,\mathcal{J}\,(Tt)\,\mathcal{T}\rangle \,. \tag{4.4}$$

Here, L, S, J, and T denote the relative orbital angular momentum, spin, total angular momentum, and isospin of particles 1 and 2 with relative momentum $p = |\mathbf{p}|$. The quantum numbers l, $s = 1/2$, j and $t = 1/2$ label the orbital angular momentum, spin, total angular momentum and isospin of particle 3 relative to the center-of-mass motion of particle 1 and 2. The 3N quantum numbers $\mathcal{J}$ and $\mathcal{T}$ define the total 3N angular momentum and isospin. We refer the reader to Ref. [227] for more details. In particular, 3N interactions do not depend on the projection quantum numbers $m_{\mathcal{J}}$ and for isospin-symmetric interactions also not on $m_{\mathcal{T}}$, hence we omit these labels in the basis states. Furthermore, only matrix elements with $\mathcal{T} = 3/2$, $T = 1$ and $m_T = -1\,(nn)$ contribute to neutron matter. In contrast to previous works, we evaluate Eq. (4.3) not directly in terms of operators but in this partial-wave basis. The basic ingredient of our normal-ordering framework are antisymmetrized 3N matrix elements normalized to the direct term of the form

$$\begin{aligned}\left\langle pq\alpha \,\middle|\, V^{\mathrm{as}}_{3\mathrm{N}} \,\middle|\, p'q'\alpha' \right\rangle &= \sum_{i=1}^{3} \left\langle pq\alpha \,\middle|\, (1 + P_{123} + P_{132}) V^{(i)}_{3\mathrm{N}} (1 + P_{123} + P_{132}) \,\middle|\, p'q'\alpha' \right\rangle , \\ &= 3 \left\langle pq\alpha \,\middle|\, (1 + P_{123} + P_{132}) V^{(1)}_{123} (1 + P_{123} + P_{132}) \,\middle|\, p'q'\alpha' \right\rangle ,\end{aligned} \tag{4.5}$$

where $(1 + P_{123} + P_{132})$ denotes the first term in the product representation of the 3N antisymmetrizer (2.67b), while the second term is the two-body antisymmetrizer $\mathscr{A}_{12}$ which is also present in the original NN force. $V^{(i)}_{3\mathrm{N}}$ is symmetric in exchanging $j, k \neq i \in \{1, 2, 3\}$ and represents a Faddeev component of the 3N interaction, i.e., $V_{3\mathrm{N}} = \sum_{i=1}^{3} V^{(i)}_{3\mathrm{N}}$ [227].

Previous normal-ordering frameworks for infinite matter have been developed for a specific 3N interaction, e.g., the leading chiral 3N interactions at N^{2}LO [43, 133, 141]. This makes it necessary to re-develop expressions for the effective interaction $\overline{V}_{3\mathrm{N}}$ for each new contribution and for each isospin asymmetry. Moreover, the treatment of more complicated 3N interactions, e.g., the subleading chiral 3N interactions at N^{3}LO [192, 193] becomes very tedious. In contrast, because the partial-wave decomposition of these 3N interactions has been completed recently [205], these contributions can be included in the present framework without additional efforts. Kai Hebeler provided us with the nonlocal 3N matrix elements up to N^{3}LO. By convention, an overall factor of $(2\pi)^6$ has to be multiplied.

Although $\overline{V}_{3\mathrm{N}}$ is an effective (two-body) interaction, there are important differences to free-space interactions: due to Galilean invariance, free-space NN interactions can only depend on the initial and final relative momenta $\mathbf{p}$ and $\mathbf{p}'$. Since the many-body rest frame defines a preferred frame the effective interaction $\overline{V}_{3\mathrm{N}}$ generally depends on the center-of-mass momentum $\mathbf{P}$. In particular, the interaction also depends on the angle between the momenta $\mathbf{p}, \mathbf{p}'$ and $\mathbf{P}$ (see also similarity to Ref. [232]), which leads to a much more complicated partial-wave structure than for free-space NN interactions. To avoid these complications, in previous works [43, 133, 141] the approximation $\mathbf{P} = 0$ has been imposed for the effective interaction. The flexibility of the present framework, however, allows to extend the calculation of $\overline{V}_{3\mathrm{N}}$ to finite momenta $\mathbf{P}$. To reduce the complexity of the effective interaction and to simplify its application in many-body calculations, we average the direction of $\mathbf{P}$ over all angles:

$$n^{\tau}_{(3\mathbf{q}+\mathbf{P})/2} \longrightarrow \Gamma^{\tau}(q,P) = \frac{1}{4\pi} \int \mathrm{d}\Omega_{\mathbf{P}}\, n^{\tau}_{(3\mathbf{q}+\mathbf{P})/2}\,, \tag{4.6}$$

with

$$\Gamma^{\tau}(q,P) = \begin{cases} 1 & (3q+P) \leqslant 2k_{\mathrm{F}}^{\tau}\,, \\ 0 & |3q-P| \geqslant 2k_{\mathrm{F}}^{\tau}\,, \\ \frac{1}{2}\int_{-1}^{\gamma} \mathrm{d}\cos\theta\, n^{\tau}_{(3\mathbf{q}+\mathbf{P})/2} & \text{else}\,, \end{cases} \tag{4.7}$$

and $\gamma = (4k_{F,\tau}^2 - 9q^2 - P^2)/(6Pq)$. Within this approximation, the effective interaction $\overline{V}_{3\mathrm{N}}$ acquires only an additional dependence on $P = |\mathbf{P}|$, whereas its partial-wave structure is still sufficiently simple so that it can straightforwardly be combined with free-space NN interactions in many-body calculations. Explicitly, we obtain for the partial-wave matrix elements normalized to the direct term:

$$\begin{aligned} \left\langle p(LS)JTm_T|\overline{V}^{\mathrm{as}}_{3\mathrm{N}}(P)|p'(L'S')JT'm_T\right\rangle = {} & \frac{(-i)^{L'-L}}{(4\pi)^2}\left(\frac{3}{4\pi}\right)^3 \int \mathrm{d}q\, q^2\, f_{\mathrm{R}}(p,q) f_{\mathrm{R}}(p',q) \\ & \times \sum_{\tau} \mathscr{C}^{\mathscr{T} m_T+\tau}_{T m_T 1/2 \tau}\, \mathscr{C}^{\mathscr{T} m_T+\tau}_{T' m_T 1/2 \tau}\, \Gamma^{\tau}(q,P) \\ & \times \sum_{\substack{l,j \\ \mathscr{J},\mathscr{T}}} \frac{2\mathscr{J}+1}{2J+1} \delta_{ll'}\delta_{jj'}\delta_{JJ'} \left\langle pq\alpha \middle| V^{\mathrm{as}}_{3\mathrm{N}} \middle| p'q\alpha' \right\rangle, \end{aligned} \tag{4.8}$$

where $f_{\mathrm{R}}(p,q)$ denotes the nonlocal 3N regulator. Following Ref. [27], we will use Eq. (2.70) with $n_{\mathrm{exp}} = 4$ but expressed in terms of the Jacobi momenta (4.2), $f_{\mathrm{R}}(p,q) = \exp[-((p^2+3q^2/4)/\Lambda_{3\mathrm{N}}^2)^4]$. Notice that we keep p, p' arbitrary throughout the derivation of Eq. (4.8), so the off-shell extrapolation employed, e.g., in Refs. [133, 141] is not needed. Because of the definition of the 3N matrix elements in Eq. (4.5), our effective potential, $\overline{V}^{\mathrm{as}}_{3\mathrm{N}} = \mathscr{A}_{123}\overline{V}_{3\mathrm{N}}\mathscr{A}_{123}$, involves two antisymmetrizers in contrast to the formal definition in Eq. (4.1). Note that, except for neutron and symmetry matter, off-diagonal matrix elements in spin and isospin quantum numbers S and T contribute to the effective potential. It depends, moreover, on the isospin projection m_T, a direct consequence of the isospin dependence of the occupation function

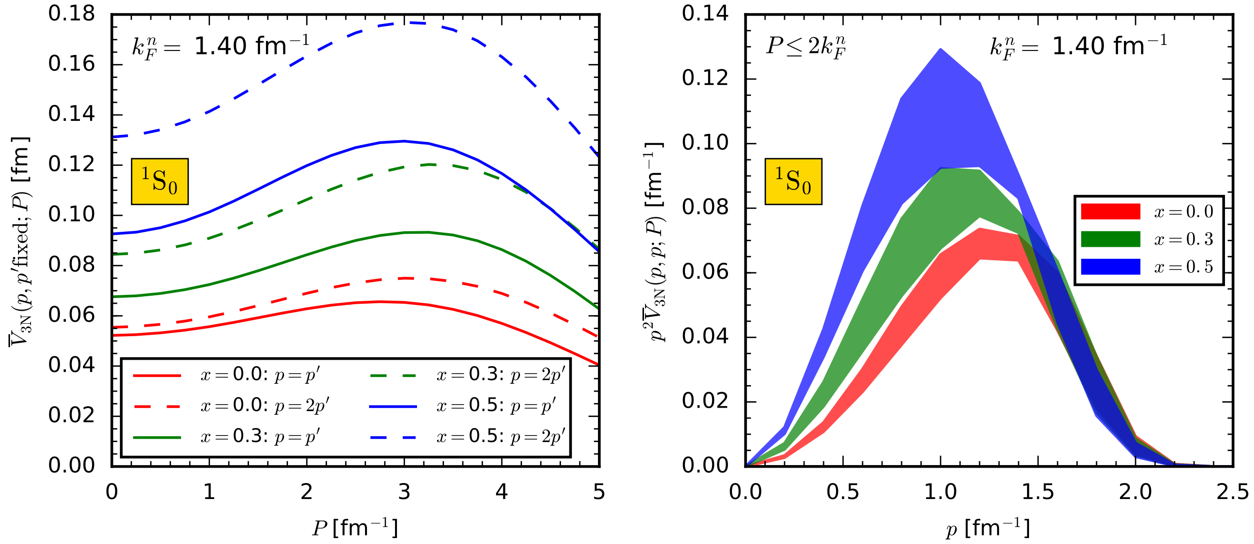

Figure 28: The left panel shows the matrix elements of the effective interaction $\overline{V}_{3\text{N}} = \overline{V}_{3\text{N}}/9$ in the $^1S_0$ channel with $m_T = -1\,(nn)$ as a function of the center-of-mass momentum P for fixed relative momenta, $p = p' = 1$ fm^{-1} (solid line) and $p = 2p' = 1$ fm^{-1} (dashed line), and proton fractions x at a neutron Fermi momentum $k_\text{F}^n = 1.4$ fm^{-1}. For the color code, see the legend in the right panel. The right panel shows the diagonal matrix elements times p^2 as a function of the relative momentum p. In the first- and second-order many-body contributions, the value of P is kinematically limited to $P \leqslant k_\text{F}^{\tau 1} + k_\text{F}^{\tau 2}$, so for $m_T = -1\,(nn)$ to $P \leqslant 2k_\text{F}^n$.

n_k^τ. Only in the case of neutron and symmetric nuclear matter, the interaction is diagonal in S, T, and also independent of the allowed m_T, because of isospin symmetry of chiral 3N forces up to N^{3}LO.

In Fig. 28, we present the results of some representative matrix elements of $\overline{V}_{3\text{N}} = \overline{V}_{3\text{N}}^{\text{as}}/9$ in the $^1S_0$ channel with $m_T = -1$ (nn) for different proton fractions x and a neutron Fermi momentum $k_\text{F}^n = 1.4$ fm^{-1}. The normalization of the matrix elements is chosen such that they can be directly combined with those of the free-space NN interaction for calculations in the Hartree-Fock approximation. The left panel shows the matrix elements at fixed relative momenta, $p = p' = 1$ fm^{-1} (solid line) and $p = 2p' = 1$ fm^{-1} (dashed line), respectively, as a function of P. Due to momentum conservation, the value of P is kinematically limited to $P \leqslant k_\text{F}^{\tau 1} + k_\text{F}^{\tau 2}$ for the first- and second-order contributions, depending on $m_T = \tau_1 + \tau_2$. The right panel shows the diagonal matrix elements with the measure p^2 as a function of the relative momentum for this range of center-of-mass momenta. The $P = 0$ results are in excellent agreement with Refs. [27, 43]. For $x = 0$, the matrix elements have a rather weak dependence on P. This suggests that neutron-matter results can be approximated reasonably well by the $P = 0$ approximation, as checked at the Hartree-Fock level in Ref. [43], while for increasing proton fractions the P dependence of the matrix elements becomes more pronounced.

For our practical calculations, we include 3N matrix elements up to $\mathscr{J} = 9/2$ for the calculation of the effective interaction $\overline{V}_{3\text{N}}$ via Eq. (4.8). We have checked that this basis space leads to well converged results for the effective potential up to partial-wave channels with $J \lesssim 4$ and include here $J \leqslant 6$. In addition, we find excellent agreement with the matrix elements of $\overline{V}_{3\text{N}}$ at $P = 0$ of Ref. [43] for neutron matter and with the corresponding results for symmetric nuclear matter [27] based on chiral 3N interactions at N^{2}LO. Following the general procedure in Refs. [205], we split the effective potential (4.8) at N^{3}LO for a given regulator, density, and proton fraction into twelve contributions where each corresponds to either one of the seven LECs c_1, c_3, c_4, c_D, c_E, C_S, and C_T, or a logic control parameter (one or zero). That is, the individual values of different Hamiltonians can be explored without needing to reconstruct the effective potential. In neutron matter, only two (nine) of those contributions are active up to $\mathrm{N^2LO}$ ($\mathrm{N^3LO}$). With the presented normal-ordering framework, we are prepared for $\mathrm{N^3LO}$ calculations of asymmetric matter once reliable fit values for c_D, c_E are available at this order [233, 234]. Such fits are subject of Sec. 5.4 within the developed Monte-Carlo framework.

4.2 Decomposed energy relations up to third order in MBPT

As already noted, our calculations of the energy per particle are based on a perturbation expansion up to third order around the Hartree-Fock state with contributions from NN and 3N forces up to $\mathrm{N^3LO}$. We partial-wave decompose the corresponding energy expressions as given in Sec. 1.3.1 and summarize here briefly the final expressions. Although neutron-matter calculations at $\mathrm{N^3LO}$ are particularly of interest, we keep the discussion general for arbitrary isospin asymmetries.

4.2.1 Hartree-Fock level

The (kinetic) energy density (1.23) of the unperturbated system reads

$$\frac{T^{(0)}}{V} = 2\int \frac{\mathrm{d}\mathbf{k}}{(2\pi)^3}\left[\frac{\mathbf{k}^2}{2m_p} n^p_{\mathbf{k}} + \frac{\mathbf{k}^2}{2m_n} n^n_{\mathbf{k}}\right] = \frac{3}{5}\left(\varepsilon^p_{\mathrm{F}}\, n_p + \varepsilon^n_{\mathrm{F}}\, n_n\right) , \tag{4.9}$$

with the Fermi energy $\varepsilon^i_{\mathrm{F}} = k^2_{\mathrm{F},i}/(2m_i)$ and the nucleon masses m_i. Since the mass splitting is less than one percent, we use the average nucleon mass, i.e., $m_i = m$. At nuclear saturation density, $n_0 = 0.16\ \mathrm{fm}^{-3}$, the kinetic energy per particle is $E/N(n_0) \simeq 36.0$ MeV ($E/A(n_0) \simeq 22.7$ MeV) in neutron matter (symmetric matter). Contributions from NN and 3N forces at the normal-ordered two-body level are included in terms of the effective potential (1.45c) and Eq. (4.8), respectively. Decomposing the NN Hartee-Fock relation (1.24) and inserting the effective NN potential leads to

$$\begin{aligned}\frac{E^{(1)}_{\mathrm{NN}}}{V} + \frac{E^{(1)}_{\overline{\mathrm{3N}}}}{V} = \frac{E^{(1)}_{\mathrm{NN}+\overline{\mathrm{3N}}}}{V} \simeq \frac{1}{4\pi^3}\int \mathrm{d}p\, p^2 \int \mathrm{d}P\, P^2 \sum_{m_T} f_{m_T}(\mathbf{p},\mathbf{P}) \sum_{L,S,J,T} (2J+1)\left(1-(-1)^{L+S+T}\right) \\ \times \left\langle p(LS)JTm_T \middle| V_{\mathrm{NN}} + \overline{V}^{\mathrm{as}}_{\mathrm{3N}}(P)/9 \middle| p(LS)JTm_T \right\rangle ,\end{aligned} \tag{4.10}$$

where the combinatorial factor ($\zeta = 1/9$) of the effective interaction $\overline{V}^{\mathrm{as}}_{\mathrm{3N}}$ is discussed in detail in Sec. 1.3.2. Note that since the matrix elements in Eq. (4.5) involve two instead of one antisymmetrizer, a relative conversion factor of 3 is required for the comparison to Eq. (1.46) and Ref. [43]. Furthermore, we have introduced the phase-space function $f_{m_T}(\mathbf{p},\mathbf{P}) = \int_{-1}^{1} \mathrm{d}\cos\theta_{\mathbf{P},\mathbf{p}}\, n^{\tau_1}_{\mathbf{P}/2+\mathbf{p}}\, n^{\tau_2}_{\mathbf{P}/2-\mathbf{p}}$, which depends only on the two-body isospin projection quantum number $m_T = \tau_1 + \tau_2$ because the integrand is symmetric in the isospin indices τ_1 and τ_2. It is important to constrain the general phase-space integral to the nonvanishing region of the Fermi–Dirac distributions,

$$I = \int_{-1}^{+1} \mathrm{d}\cos\theta_{\mathbf{p},\mathbf{P}}\, n^{\tau_1}_{\mathbf{p}+\mathbf{P}/2}\, n^{\tau_2}_{\mathbf{p}-\mathbf{P}/2}\, f(\cos(\theta_{\mathbf{p},\mathbf{P}})) = \Theta(x_{\mathrm{max}} - x_{\mathrm{min}}) \int_{x_{\mathrm{min}}}^{x_{\mathrm{max}}} \mathrm{d}\cos\theta_{\mathbf{p},\mathbf{P}}\, f(\cos(\theta_{\mathbf{p},\mathbf{P}})) . \tag{4.11}$$

In terms of $D^{\pm}_i(p,P) \equiv (k^2_{F,\tau_i} - P^2/4 - p^2)/(\pm pP)$, we obtain the limits,

$$x_{\mathrm{min}} = \max\left[-1.0, \min[+1.0, D^-_2(p,P)]\right] \quad \text{and} \quad x_{\mathrm{max}} = \min\left[+1.0, \max[-1.0, D^+_1(p,P)]\right] . \tag{4.12}$$

Since $f(\cos(\theta_{\mathbf{p},\mathbf{P}})) = 1$ at the Hartree-Fock level, this leads to $f_{m_T}(p,P) = (x_{\mathrm{max}} - x_{\mathrm{min}})\Theta(x_{\mathrm{max}} - x_{\mathrm{min}})$.

We decompose also the (exact) 3N Hartree-Fock relation (1.48) in partial waves [167],

$$
\begin{aligned}
\frac{E_{3\mathrm{N}}^{(1)}}{V} &= \frac{1}{3(2\pi)^7} \iiint \mathrm{d}p\, \mathrm{d}q\, \mathrm{d}z_1\, p^2 q^2 \sum_{\substack{T,T',M_T\\ \tau_1,\tau_2,\tau_3}} N(p,q,z_1,\tau_1,\tau_2,\tau_3)\, \mathscr{C}_{1/2\tau_2 1/2\tau_3}^{TM_T} \mathscr{C}_{1/2\tau_2 1/2\tau_3}^{T'M_T} \\
&\times \frac{1}{(4\pi)^2} \sum_{\alpha,\alpha'} \delta_{S,S'} \sum_{\bar{L},\mathscr{S},\mathscr{L},\mathscr{J}} \hat{\mathscr{S}}\hat{\mathscr{L}}\hat{\mathscr{J}} \sqrt{\hat{J}\hat{j}\hat{J}'\hat{j}'\hat{L}\hat{L}'\hat{l}\hat{l}'}(-1)^{l+l'+\mathscr{L}}\, \mathscr{C}_{l0l'0}^{\bar{L}0} \mathscr{C}_{L0L'0}^{\bar{L}0} P_{\bar{L}}(\hat{\mathbf{p}}\cdot\hat{\mathbf{q}}) \\
&\times \mathscr{C}_{TM_T 1/2\tau_1}^{\mathscr{T}M_T+\tau_1} \mathscr{C}_{T'M_T 1/2\tau_1}^{\mathscr{T}M_T+\tau_1} \langle pq\alpha|(1+P_{123}+P_{132})V_{123}^{(1)}(1+P_{123}+P_{132})|pq\alpha'\rangle \\
&\times \begin{Bmatrix} L & L' & \bar{L} \\ l' & l & \mathscr{L} \end{Bmatrix} \begin{Bmatrix} L & S & J \\ l & 1/2 & j \\ \mathscr{L} & \mathscr{S} & \mathscr{J} \end{Bmatrix} \begin{Bmatrix} L' & S & J' \\ l' & 1/2 & j' \\ \mathscr{L} & \mathscr{S} & \mathscr{J} \end{Bmatrix} \left(1-(-1)^{L+S+T}\right),
\end{aligned}
\tag{4.13}
$$

with $\{\,\cdot\,\}$ being $6J$- and $9J$-symbols, respectively, and the Legendre polynomials $P_L(\cos\theta)$. Moreover, we use the short-hand notations, e.g., $\hat{J} := 2J+1$ and additional hats to indicate unit vectors. The phase-space function reads

$$
\begin{aligned}
N(p,q,z_1,\tau_1,\tau_2,\tau_3) = \iiint & \mathrm{d}X\, X^2\, \mathrm{d}z_2\, \mathrm{d}\varphi\, \Theta\left(k_{\mathrm{F},\tau_1}^2 - \left[\frac{X^2}{9} + q^2 + \frac{2}{3}Xqf(z_1,z_2,\varphi)\right]\right) \\
& \times \Theta\left(k_{\mathrm{F},\tau_2}^2 - \left[\frac{X^2}{9} + p^2 + \frac{1}{4}q^2 + \frac{2}{3}Xpz_2 - \frac{1}{3}Xqf(z_1,z_2,\varphi) - pqz_1\right]\right) \\
& \times \Theta\left(k_{\mathrm{F},\tau_3}^2 - \left[\frac{X^2}{9} + p^2 + \frac{1}{4}q^2 - \frac{2}{3}Xpz_2 - \frac{1}{3}Xqf(z_1,z_2,\varphi) + pqz_1\right]\right),
\end{aligned}
\tag{4.14}
$$

where we introduce

$$
f(z_1,z_2,\varphi) := z_1 z_2 + \sqrt{1-z_1^2}\sqrt{1-z_2^2}\cos\varphi\,. \tag{4.15}
$$

By comparing the 3N Hartree-Fock energy (4.13) (which is exact up to partial-wave convergence) to the corresponding result obtained using the effective potential, i.e., $E_{3N}^{(1)}/V$ in Eq. (4.10), we can directly assess the quality of the approximation, $P=0$ or P-averaging, employed in Eq. (4.8).

As an benchmark of the partial-wave convergence, we compare in Fig. 29 the Hartree-Fock contributions of 3N forces to the energy per particle based on Eq. (4.13) with different truncations in $\mathscr{J}$ (following Ref. [167]) to results derived directly from evaluating the operatorial structure of the N^{2}LO 3N interactions (see Refs. [27, 43, 235]) for neutron matter (left panel) and for symmetric nuclear matter (right panel). These two independent calculations test directly the convergence of the partial-wave decomposition and should provide identical results in the limit $\mathscr{J} \leqslant \mathscr{J}_{\max} \to \infty$ up to numerical uncertainties. The results shown in Fig. 29 are exemplarily based on the Hamiltonian with SRG resolution scale $\lambda = 2\ \mathrm{fm}^{-1}$ and 3N cutoff $\Lambda_{3\mathrm{N}} = 2\ \mathrm{fm}^{-1}$ in Ref. [27], including all contributions with $J \leqslant 6$ for each 3N partial wave. We find again excellent agreement of the results for $\mathscr{J} \leqslant 9/2$, with a deviation of less than 100 keV at saturation density for neutron matter and symmetric nuclear matter. Hence, for the following we will use this basis space for the calculation of the effective interaction $\overline{V}_{3\mathrm{N}}^{\mathrm{as}}$. For completeness, we note that a similar good convergence pattern with N^{3}LO 3N forces in neutron and symmetric matter has been observed in Ref. [205] by comparing to the semianalytic calculations in Refs. [108, 140]. Due to the fast partial-wave convergence, Eq. (4.13) covers several advances of previous works along the Hartree-Fock energy of asymmetric matter and 3N forces up to N^{3}LO in one expression [27, 36, 43, 108, 140].

In Fig. 30, we compare results for the 3N Hartree-Fock energies based on the different approximations on the effective interaction (4.8). The three panels show the energy difference to the exact Hartree-

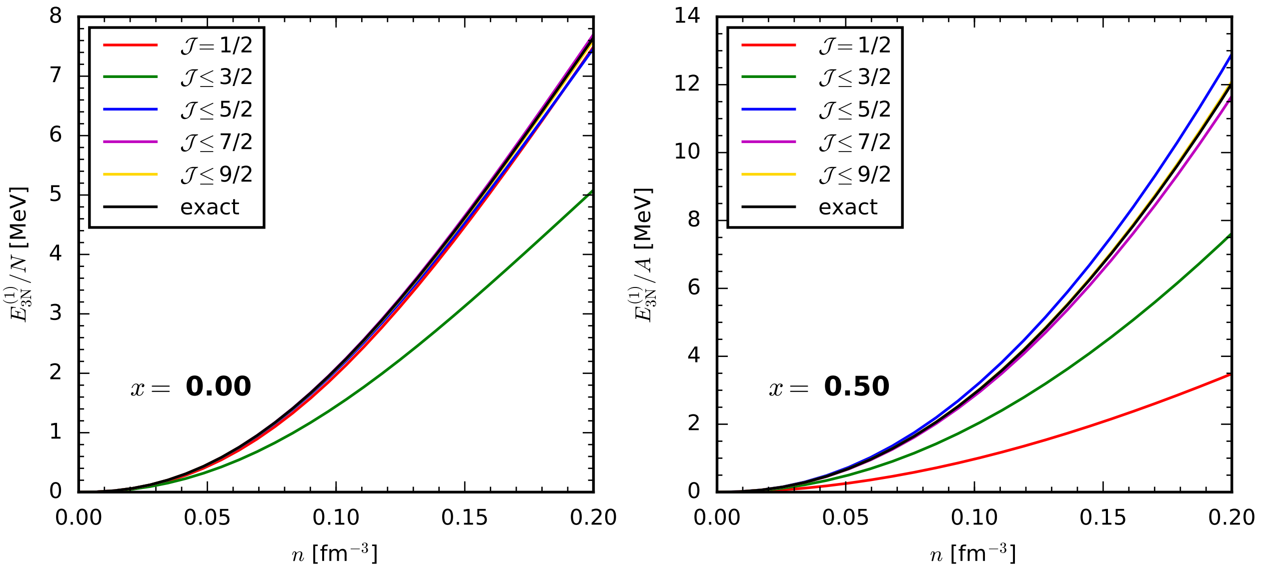

Figure 29: Exemplary partial-wave convergence of the N^{2}LO 3N contributions at the Hartree-Fock level in neutron matter (left panel) and symmetric matter (right panel) for the Hamiltonian in Ref. [27] with $\lambda/\Lambda_{3N} = 2.0/2.0\,\text{fm}^{-1}$. In neutron matter the contributions for $\mathscr{J} > 5/2$ are very small, so the individual lines are nearly indistinguishable.

Fock result (up to partial-wave convergence) obtained with Eq. (4.13) for proton fraction $x = 0$ (left panel), $x = 0.3$ (center panel), and $x = 0.5$ (right panel). The effective interaction based on the $P = 0$ approximation reproduces the exact results well up to $n \simeq (0.13-0.23)\,\text{fm}^{-3}$, depending on the proton fraction. For higher densities the deviation systematically increases, indicating a breakdown of the $P = 0$ approximation. In contrast, the results based on the P-average approximation agree well with the exact results over the entire density range.

4.2.2 Second-order contributions

According to Eq. (1.25) the second-order contribution to the energy density reads

$$\frac{E^{(2)}_{\text{NN}+\overline{3\text{N}}}}{V} = \frac{1}{16}\prod_{i=1}^{4}\left[\text{Tr}_{\sigma_i}\text{Tr}_{\tau_i}\int\frac{d\mathbf{k}_i}{(2\pi)^3}\right]\left|\left\langle 12\,\middle|\,V^{(2)}_{\text{as}}\,\middle|\,34\right\rangle\right|^2\frac{n^{\tau_1}_{\mathbf{k}_1}n^{\tau_2}_{\mathbf{k}_2}(1-n^{\tau_3}_{\mathbf{k}_3})(1-n^{\tau_4}_{\mathbf{k}_4})}{\varepsilon^{\tau_1}_{\mathbf{k}_1}+\varepsilon^{\tau_2}_{\mathbf{k}_2}-\varepsilon^{\tau_3}_{\mathbf{k}_3}-\varepsilon^{\tau_4}_{\mathbf{k}_4}} \\ \times(2\pi)^3\delta(\mathbf{k}_1+\mathbf{k}_2-\mathbf{k}_3-\mathbf{k}_4)\,. \tag{4.16}$$

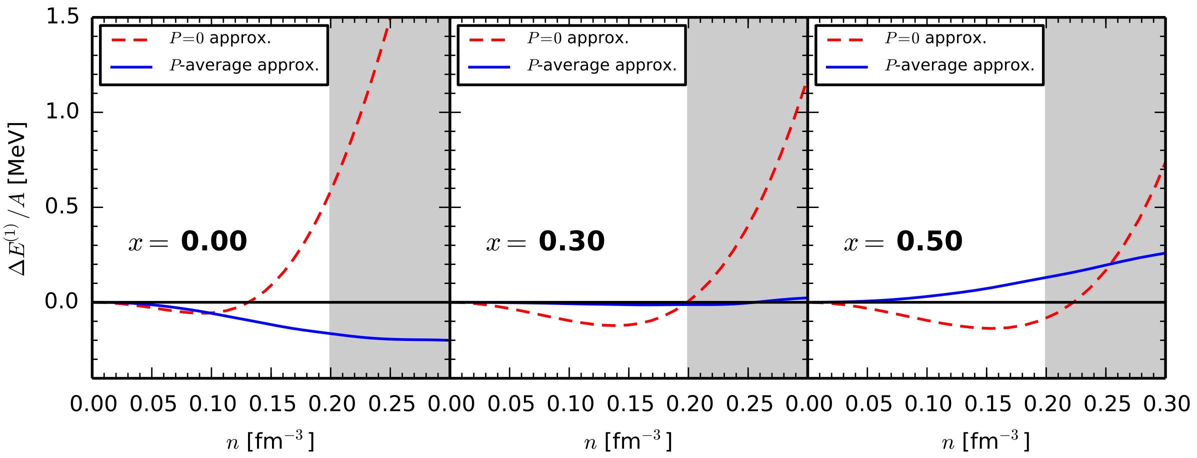

Figure 30: Comparison of 3N Hartree-Fock energies based on the Hamiltonian in Ref. [27] with $\lambda/\Lambda_{\mathrm{3N}} = 2.0/2.0\,\mathrm{fm}^{-1}$ for the $P = 0$ (red dashed) and P-average approximation (blue solid line) on the effective interaction $\overline{V}^{\mathrm{as}}_{\mathrm{3N}}$. Results are shown as difference to the exact Hartree-Fock energy for three proton fractions, $x = 0$ (left panel), $x = 0.3$ (middle panel), and $x = 0.5$ (right panel). The $P = 0$ values give larger deviations above saturation density, whereas the P-average approximation behaves more systematic over the entire density range.

Expanding in partial waves and performing the spin sums leads then to (see Refs. [43, 235])

$$
\begin{aligned}
&\sum_{S,S' M_S,M_{S'}} \langle \mathbf{p} S M_S T M_T | V_{\mathrm{as}}^{(2)} | \mathbf{p}' S' M_{S'} T' M_T \rangle \, \langle \mathbf{p}' S' M_{S'} T'' M_T | V_{\mathrm{as}}^{(2)} | \mathbf{p} S M_S T''' M_T \rangle \\
&\quad = (4\pi)^2 \sum_{S,S'} (-1)^{S+S'} \sum_{\bar{L}} P_{\bar{L}}(\cos\theta_{\mathbf{p},\mathbf{p}'}) \sum_{L,L',\tilde{L},\tilde{L}'} \sum_{J,\tilde{J}} i^{L-L'-\tilde{L}+\tilde{L}'} (-1)^{\bar{L}+\tilde{L}'+L'} \\
&\quad \times \mathscr{C}^{\bar{L}0}_{L'0\tilde{L}'0} \mathscr{C}^{\bar{L}0}_{L0\tilde{L}0} \begin{Bmatrix} L & S & J \\ \tilde{J} & \bar{L} & \tilde{L} \end{Bmatrix} \begin{Bmatrix} \tilde{L}' & S' & \tilde{J} \\ J & \bar{L} & \bar{L}' \end{Bmatrix} \\
&\quad \times (2J+1)(2\tilde{J}+1) \sqrt{(2L+1)(2L'+1)(2\tilde{L}+1)(2\tilde{L}'+1)} \\
&\quad \times \langle k'(L'S')J T'' M_T | V_{\mathrm{as}}^{(2)} | k(LS)J T''' M_T \rangle \, \langle k(\tilde{L}S)\tilde{J} T M_T | V_{\mathrm{as}}^{(2)} | k'(\tilde{L}'S')\tilde{J} T' M_T \rangle \\
&\quad \times \left[1-(-1)^{\tilde{L}+S+T}\right]\left[1-(-1)^{L'+S'+T''}\right]\left[1-(-1)^{\tilde{L}'+S'+T'}\right]\left[1-(-1)^{L+S+T'''}\right].
\end{aligned}
\tag{4.17}
$$

Here, the partial-wave interaction matrix elements are given by $V_{\mathrm{as}}^{(2)} = V_{\mathrm{NN}} + \overline{V}^{\mathrm{as}}_{\mathrm{3N}}(P)/3$ (see Ref. [43]), resulting from the normal-ordered two-body part of 3N forces. The sums over the single-particle isospin quantum numbers have to be performed explicitly, because the Fermi-Dirac distribution functions break the isospin symmetry for asymmetric matter. We stress that in general the effective interaction $\overline{V}_{\mathrm{3N}}$ couples different spin and isospin channels because of the isospin dependence of the Fermi-Dirac distribution functions in Eq. (4.3). The second-order contribution (4.16) involves additional phase-space integrals of the form

$$
\begin{aligned}
I &= \int_{-1}^{+1} \mathrm{d}\cos\theta_{\mathbf{p},\mathbf{P}} \left(1 - n^{\tau_1}_{\mathbf{p}+\mathbf{P}/2}\right)\left(1 - n^{\tau_2}_{\mathbf{p}-\mathbf{P}/2}\right) f(\cos(\theta_{\mathbf{p},\mathbf{P}})) \\
&= \Theta(x_{\max} - x_{\min}) \int_{x_{\min}}^{x_{\max}} \mathrm{d}\cos\theta_{\mathbf{p},\mathbf{P}}\, f(\cos(\theta_{\mathbf{p},\mathbf{P}})) .
\end{aligned}
\tag{4.18}
$$

Again, in terms of $D_i^{\pm}(p,P) \equiv (k_{F,\tau_i}^2 - P^2/4 - p^2)/(\pm pP)$, we obtain the limits [230],

$$x_{\min} = \max\left[-1.0, \min[+1.0, D_1^{+}(p,P)]\right] \quad \text{and} \quad x_{\max} = \min\left[+1.0, \max[-1.0, D_2^{-}(p,P)]\right]. \qquad (4.19)$$

For the evaluation of Eq. (4.16), we need to calculate the single-particle energies $\varepsilon_{\mathbf{k}}^{\tau}$, which are in general determined by the solution of the Dyson equation $\varepsilon_{\mathbf{k}}^{\tau} = k^2/(2m) + \operatorname{Re}\Sigma^{\tau}(k, \varepsilon_{\mathbf{k}}^{\tau})$. In our calculations, we either use a free spectrum or compute the self-energy in the Hartree-Fock approximation, $\Sigma_1^{(1)} = \frac{1}{2}\sum_i \langle 1i|\mathscr{A}_{12}V_{\mathrm{NN}}|1i\rangle$, and average over the external spin quantum numbers. Moreover, we average the isospin dependence, weighted by the proton fraction x [27, 43],

$$\begin{aligned}\Sigma^{(1)}(k_1,x) = \frac{1}{2\pi}\int \mathrm{d}k_2\, k_2^2 \int \mathrm{d}\cos\theta_{\mathbf{k}_1\mathbf{k}_2} &\sum_{T,M_T,\tau_1,\tau_2} w_{\tau_1}(x)\, n_{\mathbf{k}_2}^{\tau_2} \left(\mathscr{C}_{1/2\tau_1 1/2\tau_2}^{TM_T}\right)^2 \\ &\times \sum_{JSL}(2J+1)\left(1-(-1)^{L+S+T}\right) \\ &\times \left\langle k_{12}/2(LS)JTM_T \middle| V_{\mathrm{NN}} + \overline{V}_{3\mathrm{N}}^{\mathrm{as}}(P)/6 \middle| k_{12}/2(LS)JTM_T \right\rangle,\end{aligned} \qquad (4.20)$$

with $k_{12} = |\mathbf{k}_1 - \mathbf{k}_2|$ and the combinatorial factor ($\zeta = 1/6$) of the effective interaction $\overline{V}_{3\mathrm{N}}^{\mathrm{as}}$ as discussed in App. A. Notice again the additional conversion factor of 3 due to the two antisymmetrizers. The isospin weighting factor w_τ is given by

$$w_\tau(x) = \begin{cases} x & \tau = +\frac{1}{2}\ (\text{proton}), \\ 1-x & \tau = -\frac{1}{2}\ (\text{neutron}). \end{cases} \qquad (4.21)$$

In this approximation the single-particle energies are $\varepsilon(k,x) = k^2/(2m) + \Sigma^{(1)}(k,x)$ for a certain proton fraction x with m being the average nucleon mass. In case of the free spectrum, we apply only the kinetic energy as single-particle energy. In neutron and symmetric matter, the isospin weighting is equivalent to the ones in Ref. [27, 43] but includes also charge-symmetry breaking. We consider the difference in the results due to the two spectra as an uncertainty estimate of neglected higher-order contributions in MBPT. In future calculations, one may keep the single-particle energy (iso)spin-dependent and may use a self-consistent spectrum, e.g., as in Refs. [107, 111, 112] (at second order).

We have already pointed out that the residual 3N contribution (1.50), $E_{3\mathrm{N}}^{(2)}/V$, cannot be included using the effective NN potential and is thus neglected in this chapter.

4.2.3 Third-order hole-hole and particle-particle contributions

We also consider the third-order hole-hole and particle-particle contributions in Eqs. (1.29a) and (1.29c), respectively. Following Ref. [27], these can be included exactly by a modified second-order calculation

$$\frac{E_{\alpha=1,3}^{(3)}}{V} \equiv +\frac{1}{4}\sum_{\substack{ij\\ab}} \frac{\langle ij|V_{\mathrm{as}}^{(2)}|ab\rangle\, \langle ab|V_{\mathrm{resum}}^{(\alpha)}|ij\rangle}{D_{ijab}}, \qquad (4.22)$$

where one vertex is replaced by the resumed interaction,

$$\langle ab|V^{(\alpha=1)}_{\text{resum}}|ij\rangle = \frac{1}{2}\sum_{kl} \frac{\langle ab|V^{(2)}_{\text{as}}|kl\rangle\,\langle kl|V^{(2)}_{\text{as}}|ij\rangle}{D_{klab}}\,, \tag{4.23a}$$

$$\langle ab|V^{(\alpha=3)}_{\text{resum}}|ij\rangle = \frac{1}{2}\sum_{cd} \frac{\langle ab|V^{(2)}_{\text{as}}|cd\rangle\,\langle cd|V^{(2)}_{\text{as}}|ij\rangle}{D_{ijcd}}\,. \tag{4.23b}$$

We decompose Eqs. (4.23) into partial waves and carry out the sums over the intermediate states weighted by the corresponding Fermi-Dirac distributions as well as the energy denominator in the angle-averaging approximation [27, 107]. With contributions from NN and 3N forces at the normal-ordered two-body level, the included (total) third-order energy density reads then $E^{(3)}_{\text{NN}+\overline{3\text{N}}}/V = E^{(3)}_1/V + E^{(3)}_3/V$.

However, this procedure cannot be employed to the particle-hole expression (1.29b), so an explicit partial-wave decomposition of the energy expression is required. Hence, we neglect this term similar to, e.g., Refs. [27, 28, 140]. On the other hand, all third-order contributions (including the particle-hole diagram) have been partial-wave decomposed [107, 111, 112], without providing all (presumably) lengthy final expressions in a closed form. As we discuss in Sec. 5, the developed Monte-Carlo framework, on the contrary, allows a straightforward calculation of (in principle) any energy diagram in perturbation theory.

4.3 Many-body convergence: MBPT vs. SCGF

Based on the MBPT machinery described in the previous sections, we are now prepared for improved third-order calculations of asymmetric matter based on chiral NN and 3N forces up to N^{3}LO at the normal-ordered two-body level. As a first step, we study pure neutron matter since c_D, c_E do not contribute (see Sec. 2.2) and determine the (many-body) convergence. A practical rate of convergence at low-enough order is, in general, crucial when working with perturbation theory (see Sec. 3). While this could also be addressed in an in-medium Weinberg eigenvalue analysis [222], we follow here a different approach for infinite-matter calculations.

We assess the many-body convergence order-by-order by comparing to a *nonperturbative* approach, the method of self-consistent Green's functions (SCGF). In this method, the energy per particle is calculated nonperturbatively via knowledge of a dressed one-body Green's function [236]. The energy is obtained in the so-called ladder approximation, where an *infinite* sum of particle-particle and hole-hole diagrams is performed [143, 237]. Similar to the discussed MBPT calculations, particle-hole contributions are neglected. The SCGF approach has been recently extended to self-consistently include 3N forces [134]. In this extension, the ladder resummation and the self-energy are redefined incorporating normal-ordered 3N terms with respect to a dressed reference state. Residual 3N contributions are neglected as well in this approach, allowing a direct comparison to our results in MBPT. In this extended SCGF approach, the modified sum rule to obtain the total energy density in neutron matter reads [134]:

$$\frac{E_{\text{SCGF}}}{V} = 2\int \frac{\mathrm{d}\mathbf{k}}{(2\pi)^3}\int \frac{\mathrm{d}\omega}{2\pi}\frac{1}{2}\left\{\frac{k^2}{2m}+\omega\right\}A(k,\omega)f(\omega) - \frac{\langle W\rangle}{2}\,, \tag{4.24}$$

where $f(\omega)$ corresponds to the Fermi-Dirac distribution function. $A(k,\omega)$ is the spectral function; this quantity gives the probability of adding or removing a particle with momentum k which causes an excitation in energy $\mathrm{d}\omega$ in the many-body system. $\langle W\rangle$ is the expectation value of the 3N operator (see Ref. [141] for details). The present implementation of SCGF is not capable of treating the appearance of pairing below a critical temperature, for this reason calculations are always performed at finite T. The pairing instability does not affect the MBPT calculations because the energy diagrams are evaluated directly, for which the pairing singularity is integrable. The zero-temperature results in SCGF are extrapolated using the Sommerfeld expansion [143]. In this expansion, the energy can be written as a quadratic expansion in terms of $T/\varepsilon_{\mathrm{F}}$, where ε_{F} is the Fermi energy, as long as $T/\varepsilon_{\mathrm{F}} \ll 1$. A more sophisticated computational method to numerically extrapolate self-energies, spectral functions and thermodynamical properties from finite to zero temperature has been recently presented in Ref. [238]. The results using the framework of SCGF have been calculated by Arianna Carbone. A detailed review on SCGF can be found in Ref. [239].

Therefore, we extend the improved normal-ordering method of Sec. 4.1 to finite temperatures. The effective interaction $\overline{V}_{3\mathrm{N}}^{\mathrm{as}}$ in Eq. (4.1) is then evaluated using the general Fermi-Dirac distribution function. Given a total density n and temperature T in neutron matter, the chemical potential $\mu(n)$ is determined by solving the nonlinear density relation (1.54), e.g., with Brent's method,

$$n(\mu) = \frac{1}{\pi^2} \int_0^\infty \mathrm{d}k\, k^2\, n_{\mathbf{k}}(\mu)\,, \qquad \text{with} \qquad n_{\mathbf{k}}(\mu) = \frac{1}{\exp\left[\frac{\epsilon(k)-\mu}{T}\right]+1}\,. \tag{4.25}$$

We use here the free single-particle energy, i.e., $\varepsilon_{\mathbf{k}} = \mathbf{k}^2/(2m)$. Higher-order corrections to the self energy include contributions from the effective NN potential itself and would require thus an involved self-consistent solution for the spectrum. It has been found in Ref. [141] that this is only relevant for the energy per particle in neutron matter when going to higher densities. Such high densities are not considered in this work, but it will be important to check this approximation at high temperatures.

In contrast to our MBPT calculations, the SCGF code only implements the effective NN potential $\overline{V}_{3\mathrm{N}}^{\mathrm{as}}$ within the $\mathbf{P}=0$ approximation. Since we aim a benchmark of MBPT to this nonperturbative method, we focus here on this common approximation for both, MBPT and SCGF. It is shown in Sec. 4.2.1 that the resulting 3N Hartree-Fock energies are in reasonable agreement, in particular, below saturation density. Finally, we note again that once reasonable fit values for c_D and c_E are available at N^{3}LO, the described methods can be directly applied beyond neutron matter (see Sec. 5.4).

In the following, we consider unevolved NN and 3N forces up to N^{3}LO and calculate the energy per particle of infinite neutron matter in the frameworks of MBPT and SCGF. So far, in most calculations of nuclear matter NN and 3N forces were not included consistently up to the same order in the chiral expansion due to the complex structure of 3N forces at N^{3}LO [192, 193]. Only recently an efficient partial-wave decomposition of these contributions was developed in Ref. [205]. In Refs. [108, 140] the N^{3}LO 3N contributions were evaluated semianalytically for neutron matter and symmetric nuclear matter in Hartree-Fock approximation. It was in some sense unexpected that the subleading 3N forces provide significant contributions to the energy. The findings suggest that it is mandatory to investigate these contributions more systematically by including higher-order effects in the many-body expansion.

Note that, considering only NN and 3N forces at N^{3}LO is still not fully consistent in the chiral expansion as 4N forces also contribute at this order. In Refs. [108, 140, 212], however, it was demonstrated that the 4N contributions to the energy in neutron matter in the Hartree-Fock approximation are very small compared to the overall uncertainty. At saturation density, $E_{4\mathrm{N}}/N \sim -180$ keV in neutron matter and $E_{4\mathrm{N}}/A \sim -(180-230)$ keV in symmetric matter according to Refs. [108, 140] only lead to a small shift for the N^{3}LO Hamiltonians. Consequently, if not stated otherwise, we neglect 4N (and higher-body) contributions and focus on the improvement of subleading 3N forces.

We show in Fig. 31 the total energy per particle as a function of density in neutron matter at zero temperature. From left to right, the first row shows the results for the N^{3}LO NN potentials EM 500 MeV [154], EGM 450/500 MeV, and EGM 450/700 MeV [67] with leading N^{2}LO 3N forces. The momentum scales attached to the potentials correspond to different regulator cutoffs: first, the cutoff in the Lippmann-Schwinger equation and second, if not dimensionally regularized (DR), the cutoff in the 2π-exchange

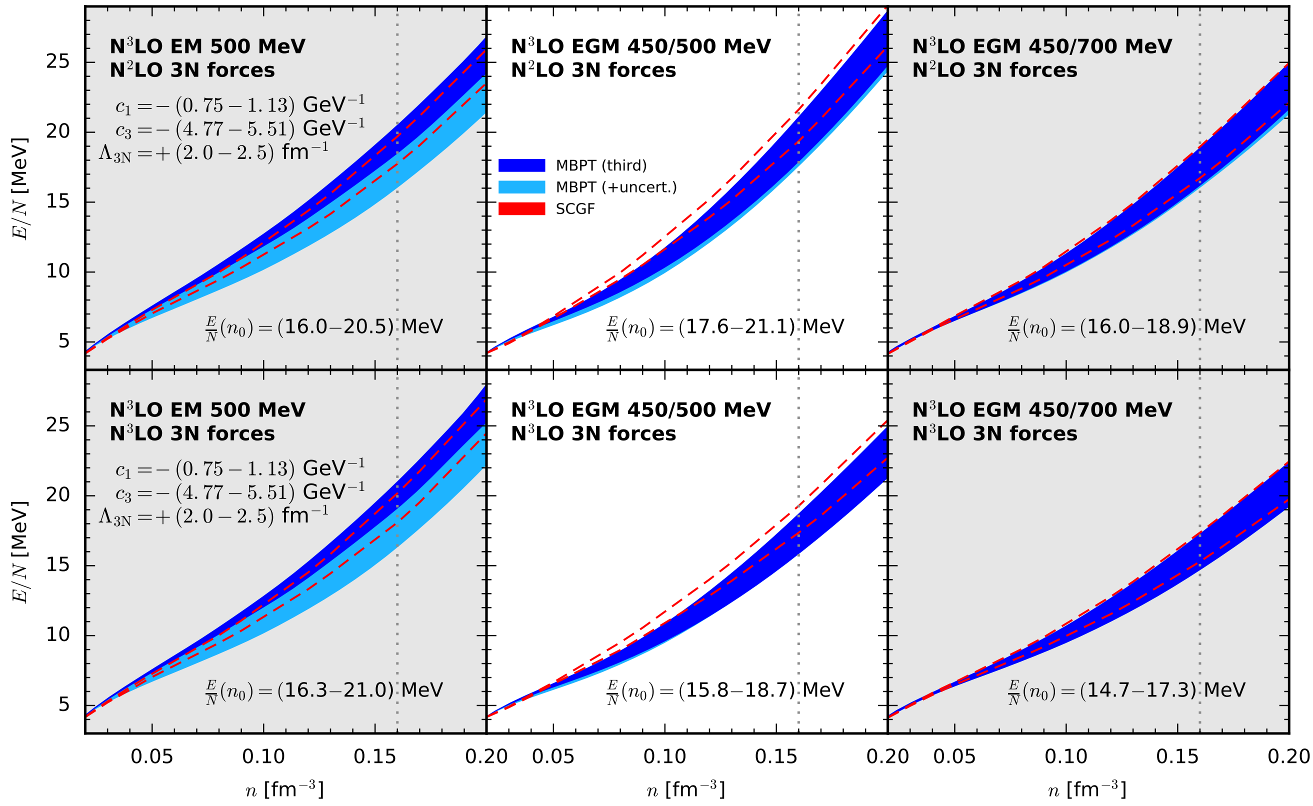

Figure 31: The energy per particle in neutron matter for three different N^{3}LO NN potentials with N^{2}LO (top row) and N^{3}LO (bottom row) 3N forces, respectively. The uncertainty bands are due to the given c_i and 3N cutoff variation. For the MBPT results, we consider in addition the maximum range of third-order calculations with a free and a Hartree-Fock spectrum (dark-blue band) plus the change from a second-order calculation with a Hartree-Fock spectrum, which is indicated by the light-blue extension of the pure third-order uncertainty band. The two bands together define the total uncertainty estimate of MBPT. The region between the two red-dashed lines denotes the uncertainty band of the SCGF method, which we do not fill for a better view. In each panel the energy range at saturation density obtained in MBPT is given.

spectral-function regularization (SFR, see also Sec. 2.1). Analogously, the second row shows the results for the same NN potentials but including 3N forces up to N^{3}LO. We consider two sources of uncertainties: from the chiral Hamiltonian and from considering only a finite order in MBPT. As stated in Fig. 31, the theoretical uncertainties due to the Hamiltonian are estimated by parameter variation in the 3N forces, i.e., the cutoff Λ_{3N} and the low-energy constants c_1 and c_3. The c_i values need to be refit at each chiral order, however, to investigate the net effect of N^{3}LO forces, we take here solely the c_i-range recommended for N^{3}LO calculations [95]. In addition to the uncertainties in the Hamiltonian, we estimate the neglected higher-order contributions in the many-body expansion by varying the single-particle energies at third order using a free and a Hartree-Fock spectrum. These bands are colored in dark blue in Fig. 31. Moreover, following Ref. [140] we include the results at second order in MBPT using a Hartree-Fock spectrum to the uncertainty estimate. This extension of the pure third-order equation of state is indicated by light-blue bands. In summary, for a given Hamiltonian, we perform in total three calculations in MBPT: two third-order calculations using the two single-particle spectra and a second-order calculation using a Hartree-Fock spectrum. Light- and dark-blue bands together characterize the total uncertainty estimate of MBPT in each panel, where the actual energy range is given at saturation density $n_0 = 0.16$ fm^{-3} (dashed vertical line).

Let us focus on the results with leading 3N forces, as shown in the first row of Fig. 31. The qualitative description does not change for the calculations with subleading 3N forces (second row in Fig. 31). Whereas the results for the two EGM potentials are almost independent of the many-body details, the effects of the variation of spectra and many-body order in MBPT are much more pronounced for EM 500 MeV: at saturation density the many-body uncertainties provide contributions of about ~ -2.5 MeV for this Hamiltonian (see light-blue band in Fig. 31). Including subleading 3N forces leads basically only to an overall shift of the bands as shown by the given energy range at saturation density. More specifically, the net 3N contribution leads to more attraction for the EGM potentials while the effect on EM 500 MeV is slightly repulsive.

To quantify the many-body convergence in more detail we compare to the results obtained in the SCGF method which are given by the region between the red-dashed lines in Fig. 31. The results in SCGF are considered to be converged in the many-body expansion (at the ladder level) and thus include only the uncertainty due to the Hamiltonian (including variations of the low-energy constants c_1, c_3). We focus again on the different NN potentials rather than on discussing the effect of subleading 3N forces. Considering the total uncertainty estimate of MBPT we find for the potentials EM 500 MeV and EGM 450/700 MeV completely overlapping bands and similar trends in density. In the case of EM 500 MeV the extended uncertainty (light-blue band) is however needed to obtain more attraction and consequently fully overlapping bands, whereas for EGM 450/700 MeV the pure third-order energy is already in remarkable agreement. In addition to the above discussion on the size of the light-blue bands this suggests that contributions beyond third-order are small for EGM 450/700 MeV and become significant for EM 500 MeV.

For EGM 450/500 MeV we observe a slightly different density dependence between the MBPT and the SCGF curves, leading to an almost total overlap at saturation density but less agreement in the region around $n \sim 0.1\ \text{fm}^{-3}$. Here, the equation of state in SCGF is slightly more repulsive. We recall that the SCGF results are extrapolated down to zero temperature from calculations performed at $T = 2$ MeV for $n \leqslant 0.05\ \text{fm}^{-3}$ and at $T = 5$ MeV for densities above. We have tested whether this discrepancy is related to the extrapolation to zero-temperature lowering the temperature down to $T = 3, 4$ MeV in densities between 0.05 and 0.10 fm^{-3}, and have found no dependency on the extrapolation.

Combining the discussions on the size of the additional many-body uncertainty and the comparison of MBPT vs. SCGF, we conclude from Fig. 31 that the perturbativeness improves from EM 500 MeV to EGM 450/500 MeV to EGM 450/700 MeV. It is remarkable that a third-order MBPT calculation compares so well with the nonperturbative case for these chiral NN potentials. We study the many-body convergence and the effect of subleading 3N forces now in more details.

In Fig. 32, we address again the many-body convergence and show order-by-order in MBPT the total energy per neutron at n_0 (first row) and $n_0/2$ (second row), analogously to Fig. 31. More specifically, we show the total energy in Hartree-Fock approximation $E^{(\text{HF})}/N$ ("HF"), second order ("2nd") and third order ("3rd"), $E^{(2)}/N$ and $E^{(3)}/N$ respectively, in comparison to the results using the SCGF method, E_{SCGF}/N ("SCGF"). For notation, we refer moreover to Sec. 1.3.2. The uncertainties are obtained as in Fig. 31 through variations of the 3N parameters and the single-particle energies. However, to study the many-body convergence the third-order bands do not include here the additional many-body uncertainty (the light-blue bands of Fig. 31). The blue (red) data points correspond to N^2LO (N^3LO) 3N forces.

For all six panels in Fig. 32, we observe similar overall patterns: comparing order-by-order to the SCGF method we observe that the second order adds always too much attraction which then is compensated by the third-order repulsion. However, the specific behavior is different for EM 500 MeV and the two EGM potentials. In the case of EM 500 MeV the large third order overcompensates the second-order repulsion. In contrast, the third-order contribution is much smaller and less repulsive for the EGM potentials as can be seen in Fig. 32 (second and third column). In particular, this is pronounced in the calculations based on EGM 450/700 MeV, which agree remarkably well with the SCGF result.

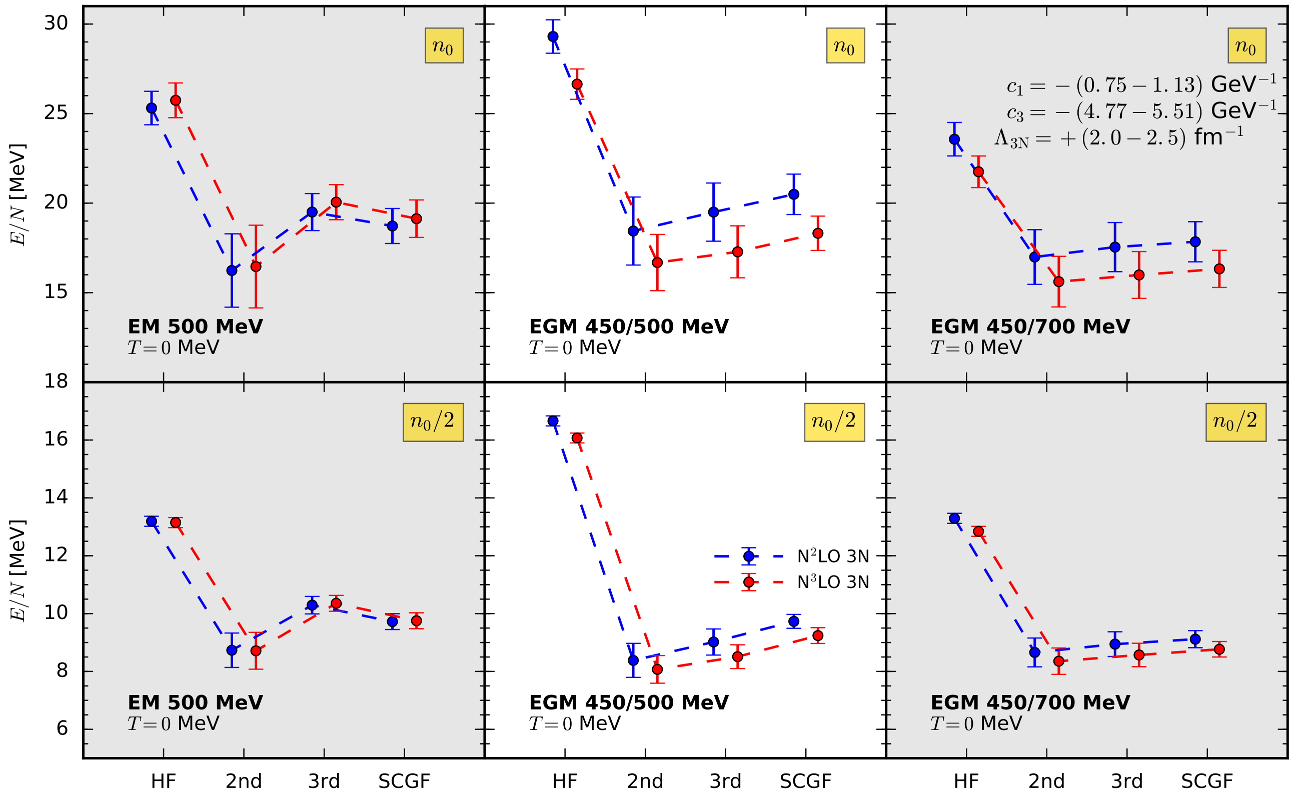

Figure 32: The energy per particle in neutron matter at different orders of MBPT is shown, up to Hartree-Fock ($E^{(\mathrm{HF})}/N$), second order ($E^{(2)}/N$) and third order ($E^{(3)}/N$), respectively, in comparison to the energies obtained from the SCGF method (E_{SCGF}/N) at n_0 (first row) and $n_0/2$ (second row), respectively. The N^{3}LO NN potentials are given in each panel. Three-body effects are included at N^{2}LO (blue) and at N^{3}LO (red), respectively. The dashed lines connecting the data points are in order to guide the eyes. The error bars are due to the c_i and $\Lambda_{3\mathrm{N}}$ variations. In this plot, the third-order calculation does not include the additional many-body uncertainty (the light-blue band in Fig. 31).

As already discussed in the description of Fig. 31, including N^{3}LO 3N forces has only a small repulsive effect on the energies based on EM 500 MeV, whereas the effect on the EGM potentials is larger but attractive. This behavior can be traced back to NN+$\overline{\mathrm{3N}}$ mixing terms that enter the calculation when including 3N forces beyond the Hartree-Fock level. We also note that the values of the low-energy constants C_S and C_T, which enter N^{3}LO 3N contributions, differ for all three potentials as summarized in Table 4. However, the many-body convergence is not altered by including contributions from subleading 3N interactions.

4.4 Full N^{3}LO calculations

The authors of Refs. [108, 140] performed the first consistent calculations at N^{3}LO including NN, 3N, and 4N forces in MBPT. In the cited works N^{3}LO NN and N^{2}LO 3N forces have been considered similarly up to third order in MBPT in terms of effective NN potentials [43], whereas subleading 3N interactions could only be included in the Hartree-Fock approximation since normal-ordering has not been worked with subleading 3N forces. Due to the advances in this work, we are now in the position to revisit and systematically improve these calculations.

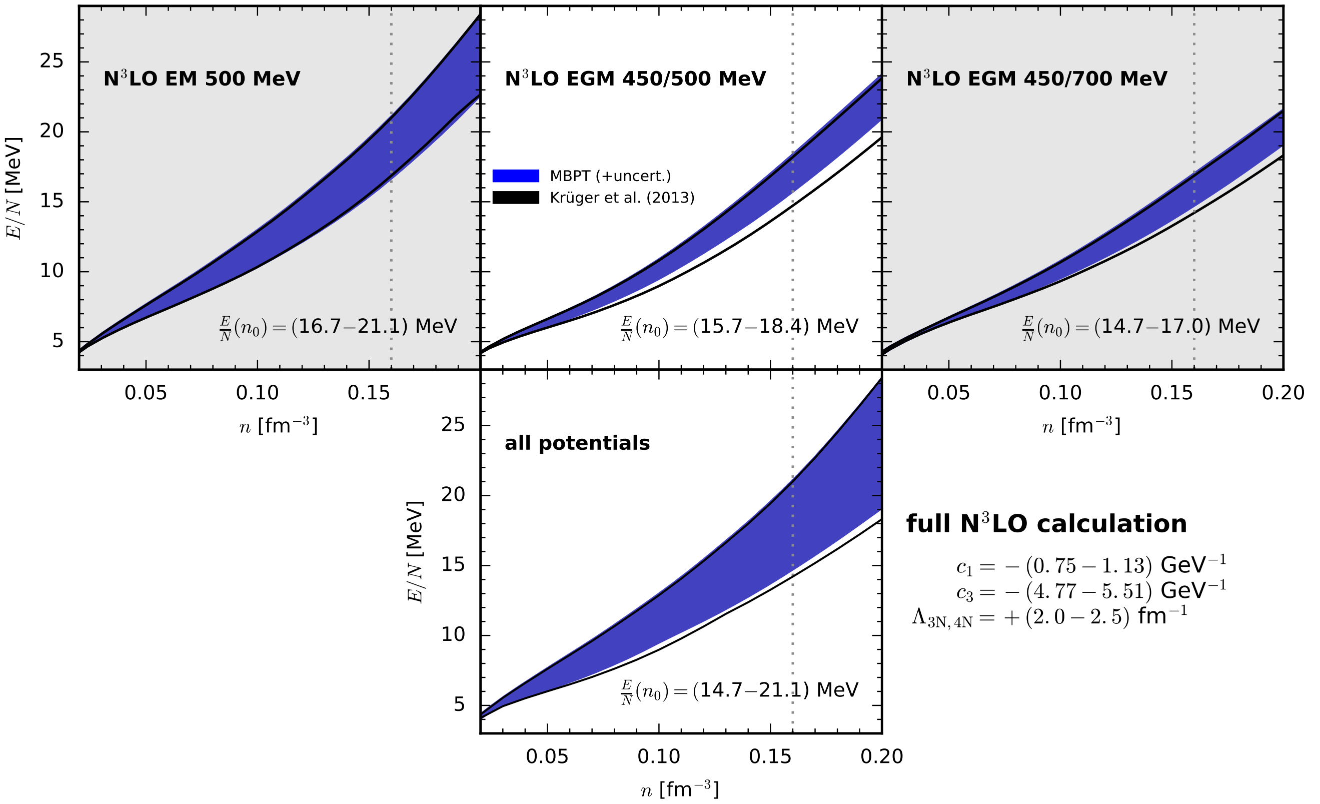

Figure 33: The energy per particle in neutron matter with consistent many-body forces at N^{3}LO for the three different NN potentials (this work: blue bands) in comparison to Krüger *et al.* (2013, black lines) [140]. The second row combines the results of the first row. In each panel, we give the energy range at saturation density obtained within the improved calculations presented in this work. See text for details.

In Fig. 33, we show our improved results for the energy of neutron matter (blue bands) for the three Hamiltonians with EM 500 MeV, EGM 450/500 MeV, and EGM 450/700 MeV (first row) and the total band merged from the previous panels (second row). The uncertainty bands cover again variations of the 3N parameters (as given in the figure), the single-particle spectrum and the additional many-body uncertainty (see also discussion of Fig. 31). We furthermore include the 4N Hartree-Fock energies provided by Thomas Krüger, and vary the 4N cutoff analogously to the 3N forces [140]. In addition, we show the results of Ref. [140] depicted by the black solid lines. For completeness, we note that we have corrected a small error in the routines of Refs. [27, 140] for the computation of the second- and third-order contribution of the N^{3}LO NN plus N^{2}LO 3N forces as well as the N^{3}LO 3N Hartree-Fock energy corresponding to the ring topology. Moreover, we are using the typo-corrected values for $\bar{\beta}_8, \bar{\beta}_9$ (see Ref. [9] for details). For a better view, we do not fill this region. We give in each panel the energy range at saturation density obtained within the improved calculations presented in this work.

We observe that the effect of adding the N^{3}LO 3N contributions beyond Hartree-Fock varies significantly between the EM 500 MeV and the two EGM potentials. For EM 500 MeV these contributions leave the uncertainty band almost unaffected. For the two EGM potentials the upper uncertainty limits remain the same while the lower increase by ~ 1 MeV (~ 0.2 MeV) for EGM 450/500 MeV (EGM 450/700 MeV), hence, decreasing the width of the uncertainty band. These findings are consistent with the observations in Ref. [140], which stated that the N^{3}LO 3N Hartree-Fock energy is smaller for EM 500 MeV while it is much larger for the two EGM potentials (see Fig. 6 of Ref. [140]). We emphasize, however, that NN and effective NN forces get mixed at second order and beyond, and therefore the net effect of these

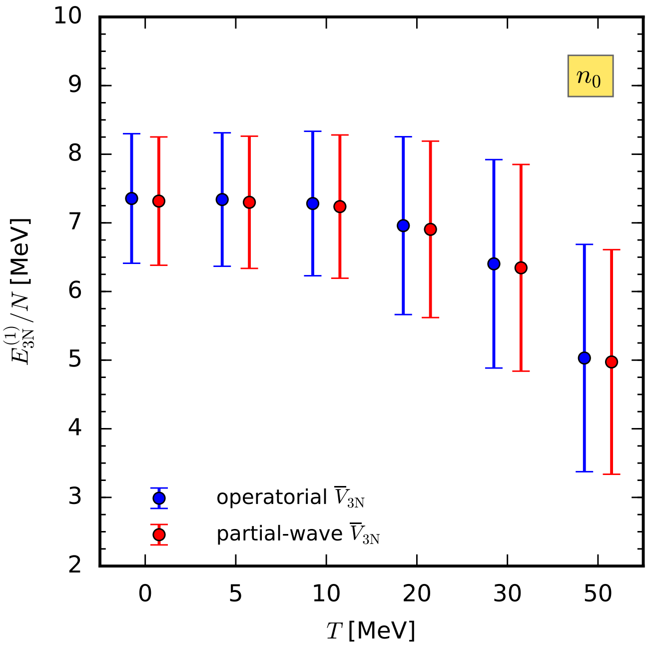

Figure 34: Comparison of the leading 3N Hartree-Fock energies at saturation density for several temperatures obtained using the effective NN potential in terms of 3N operators (blue) and the partial-wave approach (red). We include 3N matrix elements up to $\mathscr{J} \leqslant 9/2$ and $J \leqslant 6$. For the uncertainty estimate we use the same parameter variation in the 3N forces as in Fig. 31.

subleading 3N contributions cannot be easily disentangled in the many-body calculation. Combining all bands we find a total uncertainty of $E/N(n_0) = (14.7-21.1)$ MeV in neutron matter at saturation density. Compared to the corrected total band of Ref. [140] $E/N(n_0) = (14.3 - 21.1)$ MeV, we obtain a slight reduction of the lower limit of the uncertainty band. As suggested in Refs. [108, 140], these effects are indeed rather small. However, we expect the effects to be much more important as soon as the proton fraction is finite (see also discussion of symmetric nuclear matter in Ref. [140]).

4.5 Perspectives for finite-temperature calculations

We have extended the new framework for computing effective NN potentials in a partial-wave basis [28] to finite temperatures. Apart from being a necessary step to include these matrix elements in the SCGF method (due to the extrapolation from finite temperatures), this is also a crucial step for future MBPT calculations of nuclear matter at finite temperatures. In Fig. 34, we show the resulting N^{2}LO 3N Hartree-Fock energies $E^{(1)}_{3\mathrm{N}}/N(n_0, T)$ at six different temperatures in the range of $T = (0-50)$ MeV. We benchmark our new values (red) against previous results (blue) obtained via the operatorial approach [141]. The uncertainty bands are obtained through 3N parameter variation analogously to Figs. 31 and 32, whereas the single-particle spectrum does not contribute to the uncertainties since the Fermi-Dirac distribution in Eq. (4.1) is computed using a free spectrum. A similar benchmark at N^{3}LO is not possible because the operatorial approach has not been worked out to that order. We note that the 3N interaction energy decreases with temperature as shown in Fig. 34. Including also the kinetic energy would lead to a total increase in energy with increasing temperature. From Fig. 34, we can conclude that the two different methods for the normal ordering agree well at zero and finite temperature.

In addition to the 3N Hartree-Fock energies, we also benchmark the underlying interaction matrix elements of the effective potential $\overline{V}^{\mathrm{as}}_{3\mathrm{N}}$. We select a representative set of four channels, $^1S_0$, $^3P_0$, $^3P_1$, $^3P_2$,

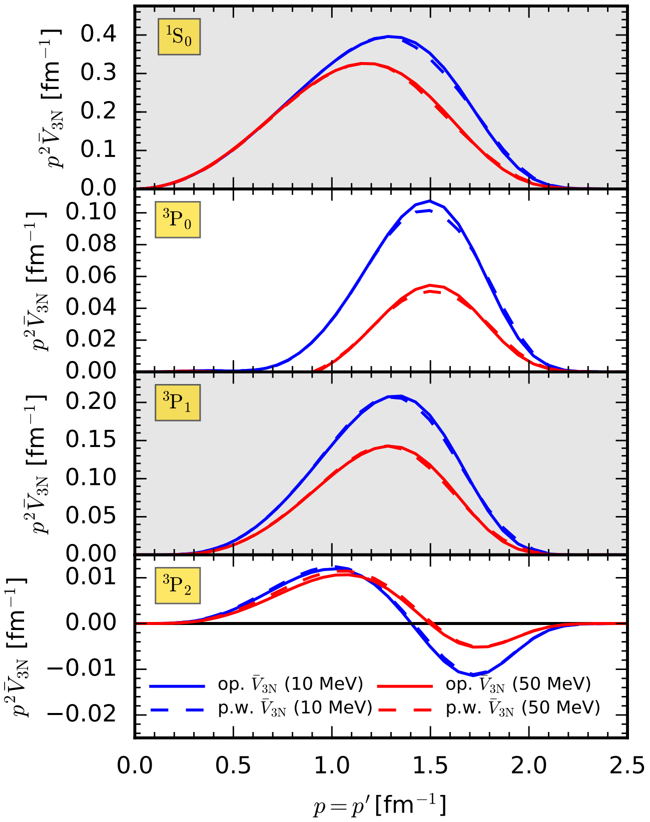

Figure 35: Momentum-space diagonal matrix elements of the density-dependent effective NN potentials at N^{2}LO for a selection of four partial-wave channels and two temperatures, $T = 10$, 50 MeV.

and two temperatures $T = 10$, 50 MeV in Fig. 35. The ones obtained in the partial-wave (operatorial) approach are plotted as dashed (solid) lines. These channels contribute to the Hartree-Fock energy presented in Fig. 34. We have also compared higher partial waves with $J \leqslant 6$ and momentum off-diagonal matrix elements for $\Lambda_{3N} = (2.0 - 2.5)$ fm^{-1}. As in Ref. [28], we find indications of an incomplete partial-wave convergence only for partial-waves channels with $J > 4$, We also checked that the agreement can be systematically improved by increasing the 3N model space, i.e., by including channels with $\mathscr{J} = 11/2, 13/2$. We found that contributions from these higher partial-wave channels provide $\lesssim 50$ keV to the energy per particle of neutron matter at saturation density. Overall, we find in Fig. 35 excellent agreement of the two methods. This shows that the computed finite-temperature matrix elements of the effective interactions up to N^{3}LO are numerically stable and, hence, suitable for future calculations of nuclear matter for astrophysical applications [41, 42].

To conclude this section, we briefly give an overview of MBPT at finite temperatures. For thermodynamical studies in nuclear matter, we refer the reader to, e.g., Refs. [37, 48, 110, 235, 240, 241]. The discussion follows roughly Refs. [110, 235, 242] and, for simplicity, we assume pure neutron matter but the extension to general isospin asymmetries is analogous. At finite temperatures, one considers a perturbation expansion of the free energy, $F(N, T, V) = \Omega(\mu, T, V) + \mu N$, around the Hartree-Fock free energy. The Legendre transformation relates the free energy and the grand-canonical potential $\Omega(\mu, T, V)$, where the chemical potential $\mu(N, T, V)$ is obtained by inverting the corresponding relation for the mean particle number (see also similar relation in Eq. (4.25)),

$$N(\mu, T, V) = -\frac{\partial \Omega}{\partial \mu}\bigg|_{T,V} . \tag{4.26}$$

Following Kohn and Luttinger [243], this inversion can be realized by Taylor-expanding the grand-canonical potential about the noninteracting chemical potential μ_0 and organizing $\Omega(\mu, T, V) = \sum_{i=0}^{\infty} \lambda^i \, \Omega_i$ as well as $\mu(N, T, V) = \sum_{i=0}^{\infty} \lambda^i \, \mu_i$ in powers of the artificial parameter λ:

$$\begin{aligned} N(\mu, T, V) &= -\sum_k \frac{\partial \Omega_k}{\partial \mu} \lambda^k = -\sum_{n,k=0}^{\infty} \frac{\lambda^k}{n!} \frac{\partial^{n+1} \Omega_k}{\partial \mu^{n+1}}\bigg|_{\mu_0} (\mu - \mu_0)^n \\ &= -\Bigg(\lambda^0 \frac{\partial \Omega_0}{\partial \mu}\bigg|_{\mu_0} + \lambda^1 \left[\frac{\partial \Omega_1}{\partial \mu}\bigg|_{\mu_0} + \mu_1 \frac{\partial^2 \Omega_0}{\partial \mu^2}\bigg|_{\mu_0} \right] \\ &\quad + \lambda^2 \left[\frac{\partial \Omega_2}{\partial \mu}\bigg|_{\mu_0} + \mu_1 \frac{\partial^2 \Omega_1}{\partial \mu^2}\bigg|_{\mu_0} + \mu_2 \frac{\partial^2 \Omega_0}{\partial \mu^2}\bigg|_{\mu_0} + \frac{\mu_1^2}{2!} \frac{\partial^3 \Omega_0}{\partial \mu^3}\bigg|_{\mu_0} \right] + \mathcal{O}(\lambda^3) \Bigg) . \end{aligned} \tag{4.27}$$

Counting the mean particle number as order zero (i.e., $\mathcal{O}(\lambda^0)$) implies that the higher-order corrections $[\,\cdot\,]$ in Eq. (4.27) vanish independently and for all λ which leads iteratively to

$$\mu_0 \equiv N = -\frac{\partial \Omega_0}{\partial \mu}\bigg|_{\mu_0}, \qquad \mu_1 = -\frac{\partial \Omega_1 / \partial \mu}{\partial^2 \Omega_0 / \partial \mu^2}\bigg|_{\mu_0}, \tag{4.28a}$$

$$\mu_2 = -\frac{1}{2\,(\partial^2 \Omega_0 / \partial \mu^2)^3}\bigg|_{\mu_0} \left(2 \frac{\partial \Omega_2}{\partial \mu} \left[\frac{\partial^2 \Omega_0}{\partial \mu^2} \right]^2 - 2 \frac{\partial \Omega_1}{\partial \mu} \frac{\partial^2 \Omega_0}{\partial \mu^2} \frac{\partial^2 \Omega_1}{\partial \mu^2} + \left[\frac{\partial \Omega_1}{\partial \mu} \right]^2 \frac{\partial^3 \Omega_0}{\partial \mu^3} \right)\bigg|_{\mu_0} . \tag{4.28b}$$

That is, $N = nV$ is solely determined by the noninteracting system. The coefficients (4.28) are then inserted into an analogous expansion for the free energy,

$$F(N) = \sum_{i=0}^{\infty} \lambda^i F_i(N), \qquad \text{with} \qquad F_i(N) = \sum_{k=0}^{\infty} \frac{1}{k!} \frac{\partial^k \Omega_i}{\partial \mu^k}\bigg|_{\mu_0} (\mu - \mu_0)^k + \mu_i N . \tag{4.29}$$

Factorizing powers of λ, one obtains the contributions, here given up to third order,

$$F_0(N) = \Omega_0(N) + \mu_0 N , \qquad F_1(N) = \Omega_1(\mu_0), \qquad F_2(N) = \Omega_2(\mu_0) - \frac{1}{2} \frac{(\partial \Omega_1 / \partial \mu)^2}{\partial^2 \Omega_0 / \partial \mu^2}\bigg|_{\mu_0}, \tag{4.30a}$$

$$F_3(N) = \Omega_3(\mu_0) - \frac{\partial \Omega_1 / \partial \mu}{6 (\partial^2 \Omega_0 / \partial \mu^2)^3}\bigg|_{\mu_0} \left\{ 6 \frac{\partial \Omega_2}{\partial \mu^2} \left[\frac{\partial^2 \Omega_0}{\partial \mu^2} \right]^2 + \frac{\partial \Omega_1}{\partial \mu} \left(-3 \frac{\partial^2 \Omega_0}{\partial \mu^2} \frac{\partial^2 \Omega_1}{\partial \mu^2} + \frac{\partial \Omega_1}{\partial \mu} \frac{\partial^3 \Omega_0}{\partial \mu^3} \right) \right\}\bigg|_{\mu_0} . \tag{4.30b}$$

Note that $\mu_i N$ with $i \geqslant 1$ chancel by construction and that the grand-canonical partition function is always evaluated at μ_0. Eventually, the limit $\lambda \to 1$ is taken in practical calculations.

The calculation of the free energy in the Hartree-Fock approximation, $F^{(\mathrm{HF})} = F_0 + F_1$, is similar to the zero-temperature case in Sec. 4.2.1 when the Heaviside step function is replaced by the general Fermi-Dirac distribution function. According to the density relation in Eqs. (4.28), we first need to calculate the free grand-canonical potential

$$\begin{aligned} \frac{\Omega_0}{V} &= -\frac{2}{\beta} \int \frac{\mathrm{d}\mathbf{k}}{(2\pi)^3} \ln\left(1 + e^{-\beta(\varepsilon_{\mathbf{k}} - \mu)}\right) = -2 \int \frac{\mathrm{d}\mathbf{k}}{(2\pi)^3} \frac{k^2}{3m} n_{\mathbf{k}}(\mu_0) \\ &= \frac{1}{3\pi^2 \beta} \left(\frac{2m}{\beta} \right)^{3/2} \Gamma\left(\frac{5}{2} \right) \mathrm{Li}_{5/2}\left(-e^{\beta \mu_0} \right) , \end{aligned} \tag{4.31}$$

using the Fermi-Dirac partition function and the Fermi-Dirac integrals,

$$F_j(x) = \frac{1}{\Gamma(j+1)} \int_0^\infty \mathrm{d}t \, \frac{t^j}{\exp[t-x]+1} = -\mathrm{Li}_{j+1}(-e^x) \,, \tag{4.32}$$

written in terms of the polylogarithmic functions $\mathrm{Li}_s(z) = \sum_{k=1}^\infty k^{-s} z^k$. Applying the identity $\frac{\mathrm{d}}{\mathrm{d}x}\mathrm{Li}_s(x) = \mathrm{Li}_{s-1}(x)/x$, the mean particle number follows immediately, and in a free spectrum, ones has

$$N = -\frac{\partial \Omega_0}{\partial \mu}\bigg|_{\mu_0} = 2 \int \frac{\mathrm{d}\mathbf{k}}{(2\pi)^3} n_{\mathbf{k}}(\mu_0) \overset{\varepsilon=\frac{k^2}{2m}}{=} -\frac{1}{3\pi^2}\left(\frac{2m}{\beta}\right)^{3/2} \Gamma\left(\frac{5}{2}\right) \mathrm{Li}_{3/2}\left(-e^{\beta\mu_0}\right) , \tag{4.33}$$

which determines μ_0 by inversion at fixed density. The purely kinetic part can now be calculated,

$$\frac{F_0}{V} = 2 \int \frac{\mathrm{d}\mathbf{k}}{(2\pi)^3} \frac{\mathbf{k}^2}{2m} n_{\mathbf{k}}(\mu_0) = -\frac{3}{2}\frac{\Omega_0}{V} \,. \tag{4.34}$$

Similarly, $F_1 = \Omega_1$ corresponds to Eq. (4.10) with the general Fermi-Dirac distribution.

Beyond Hartree-Fock, however, additional terms which are not present at $T = 0$ enter in the expansion. These are called *anomalous* as opposed to *normal* contributions. At second order, for example, one has $\Omega_2 = \Omega_2^{(n)} + \Omega_2^{(a)}$ with

$$\begin{aligned} \frac{\Omega_2^{(n)}}{V} &= \frac{1}{8}\left[\prod_{i=1}^{4} \mathrm{Tr}_{\sigma_i} \int \frac{\mathrm{d}\mathbf{k}_i}{(2\pi)^3}\right] |\langle 12|\mathscr{A}_{12} V_{\mathrm{NN}}|34\rangle|^2 \, (2\pi)^3 \, \delta(\mathbf{k}_1 + \mathbf{k}_2 - \mathbf{k}_3 - \mathbf{k}_4) \\ &\quad \times \frac{n_{\mathbf{k}_1} n_{\mathbf{k}_2} (1-n_{\mathbf{k}_3})(1-n_{\mathbf{k}_4}) - (1-n_{\mathbf{k}_1})(1-n_{\mathbf{k}_2}) n_{\mathbf{k}_3} n_{\mathbf{k}_4}}{\varepsilon_1 + \varepsilon_2 - \varepsilon_3 - \varepsilon_4} \,, \end{aligned} \tag{4.35a}$$

$$\frac{\Omega_2^{(a)}}{V} = -\frac{\beta}{2}\left[\prod_{i=1}^{3} \mathrm{Tr}_{\sigma_i} \int \frac{\mathrm{d}\mathbf{k}_i}{(2\pi)^3}\right] n_{\mathbf{k}_1} n_{\mathbf{k}_2} (1-n_{\mathbf{k}_2}) n_{\mathbf{k}_3} \, \langle 12|\mathscr{A}_{12} V_{\mathrm{NN}}|12\rangle \, \langle 23|\mathscr{A}_{12} V_{\mathrm{NN}}|23\rangle \,, \tag{4.35b}$$

such that the corresponding correction to the free energy at second order reads

$$F_2(N) = \Omega_2^{(n)}(\mu_0) + \left[\Omega_2^{(a)}(\mu_0) - \frac{1}{2}\frac{(\partial\Omega_1/\partial\mu)^2}{\partial^2\Omega_0/\partial\mu^2}\bigg|_{\mu_0}\right] . \tag{4.36}$$

Notice that Eq. (4.35a) has been rewritten in order to remove the pole at finite temperature. For isotropic Fermi systems in the zero-temperature limit, Kohn, Luttinger, and Ward [243, 244] have shown that the expansion of the free energy (4.29) reduces to the expressions discussed in Sec. 4.2, i.e., that the *anomalous* contributions cancel at each order against the so-called *anomalous* derivative terms (see $[\,\cdot\,]$ in Eq. (4.36)).

In conclusion, the presented MBPT machinery is well-prepared for finite-temperatures studies beyond Hartree-Fock with consistent NN and 3N contributions up to N^{3}LO. For second-order calculations in a free spectrum, only a few *anomalous* contributions have to be implemented [110]. Additional improvements as well as higher-order applications are currently work in progress.

5 An efficient Monte-Carlo framework for MBPT calculations

In the previous section, we have elaborated on an advanced partial-wave framework for improving current state-of-the-art calculations of asymmetric matter in MBPT up to third order. The (frequently) neglected residual 3N term at second order (see also Ref. [137]) and the third-order particle-hole contribution give furthermore rise to extensions. As shown in Ref. [111] by an explicit partial-wave decomposition, including the latter is not just a question of completeness, it can also be quite sizable in symmetric matter. However, the necessity for additional benchmarks in Ref. [112] emphasizes once more that these partial-wave calculations are generally challenging and thus have only been applied up to third order. Going to higher orders in the many-body expansion is also of interest.

On the other hand, the Hartree-Fock energies due to 3N and 4N forces were semianalytically calculated in the single-particle basis in which the corresponding energy expressions are originally defined (see, e.g., Refs. [36, 43, 140, 235]). It is not obvious whether such an approach without expanding in partial waves is also practicable beyond Hartree-Fock because of the much larger phase space and the increasing number of spin-isospin traces. Working in a partial-wave basis is here indeed efficient, e.g., in making use of symmetries of the interactions to meet computational requirements.

These considerations led us to the development of a Monte-Carlo framework for MBPT in the single-particle basis [32]. Tracing over spins and isospins is fully automated and the multidimensional momentum integrals are computed using Monte-Carlo sampling. We discuss in the following sections the three pillars of the novel framework:

(1) *Access chiral forces in a single-particle basis.* Based on their operatorial definition we express chiral many-body forces *exactly* as matrices in spin-isospin space. Our current implementation covers NN, 3N, and 4N forces up to N^3LO. Each matrix element is an analytic function of the single-particle momenta written in the programming language C++. The generation of these interaction matrices is automated and close to the formal expressions of the many-body forces to be able to handle general operator structures transparently and confidently. This part is discussed in Sec. 5.1.

(2) *Automated evaluation of energy expressions in MBPT.* Having worked out the interaction matrices Sec. 5.2 is all about applying MBPT to infinite matter in this basis. Since we face many diagrams at fourth order (or potentially higher), we automate writing optimized source codes in C++ for evaluating given energy expressions.

(3) *Multidimensional momentum integrals.* Momentum conservation and regularization typically cause deformed regions in the multidimensional phase space where the integrand is less important. As discussed in Sec. 5.3 (adaptive) Monte-Carlo algorithms are therefore most efficient and crucial to obtain converged results in these calculations.

The developed framework has various advances making it well-suited for next state-of-the-art calculations in MBPT. Some of these are:

- Many-body forces in momentum space can be accessed in calculations using their operatorial definition and independent of whether partial-wave matrix elements have been worked out (see also Ref. [137]). This allows, e.g., to assess the convergence of other partial-wave approaches.
- All approximations on normal-ordered 3N contributions, e.g., $P = 0$, are released. Normal-ordering with 4N forces is technically feasible.
- Implementing energy expressions is remarkably straightforward in a single-particle basis since algebraic transformations such as partial-wave decompositions are no longer needed. The implementation is moreover automated, especially, for higher-order applications.
- Arbitrary isospin-asymmetries are no longer associated with additional efforts.

- From a technical point of view, the framework is transparent, robust, and fast in computation.

We consider the MBPT frameworks in Secs. 4 and 5 as complementary. In particular, the improved normal ordering in Sec. 4.1 enables to include 3N contributions in calculations which are necessarily based on partial waves, such as the Weinberg analysis in Sec. 3 or solving the BCS gap equation in Sec. 6.

5.1 Chiral forces in a single-particle basis

We have developed a general method to express the formal (i.e., operatorial) chiral many-body forces in a product basis of the interacting particles. For this challenging task, we require a *transparent* computational implementation being close to their analytic definition and able to systematically handle different operator structures in momentum space. In the following, we discuss how this can be achieved.

Given the *operatorial* expression in momentum space of an (in principle) arbitrary A-body operator V_{AN} our automated method evaluates the antisymmetrized complex-valued matrix element

$$\left\langle 1'2'\ldots A' \,\middle|\, \mathscr{A}_A V_{\mathrm{AN}} \,\middle|\, 12\ldots A \right\rangle = \left\langle (\sigma_{1'}\tau_{1'})\ldots(\sigma_{A'}\tau_{A'}) \,\middle|\, \mathscr{A}_A V_{\mathrm{AN}}\left(\overline{\mathbf{p}},\overline{\mathbf{p}}'\right) \,\middle|\, (\sigma_1\tau_1)\ldots(\sigma_A\tau_A)\right\rangle , \tag{5.1}$$

in the product basis of the single-particle basis $|i\rangle \equiv |\mathbf{p}_i\sigma_i\tau_i\rangle$ and with the A-body antisymmetrizer $\mathscr{A}_A$. To separate the continuous from the discrete (finite) part of the single-particle basis, we have formally applied the eigenvalue relations on the momenta. Moreover, keeping the notation short a $3A$-dimensional momentum vector $\overline{\mathbf{p}} = \mathbf{p}_1 \oplus \mathbf{p}_2 \ldots \oplus \mathbf{p}_A$ (similar for $\overline{\mathbf{p}}'$) is introduced that concatenates the Cartesian components of all initial (finial) momenta in a single vector. The matrix elements (5.1) are nonzero if and only if the total momentum is conserved. For completeness, we note that one could also work with a finite momentum-dependent basis after discretizing the momentum space on a suitable grid (e.g., for Gauss quadrature). However, this would require an inefficient multidimensional interpolation that is also no longer exact. The parentheses distinguish different particles with labels $i = 1, \ldots, A$. For technical reasons, it is useful to adapt the binary notation $|\sigma = +1/2\rangle = |1\rangle$ and $|\sigma = -1/2\rangle = |0\rangle$. We label, moreover, protons by $|p\rangle = |1\rangle$ and neutrons by $|n\rangle = |0\rangle$, analogously to our definition in Sec. 4. For example, the state $|(01)(10)\rangle$ denotes a spin-down proton (first particle) and a spin-up neutron (second particle). These definitions are arbitrary but must be used consistently.

We stress again that we construct the matrix elements (5.1) solely based on the operatorial definition of the forces, without employing a partial-wave decomposition (see also Ref. [137]). However, not all chiral potentials are available at the level of operators; e.g., RG-evolved potentials are usually given in terms of partial waves. At the end of this section, we discuss the implementation of these potentials.

Considering the set of all configurations of spin and isospin Eq. (5.1) can be written as a matrix of rank 4^A (in spin-isospin space). Typical values of the rank are 4 ($A = 1$), 16 ($A = 2$), 64 ($A = 3$), and 256 ($A = 4$). Each matrix element is an *analytic* function of $\overline{\mathbf{p}}$ and $\overline{\mathbf{p}}'$, despite the (numerical) integrals that might be present in scalar functions. Notice that neither an approximation nor a truncation has been imposed. We now systematically construct these matrices, particularly, up to 4N forces, so $A \leqslant 4$. Nevertheless, there is no technical reason for such a constraint at this stage.

V_{AN} reduces to a sum of products involving only a few single-particle operators (i.e., by using the Cartesian definitions of the scalar and triple product) acting on the separate Hilbert spaces. That is the unity operator $\mathbb{1}$, the Cartesian components $j = x, y, z$ of the spin $\boldsymbol{\sigma}_i^{(j)} = 2\,\mathbf{S}^{(j)}$ and isospin operator $\boldsymbol{\tau}_i^{(j)} = 2\,\mathbf{T}^{(j)}$ of each particle, and *some* momentum operator depending on both $\overline{\mathbf{p}}$ and $\overline{\mathbf{p}}'$ such as the momentum transfer $\mathbf{q}$. Here, $\mathbf{S}$ and $\mathbf{T}$ denote the total spin and isospin, respectively. The following discussion is independent of the actual functional form of the momentum operator because of the eigenvalue relations. As usual for an A-body operator, they are defined by a string of tensor products,

$$\boldsymbol{\sigma}_i^{(j)} = (\mathbb{1}_2 \otimes \mathbb{1}_2)_1 \otimes \ldots \otimes \left(\boldsymbol{\sigma}_i^{(j)} \otimes \mathbb{1}_2\right)_i \otimes \ldots \otimes (\mathbb{1}_2 \otimes \mathbb{1}_2)_A \,, \tag{5.2a}$$

$$\boldsymbol{\tau}_i^{(j)} = (\mathbb{1}_2 \otimes \mathbb{1}_2)_1 \otimes \ldots \otimes \left(\mathbb{1}_2 \otimes \boldsymbol{\tau}_i^{(j)}\right)_i \otimes \ldots \otimes (\mathbb{1}_2 \otimes \mathbb{1}_2)_A \,, \tag{5.2b}$$

$$\begin{aligned} \mathbf{p}_i^{(j)} &= (\mathbb{1}_2 \otimes \mathbb{1}_2)_1 \otimes \ldots \otimes (\mathbb{1}_2 \otimes \mathbb{1}_2)_i \, \mathbf{p}_i^{(j)} \otimes \ldots \otimes (\mathbb{1}_2 \otimes \mathbb{1}_2)_A \,, \\ &= \mathbf{p}_i^{(j)} \, \mathbb{1}_A \,, \end{aligned} \tag{5.2c}$$

where $(\,\cdot\,)_i$ acts only on the ith particle and decomposes in Hilbert spaces for spin and isospin. $\mathbb{1}_A$ is the unity matrix of rank A in spin-isospin space. As already mentioned above, the momentum operator fulfills always the eigenvalue relation.

The Kronecker product gives the formal definition in Eqs. (5.2) a concrete meaning. It is defined for two matrices A and B of dimension $m \times n$ and $p \times q$, respectively, as follows

$$A \otimes B = \begin{pmatrix} A_{11}B & \cdots & A_{1n}B \\ \vdots & \ddots & \vdots \\ A_{m1}B & \cdots & A_{mn}B \end{pmatrix}, \qquad \text{with} \qquad \dim(A \otimes B) = m\,p \times n\,q\,. \tag{5.3}$$

Our method is now governed by a rather simple idea (see, e.g., the Heisenberg model in quantum mechanics): the matrix representation of the operators in Eqs. (5.2) can easily be obtained by iteratively applying the Kronecker product (5.3) to the Pauli matrices (similar for spins)

$$\tau_i^{(x)} = \begin{pmatrix} 0 & 1 \\ 1 & 0 \end{pmatrix}, \qquad \tau_i^{(y)} = \begin{pmatrix} 0 & -i \\ i & 0 \end{pmatrix}, \qquad \tau_i^{(z)} = \begin{pmatrix} 1 & 0 \\ 0 & -1 \end{pmatrix}, \tag{5.4}$$

which are defined in the basis $|1\rangle_i = (1,\,0)_i^T$ and $|0\rangle_i = (0,\,1)_i^T$ (column vectors). Corresponding to formal insertions of completeness relations (in spin-isospin space) the matrix representation of the entire V_{AN} is then given by simple matrix operations involving Eqs. (5.2).

Further, we elaborate on the imposed binary notation labeling spin-isospin states. As already noted above, the basis of the constructed matrices is the set of all 4^A configurations of

$$|\eta\rangle := |(\sigma_1\tau_1)(\sigma_2\tau_2)\ldots(\sigma_A\tau_A)\rangle \tag{5.5}$$

with $\sigma_i = 0, 1$ and $\tau_i = 0, 1$. Dropping the parentheses in Eq. (5.5) each configuration on the right-hand side can be identified as a $2A$-digit binary number $\eta_{(2)}$. Its decimal value, $\eta_{(10)} = 0,\,1,\,\ldots,\,4^A - 1$, maps the configuration to the corresponding basis vector $|\eta\rangle = (|\sigma_1\rangle \otimes |\tau_1\rangle) \otimes (|\sigma_2\rangle \otimes |\tau_2\rangle) \otimes \ldots \otimes (|\sigma_A\rangle \otimes |\tau_A\rangle)$ assuming that the basis is indexed by $\eta_{(10)}$; e.g., one has the vector $|\eta_{(10)} = 2\rangle = (0,\,0,\,1,\,0,\,\ldots,\,0)^T$ in spinor notation. In conclusion, a given spin-isospin configuration (binary number) and the position in the basis (decimal number) are uniquely related by

$$\eta_{(10)}\left(\sigma_1\tau_1\sigma_2\tau_2\ldots\,\sigma_A\tau_A\big|_{(2)}\right) = \left(4^A - 1\right) - \sum_{j=1}^{A}\left[2^{2(A-j)+1}\,\sigma_j + 2^{2(A-j)}\,\tau_j\right]. \tag{5.6}$$

For instance, with a spin-down proton (first particle) and a spin-down neutron (second particle), we have $|\eta = 0100_{(2)}\rangle \equiv |\eta = 11_{(10)}\rangle \equiv (0,\,\ldots,\,0,\,1,\,0,\,0,\,0,\,0)^T$. Notice that Eq. (5.6) reverses the ordering since the spinors $(1,\,0)^T$ and $(0,\,1)^T$ of the single-particle basis are associated with $|1\rangle_i$ and $|0\rangle_i$, respectively, in decreasing order, analogously to the larger z-axis projection of the (iso-)spin-up component. The mapping (5.6) is key in practice for addressing the correct matrix element.

A few instructive examples are in order. Using the formal definition of the Kronecker product (5.3) and the Pauli matrices (5.4), we obtain the symmetric matrix

$$\left\langle \eta' \,\middle|\, \boldsymbol{\tau}_1 \cdot \boldsymbol{\tau}_2 \,\middle|\, \eta \right\rangle = \sum_{j=1}^{3} \tau_1^{(j)} \otimes \tau_2^{(j)} = \begin{pmatrix} 1 & 0 & 0 & 0 \\ 0 & -1 & 2 & 0 \\ 0 & 2 & -1 & 0 \\ 0 & 0 & 0 & 1 \end{pmatrix} \tag{5.7}$$

in the basis $|pp\rangle$, $|pn\rangle$, $|np\rangle$, and $|nn\rangle$ according to Eq. (5.6). For simplicity, we have omitted the spin space. The corresponding normalized eigenstates in spinor notation are

$$v_1^{(\lambda=1)} = \begin{pmatrix} 1 \\ 0 \\ 0 \\ 0 \end{pmatrix}, \qquad v_2^{(\lambda=1)} = \frac{1}{\sqrt{2}} \begin{pmatrix} 0 \\ 1 \\ 1 \\ 0 \end{pmatrix}, \qquad v_3^{(\lambda=1)} = \begin{pmatrix} 0 \\ 0 \\ 0 \\ 1 \end{pmatrix}, \qquad \text{and} \qquad v_4^{(\lambda=-3)} = \frac{1}{\sqrt{2}} \begin{pmatrix} 0 \\ 1 \\ -1 \\ 0 \end{pmatrix}, \tag{5.8}$$

which correspond to the well-known isospin triplet states $|T = 1, M_T = +1, 0, -1\rangle$ and the singlet $|T = 0, M_T = 0\rangle$ with eigenvalues $\lambda = (2T(T+1) - 3)$ as indicated by the superscripts. Notice that the isospin trace vanishes because $\mathrm{Tr}(A \otimes B) = \mathrm{Tr}(A) \cdot \mathrm{Tr}(B)$ and the traceless Pauli matrices. Another example is the tensor operator and its Hermitian matrix

$$\begin{aligned} \left\langle \eta' \,\middle|\, \boldsymbol{\sigma}_1 \cdot \mathbf{q}\, \boldsymbol{\sigma}_2 \cdot \mathbf{q} \,\middle|\, \eta \right\rangle &= \sum_{i,j=1}^{3} \left[\sigma_1^{(i)} \otimes \left(q_{(i)} \mathbb{1}_2 \right) \right] \left[\sigma_2^{(j)} \otimes \left(q_{(j)} \mathbb{1}_2 \right) \right] \\ &= \begin{pmatrix} q_{(z)}^2 & (q_{(x)} - i q_{(y)}) q_{(z)} & (q_{(x)} - i q_{(y)}) q_{(z)} & (q_{(x)} - i q_{(y)})^2 \\ (q_{(x)} + i q_{(y)}) q_{(z)} & -q_{(z)}^2 & q_{(x)}^2 + q_{(y)}^2 & -(q_{(x)} - i q_{(y)}) q_{(z)} \\ (q_{(x)} + i q_{(y)}) q_{(z)} & q_{(x)}^2 + q_{(y)}^2 & -q_{(z)}^2 & -(q_{(x)} - i q_{(y)}) q_{(z)} \\ (q_{(x)} + i q_{(y)})^2 & -(q_{(x)} + i q_{(y)}) q_{(z)} & -(q_{(x)} + i q_{(y)}) q_{(z)} & q_{(z)}^2 \end{pmatrix}. \end{aligned} \tag{5.9}$$

The discussion so far focused on the direct term, the interaction matrix element (5.1), however, is anti-symmetrized by

$$\mathscr{A}_A = \sum_{a=1}^{A!} \mathrm{sign}(\pi_a) \, P_{\pi_a} \,, \tag{5.10}$$

where $P_{\pi_a} = P^{\text{mom}}_{\pi_a} P^{\text{spin}}_{\pi_a} P^{\text{iso}}_{\pi_a}$ is the permutation operator in momentum, spin, and isospin space with signature sign($\cdot$). We have already discussed the specific cases $A = 2$, 3, 4 in Sec. 2. Considering the antisymmetrizer (5.10) in Eq. (5.1) we find

$$\begin{aligned}\left\langle 1'2'\ldots A' \middle| \mathscr{A}_A V_{\text{AN}} \middle| 12\ldots A \right\rangle &= \sum_{a=1}^{A!} \langle \overline{\mathbf{p}}'| \left\langle (\sigma_{1'}\tau_{1'})\ldots(\sigma_{A'}\tau_{A'}) \middle| P^{\text{mom}}_{\pi_a} \widetilde{V}_{\text{AN}} \middle| (\sigma_1\tau_1)\ldots(\sigma_A\tau_A) \right\rangle |\overline{\mathbf{p}}\rangle \\ &= \sum_{a=1}^{A!} \left(P^{\dagger,\text{mom}}_{\pi_a} |\overline{\mathbf{p}}'\rangle \right)^{\dagger} \left\langle (\sigma_{1'}\tau_{1'})\ldots(\sigma_{A'}\tau_{A'}) \middle| \widetilde{V}^{\pi_a}_{\text{AN}} \middle| (\sigma_1\tau_1)\ldots(\sigma_A\tau_A) \right\rangle |\overline{\mathbf{p}}\rangle \\ &= \sum_{a=1}^{A!} \left\langle (\sigma_{1'}\tau_{1'})\ldots(\sigma_{A'}\tau_{A'}) \middle| \widetilde{V}^{\pi_a}_{\text{AN}} \left(\overline{\mathbf{p}}, \overline{\mathbf{p}}'_{\pi_a^\dagger} \right) \middle| (\sigma_1\tau_1)\ldots(\sigma_A\tau_A) \right\rangle . \end{aligned} \tag{5.11}$$

The permutation operators in the modified interactions $\widetilde{V}^{\pi_a}_{\text{AN}} = \text{sign}(\pi_a) P^{\text{spin}}_{\pi_a} P^{\text{iso}}_{\pi_a} V_{\text{AN}}$ permute only the basis vectors with respect to the direct term. Because of the relation to spin-isospin operators via [191]

$$P^{\text{spin}}_{ij} = \frac{\mathbb{1} + \boldsymbol{\sigma}_i \cdot \boldsymbol{\sigma}_j}{2}, \qquad \text{and} \qquad P^{\text{iso}}_{ij} = \frac{\mathbb{1} + \boldsymbol{\tau}_i \cdot \boldsymbol{\tau}_j}{2}, \tag{5.12a}$$

it is moreover straightforward to construct the corresponding permutation matrices using Eqs. (5.2). On the other hand, the explicit momentum dependence of the matrix elements requires a special treatment of $P^{\text{mon}}_{\pi_a}$. In Eq. (5.11), we therefore act first with $P^{\text{mon}}_{\pi_a}$ on the bra-state and apply then the eigenvalue relation for the momenta. Notice that strings of permutation operators are in general not Hermitian in contrast to transposition operators, e.g., $(P_{12}P_{23})^\dagger = P_{23}P_{12} \neq P_{12}P_{23}$, so clearly $\pi_a^\dagger \neq \pi_a$. As a result, each term in Eq. (5.11) has a specific $\overline{\mathbf{p}}'_{\pi_a^\dagger}$ in which only the particle labels are permuted regarding $\overline{\mathbf{p}}'$.

The application of the presented method is remarkable efficient. For illustration, we give the explicit form of the (charge-independent) 1π-exchange potential

$$V_{\text{OPE}}(\overline{\mathbf{p}}, \overline{\mathbf{p}}') \sim \left[\frac{\boldsymbol{\sigma}_1 \cdot \mathbf{q}_{(1)}\, \boldsymbol{\sigma}_2 \cdot \mathbf{q}_{(1)}}{q^2_{(1)} + m^2_\pi} - \frac{\mathbb{1} + \boldsymbol{\sigma}_1 \cdot \boldsymbol{\sigma}_2}{2} \frac{\mathbb{1} + \boldsymbol{\tau}_1 \cdot \boldsymbol{\tau}_2}{2} \frac{\boldsymbol{\sigma}_1 \cdot \mathbf{q}_{(2)}\, \boldsymbol{\sigma}_2 \cdot \mathbf{q}_{(2)}}{q^2_{(2)} + m^2_\pi} \right] \boldsymbol{\tau}_1 \cdot \boldsymbol{\tau}_2 \,, \tag{5.13}$$

with $\mathbf{q}_{(1)} = \mathbf{q}(\overline{\mathbf{p}}, \overline{\mathbf{p}}')$, $\mathbf{q}_{(2)} = \mathbf{q}(\overline{\mathbf{p}}, \overline{\mathbf{p}}'_{\pi_2^\dagger})$, and $\pi_2^\dagger = P_{ij}^\dagger = P_{ij}$; in this case, simply $\mathbf{q}_{(a)} \equiv (-1)^{a-1}\,\mathbf{p}' - \mathbf{p}$. The matrix representations of $\boldsymbol{\sigma}_i$, $\boldsymbol{\tau}_i$, and the momentum $\mathbf{p}_i$ corresponding to Eq. (5.2) are obtained within a few simple lines of code. Using *Wolfram* Mathematica, one has for an arbitrary A:

$$\sigma[\ i\ ] := \textbf{Table}[\ \textbf{KroneckerProduct}[\ \mathbb{1}_2,\ \mathbb{1}_2,\ \ldots,\ \underbrace{\textbf{PauliMatrix}[\ j\ ],\ \mathbb{1}_2}_{i\text{th particle}},\ \mathbb{1}_2,\ \mathbb{1}_2,\ \ldots\ ]\ , \{j, 3\}\ ]$$

$$\tau[\ i\ ] := \textbf{Table}[\ \textbf{KroneckerProduct}[\ \mathbb{1}_2,\ \mathbb{1}_2,\ \ldots,\ \underbrace{\mathbb{1}_2,\ \textbf{PauliMatrix}[\ j\ ]}_{i\text{th particle}},\ \mathbb{1}_2,\ \mathbb{1}_2,\ \ldots\ ]\ , \{j, 3\}\ ]$$

$$p[\ i,\ a\ ] := \textbf{Table}[\ \mathbb{1}_{4^A}\, \text{pval}[\ i,\ j\ ,\ a\ ]\ , \{j, 3\}\ ] \quad \textit{(* for each momentum operator *)}$$

Notice that the last line is only a template: each momentum operator (e.g., the momentum transfer etc.) has an individual definition in terms of the external argument “pval[$\cdot$]”. The involved vector algebra in the nuclear forces can be represented conveniently on a computer by imposing, e.g., the functions ScalarProduct[$\mathbf{v}_1$, $\mathbf{v}_2$] and TripleProduct[$\mathbf{v}_1$, $\mathbf{v}_2$, $\mathbf{v}_3$] for scalar and triple products, respectively, based on vectors having matrices as components. For simplicity, we show here only examples for NN forces, the procedure is, however, analogous for higher-body forces but involves much more terms.

To take care of the charge-dependence of the NN forces, it is convenient to introduce two sets of operators projecting on states with $|m_T = \pm 1, 0\rangle$ and $|T = 1, 0\rangle$, respectively,

$$P_{m_T=\pm1} = \frac{T_z \pm 1}{2} T_z \,, \qquad P_{m_T=0} = (1+T_z)(1-T_z)\,, \tag{5.14a}$$

$$P_{T=0} = \frac{1 - \boldsymbol{\tau}_1 \cdot \boldsymbol{\tau}_2}{4}\,, \qquad P_{T=1} = \frac{3 + \boldsymbol{\tau}_1 \cdot \boldsymbol{\tau}_2}{4}\,, \tag{5.14b}$$

where $\mathbf{T}^{(z)} = \left(\boldsymbol{\tau}_1^{(z)} + \boldsymbol{\tau}_2^{(z)}\right)/2$ is the z-component of the total isospin $\mathbf{T}$. We have already discussed how to construct the corresponding matrices in spin-isospin space. In practice, one fits linear combinations of the LECs in Sec. 2.1 to scattering data, so at LO one has the so-called spectral LECs

$$\widetilde{C}_{^1S_0}^{(m_T=\pm1,0)} = 4\pi\left(C_S^{(m_T)} - 3C_T^{(m_T)}\right), \qquad \text{and} \qquad \widetilde{C}_{^3S_1}^{(m_T=0)} = 4\pi\left(C_S^{(m_T=0)} + C_T^{(m_T=0)}\right), \tag{5.15}$$

associated with the four allowed S-wave channels. The system (5.15) is however under-determined due to the six $C_{S,T}^{(m_T=\pm1,0)}$. We exploit the freedom to choose an isospin-independent $C_T^{(np)} = C_T^{(pp)} = C_T^{(nn)}$ and determine the other LECs by inversion. Applying the projection operators (5.14a) the charge-dependent LO contact interactions can be considered by

$$O_{C,\mathrm{CD}} = C_S^{(pp)}\, P_{m_T=+1} + C_S^{(nn)}\, P_{m_T=-1} + C_S^{(np)}\, P_{m_T=0}\,, \qquad \text{and} \qquad V_S^{(0,\mathrm{cont})} = C_T^{(np)}\,, \tag{5.16}$$

in place of the scalar functions in Eq. (2.10), i.e., $V_C^{(0,\mathrm{cont})} = 0$. Note that operator $O_{C,\mathrm{CD}}$ complements the NN forces in Eq. (2.2).

Additionally, we take into account the charge-dependence of the 1π-exchange potential due to different pion masses. Using the projection operators in Eqs. (5.14a) and (5.14b) the formal definition reads

$$\begin{aligned} O_{\mathrm{OPE,CD}}(q) = \boldsymbol{\sigma}_1 \cdot \mathbf{q}\, \boldsymbol{\sigma}_2 \cdot \mathbf{q} \Big[& V_T^{(0,pp)}(q)\, P_{m_T=+1} + V_T^{(0,nn)}(q)\, P_{m_T=-1} \\ & + \left(V_T^{(0,np)}(q;\, T=1)\, P_{T=1} + V_T^{(0,np)}(q;\, T=0)\, P_{T=0}\right) P_{m_T=0} \Big], \end{aligned} \tag{5.17}$$

which also complements the NN forces in Eq. (2.2) in place of Eq. (2.9). In conclusion, we stress that even terms defined in a coupled basis are not challenging and can be included using projection operators.

Next, we apply the presented method to the formal definitions in Eqs. (2.2), (5.16) and (5.17) for NN forces, in Eqs. (2.43) for 3N forces, and in Eq. (2.71) for 4N forces in order to generate efficiently the momentum-dependent matrices in spin-isospin space. We automate moreover the conversion of *Wolfram* Mathematica's symbolic objects into function declarations in C++. The total number of matrix elements increases rapidly with 4^{2A}. However, due to the conserved number of neutrons and protons only $4^A \binom{2A}{A}$ are actually nonzero. Typical values are 8 ($A = 1$), 96 ($A = 2$), 1280 ($A = 3$), and 17920 ($A = 4$) which is relative to the total number (roughly) 50 % ($A = 1$), 38 % ($A = 2$), 31 % ($A = 3$), 27 % ($A = 4$). The interaction matrices are consequently sparse.

We define the actual values of the LECs as well as the functional form of the scalar (or structure) functions in C++. This gives us the flexibility to study a wide range of NN potentials without regenerating matrices. Among the available NN potentials one has in fact dimensional or spectral-function regularization, different power countings, and more conventional subtleties which affect particularly the pionic part even at same order in the chiral expansion. The different sets of potentials require therefore in general individual implementations. In this section, we study the EGM potentials up to N^{3}LO, the sim potentials up to N^{2}LO, and in the same convention [8] also at N^{3}LO.

For 3N and 4N forces, we split once more the forces into contributions proportional to either a physical LEC or a control parameter being zero or one (see also Sec. 4.1). Specifically, we have five matrices for c_1, c_3, c_4, c_D, c_E at N^{2}LO as well as one for C_T, two (different) for C_S, and four additional matrices for the N^{3}LO 3N forces. In addition, we obtain seven matrices for the leading 4N forces, two are proportional to C_T, one to C_T^2, and again four additional matrices.

Concerning all many-body forces we focus here on nonlocal, symmetric regulators as in Sec. 4. Since the regulator and the antisymmetrizer commute, we generate the matrices disregarding regularization and additional factors such as the Kamada-Glöckle transform in the NN forces. These are considered in the many-body calculation. However, this procedure is not mandatory and any momentum-space regulator may be included in Eq. (5.11).

As noted above, one should consider the scalar functions of the NN potentials with care due to the different conventions in the literature. Apart from being tedious work to implement the required operatorial definition (in momentum space) might not always be given. For example, RG-evolved (many-body) potentials are only available in partial waves. Moreover, since the N^{3}LO NN potential EM 500 MeV varies the regulator exponent in different partial waves (see Table F.2 in Ref. [6]) the actual operatorial definition is no longer accessible. Coordinate-space or semilocal potentials with numerical Fourier-Bessel transforms to momentum space are also settled in this category.

In these cases, we make use of the partial-wave decomposed potentials. Decoupling and summing over partial waves reverts the partial-wave decomposition (see Sec. 2.1.2). For NN forces, the reconstruction leads to the expression

$$\begin{aligned}
&\langle(\sigma_{1'}\tau_{1'})(\sigma_{1'}\tau_{2'})|\mathscr{A}_{12}V_{\mathrm{NN}}\left(\overline{\mathbf{p}},\overline{\mathbf{p}}'\right)|(\sigma_1\tau_1)(\sigma_2\tau_2)\rangle \\
&\qquad= (4\pi)^2 \sum_{J,L,L'} i^{L-L'} \sum_{S,T} \mathscr{C}^{Sm_S}_{1/2\sigma_1 1/2\sigma_2} \mathscr{C}^{Sm_{S'}}_{1/2\sigma_{1'} 1/2\sigma_{2'}} \\
&\qquad\quad\times \mathscr{C}^{Tm_T}_{1/2\tau_1 1/2\tau_2} \mathscr{C}^{Tm_T}_{1/2\tau_{1'} 1/2\tau_{2'}} V^{JT}_{LL'S}(p,p') \left[1-(-1)^{L+S+T}\right] \\
&\qquad\quad\times \sum_{M} \mathscr{C}^{JM_J}_{LMSm_S} \mathscr{C}^{JM_J}_{L'M'Sm_{S'}} Y^{*M}_{L}(\theta_{\mathbf{p}},\varphi_{\mathbf{p}}) Y^{M'}_{L'}(\theta_{\mathbf{p}'},\varphi_{\mathbf{p}'}) \,,
\end{aligned} \tag{5.18}$$

with in- and outgoing relative momenta $\mathbf{p}$ and $\mathbf{p}'$, respectively, spherical harmonics $Y_L^M(\theta_{\mathbf{p}},\varphi_{\mathbf{p}})$, and the abbreviations

$$m_S = \sigma_1 + \sigma_2 \,, \qquad m_{S'} = \sigma_{1'} + \sigma_{2'} \,, \qquad m_T = \tau_1 + \tau_2 = \tau_{1'} + \tau_{2'} \,, \tag{5.19a}$$

$$M_J = M + M_S \,, \qquad M' = M + M_S - M_{S'} \,. \tag{5.19b}$$

This partial-wave approach to the Monte-Carlo framework opens our studies to (in principle) any currently available NN potential and, in particular, it allows unbiased comparisons to our previous calculations in a partial-wave basis. The sums in Eq. (5.18) are limited by $J \leqslant J_{\max}$. In the limit $J_{\max} \to \infty$ the two representations lead to same results, whereas in practice one observes controllable deviations. It is only a technical issue of optimization to incorporate accordingly 3N matrix elements. Due to the significantly increased memory and runtime requirements this is however a challenging task. Being able to access decomposed NN and 3N forces is interesting for studying (semi)local or consistently-evolved many-body forces. Work along these lines is currently in progress but this is here clearly not yet in the focus.

The overall implementation of the chiral NN, 3N, and 4N forces up to N^{3}LO is enormous. Careful benchmarks are in order:

- *Hermiticity.* Since the A-body interactions are Hermitian the corresponding matrices in spin-isospin space fulfill the condition

$$\begin{aligned}\left\langle(\sigma_{1'}\tau_{1'})\ldots(\sigma_{A'}\tau_{A'})\right|\mathscr{A}_A V_{\mathrm{AN}}\left(\bar{\mathbf{p}},\bar{\mathbf{p}}'\right)\left|(\sigma_1\tau_1)\ldots(\sigma_A\tau_A)\right\rangle \\ =\left\langle(\sigma_1\tau_1)\ldots(\sigma_A\tau_A)\right|\mathscr{A}_A V_{\mathrm{AN}}\left(\bar{\mathbf{p}}',\bar{\mathbf{p}}\right)\left|(\sigma_{1'}\tau_{1'})\ldots(\sigma_{A'}\tau_{A'})\right\rangle^{\dagger} .\end{aligned} \tag{5.20}$$

  However, the matrices itself are, in general, *not* Hermitian unless the initial and final momenta are interchanged explicitly. We verify that the condition (5.20) is always fulfilled.

- *Scalar functions of the NN forces.* To check our implementation of the rather lengthy scalar functions V_i, W_i which enter the pionic part in Eq. (2.2) Andreas Ekström provided us with benchmark values at several momenta. This probes also the convergence of the nonanalytic spectral-function integrals.

- *Partial-wave decomposition of the NN forces.* As another application of the implemented machinery, we partial-wave decompose several NN potentials into the coupled basis $|p(LS)JTm_T\rangle$ using Eqs. (2.42). For numerical comparisons in channels with $J \leqslant 8$ Boris Carlsson provided us with the matrix elements of N^{2}LOsim 500/290 MeV. The LECs of the sim potentials are tabulated in the supplementary material of Ref. [15].

- *MBPT for infinite matter.* For consistency checks, we use both, the operatorial and the complementary partial-wave approach in Eq. (5.18) to compute the NN-only contribution to the energy per particle in neutron and symmetric matter using MBPT. We observe, in general, a remarkable partial-wave convergence beyond second order. More details can be found in the next section.

5.2 Automated computation of energy contributions for infinite-matter calculations

Taking advantage of the formalism developed in the previous section, the implementation of energy diagrams in MBPT for infinite matter is straightforward. Without needing algebraic transformations prior to computation (i.e., an involved partial-wave decomposition), the corresponding analytic expressions (like the ones in Sec. 1.3.1) can be translated directly into optimized source codes for high-performance computing. Technically, the spin- and isospin traces are automated by nested *for* loops which sum over all spin-isospin configurations of the integrand involving strings of interaction matrix elements, momentum-distribution functions, the energy denominator, regulators, and normal ordering. In contrast to the partial-wave approach in Sec. 4, the procedure here is so generic and flexible that additional (e.g., higher-order) contributions can be considered rather quickly while all approximations on the many-body interactions, such as the common $P = 0$ approximation for normal ordering [43, 133], are obsolete as they are no longer essential in this framework. The evaluation of a given energy expression is thus exact up to numerical convergence of the multidimensional integration that can be tuned, however, to the required accuracy (see also Sec. 5.3). Altogether, this method is well-suited for improving and extending widely current state-of-the-art infinite-matter calculations with consistent many-body forces at N^{3}LO.

The number of diagrams increases rapidly beyond third order in MBPT [122, 129], especially, if all normal-ordered terms are treated explicitly. Within the Monte-Carlo framework, a manual implementation of these is definitely feasible but tedious and at least inefficient. On the other hand, the procedures in the energy expressions (e.g., spin-isospin traces and normal ordering) give rise to automation instead of coding each individual term manually. That is, the computation of these contributions is realized by conceptional code templates.

Motivated by this observation, we present here an *automated* method for writing optimized source code in the language C++ that computes the energy per particle of an analytically-given expression in MBPT. Moreover, we attach the source codes with dynamically generated and context-sensitive comments, so the output is transparent and human readable. As a first application, we focus on the energy expressions

Table 5: Total dimension N_{dim} of the overall momentum integral after considering momentum conservation for several orders N_{ord} in MBPT, see Eq. (5.23). The first column refers to the many-body interactions of the energy expression. At the normal-ordered two-body level, one has $2^{N_{\text{ord}}}$ terms where up to N_{ord} NN vertices are replaced by normal-ordered 3N contributions, counted by N_{NO}. For example, $N_{\text{ord}} = 3$ "with $2 \times \overline{\text{3N}}$" denotes a third-order calculation in the configuration NN-$\overline{\text{3N}}$-$\overline{\text{3N}}$ or likewise any other permutation. In parentheses, we show the expected values of neglected contributions. See also Sec. 1.3.2 for details. Note that at third order (and beyond) also mixed contributions involving both genuine NN and 3N vertices appear which are not shown.

			total dimension N_{dim} of the integral			
vertices	A	N_{NO}	$N_{\text{ord}} = 1$	$N_{\text{ord}} = 2$	$N_{\text{ord}} = 3$	$N_{\text{ord}} = 4$
NN-only	2	0	6	9	12	15
with $1 \times \overline{\text{3N}}$	2	1	–	12	15	(18)
with $2 \times \overline{\text{3N}}$	2	2	–	15	18	(21)
with $3 \times \overline{\text{3N}}$	2	3	–	–	21	(24)
with $4 \times \overline{\text{3N}}$	2	4	–	–	–	(27)
3N-only	3	0	9	15	(21)	(27)
4N-only	4	0	12	(21)	(30)	(39)

in Sec. 1.3.1 but the general concept is by no means limited to that. Regarding the level of automation, we do not attempt formal rigor as the following method is based on our personal experience with coding these expressions. We have carefully checked that the generated source codes match our manual implementation. This is an important milestone, especially, for higher-order applications.

The automated writing of source code is computationally inexpensive. We choose *Wolfram* Mathematica as the only requirement is symbolic computation. Any other comparable language may equally be used. In the following, we sketch the concept of the developed source-code generator for further use in C++. The examples illustrate the implementation of the particle-hole contribution (1.29b) at third-order:

1. *Preparation and book-keeping.* As a first step, we make the analytic expression accessible to the computer. We organize the diagrams of interest in the following data format containing the overall (combinatorial) factor, the indices of the interaction matrix elements, and the denominator, respectively, e.g.,

$$F = +1\,, \qquad V = \{\{a,b,i,j\},\{i,c,a,k\},\{j,k,b,c\}\}\,, \qquad D = \{\{i,j,a,b\},\{j,k,b,c\}\}\,. \tag{5.21}$$

   An additional tag is required in the case of external indices (over which is not summed). For instance, the self-energy correction in the Hartree-Fock approximation is a one-body quantity depending on spin and isospin in addition to momentum. In general, this is the only input of the algorithm. All other information can be inferred, such as the order of the diagram $N_{\text{ord}} = 3 \geqslant 1$ or the indices of summation $I_a = \{a, b, c, i, j, k\}$. Notice that V may also contain different many-body matrix elements, e.g., due to normal ordering. Another useful application of this book-keeping system is the automated output of the corresponding LaTeX-code, i.e., for Sec. 1.3.1. It is also natural to check for consistency such as verifying momentum conservation. Several typos in the literature suggested us to rederive the energy expressions up to fourth order using their diagrammatic representation. For completeness, we note that future studies may employ graph theory to even automate this step. That is, the order in MBPT would be the ultimate input of such calculations. Algorithms along these lines have already been worked out (see Refs. [122, 126–128]). This technical issue, however, is clearly not needed here but gains in importance beyond fourth order. In any case, being able to evaluate systematically many diagrams is crucial.

2. *Consider momentum conservation.* Since the interaction matrix elements conserve total momentum the integrals over $N_{\mathrm{ord}}-1$ momentum vectors are trivial. The underlying (usually omitted) Dirac distributions can be expressed as a system of N_{ord} equations, e.g.,

   $$\mathbf{p}_a + \mathbf{p}_b = \mathbf{p}_i + \mathbf{p}_j\,, \qquad \mathbf{p}_i + \mathbf{p}_c = \mathbf{p}_a + \mathbf{p}_k\,, \qquad \text{and} \qquad \mathbf{p}_j + \mathbf{p}_k = \mathbf{p}_b + \mathbf{p}_c\,, \tag{5.22}$$

   as obtained from V in Eq. (5.21). To improve the numerical convergence, we exploit the ambiguity in the solution in order to favor, if possible, trivial particle integrations. As opposed to holes, particles have a larger (strictly, even infinite) phase space. For book-keeping reasons, we define the ordered set of nontrivial (trivial) labels I_n (I_t). Regarding Eq. (5.22) the integrals related to $\mathbf{p}_x$ with, e.g., $x \in I_n = \{a, i, j, k\}$ are nontrivial while $\mathbf{p}_b = -\mathbf{p}_a + \mathbf{p}_i + \mathbf{p}_j$ and $\mathbf{p}_c = \mathbf{p}_a - \mathbf{p}_i + \mathbf{p}_k$ are constrained by the other momenta, so $I_t = \{b, c\}$.

3. *Initialize the integrator.* With these prerequisites, we are now in the position to write source code that initializes an adaptive Monte-Carlo integrator (e.g., Vegas). A more detailed description can be found in Sec. 5.3. The integrator samples (pseudo-)random momentum vectors $\mathbf{p}$ of rank

   $$N_{\mathrm{dim}} = 3\,((A-1)N_{\mathrm{ord}} + N_{\mathrm{NO}} + 1) \tag{5.23}$$

   in the unit-hyper cube, i.e., $[0,1]^{N_{\mathrm{dim}}}$. The (nontrivial) three-dimensional vectors in $\mathbf{p} = \mathbf{p}_a \oplus \mathbf{p}_i \oplus \mathbf{p}_j \oplus \mathbf{p}_k$ are indexed by I_n. Here, $A \geqslant 1$ corresponds to the (possibly effective) A-body matrix elements of the energy expression and $N_{\mathrm{NO}} \leqslant N_{\mathrm{ord}}$ is the number of particles which are summed over the reference state for normal ordering. For instance, a third-order calculation ($N_{\mathrm{ord}} = 3$) at the normal-ordered two-body level ($A = 2$) with $N_{\mathrm{NO}} = 2$ effective NN vertices, e.g., NN-$\overline{\mathrm{3N}}$-$\overline{\mathrm{3N}}$, has $N_{\mathrm{dim}} = 18$. Table 5 summarizes the relevant values for this work, ranging from 6 to 21.

4. *Definition of the integrand.* In this step, we automate coding the complex-valued integrand function:

   - Governed by the spherical symmetry of the Fermi sea, we linearly transform the sampled unit-hyper cube to spherical coordinates with magnitudes in the range

     $$0 \leqslant p_{i,j,\ldots} \leqslant \max\left(k_{\mathrm{F}}^{n},\, k_{\mathrm{F}}^{p}\right)\,, \qquad \text{and} \qquad \min\left(k_{\mathrm{F}}^{n},\, k_{\mathrm{F}}^{p}\right) \leqslant p_{a,b,\ldots} \leqslant \Lambda_{\mathrm{lim}}\,, \tag{5.24}$$

     for holes and particles, respectively. The actual phase space is then further constrained by the isospin- and momentum-dependent distribution functions during the calculation. Neutron and symmetric matter allow for additional optimization. The particle phase space is infinite, i.e., $\Lambda_{\mathrm{lim}} \to \infty$, in practice, however, we set a large although finite cutoff $\Lambda_{\mathrm{lim}} \sim (10-15)\,\mathrm{fm}^{-1}$ that is reliable for the regularized interactions considered here. Its specific value affects the rate of convergence. In fact, given a diagram, Λ_{lim} can be constrained analytically in terms of the cutoff by exploiting momentum conservation. Our employed range is rather conservative. Since the overall phase space is typically large, whereas some regions are suppressed or even vanishing, the rate benefits significantly from adaptive algorithms.

   - We consider momentum conservation in Cartesian coordinates. Once $\mathbf{p}_x$ with $x \in I_t$ is determined by $\mathbf{p}$ according to step (2), all momenta (in I_a) are properly defined. For each matrix element in V individually, we set up the Cartesian initial and final $3A$-dimensional momentum vectors $\overline{\mathbf{p}}$ and $\overline{\mathbf{p}}'$, respectively, as given in the previous section.

- The indices in I_a lead to nested *for* loops over all binary spin-isospin configurations. Checking for nonzero phase space and total-isospin conservation (see Sec. 5.1) helps to keep the runtime tractable. The denominator follows from D, where the single-particle energy in a Hartree-Fock spectrum is prestored for interpolation on a dense grid. Notice that depending on N_{ord} the body of the *for* loops may contain additional sums due to normal ordering. For each interaction matrix element, we determine the position in the spin-isospin basis η, η' via Eq. (5.6) and call the corresponding complex-valued function in C++ at $\overline{\mathbf{p}}$, $\overline{\mathbf{p}}'$.

- Finally, we multiply global spin- and isospin-independent factors such as the (symmetric) regulators, the Jacobi determinant, or combinatorial factors. In case of a spin-isospin averaged single-particle spectrum, the energy denominator may also be factorized here. Notice that this is the approximation we used in our partial-wave calculations in Sec. 4.

As a first application at zero temperature, we consider the energy expressions in Secs. 1.3.1 and 1.3.2, respectively. Apart from improving our partial-wave calculations in Sec. 4, especially in terms of normal ordering, the contributions from NN forces up to fourth order in MBPT, the third-order particle-hole diagram including normal-ordered 3N forces, and from the residual 3N term at second order are added. Accounting for the latter was so far only possible in very specific cases, like contact interactions [245]. We treat all diagrams induced by normal-ordered vertices separately following our discussion in Sec. 1.3.2. Technically, this allows here moreover to factorize one single multidimensional integral for Monte-Carlo integration. At third order, index relabeling reveals that the hole-hole and particle-particle contribution in the pairs NN-NN-$\overline{\text{3N}}$, $\overline{\text{3N}}$-NN-NN and $\overline{\text{3N}}$-$\overline{\text{3N}}$-NN, NN-$\overline{\text{3N}}$-$\overline{\text{3N}}$, respectively, are each equal, so only 20 (instead of 24) diagrams are independent. At fourth order, we count 624 diagrams in total. While similar arguments may help still many contributions will remain. The Monte-Carlo framework is well-suited to tackle this challenge, as a first step, however, we consider only NN contributions at fourth order. To estimate the neglected 3N contributions, we employ our $P = 0$-approximated effective NN potentials (see Sec. 4.1) at the level of partial waves using Eq. (5.18). This has the advantage that the sum of all sub-diagrams is computed at once.

Assuming that the energy expressions are available in a closed form, there are only two technical issues that may hinder going up to fifth order (or even higher). That is, the numerical convergence of the multidimensional integrals and computer resources, specifically, a reasonable runtime. Compared to the partial-wave method in Sec. 4, up to 21-dimensional integrals are certainly *high-dimensional*, however, still far away from being at the cutting-edge (see, e.g., variational Monte-Carlo and Sec. 5.3). The overall runtime is therefore the more crucial factor. In fact, the implementation of presented framework requires optimization to a high level. To obtain converged results the integrand is typically sampled at $10-20$ million random points, whereas the increasing number of both, the spin-isospin configurations and the interaction vertices makes the runtime quite sensitive to how efficient the many-body interaction matrix elements can be computed. Hence, we systematically avoid reevaluations of same expressions, e.g., by algebraic transformations or defining additional scalar functions. Eventually, also thanks to the professional Christian Iwainsky from the Lichtenberg-Hochleistungsrechner of the Technische Universität Darmstadt, we achieved an excellent overall performance which is very encouraging for pushing the limits even further.

Concluding the section, we carefully check the results of this framework. Some of these are:

- *Third-order calculation in partial waves.* Referring to Refs. [111, 112] Jeremy Holt provided us with third-order results (including the particle-hole term) in symmetric matter at several densities based on the N^{3}LO NN potential EM 500 MeV. At saturation density, we find agreement within ~ 1 % (or better), except for the particle-hole contribution, where the larger deviation of $\sim (5-10)$ % is likely related to the (reduced) partial-wave convergence of the provided values. In addition, our results agree within ~ 1 % (or even better) with the semianalytic third-order particle-hole contributions obtained in Ref. [112] for two test interactions.

- *$k_F a_s$ expansion: third-order particle-hole term.* The low-density expansion of the energy per particle in powers of $k_F a_s$ is well-known (see also Ref. [246] and references therein). Following Ref. [112] we compare our particle-hole results at third order in neutron and symmetric nuclear matter, respectively, to the corresponding term in the semianalytic expansion (see also Ref. [113])

$$\left.\frac{E(k_F)}{N}\right|_{\text{PNM}} = 2.79505\,\frac{k_F^5}{\pi^4 m} a_s^3 \quad \text{and} \quad \left.\frac{E(k_F)}{A}\right|_{\text{SNM}} = 1.04814\,\frac{k_F^5}{\pi^4 m}(a_s + a_t)(5a_s^2 - 14a_s a_t + 5a_t^2)\,, \tag{5.25}$$

  which relies on the LO contact interactions $C_S = -\frac{\pi}{m}(a_s + 3a_t)$ and $C_T = -\frac{\pi}{m}(a_t - a_s)$. a_s and a_t are the S-wave scattering lengths. Since the particle-hole contribution does not diverge with $\Lambda \to \infty$, i.e., $f_R \equiv 1$, Eqs. (5.25) allow a direct benchmark at all densities. Although the phase space is huge without regulator functions our method can reproduce Eq. (5.25) with (in principle) arbitrary accuracy, no matter which density or scattering length we have tested.

- *Hartree-Fock energy of the N^{3}LO 3N and 4N forces.* We agree within $\lesssim 1\,\text{keV}$ with the 3N and 4N Hartree-Fock energies at N^{3}LO obtained seminanalytically in Refs. [108, 140] for neutron and symmetric matter (see also Refs. [31, 205]). The results have been provided by Kai Hebeler, Thomas Krüger, and Ingo Tews. Notice that all methods use a single-particle basis.

- *Various other contributions.* We compare moreover to the semianalytic calculations by Alex Dyhdalo up to second order (including the residual 3N contribution) based on LO NN and N^{2}LO 3N forces (see also Ref. [18]). Additional third-order benchmarks have been provided by Kai Hebeler.

- *Numerical convergence.* We use different strategies to assess the convergence of the multidimensional integrals. These include different Monte-Carlo algorithms (see Sec. 5.3) as well as varying the number of sampling points and iterations. We also check that the results are independent of Λ_{lim}. We aim a numerical uncertainty of $\sim 1\,\text{keV}$ per individual contribution.

5.3 Multidimensional integration using Monte Carlo

In a broad sense, Monte Carlo refers to various strong computational methods that are based on random numbers. As it is an integral part of the developed framework for MBPT, we briefly emphasize here the specific aspect of numerical integration over multidimensional hypervolumes and discuss conceptual differences with the quadrature methods employed in the other projects of this thesis. We also refer the reader to Refs. [247–249] and the references therein.

For computation, an integral over the (hyper-)volume V is approximated by a discrete sum,

$$I[f] := \int_V \mathrm{d}\mathbf{x}\, f(\mathbf{x}) \equiv \int_V \mathrm{d}\mathbf{x} \left[\frac{f(\mathbf{x})}{p(\mathbf{x})}\right] p(\mathbf{x}) \simeq I_N[f] \qquad \text{with} \qquad \lim_{N\to\infty} I_N[f] = I[f]\,, \tag{5.26}$$

where we introduce (for now) an arbitrary function with $p(\mathbf{x}) > 0$ everywhere in V. Furthermore, we assume that the integral exists, i.e., that it has a finite value. Note that $I_N[f]$ might even be exact at finite N depending on the integrand and the applied algorithm. In the other projects of this thesis, we set $p(x) \equiv 1$ and employ $I_N[f] = \sum_{i=1}^{N} w_i f(\mathbf{x}_i)$. The weights w_i as well as the sampling points $\mathbf{x}_i$ are predetermined by the quadrature formula (in multiple dimensions, also called cubature [250, 251]), e.g., Gauss quadrature or the simple trapezoidal rule. Quadrature is therefore a common tool for converting integral equations to matrix equations, see Secs. 3 and 6 for applications. To evaluate multidimensional integrals, however, these methods are less efficient as the following example demonstrates: approximating a 21-dimensional integral by only 10 sampling points in each direction, would lead to $N = 10^{21}$ integrand evaluations while the convergence is likely still poor.

On the other hand, the *nondeterministic* Monte-Carlo methods consider $p(\mathbf{x})$ as a probability density, i.e., $I[p] = 1$, such that $I[f] \equiv \langle f/p \rangle$ is the expectation value,

$$\langle g \rangle := \int_V \mathrm{d}\mathbf{x}\, g(\mathbf{x})\, p(\mathbf{x}), \tag{5.27}$$

of the integrand function $[\,\cdot\,]$ in Eq. (5.26). The integral is then approximated by the *statistical* average

$$I_N[f] \equiv \left\langle \frac{f}{p} \right\rangle_N = \frac{1}{N} \sum_{i=1}^{N} \frac{f(\mathbf{x}_i)}{p(\mathbf{x}_i)}. \tag{5.28}$$

where $\mathbf{x}_i$ are (pseudo-)random vectors independently sampled from a distribution function in V with probability density $p(\mathbf{x})$. As a result, even complicated (e.g., deformed) volumes are accessible to Monte-Carlo integration without much effort. The statistical average (5.28), moreover, does not rely on continuous functions. These features are advantageous compared to the Gaussian quadrature in Sec. 4.2, where constraining the integral to the (continuous) nonvanishing region of overlapping distribution functions was crucial for convergence.

Because of the central-limit theorem for large N (ideally, $N \to \infty$), results from multiple evaluations of Eq. (5.28) are distributed according to the normal distribution with expectation value $I[f]$ and variance

$$\sigma^2 = \frac{\sigma^2_{f/p}}{N}, \qquad \text{where} \qquad \sigma^2_{f/p} = \left\langle \frac{f^2}{p^2} \right\rangle - \left\langle \frac{f}{p} \right\rangle^2. \tag{5.29}$$

Thus, assuming that the integrals in Eq. (5.29) exist, Monte-Carlo integration is associated with an uncertainty estimate $\delta = \pm\sigma_{f/p}/\sqrt{N}$ which is independent of the dimension d of the integral as opposed to the quadrature rules described above. Since $\sigma_{f/p}$ depends on two unknown integrals, one uses in practice likewise the Monte-Carlo approximated standard deviation [247]

$$\sigma^{(N)}_{f/p} = \sqrt{\frac{1}{N-1}\left(\left\langle \frac{f^2}{p^2} \right\rangle_N - \left\langle \frac{f}{p} \right\rangle_N^2 \right)} \tag{5.30}$$

as a 1σ-uncertainty estimate, so $I[f] \approx I_N[f] \pm \sigma^{(N)}_{f/p}/\sqrt{N}$. Note that the true value is not necessarily inside this interval.

On a case by case basis, specific knowledge of the integrand may help to reduce the variance (5.29) by choosing a suitable $p(\mathbf{x})$. Minimizing $\sigma^2_{f/p}$, in fact, leads to the optimal probability density [249]

$$p(\mathbf{x}) = \frac{|f(\mathbf{x})|}{I[|f|]}, \tag{5.31}$$

but this is unfortunately not of practical use. Advanced Monte-Carlo methods on the contrary, follow two complementary adaptive strategies for variance reduction. While *importance sampling* concentrates the random samples in regions where the magnitude of the integrand is largest, *stratified sampling* favors regions of largest variance. Lepage's well-known Vegas algorithm [247] adapts a piecewise-constant *separable* probability density, i.e., $p(\mathbf{x}) \propto \prod_{i=1}^{d} p_i(x_i)$ to mimic the ideal choice. This specific approach keeps the weight function manageable but comes along with the drawback that the efficiency drops significantly when the important regions of the integrand are not aligned with the coordinate axes [248, 249]. A hybrid subregion-adaptive Vegas algorithm (called Suave), for instance, has been implemented (among several others) in the library "CUBA" [248] to combine the advantages of Vegas' importance sampling and stratified sampling which subdivides V into smaller volumes. Meeting all the requirements "CUBA" is our choice for this project: it is parallelized [252], one can easily switch between several algorithms, and it implements different random-number generators. The low-discrepancy sequences (quasi-random numbers) may improve the rate of convergence compared to pseudo-random numbers.

To mention just one direct application in physics (see also Refs. [149–151]), the discussed Monte-Carlo integration allows constraining ground-state energies. Using the Rayleigh-Ritz principle, the so-called variational Monte Carlo method (VMC) determines an upper bound on the true ground state energy E_0 of an A-body system. Let $\Psi_T(\mathbf{R}, \{\alpha\})$ be a trial wave function that is parametrized by the set $\{\alpha\}$ in order to approximate the true ground-state wave function. The expectation value of the Hamiltonian H is given by [149]

$$E_V^\alpha = \frac{\int d\mathbf{R}\, \Psi_T^\dagger(\mathbf{R}, \{\alpha\}) H \Psi_T(\mathbf{R}, \{\alpha\})}{\int d\mathbf{R}'\, |\Psi_T(\mathbf{R}', \{\alpha\})|^2} \equiv \int d\mathbf{R}\, E_L^\alpha(\mathbf{R})\, p(\mathbf{R}) \simeq \frac{1}{N} \sum_{i=1}^{N} E_L^\alpha(\mathbf{R}_i)\,, \tag{5.32}$$

with

$$E_L^\alpha(\mathbf{R}) = \Psi_T^{-1}(\mathbf{R}, \{\alpha\}) H \Psi_T(\mathbf{R}, \{\alpha\}) \qquad \text{and} \qquad p(\mathbf{R}) = \frac{|\Psi_T(\mathbf{R}, \{\alpha\})|^2}{\int d\mathbf{R}'\, |\Psi_T(\mathbf{R}', \{\alpha\})|^2}\,, \tag{5.33}$$

where $\mathbf{R} = (\mathbf{r}_1, \mathbf{r}_2, \ldots, \mathbf{r}_A)$ is a $3A$-dimensional vector in coordinate space. Monte Carlo is key for computing the multidimensional integral (5.32) in terms of the statistical average (5.28) and the (pseudo-)random vectors $\mathbf{R}_i$ sampled according to the distribution with probability density $p(\mathbf{R})$. Since the Rayleigh-Ritz principle states that $E_V^\alpha \geqslant E_0$ the parameters $\{\alpha\}$ are tuned to obtain the lowest possible bound based on the trial-wave function. The equal sign holds if and only if $\Psi_{\text{g.s.}} \equiv \Psi_{\text{T}}^\alpha$ for some configuration $\{\alpha\}$.

5.4 Saturation properties with NN and 3N forces at N^{3}LO

Recent calculations of medium-mass and heavy nuclei have demonstrated the importance of realistic saturation properties of infinite matter for nuclear forces derived within chiral EFT [4, 14, 23, 29, 253]. While most NN and 3N interactions fitted to only two- and few-body observables are able to predict light nuclei in agreement with experimental data, the theoretical uncertainties tend to increase rapidly with increasing mass number $A \gtrsim 16$ (see, e.g., Ref. [15]) and significant discrepancies to experiment are usually found (see Fig. 1) for properties of heavy nuclei [24]. There have been efforts to include properties of heavier nuclei in the optimization of chiral nuclear forces [14]. Such interactions tend to exhibit more realistic saturation properties of nuclear matter and also show improved agreement with experiment for energies and radii of medium-mass and heavy nuclei [4, 25, 26]. However, the explicit incorporation of nuclear-matter properties in the optimization process of nuclear forces was not feasible so far due to the lack of computational efficiency of such calculations. The new Monte-Carlo framework is tailored for such a task.

In Fig. 36 we present results for the energy per particle in symmetric nuclear matter and neutron matter based on the Hebeler+ [27] and NNLOsim [15] NN and 3N interactions up to fourth order in MBPT. For symmetric matter we indicate the empirical saturation region by a box with the boundaries

$$n_0 = (0.164 \pm 0.007)\,\text{fm}^{-3}\,, \qquad \text{and} \qquad \frac{E}{A}(\beta = 0, n_0) = -(15.86 \pm 0.37 \pm 0.2)\,\text{MeV}\,, \tag{5.34}$$

where the first uncertainties are as in Ref. [28] and we add an additional 0.2 MeV from Ref. [38]. In addition, we give results for the range of the symmetry energy $E_{\text{sym}} = E/N - E/A$ in the qudratic expan-

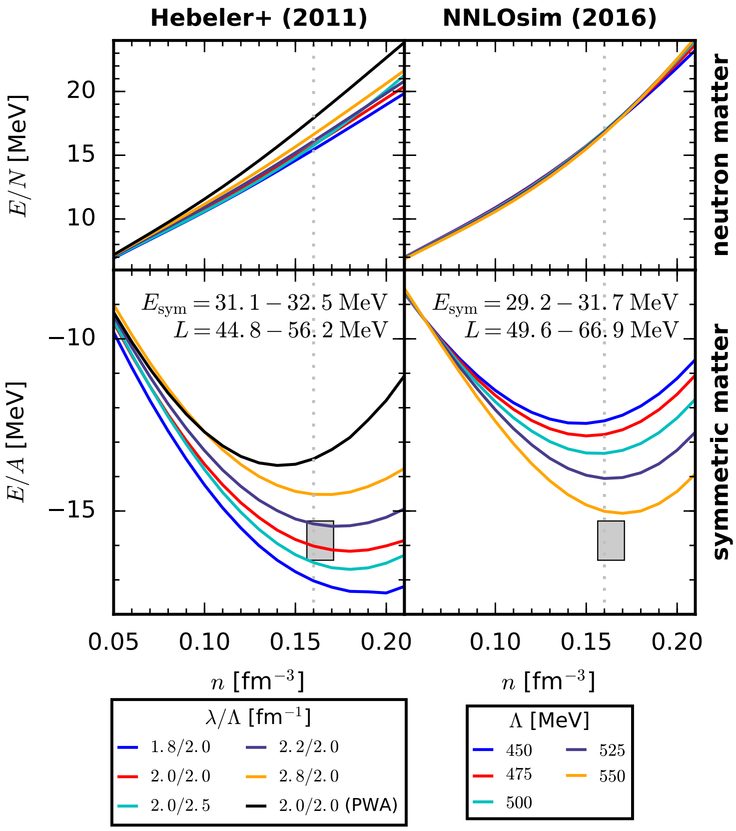

Figure 36: Energy per particle of neutron matter (top row) and symmetric nuclear matter (bottom row) based on the Hebeler+ [27] and NNLOsim [15] NN plus 3N interactions (columns). Results are shown for $\lambda/\Lambda_{\rm 3N}$ (in fm^{-1}) for the interactions of Ref. [27] and $\Lambda_{\rm NN} = \Lambda_{\rm 3N}$ (in MeV) for the interactions of Ref. [15]. For symmetric matter, the gray box denotes the saturation region in Eq. (5.34). We also give the symmetry energy $E_{\rm sym} = E/N - E/A$ and its slope parameter L at $n_0 = 0.16\,\text{fm}^{-1}$ (indicated by the dashed vertical line).

sion (1.2) as well as its slope parameter $L = 3n_0\partial_n E_{\rm sym}$ at saturation density $n_0 = 0.16\,\text{fm}^{-1}$. Both are predicted by narrow ranges.

The Hebeler+ interactions were obtained by a SRG evolution of the N^{3}LO NN potential of Ref. [154] to different resolution scales λ, whereas the 3N couplings c_D and c_E were fixed at these resolution scales by fits to the ^{3}H binding energy and the ^{4}He charge radius. Despite being fitted to only few-body data, these interactions are able to reproduce empirical saturation in Fig. 36 within uncertainties given by the band of the Hebeler+ interactions [27]. In addition, recent calculations of medium-mass and heavy nuclei based on some of these interactions show remarkable agreement (see, e.g., Fig. 1) with experimental data [4, 23, 25, 26, 30, 46] and thus offer new ab initio possibilities to investigate the nuclear chart.

The second column of Fig. 36 shows results for the NNLOsim potentials [15] (using $T_{\rm rel} = 290\,\text{MeV}$) for different cutoff values (see legend). These interactions were obtained by a simultaneous fit of all LECs to two-body and few-body data. We observe a weak cutoff dependence for these potentials in neutron matter over the entire density range and in symmetric matter up to $n \lesssim 0.08\,\text{fm}^{-3}$. At higher densities, the variation of the energy per particle increases up to $\sim 3\,\text{MeV}$ at $n_0 = 0.16\,\text{fm}^{-1}$ with a very similar density dependence. Overall, all the NNLOsim interactions turn out to be too repulsive compared to the empirical saturation region.

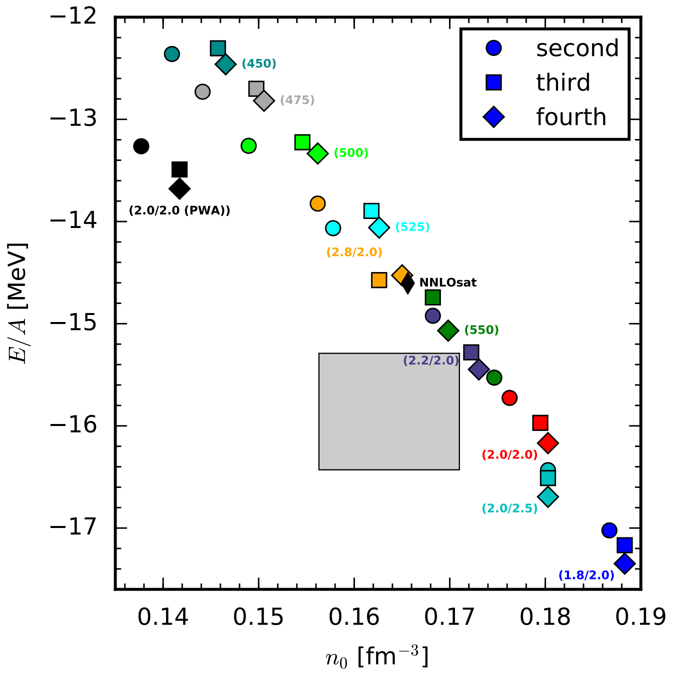

Figure 37: Correlation between the calculated saturation density n_0 and saturation energy E/A for the Hebeler+ [27] and NNLOsim [15] NN and 3N interactions obtained at second, third, and fourth order in MBPT. The values of λ/Λ_{3N} and $\Lambda_{NN} = \Lambda_{3N}$ as well as the saturation region are as in Fig. 36. The diamond refers to the NNLOsat result [14].

We study the many-body convergence of the Hebeler+ and NNLOsim interactions by plotting in Fig. 37 the calculated saturation energy as a function of the calculated saturation density at second, third, and fourth order in MBPT. The annotated values denote the cutoff scales of the different potentials (see legend of Fig. 36). For all shown interactions, we observe a very good convergence in the many-body expansion, indicating that these chiral low-momentum interactions are perturbative over this density regime. Moreover, we find a pronounced linear correlation band (similar to the Coester line [254] for NN potentials), which however overlaps with the empirical saturation region as 3N forces are included. Note that the Hebeler+ interaction that breaks most from the linear correlation is “2.0/2.0 (PWA)”, for which the c_i values in the 3N forces are significantly larger.

Finally, in Table 6 we show the hierarchy of contributions from second, third, and fourth order at $n = 0.16\,\text{fm}^{-3}$ for the Hebeler+ “1.8/2.0” interaction, which is most commonly used in the recent ab initio calculations of medium-mass and heavy nuclei. At second order, we give the contributions from NN interactions (NN-only), from NN plus 3N contributions that can be represented in form of a density-dependent two-body interactions (NN+3N), and the residual 3N contributions (3N res.). We find that the residual 3N term is significantly smaller compared to the other contributions. This justifies that this contribution was usually neglected in previous calculations (as in Sec. 4) because it requires an explicit treatment of 3N forces in MBPT. However, note that this in general depends on details of the NN and 3N interactions [18]. Furthermore, we find that the third-order contributions are significantly smaller than the second-order terms for all studied interactions. The fourth-order contributions are particularly small for the “1.8/2.0” interaction, but also in the other cases smaller than the third-order contributions.

The observed convergence pattern indicates that the studied nonlocal interactions are sufficiently perturbative and allow calculations with controlled many-body uncertainties. This offers the possibility to use the new Monte-Carlo framework for constraining the 3N couplings using information from nuclear matter. In this work, we demonstrate this using the N^{2}LO and N^{3}LO NN potentials of Entem, Mach-

Table 6: Contributions to the energy per particle at $n = 0.16\,\mathrm{fm}^{-1}$ in symmetric nuclear matter at consecutive orders in MBPT based on the Hebeler+ [27] interaction with $\lambda/\Lambda_{3\mathrm{N}} = 1.8/2.0\ \mathrm{fm}^{-1}$ and the N^{2}LO plus N^{3}LO interactions of this work with Λ/c_D for the central c_D fit value (black diamonds) in Fig. 39. All energies are in MeV. Contributions from 3N forces at fourth order in MBPT are not included in our fits. The corresponding values given below are an uncertainty estimate using normal-ordered 3N contributions in the $P = 0$ approximation (see Refs. [28, 43]).

chiral order	"Λ/c_D"	second order			third order	fourth order	
		NN-only	NN+3N	3N res.	NN+3N	NN-only	NN+3N
N^{3}LO/N^{2}LO	$\lambda/\Lambda_{3\mathrm{N}} = 1.8/2.0$	−2.30	−2.24	−0.40	−0.10	−0.20	–
N^{2}LO	$450/+2.50$	−6.23	−13.38	−0.42	−2.08	0.07	0.24
	$500/-1.50$	−8.61	−14.49	−0.66	−0.77	0.32	0.75
N^{3}LO	$450/+0.50$	−8.93	−15.54	−0.38	−2.85	0.61	0.92
	$500/-3.00$	−10.63	−14.65	−0.87	−1.00	0.65	1.10

leidt and Nosyk (EMN) [11] with $\Lambda = 450\,\mathrm{MeV}$ and $\Lambda = 500\,\mathrm{MeV}$. As a first step, we fit to the ^{3}H binding energy, which leads to a relation of the 3N couplings c_D and c_E shown in Fig. 38. For the fits, we include all 3N contributions consistently up to N^{2}LO and N^{3}LO, respectively. The corresponding 3N matrix elements were computed as in Ref. [205]. We use $\Lambda_{3\mathrm{N}} = \Lambda_{\mathrm{NN}} = \Lambda$ and a nonlocal regulator of the form $f_\Lambda(p,q) = \exp[-((p^2 + 3/4q^2)/\Lambda^2)^4]$ for the Jacobi momenta p and q of the initial and final states [191]. For all cutoff values and chiral orders, we obtain c_E couplings of natural size in the wide c_D range explored.

As a second step, we calculate nuclear matter for the range of 3N couplings and determine the saturation point. In Fig. 39, we present the saturation points at N^{2}LO and N^{3}LO as a function of the c_D and at different orders in MBPT. Similar to the interactions shown in Fig. 37, we find a natural convergence pattern. Note that the shown points on the trajectories correspond to different c_D values at second order compared to third and fourth order. Contributions at third order are therefore more significant in these cases, whereas fourth-order corrections are again much smaller as shown in Table 6. In general, Fig. 37 demonstrates that it is possible to determine natural c_D/c_E combinations at N^{2}LO and N^{3}LO with reasonable saturation properties for both cutoff cases considered. However, with respect to our N^{2}LO results, N^{3}LO contributions provide slightly too much repulsion.

In each panel of Fig. 39, we mark the three couplings that provide a reasonable fit to the saturation region by black diamonds, whereas the actual c_D/c_E values are given in the annotations in Fig. 38. The resulting equations of state of symmetric nuclear matter and neutron matter at N^{2}LO and N^{3}LO are shown in Fig. 40. Note that only two lines are present in neutron matter since the shorter-range 3N interactions do not contribute [43]. For completeness, the calculated N^{3}LO 4N Hartree-Fock energies at n_0 are $\sim 150\,\mathrm{keV}$ for both cutoffs, which is indeed negligible compared to the overall uncertainty [140]. As for the Hebeler+ and NNLOsim results, the symmetry energy and the L parameter are predicted with a remarkably narrow range. In symmetric matter, we also observe a weak cutoff dependence at N^{3}LO, whereas the results for $\Lambda = 450\,\mathrm{MeV}$ are clearly separated from $\Lambda = 500\,\mathrm{MeV}$ at N^{2}LO. Finally, we estimate the theoretical uncertainty [9] from the chiral expansion following Eq. (1.12), using $Q = p/\Lambda_b$ with breakdown scale $\Lambda_b = 500\,\mathrm{MeV}$ and average momentum $p = \sqrt{3/5}\,k_\mathrm{F}$. The bands overlap from N^{2}LO to N^{3}LO, and we clearly see that the theoretical uncertainties are significantly reduced at N^{3}LO.

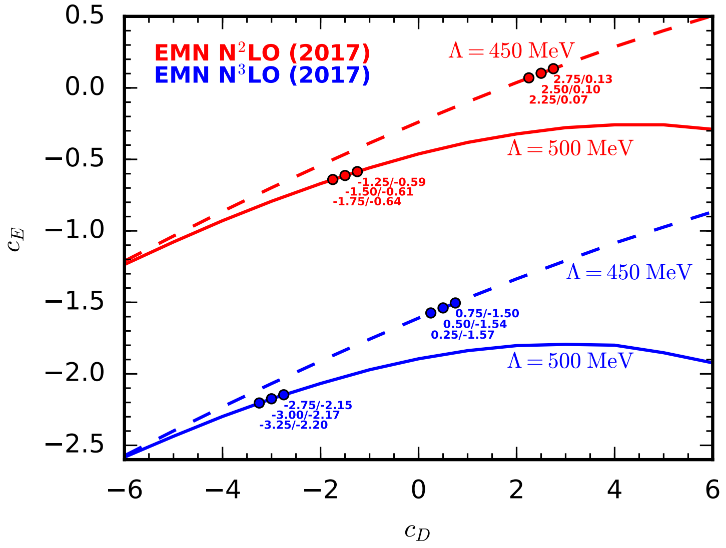

Figure 38: Three-nucleon couplings c_D and c_E that reproduce the ^{3}H binding energy using the EMN NN potentials of Ref. [11] with $\Lambda = 450\,\text{MeV}$ (dashed line) and $\Lambda = 500\,\text{MeV}$ (solid line) at N^{2}LO (red) and N^{3}LO (blue) combined with consistent 3N interactions at these orders with $\Lambda_{\text{3N}} = \Lambda_{\text{NN}} = \Lambda$. The points (diamonds) on each line correspond to the fits to the empirical saturation region (see Fig. 39), while the annotated numbers give the corresponding values of c_D/c_E.

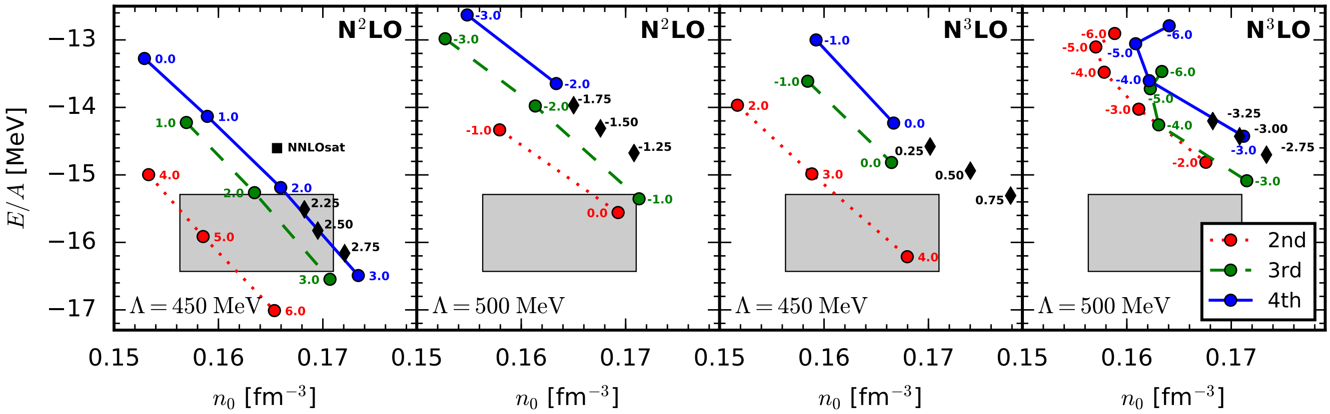

Figure 39: Saturation density and energy at different orders in MBPT for the NN and 3N interactions at N^{2}LO and N^{3}LO of Fig. 38 (at N^{3}LO 4N interactions are negligible). The points are for different values of c_D (annotated numbers), while the red-dotted, green-dashed, and blue-solid lines correspond to calculations at second, third, and fourth order in MBPT. The left (right) two panels are for N^{2}LO (N^{3}LO) with $\Lambda = 450\,\text{MeV}$ and $\Lambda = 500\,\text{MeV}$. The diamonds in each panel represent the calculations with a simultaneous good reproduction of both saturation density and energy at fourth order in MBPT. The empirical saturation region is given by the gray box (see Fig. 36).

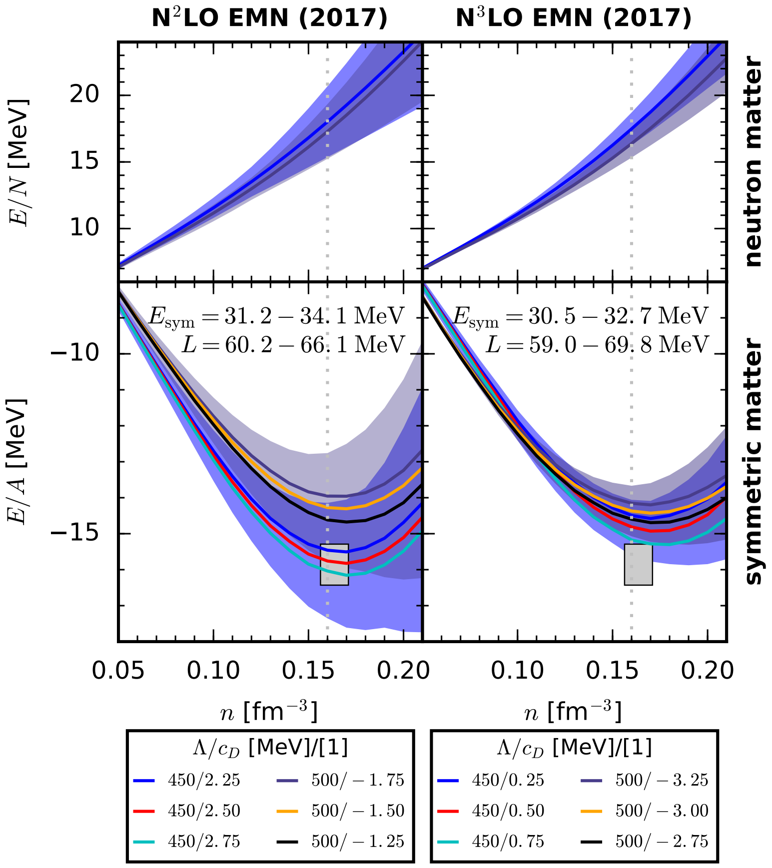

Figure 40: Energy per particle in neutron matter (top row) and symmetric nuclear matter (bottom row) based on chiral interactions at N^{2}LO (first column) and N^{3}LO (second column) fit to the empirical saturation region (see Fig. 39). The fits are labeled by Λ/c_D in the legend. As in Fig. 40, we also give the symmetry energy E_{sym} and its slope parameter L at each order. The blue ($\Lambda = 500$ MeV) and gray ($\Lambda = 450$ MeV) bands estimate the theoretical uncertainty following Ref. [9].

6 BCS pairing gaps in neutron matter: uncertainties and 3N forces

A quantitative understanding of nuclear superfluidity plays a central role for a wide range of phenomena, from the structure of nuclei [255–258] to the cooling of neutron stars [259–262]. This chapter discusses our work on the zero-temperature BCS pairing gap in neutron matter in the $^1S_0$ and $^3P_2$–$^3F_2$ channel [106] based on the recent local (GT+) and semilocal (EKM) chiral NN interactions up to N^{2}LO and N^{4}LO, respectively (see Table 2). We also employ the improved uncertainty estimate by Epelbaum *et al.* [9, 10], which is not based on parameter variation but on an order-by-order analysis in the chiral expansion, as discussed in Sec. 1.2.3.

Obtaining self-consistent solutions of the BCS gap equation is computationally challenging. We demonstrate that the modified version of Broyden's method [263] for solving general nonlinear equations is well applicable. Combined with the usual method of Khodel *et al.* [264] it allows us to assess systematically the iterative convergence. Furthermore, we study the impact of 3N forces on the pairing gap at the normal-ordered two-body level. Taking advantage of the improved normal-ordering method presented in Sec. 4.1 we consider here for the first time N^{3}LO 3N contributions to the BCS pairing interaction.

6.1 BCS pairing and the energy gap

Setting the stage for our calculations we briefly discuss the derivation of the gap equation in the so-called BCS approximation and refer to Refs. [265, 266] for more details as well as general introductions into superconductivity. We follow here the variational approach similar to Refs. [267, 268]. There exist also several other deriviations, e.g., via a Weinberg eigenvalue analysis (see Sec. 3) based on the Nambu–Gor'kov Green's function [223], or using Gor'kov equations [269]. In second quantization (for notation see Sec. 1.3.2), the pairing Hamiltonian involving a NN interaction reads

$$H = \sum_{\mathbf{k}\sigma} \varepsilon(\mathbf{k})\, a^\dagger_{\mathbf{k}\sigma} a_{\mathbf{k}\sigma} + \sum_{\mathbf{k}\mathbf{k}'} \langle \mathbf{k}|V_{\text{NN}}|\mathbf{k}'\rangle\; a^\dagger_{\mathbf{k}\uparrow} a^\dagger_{-\mathbf{k}\downarrow} a_{-\mathbf{k}'\downarrow} a_{\mathbf{k}'\uparrow} \,. \tag{6.1}$$

The operator $a^\dagger_{\mathbf{k}\sigma}$ ($a_{\mathbf{k}\sigma}$) creates (annihilates) a particle with momentum $\mathbf{k}$ and spin projection $\sigma = \uparrow, \downarrow$, whereas $\varepsilon(\mathbf{k})$ is the single-particle energy. Notice that Eq. (6.1) is *reduced* to scattering of paired states with zero total momentum and antiparallel spins (spin singlet). Contributions other than that are consequently not considered. To study the instability of the normal ground state (Fermi sea) due to the formation of bosonic Cooper pairs which eventually condense, one may apply the Rayleigh-Ritz variational principle (see Sec. 5.3) to the Hamiltonian (6.1) and a given trial function. Bardeen, Cooper, and Schrieffer made an educated ansatz for the ground-state wave function [267, 268],

$$|\Psi_{\text{BCS}}\rangle = \prod_{\mathbf{k}} \left(u_{\mathbf{k}} + v_{\mathbf{k}}\, a^\dagger_{\mathbf{k}\uparrow} a^\dagger_{-\mathbf{k}\downarrow} \right) |0\rangle \,, \tag{6.2}$$

where each particle is either paired or unpaired: $|\Psi_{\text{BCS}}\rangle$ is normalized, hence, $v_{\mathbf{k}}^2$ denotes the probability that a Cooper pair $|\mathbf{k}\uparrow, -\mathbf{k}\downarrow\rangle$ is occupied, while $u_{\mathbf{k}}^2 = 1 - v_{\mathbf{k}}^2$ is the probability for being unoccupied. The two coefficients can be chosen to be real and positive. It is important to stress that Eq. (6.2) is not an eigenstate of the particle-number operator $N = \sum_{\mathbf{k}\sigma} a^\dagger_{\mathbf{k}\sigma} a_{\mathbf{k}\sigma}$, i.e., the variance $\langle N^2\rangle - \langle N\rangle^2 = 4\sum_{\mathbf{k}} u_{\mathbf{k}}^2 v_{\mathbf{k}}^2$ is in general nonzero. Therefore, only the mean particle number of the system,

$$\langle N\rangle = \langle \Psi_{\text{BCS}}| \sum_{\mathbf{k}\sigma} a^\dagger_{\mathbf{k}\sigma} a_{\mathbf{k}\sigma} |\Psi_{\text{BCS}}\rangle = 2\sum_{\mathbf{k}} v_{\mathbf{k}}^2 \,, \tag{6.3}$$

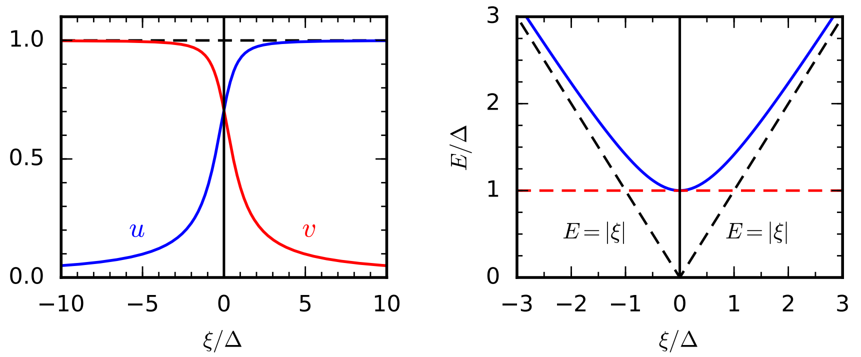

Figure 41: Left panel: distribution functions $u_\mathbf{k}$ (blue line) and $v_\mathbf{k}$ (red line) plotted as a function of ξ/Δ. Right panel: scaled quasiparticle excitation energy E/Δ (blue line). The red-dashed horizontal line indicates the energy gap.

is definite, as usual when working in the grand canonical ensemble. Minimizing the variational energy corresponding to the BCS wave function (6.2),

$$E_V^{u_\mathbf{k},\,v_\mathbf{k}} := \langle H\rangle - \mu\,\langle N\rangle = 2\sum_\mathbf{k} \xi(\mathbf{k})\,v_\mathbf{k}^2 + \sum_{\mathbf{k}\mathbf{k}'} \langle\mathbf{k}|V_\mathrm{NN}|\mathbf{k}'\rangle\; u_\mathbf{k} v_\mathbf{k} u_{\mathbf{k}'} v_{\mathbf{k}'}\,, \tag{6.4}$$

subject to $u_\mathbf{k}^2 + v_\mathbf{k}^2 = 1$, determines the coefficients $u_\mathbf{k}$ and $v_\mathbf{k}$ (in analogy to Eq. (5.32)). Note that the chemical potential μ in the additional term $-\mu\,\langle N\rangle$ is imposed to keep $\langle N\rangle$ constant, shifting the single-particle energy in $\xi(\mathbf{k}) = \varepsilon(\mathbf{k}) - \mu$. Due to the constraint of the minimization it is natural to substitute $u_\mathbf{k} = \sin\theta_\mathbf{k}$ as well as $v_\mathbf{k} = \cos\theta_\mathbf{k}$ in Eq. (6.4). The necessary condition for minima, $\frac{\partial}{\partial\theta_\mathbf{k}} E_V^{\theta_\mathbf{k}} = 0$, leads then to the relation

$$\tan 2\theta_\mathbf{k} = \frac{\sum_{\mathbf{k}'} \langle\mathbf{k}|V_\mathrm{NN}|\mathbf{k}'\rangle \sin 2\theta_{\mathbf{k}'}}{2\xi(\mathbf{k})} \equiv -\frac{\Delta(\mathbf{k})}{\xi(\mathbf{k})}\,, \tag{6.5}$$

and the definition of the pairing gap,

$$\Delta(\mathbf{k}) = -\sum_{\mathbf{k}'} \langle\mathbf{k}|V_\mathrm{NN}|\mathbf{k}'\rangle\, u_{\mathbf{k}'} v_{\mathbf{k}'} = -\frac{1}{2}\sum_{\mathbf{k}'} \langle\mathbf{k}|V_\mathrm{NN}|\mathbf{k}'\rangle \sin 2\theta_{\mathbf{k}'}\,. \tag{6.6}$$

In terms of the quasiparticle excitation energy $E(\mathbf{k}) = \sqrt{\xi^2(\mathbf{k}) + \Delta^2(\mathbf{k})}$, Eq. (6.5) can be split into,

$$2u_\mathbf{k} v_\mathbf{k} = \sin 2\theta_\mathbf{k} = \frac{\Delta(\mathbf{k})}{E(\mathbf{k})}\,, \qquad v_\mathbf{k}^2 - u_\mathbf{k}^2 = \cos 2\theta_\mathbf{k} = -\frac{\xi(\mathbf{k})}{E(\mathbf{k})}\,, \tag{6.7}$$

such that the second expression combined with $u_\mathbf{k}^2 + v_\mathbf{k}^2 = 1$ sets the distribution functions

$$u_\mathbf{k}^2 = \frac{1}{2}\left[1 + \frac{\xi(\mathbf{k})}{E(\mathbf{k})}\right], \qquad v_\mathbf{k}^2 = \frac{1}{2}\left[1 - \frac{\xi(\mathbf{k})}{E(\mathbf{k})}\right]. \tag{6.8}$$

The left panel in Fig. 41 shows these as a function of ξ/Δ.

Altogether, the pairing gap $\Delta(\mathbf{k})$ in the BCS approximation is given by the self-consistent solution of the coupled nonlinear equations

$$\Delta(\mathbf{k}) = -\sum_{\mathbf{k}'} \langle \mathbf{k}|V_{\mathrm{NN}}|\mathbf{k}'\rangle \frac{\Delta(\mathbf{k}')}{2E(\mathbf{k}')}, \qquad \langle N\rangle = \sum_{\mathbf{k}} \left[1 - \frac{\xi(\mathbf{k})}{E(\mathbf{k})}\right]. \tag{6.9}$$

Given a mean particle number $\langle N\rangle$, the second relation determines the chemical potential μ, similar to the procedure in Sec. 4.3 at finite temperatures. For completeness, we note that diagonalizing the Hamiltonian (6.1) leads to the same expressions (see Refs. [265, 270]). In case of repulsive interactions, only the trivial solution $\Delta(\mathbf{k}) = 0$ exists, so $v_{\mathbf{k}} = \Theta(k_{\mathrm{F}} - \mathbf{k})$ as well as $u_{\mathbf{k}} = \Theta(\mathbf{k} - k_{\mathrm{F}})$ are the usual distribution functions of holes and particles, respectively, at zero temperature. The BCS state (6.2) thus reduces to the normal Fermi gas. For attractive interactions close to the Fermi surface, a condensate of Cooper pairs may occur, resulting in nontrivial solutions $\Delta(\mathbf{k})$ and a smeared out Fermi surface as depicted in Fig. 41 (left panel). The single-particle spectrum develops a gap $\Delta(\mathbf{k})$ corresponding to the minimum excitation energy $2\Delta(\mathbf{k})$ that is required to break a Cooper pair (see right panel in Fig. 41).

To decouple the system (6.9) we use $\mu = \varepsilon(k_{\mathrm{F}})$ in the energy denominator of the gap equation, assuming that the Fermi surface is still sufficiently sharp. This approximation (e.g., recently used in Refs. [225, 271]) is reliable as long as Δ/μ is small [272], a requirement that is met here here but typically not at low densities (see also Refs. [157, 273]). The remaining BCS gap equation (6.9) can be expressed as a 2×2 matrix in single-particle spin space, so that the relation to be solved in this chapter reads [269]

$$\Delta_{\alpha\alpha'}(\mathbf{k}) = -\sum_{\substack{\beta,\beta'\\ \mathbf{k}'}} \frac{\langle \mathbf{k}\alpha\alpha'|V_{\mathrm{NN}}|\mathbf{k}'\beta\beta'\rangle\, \Delta_{\beta\beta'}(\mathbf{k}')}{2\sqrt{\xi^2(k') + \frac{1}{2}\mathrm{Tr}\left[\Delta\Delta^\dagger\right](\mathbf{k}')}}. \tag{6.10}$$

The greek indices indicate the single-particle spin states $|\uparrow,\downarrow\rangle$ and $\mathrm{Tr}[\,\cdot\,]$ is the trace in spin space. Similar to our infinite-matter studies, we consider a free and a Hartree-Fock single-particle spectrum. The latter adds self-energy corrections (4.20) to the kinetic energy due to NN and (if present) 3N forces at the normal-ordered two-body level. Technical details can be found in Sec. 4.2.2. The corresponding effective mass m^* evaluated at the Fermi surface is then given by

$$\frac{m^*(k_{\mathrm{F}})}{m} = \left(\frac{m}{k}\frac{d\varepsilon(k)}{dk}\right)^{-1}\Bigg|_{k=k_{\mathrm{F}}}. \tag{6.11}$$

Comparing calculations in the different spectra serves as a simple measure for the dependence of the pairing gap on the single-particle energy: $m^\star/m < 1$ leads to a suppression, $m^\star/m > 1$ to an amplification.

At the BCS level, pairing gaps in uniform neutron matter have been investigated based on chiral interactions, e.g., in Refs. [43, 225, 238, 271, 274]. The BCS approximation is particularly useful to test the sensitivity to nuclear forces. However, there are important contributions beyond BCS due to screening and vertex corrections [232, 275–280], which affect pairing gaps significantly (see also the discussions in Refs. [272, 281]). For QMC calculations at low densities we refer the reader to Refs. [157, 273, 281, 282]. Even in the very dilute limit $k_{\mathrm{F}}|a_s| \ll 1$, where a_s is the (neutron-neutron) scattering length, Gor'kov and Melik-Barkhudarov [283] showed that including induced interactions suppresses the BCS result in the $^1S_0$ channel,

$$\Delta_{\mathrm{BCS}}(k_{\mathrm{F}}) = \frac{8}{e^2}\frac{k_{\mathrm{F}}^2}{2m} \exp\left(\frac{\pi}{2k_{\mathrm{F}}a_s}\right), \tag{6.12}$$

by a remarkable factor of $(4e)^{-\frac{1}{3}} \approx 0.45$. Such corrections are evidently considerable, particularly, regarding the microscopic description of cooling in neutron stars [259, 262], but the results obtained in the various approaches can be quite different at the relevant densities (e.g., see Fig. 9 in Ref. [281]). The self-consistent Green's function method and Fermi liquid theory have recently been applied to work further along these lines [238, 284].

Contributions beyond BCS are not addressed in this work since we focus on the comparison of pairing gaps based on chiral interactions with new regularization schemes, including systematic uncertainty estimates, and the role of 3N forces up to N^{3}LO.

6.2 Solving the BCS gap equation

Practically, Eq. (6.10) is solved in a partial-wave representation. We review the decomposition in App. B in order to clarify the conventions and approximations used. As shown in the appendix the angular integration can be carried out analytically if the pairing gap in the energy denominator in Eq. (6.10) is averaged over all spatial directions:

$$\Delta^2(\mathbf{k}) \equiv \frac{1}{2}\mathrm{Tr}\left[\Delta\Delta^\dagger\right] \xrightarrow{\text{average}} \frac{1}{2}\int \frac{\mathrm{d}\Omega_{\mathbf{k}}}{4\pi}\mathrm{Tr}\left[\Delta\Delta^\dagger\right] = \sum_{l,S,J} |\Delta^J_{lS}(k)|^2 \,. \tag{6.13}$$

In this approximation (introduced in Ref. [285]) the partial-wave decomposed gap equation takes the form [264]

$$\Delta^J_{lS}(k) = -\int_0^\infty \frac{\mathrm{d}k'\,k'^2}{\pi}\sum_{l'} \frac{i^{l'-l}V^J_{ll'S}(k,k')\Delta^J_{l'S}(k')}{\sqrt{\xi^2(k') + \sum_{\tilde{l},\tilde{S},\tilde{J}} |\Delta^{\tilde{J}}_{\tilde{l}\tilde{S}}(k')|^2}} \,. \tag{6.14}$$

The different angular momenta l, $l' = |J \pm 1|$ are coupled in the spin-triplet channel, whereas in the singlet channel we obtain $l' = l$. We note that due to the energy denominator the solutions of Δ^J_{lS} are generally coupled, even if the interaction does not couple these channels. However, in practice Eq. (6.14) can be solved to a very good approximation independently for fixed quantum numbers S and J, because they are dominated by the channel in which the pairing interaction is most attractive at a given density. This and angle averaging are commonly used approximations, e.g., recently in Refs. [225, 271, 286]. The latter is exact for the $^1S_0$ channel and has been shown in Refs. [264, 285] to be a good approximation when used for the average value of the gap at the Fermi surface. We note that the angle-averaging approximation tends to slightly overestimate the gap according to the discussion in Section 5 of Ref. [264]. Studying anisotropic and nondegenerate gaps with respect to the quantum number M would require keeping its angle dependence as in Refs. [264, 287].

Here, we solve Eq. (6.14) in pure neutron matter for the most attractive channels of the nuclear interactions, as inferred from the scattering phase shifts in Fig. 42: the spin-singlet channel $^1S_0$ and the triplet channel $^3P_2$—$^3F_2$. The other channels in the triplet P-wave, $^3P_0$ and $^3P_1$, as well as in higher partial waves are less attractive or even repulsive at the densities considered in this work. We have checked that this also holds with the inclusion of 3N forces. Following Eq. (6.13) we plot the total gap $\Delta(k_\mathrm{F}) = \sqrt{\sum_l \Delta_l^2(k_\mathrm{F})}$ evaluated on the Fermi surface to estimate the pairing energy.

6.2.1 Numerical challenges and direct-iteration method

The nonlinear gap equation (6.14) can be solved iteratively until a self-consistent solution is obtained. However, such approaches are computationally challenging and require more advanced algorithms. The

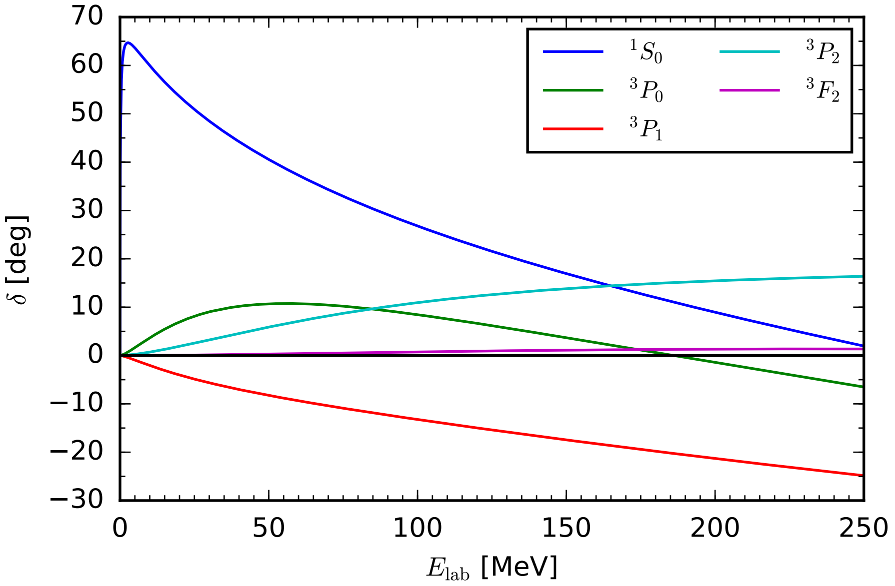

Figure 42: Scattering phase shifts in the lowest partial waves which are active in neutron matter as function of the laboratory energy $E_{\text{lab}} = 2k_{\text{F}}^2/m$. Positive (negative) phase shifts indicate attractive (repulsive) interactions in that channel. For low energies, the dominant attraction is in the $^1S_0$ channel, whereas for $E_{\text{lab}} \gtrsim 160\,\text{MeV}$ (corresponding to $k_{\text{F}} \simeq 1.4\,\text{fm}^{-1}$) it is the $^3P_2$ channel coupled to the $^3F_2$ channel. Notice that the data is based on the Nijmegen partial-wave analysis [185] for neutron-proton scattering, however, isospin symmetry is only weakly broken. The figure has been adapted from Ref. [281].

simplest and straightforward method that takes directly the right-hand side of Eq. (6.14) $I[\,\cdot\,]$ in the mth iteration step,

$$\boldsymbol{\Delta}_{\text{out}}^{(m)} = I\left[\boldsymbol{\Delta}_{\text{in}}^{(m)}\right] \quad \text{with} \tag{6.15a}$$

$$\boldsymbol{\Delta}_{\text{in}}^{(m+1)} = \boldsymbol{\Delta}_{\text{out}}^{(m)}, \tag{6.15b}$$

converges poorly, if at all. Instead, it typically converges to the (mathematically also valid) trivial solution $\Delta = 0$, especially if the nontrivial solution is small. We refer also to Ref. [288] for a general discussion of iterative methods in the context of nuclear physics. In Eqs. (6.15) we define a gap vector $\boldsymbol{\Delta}$ having as components the partial-wave gaps Δ_l sampled each on a Gauss momentum mesh with N_p points. The basis size of this vector is N_p (spin singlet) and $2N_p$ (spin triplet), respectively.

In addition to issues with methodical convergence, also the evaluation of the integral in Eq. (6.14) requires some care. Since the pairing gap is typically a small energy scale, the integrand exhibits a strong peak structure for momenta close to the Fermi surface. This *quasisingularity* of the BCS gap equation has to be treated carefully when evaluating the integral numerically. We observe that Gauss quadrature converges only if multiple dense integration meshes concentrated around the peak position are well distributed over the entire interval (see also Ref. [289]). The presence of the peak makes the integral nevertheless quite sensitive to variations in $\Delta(k_{\text{F}})$ and can complicate obtaining a stable self-consistent solution. In order to address these convergence issues, various methods have been applied in the literature, for example the quasilinear and linear method of Khodel *et al.* [264] and Krotscheck [290], respectively, or the instability analysis based on in-medium Weinberg eigenvalues [223, 225, 291].

We employ two independent algorithms to assess the methodical convergence of our results. These are discussed in detail in the next sections. As it is often referred to, we quantify briefly the term *convergence*. Let us consider a general solver that returns the vectors $\mathbf{\Delta}_{\text{in}}^{(m)}$ and $\mathbf{\Delta}_{\text{out}}^{(m)}$ after the mth iteration, specified by an update rule, for instance of the simple form in Eq. (6.15b). The solver is stable if the norm of the difference,

$$\mathbf{F}^{(m)} = \mathbf{\Delta}_{\text{out}}^{(m)} - \mathbf{\Delta}_{\text{in}}^{(m)} , \tag{6.16}$$

decreases with m, eventually becomes smaller than an arbitrary fixed threshold value and finally a self-consistent solution is found if $|\mathbf{F}^{(m)}| = 0$. In practice, a small but finite threshold serves as a break condition for the self-consistency cycle. We check the break condition for 5 to 10 additional iterations once it is fulfilled.

6.2.2 Khodel's method

The method of Khodel *et al.* was first presented in Refs. [264, 292] and has been widely used in nuclear physics since then (see, e.g., Refs. [225, 271, 286] for recent applications). It is based on a reformulation of the gap equation (6.14) such that the peak of the integrand, causing the large sensitivity to $\Delta(k_{\text{F}})$, is removed. This is achieved by rewriting the potential $V_{ll'}(k,k')$ in a separable part

$$\phi_{ll'}(k) = \frac{V_{ll'}(k,k_{\text{F}})}{v_{ll'}} \quad \text{and} \quad \phi_{ll'}^{T}(k') = \frac{V_{ll'}(k_{\text{F}},k')}{v_{ll'}} , \tag{6.17}$$

where the definition $v_{ll'} = V_{ll'}(k_{\text{F}},k_{\text{F}}) \neq 0$ normalizes $\phi_{ll'}(k_{\text{F}}) = \phi_{ll'}^{T}(k_{\text{F}}) = 1$, and a remainder

$$W_{ll'}(k,k') = V_{ll'}(k,k') - v_{ll'}\phi_{ll'}(k)\phi_{ll'}^{T}(k') , \tag{6.18}$$

which vanishes when at least one argument is on the Fermi surface. This property is key to removing the peak. Inserting the remainder (6.18) in the gap equation (6.14) gives

$$\Delta_l(k) + \sum_{l'} i^{l'-l} \int_0^\infty \frac{\mathrm{d}k'k'^2}{\pi} W_{ll'}(k,k') \frac{\Delta_{l'}(k')}{\sqrt{\xi^2(k')+\Delta^2(k')}} = \sum_{l'} D_{ll'}\phi_{ll'}(k) , \tag{6.19}$$

with the coefficients defined as

$$D_{ll'} = -i^{l'-l} v_{ll'} \int_0^\infty \frac{\mathrm{d}k k^2}{\pi} \frac{\phi_{ll'}^{T}(k)\Delta_{l'}(k)}{\sqrt{\xi^2(k)+\Delta^2(k)}} . \tag{6.20}$$

The partial-wave gap Δ_l in Eq. (6.19) can be written as linear combinations of shape functions $\chi_l^{l_1 l_2}(k)$

$$\Delta_l(k) = \sum_{l_1,l_2} D_{l_1 l_2}\chi_l^{l_1 l_2}(k) , \tag{6.21}$$

and thus one obtains an equation for the momentum dependence of the partial-wave gaps

$$\chi_l^{l_1 l_2}(k) + \sum_{l'} i^{l'-l} \int_0^\infty \frac{\mathrm{d}k'k'^2}{\pi} W_{ll'}(k,k') \frac{\chi_{l'}^{l_1 l_2}(k')}{\sqrt{\xi^2(k')+\Delta^2(k')}} = \delta_{ll_1}\phi_{l_1 l_2}(k) . \tag{6.22}$$

Since $W_{ll'}$ vanishes by construction if at least one argument is on the Fermi surface, the integral in Eq. (6.22) is dominated by a momentum region where $\Delta(k)$ is far less important than $\xi(k)$. The shape functions therefore only depend weakly on $\Delta(k)$. This allows us to treat Eq. (6.22) to a good approximation as quasilinear; that means by approximating $\Delta(k)$ by a constant. Consequently, the momentum dependence of the gap converges rapidly in Khodel's method and almost independently of their magnitudes (6.20) due to the separation (6.21).

In practice, the iteration scheme works as follows [264]: each momentum dependence is sampled on a suitable Gauss mesh to ensure convergence of the quadrature. Given $\Delta(k)$ from the previous iteration, one solves Eq. (6.22) for the shape functions $\chi_l^{l_1 l_2}(k)$ by matrix inversion. For the first iteration a small constant value, e.g., $\Delta(k) = 1$ keV, serves as a suitable starting point. We checked that our final results are independent of that choice. The coefficients $D_{ll'}$ can then be determined via Eq. (6.20) combined with Eq. (6.21) using a nonlinear solver such as the Newton-Raphson method. With the new $D_{ll'}$ and $\chi_l^{l_1 l_2}(k)$ Eq. (6.21) updates the partial-wave gaps $\Delta_l(k)$. It follows directly from Eq. (6.22) that $\chi_l^{l_1 l_2}(k_\mathrm{F}) = \delta_{ll_1}$ for all l_2, so the total gap on the Fermi surface for the next iteration step is simply $\Delta_l(k_\mathrm{F}) = \sum_{l_2} D_{ll_2}$. The procedure is repeated until self-consistency is reached, typically within a few iterations.

6.2.3 Modified Broyden's method

Alternatively to Khodel's method, we solve for the gap by a modified version of the direct-iteration method in Eqs. (6.15). Since Eq. (6.15b) is known to be too simplistic, more advanced update rules are crucial to achieve convergence. As a first step, the stability of the convergence can be improved significantly by dampening the update prescription. The simplest modification involves a linear superposition of the input and output vector of the current iteration:

$$\mathbf{\Delta}_\mathrm{in}^{(m+1)} = \alpha \mathbf{\Delta}_\mathrm{out}^{(m)} + (1-\alpha)\mathbf{\Delta}_\mathrm{in}^{(m)} = \mathbf{\Delta}_\mathrm{in}^{(m)} + \alpha\, \mathbf{F}^{(m)}\,, \tag{6.23}$$

where α is the damping factor. We attempted to find suitable values for α that lead to reliable convergence patterns for various NN interactions over a typical range of densities. However, we found that using *simple mixing* still results in too many discontinuities of the gap as a function of density in order to be useful in practice. These numerical artifacts had to be removed by fine-tuning the damping factor for different densities. Hence, reliable calculations for the gap require more sophisticated updates.

We now demonstrate that Broyden's method for solving general nonlinear equations is in particular well suited for the gap equation (6.14). Specifically, we make use of a modified version of Broyden's method developed in Ref. [263]. It is a fast, stable and computationally efficient quasi-Newton-Raphson method with the advantage of a simple but powerful update rule. The inverse of the Jacobian is approximated by the knowledge of previous iterations without needing to store or to process high-rank matrices. We review here briefly the ingredients to obtain stable results for the gap and refer to the original Ref. [263] as well as to Ref. [288] for first applications to the nuclear many-body problem.

In the modified version of Broyden's method, the gap vector after the mth iteration is updated according to the rule

$$\mathbf{\Delta}_\mathrm{in}^{(m+1)} = \mathbf{\Delta}_\mathrm{in}^{(m)} + \alpha\, \mathbf{F}^{(m)} - \sum_{n=1}^{m-1} w_n \gamma_{mn} \mathbf{u}^{(n)}\,, \tag{6.24}$$

with the definitions

$$\gamma_{mn} = \sum_{k=1}^{m-1} c_{km} \beta_{kn}\,, \qquad \beta_{kn} = (w_0^2 \mathbb{1} + a)^{-1}_{kn}\,, \tag{6.25a}$$

$$c_{km} = w_k\, \delta\mathbf{F}^{(k)\dagger} \mathbf{F}^{(m)}\,, \qquad a_{kn} = w_k w_n\, \delta\mathbf{F}^{(n)\dagger} \delta\mathbf{F}^{(k)}\,, \tag{6.25b}$$

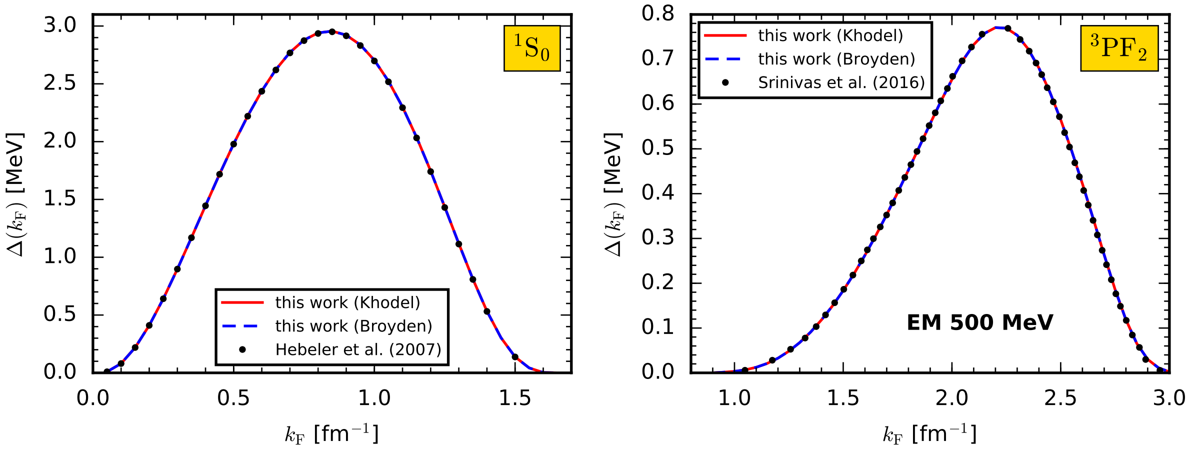

Figure 43: Comparison of the gap Δ as a function of Fermi momentum k_F in the $^1S_0$ (left panel) and $^3P_2{-}^3F_2$ channel (right panel) obtained using Khodel's method (red-solid line) and via the new modified direct-iteration method (blue-dashed line). Exemplarily, we show the gaps based on the N^{3}LO NN potential EM 500 MeV [154]. The values from Refs. [225, 274] are depicted by black dots. We find in general very good agreement, especially, the two methods of this work demonstrate excellent methodical convergence.

and

$$\mathbf{u}^{(n)} = \alpha\,\delta\mathbf{F}^{(n)} + \delta\boldsymbol{\Delta}^{(n)}\,, \qquad \delta\boldsymbol{\Delta}^{(n)} = \frac{\boldsymbol{\Delta}_\mathrm{in}^{(n+1)} - \boldsymbol{\Delta}_\mathrm{in}^{(n)}}{|\mathbf{F}^{(n+1)} - \mathbf{F}^{(n)}|}\,, \qquad \delta\mathbf{F}^{(n)} = \frac{\mathbf{F}^{(n+1)} - \mathbf{F}^{(n)}}{|\mathbf{F}^{(n+1)} - \mathbf{F}^{(n)}|}\,, \tag{6.25c}$$

where $\delta\mathbf{F}^{(n)}$ is normalized, $\delta\mathbf{F}^{(n)\dagger}\delta\mathbf{F}^{(n)} = 1$. The procedure requires to store $\boldsymbol{\Delta}_\mathrm{in}^{(m)}$ and $\mathbf{F}^{(m)}$ of the current iteration as well as $\mathbf{u}^{(m)}$ and $\delta\mathbf{F}^{(m)}$ of all previous steps. Since a_{kn} is typically of rank much smaller than that of the full Jacobian it can be stored for efficiency. Although the update rule (6.24) includes simple mixing, the additional correction usually allows larger damping factors α, which typically leads to accelerated convergence. Besides guesses for $\boldsymbol{\Delta}_\mathrm{in}^{(1)}$ and α, the weights w_m have to be chosen as well, whereas $w_0 = 0.01$ needs to be sufficiently small [263]. We use $w_m = 1$, $m \geqslant 1$, similar to Ref. [288]. In addition, Ref. [263] suggested $w_m = \min\left(1, \sqrt{(\mathbf{F}^{(m)\dagger}\mathbf{F}^{(m)})^{-1}}\right)$ to promote solutions of advanced convergence.

6.2.4 Benchmarks

We show in Fig. 43 an exemplary benchmark for the gap $\Delta(k_\mathrm{F})$ obtained with Khodel's method (red-solid lines) and with the modified direct-iteration method (blue-dashed lines) in comparison to the literature (points) [225, 274]. The gaps are based on the N^{3}LO NN potential EM 500 MeV [154] in the channels $^1S_0$ (left panel) and $^3P_2{-}^3F_2$ (right panel). We use the same optimized Gauss mesh and observe in general almost perfect agreement of the two methods (deviations are of order of 10 eV) for the singlet as well as the triplet channel. Furthermore, the results in Fig. 43 agree well with the literature, also in the regions of small gaps. In practice, Khodel's method requires typically 2 to 3 times fewer steps to converge while the computational runtime is shorter for the modified direct-iteration method due to its simplicity. In rare cases the modified direct-iteration method leads to apparent discontinuities in the gap as a function of k_F. In all of our calculations we could easily recover these by modifying slightly the damping factor α. On the other hand, Khodel's method in its usual implementation is naturally unstable if the $V_{ll'}(k,k)$ gets small or has even nodes. For completeness, we note that there is a modified version of Khodel's method in Ref. [292] accounting for nodes $V_{ll'}(k,k) = 0$.

Based on these benchmarks, we conclude that the two algorithms are both reliable. Comparing the results of Khodel's method and the modified direct-iteration method allows us to assess the methodical convergence of our calculations. Such an independent benchmark is particularly important for density regions of slow convergence, as discussed above. We therefore do not recommend a specific single method but emphasize the strength of the combined approach. For the results presented in the following sections we have checked that both independent methods provide (practically) identical results.

6.3 Results with local and semilocal NN potentials

In Figs. 44 and 45, we present the gap in the $^1S_0$ channel based on the local GT+ [16, 17] and semilocal EKM potentials [9, 10] up to N^{2}LO and N^{4}LO, respectively. A detailed description of these new NN potentials can be found in Sec. 2.1.1. Each row corresponds to the regulators with $R_0 = 0.9$, 1.0, 1.1 and 1.2 fm as annotated. The left (middle) column depicts the gap $\Delta(k_\mathrm{F})$ at different orders using a free (Hartree-Fock) spectrum, whereas the right column shows the corresponding effective mass $m^*(k_\mathrm{F})/m$ from the Hartree-Fock spectrum. Following the approach by Epelbaum *et al.* [9, 10] discussed in Sec. 1.2.3, we use the chiral expansion to assign theoretical uncertainties to the results for $\Delta(k_\mathrm{F})$ (plotted as solid lines). The boundaries of the shaded uncertainty bands $\Delta(k_\mathrm{F}) \pm \delta\Delta$ are highlighted by dashed lines. We restrict the bands to the region of positive energies. To be specific, we focus here on uncertainties at N^{2}LO and beyond ($i \geqslant 3$),

$$\delta\Delta^{(i)} = \max_{3\leqslant j\leqslant i} \left(Q^{i+1-j} \left|\mathrm{d}\Delta^{(j)}\right| \right) . \tag{6.26}$$

We do not show uncertainties at LO and NLO, because at these orders the scattering phase shifts are not well reproduced at the relevant momenta, particularly not in the coupled $^3P_2{-}^3F_2$ channel. Note that, in contrast to Eq. (1.12), we neglect for the above reason the LO contributions to the higher-order uncertainties in Eq. (6.26). Moreover, we do not consider the additional constraint (1.13) that ensures that the next order always lies within the uncertainty band of the previous order by taking into account information of higher-order results in the chiral expansion. Since the pairing gap results from attractive interactions of two particles on the Fermi surface we use in the following the Fermi momentum k_F for the typical momentum in the expansion parameter (1.9). Hence, we use $Q := Q(p = k_\mathrm{F})$ in Eq. (6.26). This scaling is in general only expected to be valid for complete calculations involving all many-body forces at a given chiral order. In this work, we present results based on local and semilocal interactions without contributions from many-body forces. Complete calculations with full uncertainty estimates will be possible as soon as partial-wave matrix elements of the corresponding 3N forces are available. For both, local and semilocal NN interactions, we choose the breakdown scale

$$\Lambda_b = \begin{cases} 600\,\mathrm{MeV} & \text{for } R_0 = 0.8,\, 0.9,\, 1.0\,\mathrm{fm}\,, \\ 500\,\mathrm{MeV} & \text{for } R_0 = 1.1\,\mathrm{fm}\,, \text{ and} \\ 400\,\mathrm{MeV} & \text{for } R_0 = 1.2\,\mathrm{fm}\,, \end{cases} \tag{6.27}$$

for the different coordinate-space cutoffs R_0 of the interactions according to Ref. [9]. A similar mapping has to be worked out for potentials solely regularized in momentum space (see also Sec. 2.1.1).

At NLO and beyond we observe that the $^1S_0$ gap agrees up to $k_\mathrm{F} \sim (0.6 - 0.8)\,\mathrm{fm}^{-1}$, depending only slightly on the regulator for local potentials. As investigated in detail, e.g., in Ref. [274], the pairing gaps are strongly constrained by phase shifts, so the LO gaps are expected to be different. For $R_0 \geqslant 1.0\,\mathrm{fm}$ we find that the gaps at N^{3}LO and N^{4}LO agree well over the entire density range. Generally, the gap uncertainties based on Eq. (6.26) are very small for the highest chiral orders. We emphasize however that these include only contributions from the chiral expansion, whereas neglected higher-order many-body corrections are not assessed.

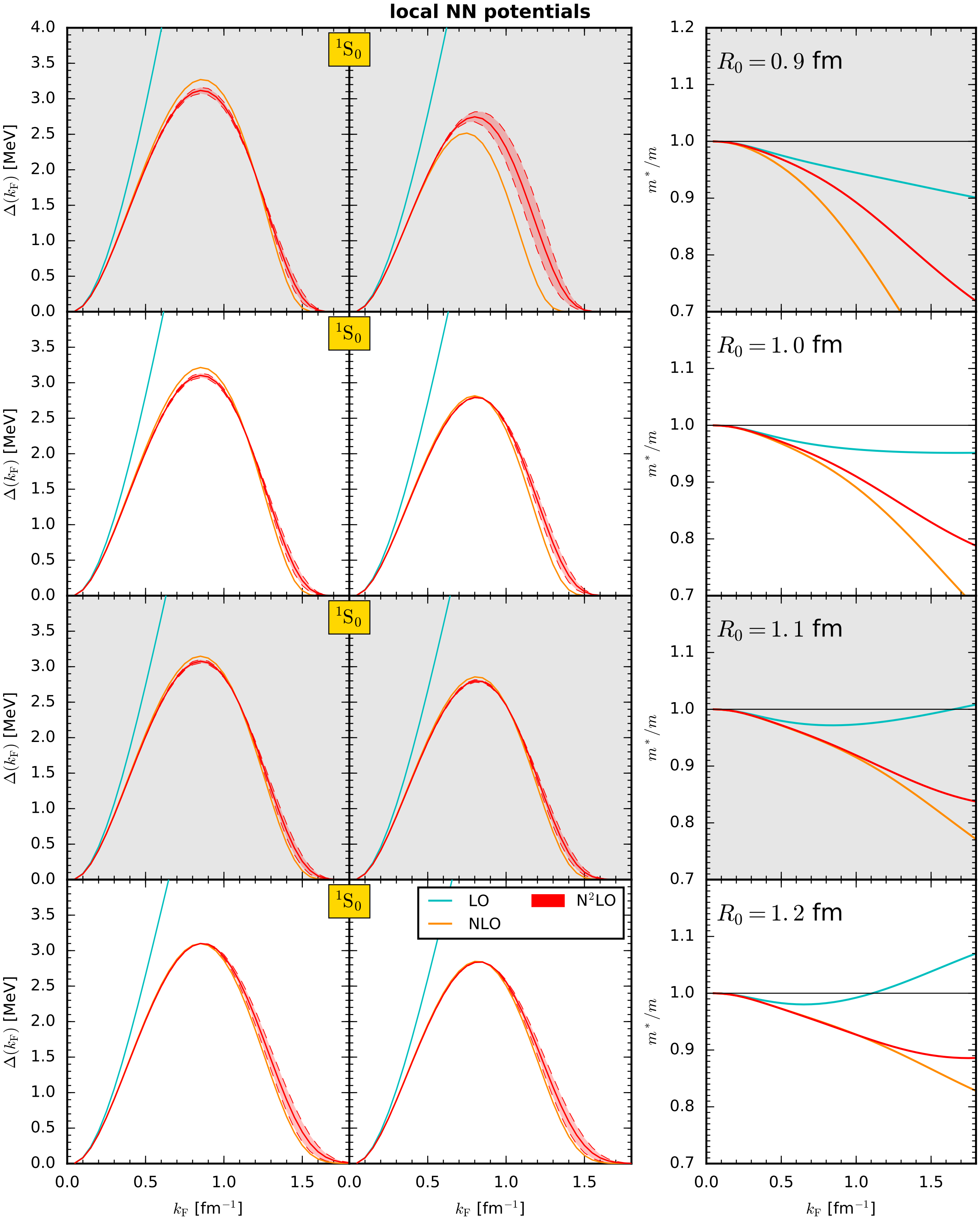

Figure 44: Gap Δ as a function of Fermi momentum k_F in the $^1S_0$ channel for the four local GT+ potentials with $R_0 = (0.9 - 1.2)$ fm (rows), each up to N^{2}LO with a free (left column) and a Hartree-Fock spectrum (middle column), respectively. The third column shows the effective mass at the Fermi surface corresponding to the Hartree-Fock spectrum. As discussed in the text, the uncertainty bands (if present) are depicted by the color-filled region between the dashed lines while the actual calculation is plotted as solid line. There are no uncertainties shown for LO and NLO; for details see text.

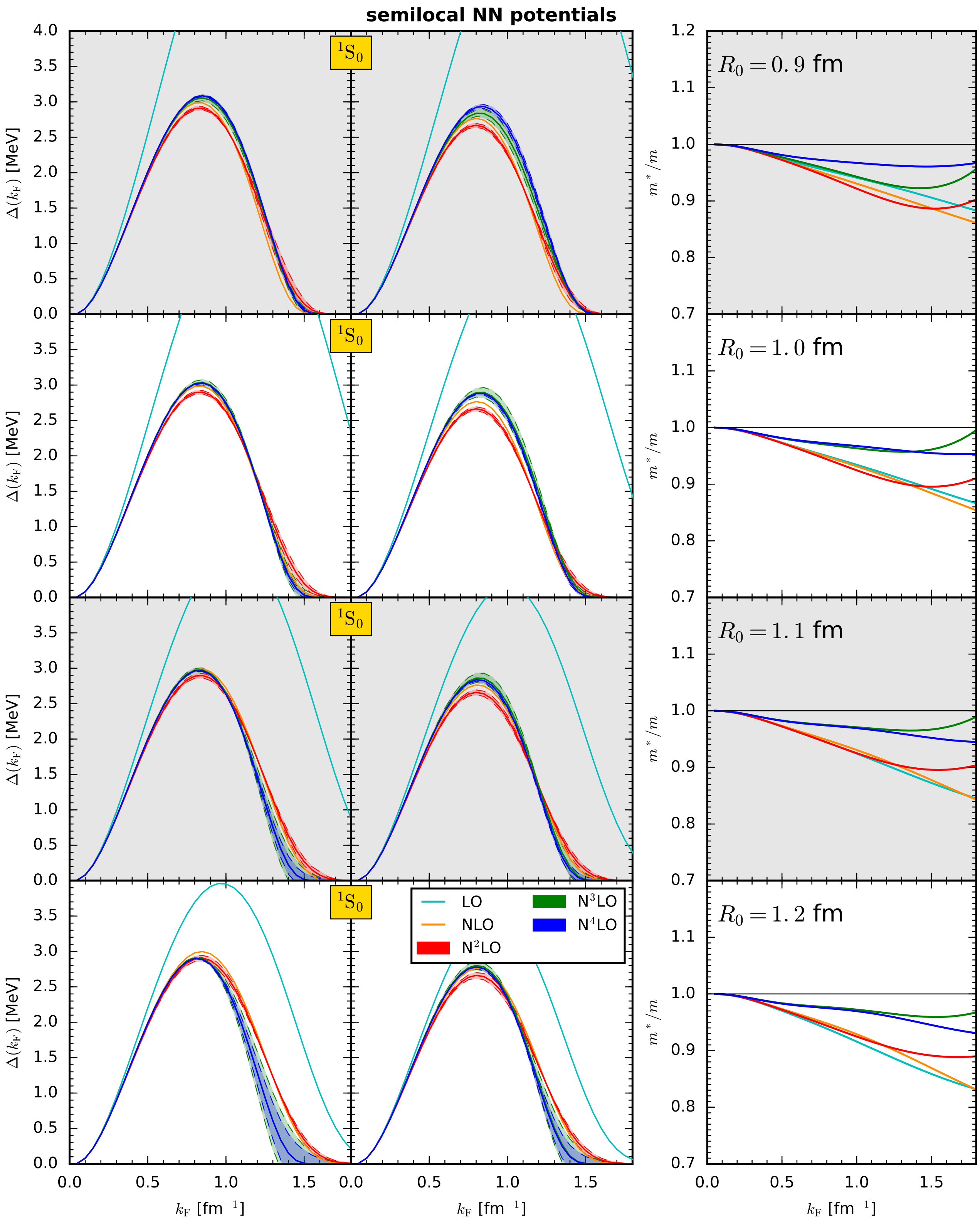

Figure 45: Gap Δ as a function of Fermi momentum k_F in the $^1S_0$ channel for the four semilocal EKM potentials with $R_0 = (0.9 - 1.2)$ fm (rows), each up to N^{4}LO with a free (left column) and a Hartree-Fock spectrum (middle column), respectively. The third column shows the effective mass at the Fermi surface corresponding to the Hartree-Fock spectrum. There are no uncertainties shown for LO and NLO; for details see text.

In addition, we find that the sensitivity of the pairing gap to the energy spectrum is rather small and affects mainly the maximum value of the gap. For both, local and semilocal potentials we find $\Delta_{\text{max}} \sim (2.7-3.1)\,\text{MeV}$ at $k_{\text{F}} \sim (0.8-0.9)\,\text{fm}^{-1}$ for the highest chiral order and all cutoffs. The rather small suppression due to the spectrum can directly be understood based on the fact that the ratio $m^*(k_{\text{F}})/m$ is close to one for all regulators and chiral orders (right columns).

In Figs. 46 and 47 we show the ${}^3P_2$–${}^3F_2$ gap based on the same NN potentials. Since ${}^3P_2$–${}^3F_2$ pairing takes place at higher densities than in the ${}^1S_0$ channel, the uncertainties are much larger. The maximum of the LO pairing gap for the local potentials changes significantly with increasing R_0, indicating that the results are strongly affected by regulator artifacts at this order. On the other hand, the pairing gap for the semilocal potentials at LO is zero for all densities and cutoff values and therefore not shown in Fig. 47. These results reflect the poor description of the phase shifts at this order, from only the 1π-exchange interaction for the semilocal case.

At higher chiral orders it is not straightforward to extract robust quantitative trends for the ${}^3P_2$–${}^3F_2$ gap. In general, the gap opens around densities of $k_{\text{F}} \sim 1\,\text{fm}^{-1}$ for all considered interactions. For the semilocal potentials the results at N^{3}LO and N^{4}LO agree well up to $k_{\text{F}} \sim 1.6\,\text{fm}^{-1}$. Also the corresponding uncertainty bands strongly overlap in this density region. We find the maximum gap values at N^{2}LO and higher orders in the density range $k_{\text{F}} = (1.6-2.1)\,\text{fm}^{-1}$ for all interactions. Overall, the large uncertainties at high densities reflect the regulator dependences and the breakdown of the chiral expansion. In particular, for a Fermi momentum $k_{\text{F}} = 2.0\,\text{fm}^{-1}$ the expansion parameter $Q(k_{\text{F}})$ defined in Eq. (1.9) is

$$Q\left(2.0\,\text{fm}^{-1}\right) = \begin{cases} 0.66 & R_0 = 0.8,\, 0.9,\, 1.0\,\text{fm}\,, \\ 0.79 & R_0 = 1.1\,\text{fm}\,, \text{ and} \\ 0.99 & R_0 = 1.2\,\text{fm}\,. \end{cases} \tag{6.28}$$

Clearly, it is not obvious that the chiral expansion is efficient anymore in this density regime.

6.4 Results with 3N forces up to N^{3}LO

We also study the pairing gaps based on three nonlocal N^{3}LO NN potentials combined with N^{2}LO and N^{3}LO 3N forces at the normal-ordered two-body level. The contributions of N^{2}LO 3N forces to the BCS pairing gap have already been studied via normal ordering (e.g., in Refs. [43, 225, 271, 293]) which can be performed directly based on the operatorial definition of the 3N interactions, as in Refs. [43, 133]. However, this approach becomes rather cumbersome for subleading 3N forces at N^{3}LO due to the involved operator structures at this order. In order to study these N^{3}LO contributions we make use of the improved normal-ordering method discussed in Sec. 4.1 and evaluate the density-dependent effective NN potential $V^{\text{as}}_{\text{NN+3N}} = V^{\text{as}}_{\text{NN}} + \zeta\,\overline{V}^{\text{as}}_{\text{3N}}$ in Eq. (1.45c) using the partial-wave decomposition of the 3N forces. In contrast to a Galilean-invariant NN interaction, the effective potentials depend in general on the total momentum $\mathbf{P}$ of the two remaining particles after summing one particle over occupied states in the Fermi sea. At the BCS level, the paired particles are in back-to-back kinematics and, therefore, we have $\mathbf{P} = 0$. The combinatorial factor $\zeta = 1$ has to be consistent to the type of quantity of interest and is carefully determined in App. A for this particular calculation (see also Ref. [43]).

Similar to our infinite-matter calculations in Sec. 4, the antisymmetrized 3N interactions are regularized by the nonlocal regulator (2.70) with $n_{\text{exp}} = 4$ and expressed in terms of the Jacobi momenta (4.2), $f_{\text{R}}(p,q) = \exp[-((p^2+3q^2/4)/\Lambda^2_{\text{3N}})^4]$. The corresponding 3N matrix elements are currently available up to N^{3}LO [205] with a large enough truncation on the three- and two-body total angular momenta $\mathscr{J} \leqslant 9/2$ and $J \leqslant 6$, respectively, to obtain well converged 3N Hartree-Fock energies in neutron and symmetric nuclear matter (see Sec. 4.1 for details). Once available, it will be straightforward to incorporate also local or semilocal 3N interactions. Work in this direction is currently in progress. Following

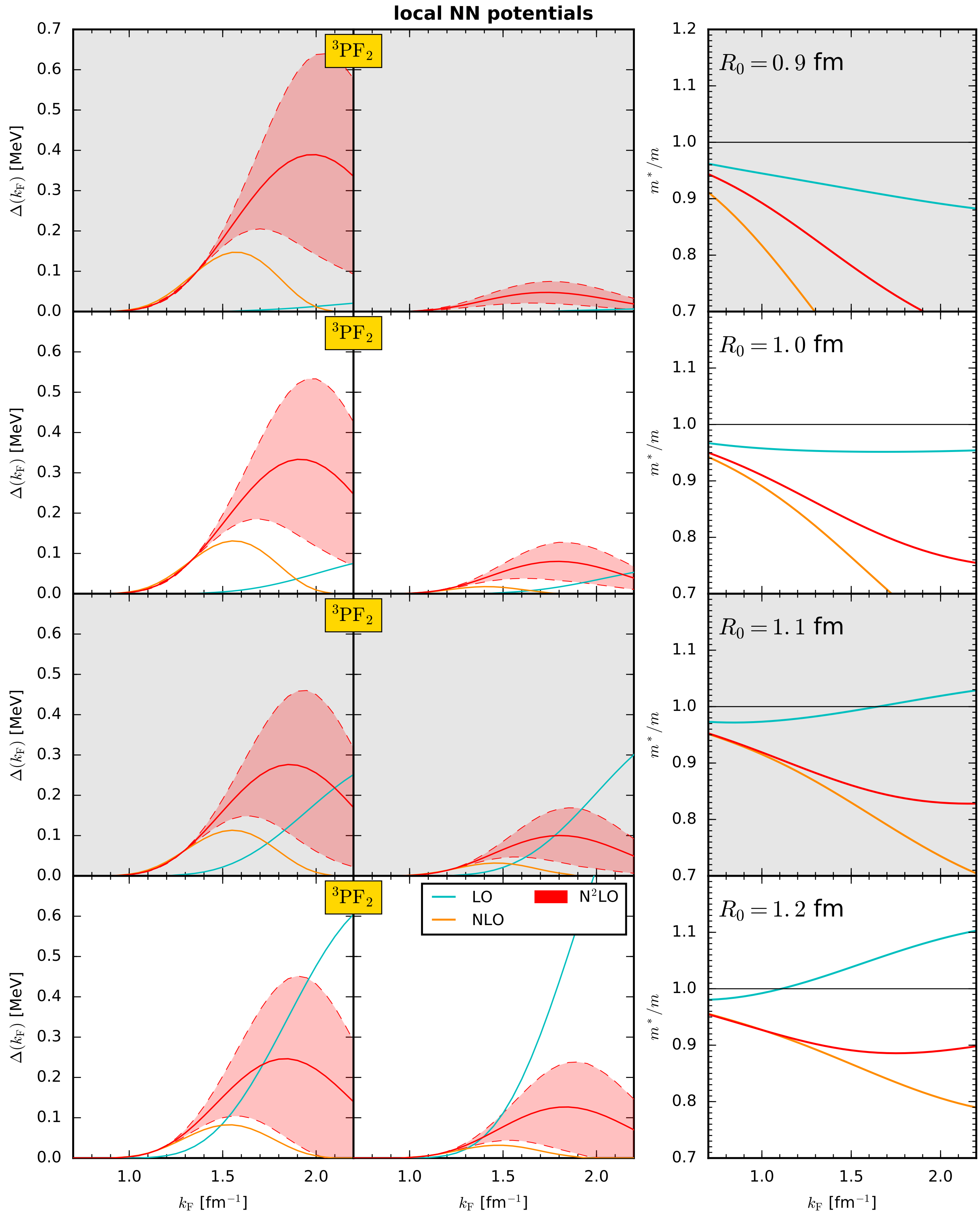

Figure 46: Gap Δ as a function of Fermi momentum k_F in the $^3P_2-^3F_2$ channel for the four local GT+ potentials with $R_0 = (0.9 - 1.2)$ fm (rows), each up to N^{2}LO with a free (left column) and a Hartree-Fock spectrum (middle column), respectively. The third row shows the effective mass at the Fermi surface corresponding to the Hartree-Fock spectrum. There are no uncertainties shown for LO and NLO; for details see text.

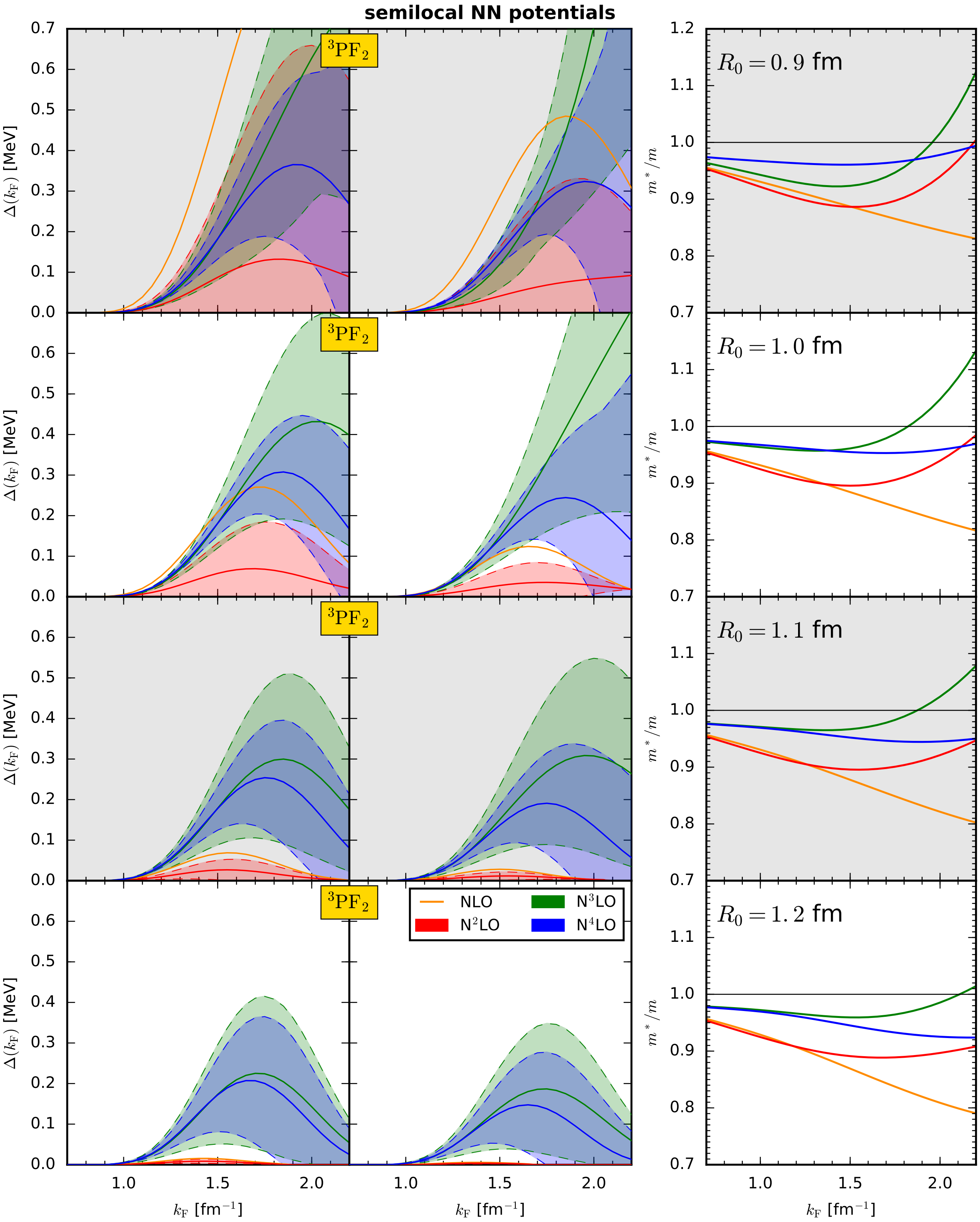

Figure 47: Gap Δ as a function of Fermi momentum k_F in the $^3P_2$–$^3F_2$ channel for the four semilocal EKM potentials with $R_0 = (0.9 - 1.2)$ fm (rows), each up to N^{4}LO with a free (left column) and a Hartree-Fock spectrum (middle column), respectively. The third row shows the effective mass at the Fermi surface corresponding to the Hartree-Fock spectrum. There are no uncertainties shown for LO and NLO; for details see text.

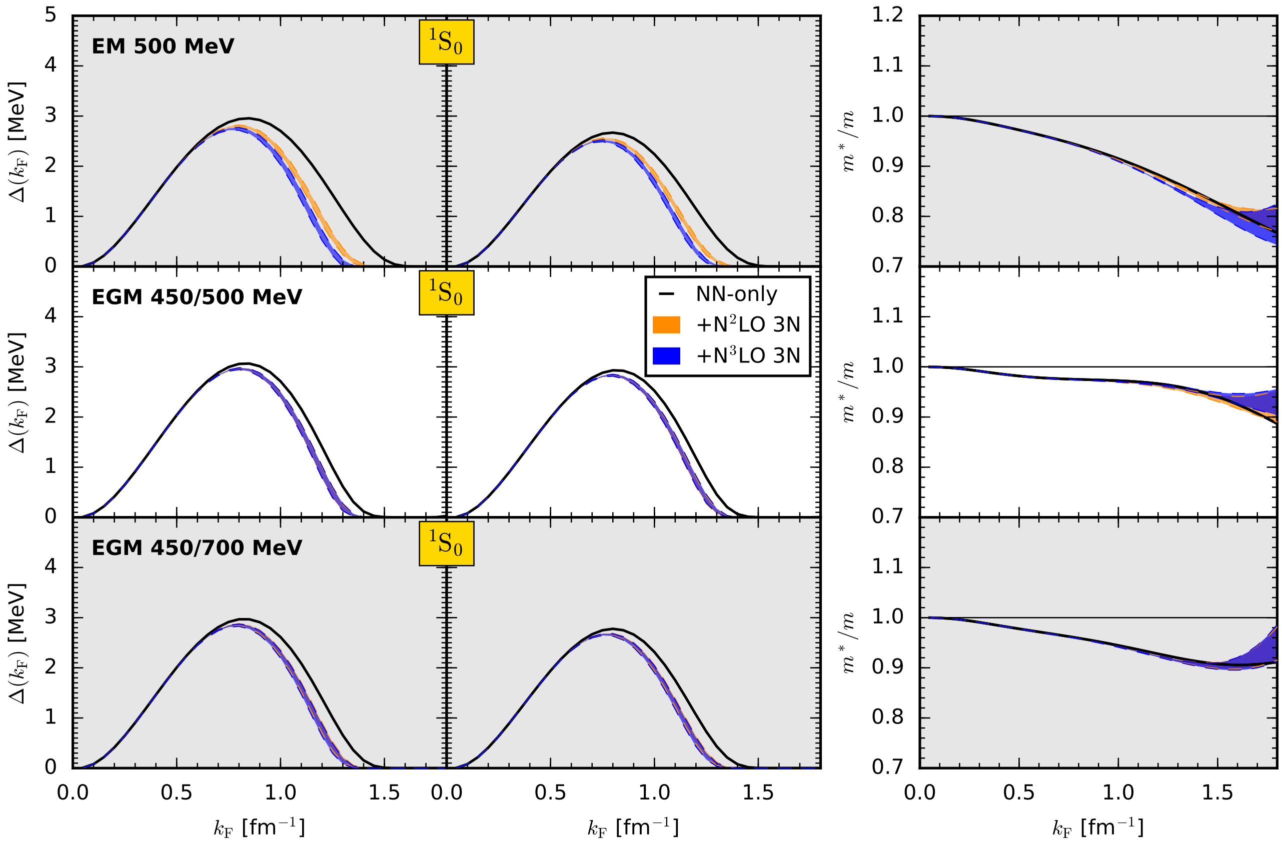

Figure 48: Gap Δ as a function of Fermi momentum k_F in the $^1S_0$ channel with a free (left column) and a Hartree-Fock spectrum (middle column) for the bare N^{3}LO NN potentials EM 500 MeV (first row), EGM 450/500 MeV (second row), and EGM 450/700 MeV (third row). The third column shows the effective mass at the Fermi surface corresponding to the Hartree-Fock spectrum. The NN-only results are plotted as black-solid lines. Variations of the 3N parameters c_1, c_3, and Λ_{3N} determine the uncertainty bands as discussed in the text.

the paradigm to regularize NN and many-body forces consistently, we do not show results for local or semilocal NN forces combined with nonlocal 3N interactions. Instead, we use the nonlocal N^{3}LO NN potentials EM 500 MeV [154], EGM 450/500 MeV, and EGM 450/700 MeV [67] with the 3N uncertainty estimate governed by variation of the 3N parameters c_1, c_3, and $\Lambda_{3N} = (2.0-2.5)\,\text{fm}^{-1}$. As recommended in Ref. [95], we take for calculations with N^{2}LO 3N forces the ranges $c_1 = -(0.37-0.73)\,\text{GeV}^{-1}$, $c_3 = -(2.71-3.38)\,\text{GeV}^{-1}$ and with N^{3}LO 3N forces $c_1 = -(0.75-1.13)\,\text{GeV}^{-1}$, $c_3 = -(4.77-5.51)\,\text{GeV}^{-1}$. The values for C_T are given in Table 4.

Our neutron-matter results are shown in Figs. 48 and 49 in the $^1S_0$ and $^3P_2$–$^3F_2$ channel, respectively, where the rows correspond to the mentioned NN potentials as annotated. The left and middle columns depict the gaps $\Delta(k_F)$ using a free and a Hartree-Fock spectrum, respectively, whereas the right column shows the corresponding Hartree-Fock effective mass. NN-only results are plotted as black-solid lines, with the inclusion of the leading (subleading) 3N forces by orange (blue) uncertainty bands.

Figures 44, 45, and 48 show that the $^1S_0$ gaps at N^{3}LO without 3N forces are in good agreement. This observation can be traced back to the well-reproduced phase shifts at this order. Contributions from 3N forces do not change the results for the pairing gaps at low densities, $k_F \lesssim (0.7-0.8)\,\text{fm}^{-1}$, and only lead to a minor suppression at higher densities. The uncertainty bands including 3N forces are very small

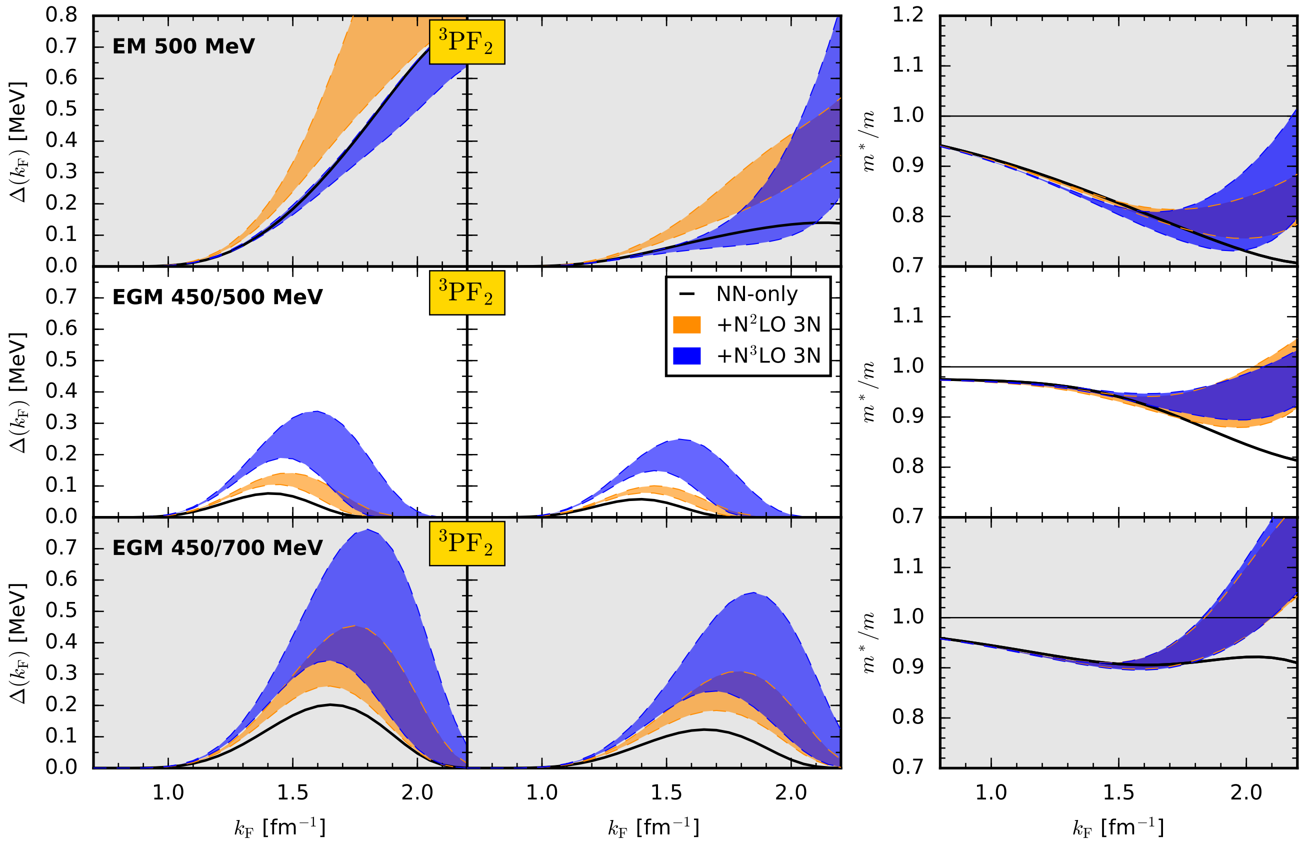

Figure 49: Gap Δ as a function of Fermi momentum k_F in the $^3P_2$—$^3F_2$ channel with a free (left column) and a Hartree-Fock spectrum (middle column) for the bare N^{3}LO NN potentials EM 500 MeV (first row), EGM 450/500 MeV (second row), and EGM 450/700 MeV (third row). The third column shows the effective mass at the Fermi surface corresponding to the Hartree-Fock spectrum. The NN-only results are plotted as black-solid lines. Variations of the 3N parameters c_1, c_3, and Λ_{3N} determine the uncertainty bands as discussed in the text.

for all potentials at N^{2}LO as well as N^{3}LO. In addition, self-energy contributions to the single-particle energies are small.

We show the corresponding results for the $^3P_2$—$^3F_2$ channel in Fig. 49. Since the relevant densities are higher than in the $^1S_0$ channel, the impact of 3N forces is generally larger for the pairing gap and also for the effective mass. We observe nonvanishing gaps for the three investigated NN potentials in all considered cases. In contrast to the $^1S_0$ channel the inclusion of 3N forces typically provides additional attraction and hence increases the pairing gap, except for the EM 500 MeV potential with subleading 3N forces. As shown in the right column, 3N contributions generally tend to enhance the effective mass (see also Ref. [43]), even to values greater than one at the Hartree-Fock level. We find in general that the results for the $^3P_2$—$^3F_2$ pairing gaps differ significantly for the various potentials and that it is delicate to extract robust quantitative predictions based on our results.

7 Summary and outlook

In this thesis we have used nuclear matter as an ideal system to test nuclear forces and to predict key quantities for neutron stars. The development of novel many-body frameworks led us to state-of-the-art calculations of the equation of state of neutron and symmetric matter at high orders in the chiral expansion as well as in the many-body expansion. On the other hand, the improved treatment of 3N forces in terms of effective two-body potentials enables first applications of N^{3}LO 3N forces to nuclear matter within general partial-wave approaches. Taking advantage of these developments, we explored Hamiltonians based on consistent chiral forces up to N^{3}LO and specified those with realistic saturation properties. These can be used in ab initio calculations for both nuclear matter as well as finite nuclei. In the following we summarize the key results of each section and emphasize future work.

We performed a comprehensive Weinberg eigenvalue analysis in free space of a representative set of modern chiral NN interactions [188], which have been developed within different regularization schemes. This gave us quantitative insights into their perturbativeness as well as the scheme dependences. Dominated by shallow (or nearly) bound states in the $^1S_0$ and $^3S_1$–$^3D_1$ channels, the attractive eigenvalues of the investigated potentials showed a universal behavior at all chiral orders. In contrast, the repulsive eigenvalues are sensitive to the specific details of the interaction, e.g., the regularization scheme, particularly for the short-range parts. That is, the Weinberg eigenvalues may behave quite differently with respect to the chiral order or the given class of interactions. While the local potentials developed large repulsive eigenvalues from LO to NLO, the semilocal potentials remain perturbative up to N^{2}LO. The latter become nonperturbative only at N^{3}LO and N^{4}LO. We traced back this sudden increase at N^{3}LO to the presence of new short-range couplings appearing at this order. In comparison, the investigated nonlocal potentials tend to remain more perturbative throughout all orders. Moreover, we found that a direct comparison of coordinate-space cutoff values for the GT+ as well as EKM interactions can be quite misleading and should be taken with care due to the different functional forms of the employed regulators. In future work, our analysis can directly be extended to study regulator artifacts at finite density using in-medium Weinberg eigenvalues and to account for 3N interactions to assess their perturbativeness. Furthermore, it would be interesting to compare Δ-less with Δ-full potentials. In fits of next-generation nuclear potentials Weinberg eigenvalues may serve as a useful feedback by pointing to subtle issues in the fitting procedure or by offering a tool to assess alternative regulator choices.

We then set up the machinery for asymmetric-matter calculations in MBPT up to third order in a partial-wave basis. The contributions from 3N forces beyond the Hartree-Fock approximation are considered in terms of our novel normal-ordering framework [28], which is based on 3N partial-wave matrix elements rather than the corresponding operatorial expressions. This makes it possible to generalize the computation of density-dependent effective two-body interactions, e.g., to improve the usual approximation of zero center-of-mass momentum. In addition, including contributions from subleading 3N interactions at N^{3}LO is then straightforward since the corresponding partial-wave matrix elements have been worked out recently. This enables interesting applications of subleading 3N forces to nuclear matter, as shown in this thesis.

Applying the normal-ordering method, we have significantly improved previous state-of-the-art neutron-matter calculations in MBPT at N^{3}LO by including for the first time subleading 3N contributions beyond the Hartree-Fock approximation [31]. For consistency with the EFT expansion, we also considered 4N Hartree-Fock energies in our N^{3}LO calculations. Benchmarking these calculations against results obtained in the nonperturbative SCGF method enabled us to assess the many-body convergence in the ladder channel. We observed a systematic convergence at third order in MBPT, where the specific pattern depends on the details of the employed Hamiltonian. Furthermore, we extended the improved normal-ordering method to finite temperatures. The corresponding 3N Hartree-Fock energies as well as partial-wave matrix elements agree well with previous studies which were limited to N^{2}LO. These benchmarks demonstrate that we are now in the position to perform calculations of asymmetric matter including all NN and 3N contributions up to N^{3}LO, both, at zero and at finite temperatures. Since all 3N topologies contribute to these systems, reliable fits of the 3N LECs c_D and c_E at this order were however in order.

We presented a new Monte-Carlo framework [32] for calculations of nuclear matter, which is ideal to include higher-order contributions from chiral interactions and is capable of going to high-enough orders in the many-body expansion for suitable interactions. Our calculations are directly performed in a single-particle product basis $|\mathbf{k}_i \sigma_i \tau_i\rangle$, without needing involved partial-wave decompositions. Tracing over spin $|\sigma_i\rangle$ and isospin states $|\tau_i\rangle$ of each particle with label i is fully automated, whereas the multidimensional integrals over the momenta $\mathbf{k}_i$ can be computed efficiently using adaptive Monte-Carlo algorithms. This makes implementing arbitrary energy diagrams straightforward, even up to high orders in MBPT, while the approximations in normal ordering are released. However, it is well known that the number of diagrams at each order increases rapidly. Within our Monte-Carlo framework, a manual implementation of these would be feasible but still tedious and at least inefficient. We therefore developed an automatic code generator based on the analytic form of a given diagram. The output in C++ is transparent and well readable, including dynamically generated comments. In addition, we worked out a general method to express chiral interactions exactly as matrices in spin-isospin space, where the matrix elements are analytic functions of the single-particle momenta $\mathbf{k}_i$ in the programming language C++ for general use. The automated generation of these interaction matrices is close to the operatorial definition of chiral forces to account transparently for the rich operator structures of NN, 3N, and 4N interactions, which we implemented with nonlocal regulators up to N^{3}LO. Higher orders may be included accordingly whether or not the partial-wave matrix elements have been worked out. To be able to incorporate NN interactions whose operatorial definitions is not directly accessible (e.g., RG-evolved potentials), we sum the contributions from all partial-wave channels for each Monte-Carlo sampling point. Specifically, we considered in this first application all contributions from NN interactions up to fourth order in MBPT and from normal-ordered 3N forces up to third order. The second order includes the residual 3N-3N diagram, which has only been evaluated so far for contact interactions. We treat particle-hole and particle-particle or hole-hole contributions on an equal footing, in contrast to former partial-wave-based calculations.

The framework was then applied to the calculation of the symmetric- and neutron-matter energy per particle in an expansion around Hartree Fock, but it can be easily generalized to expansions around other reference states. This enabled first benchmarks of chiral low-momentum interactions to fourth order in MBPT showing a systematic order-by-order convergence. We used this to develop new chiral interactions at N^{2}LO and N^{3}LO, including NN, 3N, and 4N interactions at N^{3}LO, where the 3N couplings are fit to the triton and to saturation properties. Our work showed that a good description of nuclear matter at these orders is possible, with a systematic behavior from N^{2}LO to N^{3}LO and natural LECs. It will be exciting to see what these interactions predict for nuclei and for the equation of state for astrophysics, as a first step towards guiding fits of next-generation chiral interactions. The extension of this framework to finite temperatures is currently work in progress.

Finally, we studied BCS pairing gaps in neutron matter in the singlet $^1S_0$ and the triplet $^3P_2$–$^3F_2$ channel [106]. We benchmarked and optimized two different algorithms that allow together a reliable as well as accurate solution of the nonlinear BCS gap equation. With these advances, we studied the gap order-by-order based on the local (up to N^{2}LO) and the semilocal (up to N^{4}LO) NN interactions for a range of coordinate-space cutoffs. At the highest chiral orders, the results in the $^1S_0$ channel agree for all interactions over the entire density region. However, in the $^3P_2$–$^3F_2$ channel the situation is much less clear since the results generally depend on the details of the interactions and the chiral order. The relevant Fermi-momentum scales are already close to the EFT breakdown scale of the corresponding interactions, so the observed strong regulator dependence is not surprising. For estimating theoretical uncertainties of the Hamiltonian, we followed the new method in Ref. [9] with two modifications. The obtained uncertainties are small for the $^1S_0$ channel for all densities, but sizable in the $^3P_2$–$^3F_2$ channel. In the latter case, only the bands at N^{3}LO as well as N^{4}LO are of comparable size and overlapping. Our calculations beyond NLO are not complete from an EFT perspective since no 3N forces have been considered for these interactions. Hence, the analysis should be revisited as soon as the calculation of local or semilocal 3N partial-wave matrix elements has been completed. This is currently work in progress. In addition, we also investigated the impact of 3N forces on the pairing gap for nonlocal N^{3}LO potentials. Using the improved normal-ordering method, we were able to incorporate for the first time subleading 3N contributions in the gap equation. We found only small repulsive effects from 3N forces in the $^1S_0$ channel, whereas in the $^3P_2$–$^3F_2$ channel the effects from 3N forces are larger and lead to attractive contributions in most cases. Also for these interactions, significant regulator dependences in the $^3P_2$–$^3F_2$ channel were observed. We eventually concluded that the high densities relevant for $^3P_2$–$^3F_2$ pairing reach the limit of the employed chiral EFT interactions. It is therefore not possible to draw final quantitative conclusions on the size of the $^3P_2$–$^3F_2$ gap in neutron matter. However, we found nonvanishing gaps for all employed realistic NN potentials, also when including 3N contributions. The developed methods can be used for improved studies of pairing gaps in the future. In particular, the generalized treatment of 3N forces in terms of partial waves allows us to incorporate consistently-evolved NN and 3N forces. This is of interest for pairing-gap calculations which account for corrections beyond the BCS level since SRG-evolved forces are expected to exhibit an improved many-body convergence.

A Normal-ordering symmetry factors

In this section we discuss the symmetry factor ζ that appears in the interaction kernel (1.45c) for normal-ordered 3N contributions in the normal self-energy Σ and the anomalous self-energy Δ. For this we consider a general Hamiltonian of the form

$$\hat{H} = \hat{T} + \hat{V}_{\text{NN}} + \hat{V}_{\text{3N}} \,, \tag{A.1}$$

where $\hat{T}$ represents the kinetic energy, $\hat{V}_{\text{NN}}$ all two-nucleon interactions and $\hat{V}_{\text{3N}}$ three-nucleon interactions. By using Wick's theorem (1.41) we can recast the Hamiltonian exactly in an equivalent form by normal ordering all operators with respect to a given reference state. For the treatment of superfluid systems (normal systems) it is convenient to choose the BCS state (Fermi sphere) as reference state. We represent $\hat{V}_{\text{NN}}$ and $\hat{V}_{\text{3N}}$ in terms of antisymmetrized matrix elements:

$$\hat{V}_{\text{NN}} = \frac{1}{4} \sum_{ijkl} \big\langle ij | V_{\text{NN}}^{\text{as}} | kl \big\rangle \, \hat{a}_i^\dagger \hat{a}_j^\dagger \hat{a}_l \hat{a}_k \,, \qquad \text{and} \qquad \hat{V}_{\text{3N}} = \frac{1}{36} \sum_{ijklmn} \big\langle ijk | V_{\text{3N}}^{\text{as}} | lmn \big\rangle \, \hat{a}_i^\dagger \hat{a}_j^\dagger \hat{a}_k^\dagger \hat{a}_n \hat{a}_m \hat{a}_l \,, \tag{A.2}$$

where the indices represent generic single-particle quantum numbers. When applying Wick's theorem with respect to a BCS reference state it is important to note that both normal contractions (connecting a creation operator with an annihilation operator) as well as anomalous contractions (connecting two creation or two annihilation operators) contribute. For the normal self-energy Σ the relevant contractions are of the form (see also Sec. 1.3.2)

$$\frac{1}{4} \sum_{ijkl} \big\langle ij | V_{\text{NN}}^{\text{as}} | kl \big\rangle \, \hat{a}_i^\dagger \overbracket{\hat{a}_j^\dagger \hat{a}_l} \hat{a}_k \,, \tag{A.3}$$

$$\frac{1}{36} \sum_{ijklmn} \big\langle ijk | V_{\text{3N}}^{\text{as}} | lmn \big\rangle \, \hat{a}_i^\dagger \overbracket{\hat{a}_j^\dagger \overbracket{\hat{a}_k^\dagger \hat{a}_n} \hat{a}_m \hat{a}_l} \,, \tag{A.4}$$

whereas for the anomalous self-energy Δ the relevant contractions take the form

$$\frac{1}{4} \sum_{ijkl} \big\langle ij | V_{\text{NN}}^{\text{as}} | kl \big\rangle \, \overbracket{\hat{a}_i^\dagger \hat{a}_j^\dagger} \hat{a}_l \hat{a}_k \,, \tag{A.5}$$

$$\frac{1}{36} \sum_{ijklmn} \big\langle ijk | V_{\text{3N}}^{\text{as}} | lmn \big\rangle \, \overbracket{\hat{a}_i^\dagger \hat{a}_j^\dagger} \overbracket{\hat{a}_k^\dagger \hat{a}_n} \hat{a}_m \hat{a}_l \,. \tag{A.6}$$

Since the interaction operators are represented as antisymmetrized matrix elements all different possible choices of picking creation or annihilation operators are equivalent and just lead to combinatorial factors. Hence, in order to determine ζ it is necessary to count the number of different contractions c_N. We obtain: $c_N = 4$ for Eq. (A.3), $c_N = 18$ for Eq. (A.4), $c_N = 1$ for Eq. (A.5) and $c_N = 9$ for Eq. (A.6). Combining these combinatorial factors with the prefactors $1/4$ and $1/36$ of the NN and 3N interactions we directly obtain $\zeta = 1/2$ for Σ and $\zeta = 1$ for Δ. We also note that in the present work we approximate the normal contractions in Eq. (A.6) by their contributions in normal systems. It has been shown in Ref. [141] that the inclusion of correlations in the reference state has only very small effects on the matrix elements of the normal-ordered 3N contributions for nuclear-matter calculations. In addition to contributions from normal contractions in Eq. (A.6) we also obtain nonvanishing contributions from multiple anomalous contractions. However, these contributions are small since such terms only include contributions from momenta around the Fermi surface and are of higher order in the gap.

B Partial-wave decomposition of the BCS gap equation

We briefly review the partial-wave decomposition of the gap equation (6.10) and specify the conventions used in this work. Following Refs. [264, 294, 295] we decompose the gap matrix in the form

$$\Delta_{\alpha\alpha'}(\mathbf{k}) = \sum_{\substack{l,S\\J,M}} \sqrt{\frac{8\pi}{2J+1}}\,\Delta^{JM}_{lS}(k)\left(G^{JM}_{lS}(\hat{\mathbf{k}})\right)_{\alpha\alpha'}\,, \tag{B.1}$$

and accordingly the nuclear interaction

$$(4\pi)^{-2}\,\langle \mathbf{k}\alpha\alpha'|\mathscr{A}_{12}V_{\mathrm{NN}}|\mathbf{k}'\beta\beta'\rangle = \sum_{\substack{l,l',S\\J,M}} i^{l'-l}\left(G^{JM}_{lS}(\hat{\mathbf{k}})\right)_{\alpha\alpha'}\left(G^{JM}_{l'S}(\hat{\mathbf{k}}')\right)^{*}_{\beta\beta'} V^{J(M)}_{ll'S}(k,k')\,, \tag{B.2}$$

with

$$\left(G^{JM}_{lS}(\hat{\mathbf{k}})\right)_{\alpha\alpha'} = \sum_{m,m_S} \mathscr{C}^{Sm_S}_{1/2\alpha 1/2\alpha'}\,\mathscr{C}^{JM}_{lmSm_S}\,Y^{m}_{l}(\hat{\mathbf{k}})\,. \tag{B.3}$$

These functions obey the orthogonality relations

$$\int \mathrm{d}\Omega_{\mathbf{k}} \sum_{\beta,\beta'}\left[\left(G^{JM}_{l'S}(\hat{\mathbf{k}}')\right)^{*}_{\beta\beta'}\left(G^{J'M'}_{l''S'}(\hat{\mathbf{k}}')\right)_{\beta\beta'}\right] = \delta_{ll'}\delta_{MM'}\delta_{JJ'}\delta_{SS'}\,. \tag{B.4}$$

The J-dependent factor in Eq. (B.1) is chosen such that the gap equation in partial-wave representation takes a particularly simple form. Inserting Eqs. (B.1) and (B.2) in the gap equation (6.10) results in

$$\begin{aligned}(4\pi)^{-2}\sum_{\substack{l,S\\J,M}} \frac{\Delta^{JM}_{lS}(k)}{\sqrt{2J+1}}\left(G^{JM}_{lS}(\hat{\mathbf{k}})\right)_{\alpha\alpha'} = &-\int \frac{\mathrm{d}k'\,k'^2}{(2\pi)^3} \sum_{\substack{l,l',J,M,S\\l'',J',M',S'}} i^{l'-l}\left(G^{JM}_{lS}(\hat{\mathbf{k}})\right)_{\alpha\alpha'} V^{J(M)}_{ll'S}(k,k')\\ &\times \frac{\Delta^{J'M'}_{l''S'}(k')}{\sqrt{2J'+1}} \int \mathrm{d}\Omega_{\mathbf{k}'} \frac{\sum_{\beta,\beta'}\left[\left(G^{JM}_{l'S}(\hat{\mathbf{k}}')\right)^{*}_{\beta\beta'}\left(G^{J'M'}_{l''S'}(\hat{\mathbf{k}}')\right)_{\beta\beta'}\right]}{2\sqrt{\xi^2(k')+\frac{1}{2}\mathrm{Tr}\left[\Delta\Delta^{\dagger}\right](\mathbf{k}')}}\,.\end{aligned} \tag{B.5}$$

This equation can be simplified significantly by averaging the energy gap in the denominator over all angles, specifically,

$$\frac{1}{2}\mathrm{Tr}\left[\Delta\Delta^{\dagger}\right] \xrightarrow{\text{average}} \frac{1}{2}\int \frac{\mathrm{d}\Omega_{\mathbf{k}}}{4\pi}\mathrm{Tr}\left[\Delta\Delta^{\dagger}\right] = \sum_{l,S,J}|\Delta^{J}_{lS}(k')|^2 \equiv D^2(k)\,. \tag{B.6}$$

Because of the degeneracy with respect to the quantum number M in this approximation we summed here over all allowed values and used identity (B.4). Projecting out the components in Eq. (B.5) leads to the partial-wave decomposed gap equation (6.14)

$$\Delta^{J}_{lS}(k) = -\int_0^\infty \frac{\mathrm{d}k'\,k'^2}{\pi}\sum_{l'} \frac{i^{l'-l}V^{J}_{ll'S}(k,k')\Delta^{J}_{l'S}(k')}{\sqrt{\xi^2(k')+\sum_{\tilde{l},\tilde{S},\tilde{J}}|\Delta^{\tilde{J}}_{\tilde{l}\tilde{S}}(k')|^2}}\,. \tag{B.7}$$

C List of abbreviations

Table 7: Abbreviations used in the present thesis.

abbreviation	full text
3N	three-nucleon
4N	four-nucleon
AFDMC	auxiliary-diffusion Monte Carlo
BCS	Bardeen, Cooper, and Schrieffer (1957)
CC	coupled cluster
DMC	diffusion Monte Carlo
DR	dimensional regularization
EFT	effective field theory
HF	Hartree-Fock
IM-SRG	in-medium similarity renormalization group
LEC	low-energy constant
LO	leading order
MBPT	many-body perturbation theory
N$^{\nu}$LO	(next-to)$^{\nu}$ leading order
NN	nucleon-nucleon
PWA	partial-wave analysis
QMC	quantum Monte Carlo
RG	renormalization group
SCGF	self-consistent Green's function
SFR	spectral function regularization
SRG	similarity renormalization group

References

[1] K. Hebeler, J. D. Holt, J. Menéndez, and A. Schwenk, Ann. Rev. Nucl. Part. Sci. **65**, 457 (2015).

[2] H. Heiselberg and V. Pandharipande, Annu. Rev. Nucl. Part. Sci. **50**, 481 (2000).

[3] J. M. Lattimer, Ann. Rev. Nucl. Part. Sci. **62**, 485 (2012).

[4] G. Hagen, A. Ekström, C. Forssén, G. R. Jansen, W. Nazarewicz, T. Papenbrock, K. A. Wendt, S. Bacca, N. Barnea, B. Carlsson, C. Drischler, K. Hebeler, M. Hjorth-Jensen, M. Miorelli, G. Orlandini, A. Schwenk, and J. Simonis, Nat. Phys. **12**, 186 (2016).

[5] E. Epelbaum, H.-W. Hammer, and U.-G. Meißner, Rev. Mod. Phys. **81**, 1773 (2009).

[6] R. Machleidt and D. R. Entem, Phys. Rep. **503**, 1 (2011).

[7] R. Machleidt, Symmetry **8** (2016).

[8] D. R. Entem, N. Kaiser, R. Machleidt, and Y. Nosyk, Phys. Rev. C **91**, 014002 (2015).

[9] E. Epelbaum, H. Krebs, and U.-G. Meißner, Eur. Phys. J. A **51**, 53 (2015).

[10] E. Epelbaum, H. Krebs, and U.-G. Meißner, Phys. Rev. Lett. **115**, 122301 (2015).

[11] D. R. Entem, R. Machleidt, and Y. Nosyk, Phys. Rev. C **96**, 024004 (2017).

[12] D. R. Entem, N. Kaiser, R. Machleidt, and Y. Nosyk, Phys. Rev. C **92**, 064001 (2015).

[13] A. Ekström, G. Baardsen, C. Forssén, G. Hagen, M. Hjorth-Jensen, G. R. Jansen, R. Machleidt, W. Nazarewicz, T. Papenbrock, J. Sarich, and S. M. Wild, Phys. Rev. Lett. **110**, 192502 (2013).

[14] A. Ekström, G. R. Jansen, K. A. Wendt, G. Hagen, T. Papenbrock, B. D. Carlsson, C. Forssén, M. Hjorth-Jensen, P. Navrátil, and W. Nazarewicz, Phys. Rev. C **91**, 051301(R) (2015).

[15] B. D. Carlsson, A. Ekström, C. Forssén, D. F. Strömberg, G. R. Jansen, O. Lilja, M. Lindby, B. A. Mattsson, and K. A. Wendt, Phys. Rev. X **6**, 011019 (2016).

[16] A. Gezerlis, I. Tews, E. Epelbaum, S. Gandolfi, K. Hebeler, A. Nogga, and A. Schwenk, Phys. Rev. Lett. **111**, 032501 (2013).

[17] A. Gezerlis, I. Tews, E. Epelbaum, M. Freunek, S. Gandolfi, K. Hebeler, A. Nogga, and A. Schwenk, Phys. Rev. C **90**, 054323 (2014).

[18] A. Dyhdalo, R. J. Furnstahl, K. Hebeler, and I. Tews, Phys. Rev. C **94**, 034001 (2016).

[19] R. J. Furnstahl, N. Klco, D. R. Phillips, and S. Wesolowski, Phys. Rev. C **92**, 024005 (2015).

[20] R. J. Furnstahl, D. R. Phillips, and S. Wesolowski, J. Phys. G **42**, 034028 (2015).

[21] S. Wesolowski, N. Klco, R. J. Furnstahl, D. R. Phillips, and A. Thapaliya, J. Phys. G **43**, 074001 (2016).

[22] M. Wang, G. Audi, A. H. Wapstra, F. G. Kondev, M. MacCormick, X. Xu, and B. Pfeiffer, Chin. Phys. C **36**, 1603 (2012).

[23] J. Simonis, S. R. Stroberg, K. Hebeler, J. D. Holt, and A. Schwenk, Phys. Rev. C **96**, 014303 (2017).

[24] S. Binder, J. Langhammer, A. Calci, and R. Roth, Phys. Lett. B **736**, 119 (2014).

[25] R. F. Garcia Ruiz, M. L. Bissell, K. Blaum, A. Ekström, N. Frömmgen, G. Hagen, M. Hammen, K. Hebeler, J. D. Holt, G. R. Jansen, M. Kowalska, K. Kreim, W. Nazarewicz, R. Neugart, G. Neyens, W. Nörtershäuser, T. Papenbrock, J. Papuga, A. Schwenk, J. Simonis, K. A. Wendt, and D. T. Yordanov, Nat. Phys. **12**, 594 (2016).

[26] G. Hagen, G. R. Jansen, and T. Papenbrock, Phys. Rev. Lett. **117**, 172501 (2016).

[27] K. Hebeler, S. K. Bogner, R. J. Furnstahl, A. Nogga, and A. Schwenk, Phys. Rev. C **83**, 031301(R) (2011).

[28] C. Drischler, K. Hebeler, and A. Schwenk, Phys. Rev. C **93**, 054314 (2016).

[29] A. Ekström, G. Hagen, T. D. Morris, T. Papenbrock, and P. D. Schwartz, arXiv:1707.09028 .

[30] T. D. Morris, J. Simonis, S. R. Stroberg, C. Stumpf, G. Hagen, J. D. Holt, G. R. Jansen, T. Papenbrock, R. Roth, and A. Schwenk, arXiv:1709.02786 .

[31] C. Drischler, A. Carbone, K. Hebeler, and A. Schwenk, Phys. Rev. C **94**, 054307 (2016).

[32] C. Drischler, K. Hebeler, and A. Schwenk, arXiv:1710.08220 .

[33] H. A. Bethe and R. F. Bacher, Rev. Mod. Phys. **8**, 82 (1936).

[34] J. M. Lattimer, Nucl. Phys. A **928**, 276 (2014).

[35] J. M. Lattimer, Int. J. Mod. Phys. E **26**, 1740014 (2017).

[36] C. Drischler, V. Somà, and A. Schwenk, Phys. Rev. C **89**, 025806 (2014).

[37] C. Wellenhofer, J. W. Holt, and N. Kaiser, Phys. Rev. C **93**, 055802 (2016).

[38] G. F. Bertsch and D. Bingham, arXiv:1703.08844 .

[39] J. Piekarewicz and M. Centelles, Phys. Rev. C **79**, 054311 (2009).

[40] M. B. Tsang, J. R. Stone, F. Camera, P. Danielewicz, S. Gandolfi, K. Hebeler, C. J. Horowitz, J. Lee, W. G. Lynch, Z. Kohley, R. Lemmon, P. Möller, T. Murakami, S. Riordan, X. Roca-Maza, F. Sammarruca, A. W. Steiner, I. Vidaña, and S. J. Yennello, Phys. Rev. C **86**, 015803 (2012).

[41] K. Hebeler, J. M. Lattimer, C. J. Pethick, and A. Schwenk, Phys. Rev. Lett. **105**, 161102 (2010).

[42] K. Hebeler, J. M. Lattimer, C. J. Pethick, and A. Schwenk, Astrophys. J. **773**, 11 (2013).

[43] K. Hebeler and A. Schwenk, Phys. Rev. C **82**, 014314 (2010).

[44] S. Gandolfi, J. Carlson, and S. Reddy, Phys. Rev. C **85**, 032801(R) (2012).

[45] C. J. Horowitz, E. F. Brown, Y. Kim, W. G. Lynch, R. Michaels, A. Ono, J. Piekarewicz, M. B. Tsang, and H. H. Wolter, J. Phys. G: Nucl. Part. Phys. **41**, 093001 (2014).

[46] J. Birkhan, M. Miorelli, S. Bacca, S. Bassauer, C. A. Bertulani, G. Hagen, H. Matsubara, P. von Neumann-Cosel, T. Papenbrock, N. Pietralla, V. Y. Ponomarev, A. Richter, A. Schwenk, and A. Tamii, Phys. Rev. Lett. **118**, 252501 (2017).

[47] C. J. Horowitz, K. S. Kumar, and R. Michaels, Eur. Phys. J. A **50**, 48 (2014).

[48] C. Wellenhofer, J. W. Holt, and N. Kaiser, Phys. Rev. C **92**, 015801 (2015).

[49] T. Kortelainen, M. Lesinski, J. Moré, W. Nazarewicz, J. Sarich, N. Schunck, M. V. Stoitsov, and S. Wild, Phys. Rev. C **82**, 024313 (2010).

[50] P. Danielewicz and J. Lee, Nucl. Phys. A **922**, 1 (2014).

[51] L.-W. Chen, C. M. Ko, B.-A. Li, and J. Xu, Phys. Rev. C **82**, 024321 (2010).

[52] M. B. Tsang, Y. Zhang, P. Danielewicz, M. Famiano, Z. Li, W. G. Lynch, and A. W. Steiner, Phys. Rev. Lett. **102**, 122701 (2009).

[53] A. Tamii, I. Poltoratska, P. von Neumann-Cosel, Y. Fujita, T. Adachi, *et al.*, Phys. Rev. Lett. **107**, 062502 (2011).

[54] X. Roca-Maza, M. Brenna, G. Colò, M. Centelles, X. Viñas, B. K. Agrawal, N. Paar, D. Vretenar, and J. Piekarewicz, Phys. Rev. C **88**, 024316 (2013).

[55] L. Trippa, G. Colo, and E. Vigezzi, Phys. Rev. C **77**, 061304 (2008).

[56] J. M. Lattimer and A. W. Steiner, Eur. Phys. J. A **50**, 40 (2014).

[57] J. M. Lattimer and Y. Lim, Astrophys. J. **771**, 51 (2013).

[58] J. Antoniadis, P. C. C. Freire, N. Wex, T. M. Tauris, R. S. Lynch, M. H. van Kerkwijk, M. Kramer, C. Bassa, V. S. Dhillon, T. Driebe, J. W. T. Hessels, V. M. Kaspi, V. I. Kondratiev, N. Langer, T. R. Marsh, M. A. McLaughlin, T. T. Pennucci, S. M. Ransom, I. H. Stairs, J. van Leeuwen, J. P. W. Verbiest, and D. G. Whelan, Science **340**, 1233232 (2013).

[59] J. M. Lattimer and M. Prakash, Science **304**, 536 (2004).

[60] N. Andersson, V. Ferrari, D. I. Jones, K. D. Kokkotas, B. Krishnan, J. S. Read, L. Rezzolla, and B. Zink, Gen. Rel. Grav. **43**, 409 (2011).

[61] A. L. Watts, N. Andersson, D. Chakrabarty, M. Feroci, K. Hebeler, G. Israel, F. K. Lamb, M. C. Miller, S. Morsink, F. Özel, A. Patruno, J. Poutanen, D. Psaltis, A. Schwenk, A. W. Steiner, L. Stella, L. Tolos, and M. van der Klis, Rev. Mod. Phys. **88**, 021001 (2016).

[62] A. Bauswein, H.-T. Janka, K. Hebeler, and A. Schwenk, Phys. Rev. D **86**, 063001 (2012).

[63] A. Bauswein, N. Stergioulas, and H.-T. Janka, Phys. Rev. D **90**, 023002 (2014).

[64] A. Bauswein, N. Stergioulas, and H.-T. Janka, Eur. Phys. J. A **52**, 56 (2016).

[65] P. Demorest, T. Pennucci, S. Ransom, M. Roberts, and J. Hessels, Nature **467**, 1081 (2010).

[66] J. M. Lattimer and M. Prakash, Astrophys. J. **550**, 426 (2001).

[67] E. Epelbaum, W. Glöckle, and U.-G. Meißner, Nucl. Phys. A **747**, 362 (2005).

[68] E. Epelbaum, Prog. Part. Nucl. Phys. **57**, 654 (2006).

[69] E. Epelbaum, Prog. Part. Nucl. Phys. **67**, 343 (2012).

[70] H.-W. Hammer, A. Nogga, and A. Schwenk, Rev. Mod. Phys. **85**, 197 (2013).

[71] F. Wilczek, Annu. Rev. Nucl. Part. Sci. **32**, 177 (1982).

[72] R. Aaij *et al.* (LHCb Collaboration), Phys. Rev. Lett. **115**, 072001 (2015).

[73] R. Aaij, B. Adeva, M. Adinolfi, Z. Ajaltouni, S. Akar, J. Albrecht, F. Alessio, M. Alexander, S. Ali, G. Alkhazov, *et al.* (LHCb Collaboration), Phys. Rev. D **95**, 012002 (2017).

[74] R. Aaij, B. Adeva, M. Adinolfi, Z. Ajaltouni, S. Akar, J. Albrecht, F. Alessio, M. Alexander, S. Ali, G. Alkhazov, *et al.* (LHCb Collaboration), Phys. Rev. Lett. **118**, 022003 (2017).

[75] S. Bethke, Prog. Part. Nucl. Phys. **58**, 351 (2007).

[76] I. Hinchliffe and A. Manohar, Annu. Rev. Nucl. Part. Sci. **50**, 643 (2000).

[77] G. Sterman, J. Smith, J. C. Collins, J. Whitmore, R. Brock, J. Huston, J. Pumplin, W.-K. Tung, H. Weerts, C.-P. Yuan, S. Kuhlmann, S. Mishra, J. G. Morfín, F. Olness, J. Owens, J. Qiu, and D. E. Soper, Rev. Mod. Phys. **67**, 157 (1995).

[78] D. J. Gross and F. Wilczek, Phys. Rev. Lett. **30**, 1343 (1973).

[79] H. D. Politzer, Phys. Rev. Lett. **30**, 1346 (1973).

[80] S. R. Beane, W. Detmold, K. Orginos, and M. J. Savage, Prog. Part. Nucl. Phys. **66**, 1 (2011).

[81] P. Klos, J. E. Lynn, I. Tews, S. Gandolfi, A. Gezerlis, H. W. Hammer, M. Hoferichter, and A. Schwenk, Phys. Rev. C **94**, 054005 (2016).

[82] C. Patrignani *et al.* (Particle Data Group), Chin. Phys. C **40**, 100001 (2016).

[83] D. B. Kaplan, in *Lectures delivered at the 17th National Nuclear Physics Summer School 2015, Berkeley, June 6-17, 2005* (2005).

[84] J. Goldstone, A. Salam, and S. Weinberg, Phys. Rev. **127**, 965 (1962).

[85] S. Weinberg, Phys. Lett. B **251**, 288 (1990).

[86] S. Weinberg, Nucl. Phys. B **363**, 3 (1991).

[87] S. Weinberg, Phys. Lett. B **295**, 114 (1992).

[88] S. Weinberg, Physica A **96**, 327 (1979).

[89] P. F. Bedaque and U. van Kolck, Annu. Rev. Nucl. Part. Sci. **52**, 339 (2002).

[90] S. König, H. W. Grießhammer, H.-W. Hammer, and U. van Kolck, Phys. Rev. Lett. **118**, 202501 (2017).

[91] M. Lacombe, B. Loiseau, J. M. Richard, R. V. Mau, J. Côté, P. Pirès, and R. de Tourreil, Phys. Rev. C **21**, 861 (1980).

[92] R. B. Wiringa, V. G. J. Stoks, and R. Schiavilla, Phys. Rev. C **51**, 38 (1995).

[93] R. Machleidt, Phys. Rev. C **63**, 024001 (2001).

[94] E. Epelbaum, arXiv:1510.07036 .

[95] H. Krebs, A. Gasparyan, and E. Epelbaum, Phys. Rev. C **85**, 054006 (2012).

[96] H. Krebs, A. Gasparyan, and E. Epelbaum, Phys. Rev. C **87**, 054007 (2013).

[97] J. A. Melendez, S. Wesolowski, and R. J. Furnstahl, Phys. Rev. C **96**, 024003 (2017).

[98] K. A. Wendt, B. D. Carlsson, and A. Ekström, arXiv:1410.0646 .

[99] A. Ekström, B. D. Carlsson, K. A. Wendt, C. Forssén, M. Hjorth-Jensen, R. Machleidt, and S. M. Wild, J. Phys. G: Nucl. Part. Phys. **42**, 034003 (2015).

[100] B. D. Carlsson, Phys. Rev. C **95**, 034002 (2017).

[101] M. Schindler and D. Phillips, Ann. Phys. **324**, 682 (2009), [Erratum: Ann. Phys. **324**, 2051 (2009)].

[102] S. Binder, A. Calci, E. Epelbaum, R. J. Furnstahl, J. Golak, K. Hebeler, H. Kamada, H. Krebs, J. Langhammer, S. Liebig, P. Maris, U.-G. Meißner, D. Minossi, A. Nogga, H. Potter, R. Roth, R. Skibiński, K. Topolnicki, J. P. Vary, and H. Witała (LENPIC Collaboration), Phys. Rev. C **93**, 044002 (2016).

[103] J. E. Lynn, I. Tews, J. Carlson, S. Gandolfi, A. Gezerlis, K. E. Schmidt, and A. Schwenk, Phys. Rev. Lett. **116**, 062501 (2016).

[104] J. E. Lynn, I. Tews, J. Carlson, S. Gandolfi, A. Gezerlis, K. E. Schmidt, and A. Schwenk, arXiv:1706.07668 .

[105] D. Lonardoni, J. Carlson, S. Gandolfi, J. E. Lynn, K. E. Schmidt, A. Schwenk, and X. Wang, arXiv:1709.09143 .

[106] C. Drischler, T. Krüger, K. Hebeler, and A. Schwenk, Phys. Rev. C **95**, 024302 (2017).

[107] L. Coraggio, J. W. Holt, N. Itaco, R. Machleidt, and F. Sammarruca, Phys. Rev. C **87**, 014322 (2013).

[108] I. Tews, T. Krüger, K. Hebeler, and A. Schwenk, Phys. Rev. Lett. **110**, 032504 (2013).

[109] J. W. Holt, N. Kaiser, and W. Weise, Prog. Part. Nucl. Phys. **73**, 35 (2013).

[110] C. Wellenhofer, J. W. Holt, N. Kaiser, and W. Weise, Phys. Rev. C **89**, 064009 (2014).

[111] L. Coraggio, J. W. Holt, N. Itaco, R. Machleidt, L. E. Marcucci, and F. Sammarruca, Phys. Rev. C **89**, 044321 (2014).

[112] J. W. Holt and N. Kaiser, Phys. Rev. C **95**, 034326 (2017).

[113] N. Kaiser, Eur. Phys. J. A **53**, 104 (2017).

[114] R. Roth and J. Langhammer, Phys. Lett. B **683**, 272 (2010).

[115] J. Langhammer, R. Roth, and C. Stumpf, Phys. Rev. C **86**, 054315 (2012).

[116] A. Tichai, J. Langhammer, S. Binder, and R. Roth, Phys. Lett. B **756**, 283 (2016).

[117] A. Tichai, E. Gebrerufael, and R. Roth, arXiv:1703.05664 .

[118] S. Wilson, *Electron Correlation in Molecules*, 1st ed. (Oxford University Press, 1984).

[119] I. Shavitt and R. J. Bartlett, *Many-Body Methods in Chemistry and Physics: MBPT and Coupled-Cluster Theory*, Cambridge Molecular Science (Cambridge University Press, 2009).

[120] A. Szabo and N. Ostlund, *Modern Quantum Chemistry: Introduction to Advanced Electronic Structure Theory*, Dover Books on Chemistry (Dover Publications, 1989).

[121] W. Dickhoff and D. Van Neck, *Many-body Theory Exposed!: Propagator Description of Quantum Mechanics in Many-body Systems*, 1st ed. (World Scientific, 2005).

[122] P. D. Stevenson, Int. J. Mod. Phys. C **14**, 1135 (2003).

[123] J. Goldstone, Proceedings of the Royal Society of London A: Mathematical, Physical and Engineering Sciences **239**, 267 (1957).

[124] G. Hagen, T. Papenbrock, M. Hjorth-Jensen, and D. J. Dean, Rep. Prog. Phys. **77**, 096302 (2014).

[125] R. J. Bartlett and M. Musiał, Rev. Mod. Phys. **79**, 291 (2007).

[126] J. Paldus and H. Wong, Comput. Phys. Commun. **6**, 1 (1973).

[127] H. Wong and J. Paldus, Comput. Phys. Commun. **6**, 9 (1973).

[128] J. Lyons, D. Moncrieff, and S. Wilson, Comput. Phys. Commun. **84**, 91 (1994).

[129] N. J. A. Sloane, https://oeis.org/A064732, the Encyclopedia of Integer Sequences: Number of labeled Hugenholtz diagrams with n nodes.

[130] S. Wilson and D. M. Silver, Int. J. Quantum Chem. **15**, 683 (1979).

[131] G. H. Diercksen and S. Wilson, eds., *Methods in Computational Molecular Physics*, Nato Science Series C: Mathematical and Physical Sciences, Vol. 113 (D. Reidel Publishing Company, Dordrecht, Holland, 1983).

[132] A. Lovato, O. Benhar, S. Fantoni, A. Yu. Illarionov, and K. E. Schmidt, Phys. Rev. C **83**, 054003 (2011).

[133] J. W. Holt, N. Kaiser, and W. Weise, Phys. Rev. C **81**, 024002 (2010).

[134] A. Carbone, A. Cipollone, C. Barbieri, A. Rios, and A. Polls, Phys. Rev. C **88**, 054326 (2013).

[135] R. Roth, S. Binder, K. Vobig, A. Calci, J. Langhammer, and P. Navrátil, Phys. Rev. Lett. **109**, 052501 (2012).

[136] E. Gebrerufael, K. Vobig, H. Hergert, and R. Roth, Phys. Rev. Lett. **118**, 152503 (2017).

[137] G. Hagen, T. Papenbrock, A. Ekström, K. Wendt, G. Baardsen, S. Gandolfi, M. Hjorth-Jensen, and C. J. Horowitz, Phys. Rev. C **89**, 014319 (2014).

[138] G. C. Wick, Phys. Rev. **80**, 268 (1950).

[139] S. K. Bogner, R. J. Furnstahl, and A. Schwenk, Prog. Part. Nucl. Phys. **65**, 94 (2010).

[140] T. Krüger, I. Tews, K. Hebeler, and A. Schwenk, Phys. Rev. C **88**, 025802 (2013).

[141] A. Carbone, A. Rios, and A. Polls, Phys. Rev. C **90**, 054322 (2014).

[142] G. Baardsen, A. Ekström, G. Hagen, and M. Hjorth-Jensen, Phys. Rev. C **88**, 054312 (2013).

[143] A. Rios, A. Polls, and I. Vidaña, Phys. Rev. C **79**, 025802 (2009).

[144] A. Carbone, A. Polls, and A. Rios, Phys. Rev. C **88**, 044302 (2013).

[145] S. Gandolfi, A. Lovato, J. Carlson, and K. E. Schmidt, Phys. Rev. C **90**, 061306 (2014).

[146] I. Tews, S. Gandolfi, A. Gezerlis, and A. Schwenk, Phys. Rev. C **93**, 024305 (2016).

[147] G. Hagen, T. Papenbrock, D. J. Dean, A. Schwenk, A. Nogga, M. Włoch, and P. Piecuch, Phys. Rev. C **76**, 034302 (2007).

[148] S. Binder, P. Piecuch, A. Calci, J. Langhammer, P. Navrátil, and R. Roth, Phys. Rev. C **88**, 054319 (2013).

[149] W. M. C. Foulkes, L. Mitas, R. J. Needs, and G. Rajagopal, Rev. Mod. Phys. **73**, 33 (2001).

[150] J. Carlson, S. Gandolfi, F. Pederiva, S. C. Pieper, R. Schiavilla, K. E. Schmidt, and R. B. Wiringa, Rev. Mod. Phys. **87**, 1067 (2015).

[151] F. Pederiva, A. Roggero, and K. E. Schmidt, "Variational and diffusion monte carlo approaches to the nuclear few- and many-body problem," in *An Advanced Course in Computational Nuclear Physics: Bridging the Scales from Quarks to Neutron Stars*, edited by M. Hjorth-Jensen, M. P. Lombardo, and U. van Kolck (Springer International Publishing, Cham, 2017) pp. 401–476.

[152] J. E. Lynn, J. Carlson, E. Epelbaum, S. Gandolfi, A. Gezerlis, and A. Schwenk, Phys. Rev. Lett. **113**, 192501 (2014).

[153] S. Gandolfi, F. Pederiva, S. Fantoni, and K. E. Schmidt, Phys. Rev. Lett. **98**, 102503 (2007).

[154] D. R. Entem and R. Machleidt, Phys. Rev. C **68**, 041001(R) (2003).

[155] S. Gandolfi, A. Gezerlis, and J. Carlson, Annu. Rev. Nucl. Part. Sci. **65**, 303 (2015).

[156] E. Epelbaum, H. Krebs, D. Lee, and U.-G. Meißner, Eur. Phys. J. A **40**, 199 (2009).

[157] A. Gezerlis and J. Carlson, Phys. Rev. C **81**, 025803 (2010).

[158] A. Akmal, V. R. Pandharipande, and D. G. Ravenhall, Phys. Rev. C **58**, 1804 (1998).

[159] F. Wegner, Ann. Phys. **506**, 77 (1994).

[160] S. D. Glazek and K. G. Wilson, Phys. Rev. D **48**, 5863 (1993).

[161] S. D. Glazek and K. G. Wilson, Phys. Rev. D **49**, 4214 (1994).

[162] R. J. Furnstahl and K. Hebeler, Rep. Prog. Phys. **76**, 126301 (2013).

[163] S. K. Bogner, R. J. Furnstahl, and R. J. Perry, Phys. Rev. C **75**, 061001(R) (2007).

[164] E. Anderson, S. K. Bogner, R. J. Furnstahl, E. D. Jurgenson, R. J. Perry, and A. Schwenk, Phys. Rev. C **77**, 037001 (2008).

[165] E. D. Jurgenson, P. Navrátil, and R. J. Furnstahl, Phys. Rev. Lett. **103**, 082501 (2009).

[166] K. Hebeler, Phys. Rev. C **85**, 021002(R) (2012).

[167] K. Hebeler and R. J. Furnstahl, Phys. Rev. C **87**, 031302 (2013).

[168] P. J. Mohr, B. N. Taylor, and D. B. Newell, Rev. Mod. Phys. **84**, 1527 (2012).

[169] J. Beringer *et al.* (Particle Data Group), Phys. Rev. D **86**, 010001 (2012).

[170] M. Piarulli, L. Girlanda, R. Schiavilla, R. Navarro Pérez, J. E. Amaro, *et al.*, Phys. Rev. C **91**, 024003 (2015).

[171] M. Piarulli, L. Girlanda, R. Schiavilla, A. Kievsky, A. Lovato, L. E. Marcucci, S. C. Pieper, M. Viviani, and R. B. Wiringa, Phys. Rev. C **94**, 054007 (2016).

[172] E. Epelbaum, W. Glöckle, and U.-G. Meißner, Eur. Phys. J. A **19**, 125 (2004).

[173] E. Epelbaum, W. Glöckle, and U.-G. Meißner, Eur. Phys. J. A **19**, 401 (2004).

[174] N. Fettes, U.-G. Meißner, and S. Steininger, Nucl. Phys. A **640**, 199 (1998).

[175] E. Epelbaum, U.-G. Meißner, and W. Glöckle, Nucl. Phys. A **714**, 535 (2003).

[176] N. Kaiser, R. Brockmann, and W. Weise, Nucl. Phys. A **625**, 758 (1997).

[177] V. Bernard, N. Kaiser, and U.-G. Meißner, Nucl. Phys. A **615**, 483 (1997).

[178] H. Krebs, E. Epelbaum, and U.-G. Meißner, Eur. Phys. J. A **32**, 127 (2007).

[179] N. Kaiser, Phys. Rev. C **64**, 057001 (2001).

[180] N. Kaiser, Phys. Rev. C **61**, 014003 (1999).

[181] N. Kaiser, Phys. Rev. C **62**, 024001 (2000).

[182] N. Kaiser, Phys. Rev. C **63**, 044010 (2001).

[183] G. Brown, A. Jackson, and T. Kuo, Nucl. Phys. A **133**, 481 (1969).

[184] H. Kamada and W. Glöckle, Phys. Rev. Lett. **80**, 2547 (1998).

[185] V. G. J. Stoks, R. A. M. Klomp, M. C. M. Rentmeester, and J. J. de Swart, Phys. Rev. C **48**, 792 (1993), Nijmegen NN online program, http://nn-online.org/.

[186] M. Hoferichter, J. Ruiz de Elvira, B. Kubis, and U.-G. Meißner, Phys. Rev. Lett. **115**, 192301 (2015).

[187] J. R. Bergervoet, P. C. van Campen, W. A. van der Sanden, and J. J. de Swart, Phys. Rev. C **38**, 15 (1988).

[188] J. Hoppe, C. Drischler, R. J. Furnstahl, K. Hebeler, and A. Schwenk, Phys. Rev. C **96**, 054002 (2017).

[189] K. Erkelenz, R. Alzetta, and K. Holinde, Nucl. Phys. A **176**, 413 (1971).

[190] U. van Kolck, Phys. Rev. C **49**, 2932 (1994).

[191] E. Epelbaum, A. Nogga, W. Glöckle, H. Kamada, U.-G. Meißner, and H. Witała, Phys. Rev. C **66**, 064001 (2002).

[192] V. Bernard, E. Epelbaum, H. Krebs, and U.-G. Meißner, Phys. Rev. C **77**, 064004 (2008).

[193] V. Bernard, E. Epelbaum, H. Krebs, and U.-G. Meißner, Phys. Rev. C **84**, 054001 (2011).

[194] E. Epelbaum, U.-G. Meißner, and J. E. Palomar, Phys. Rev. C **71**, 024001 (2005).

[195] A. Nogga, S. K. Bogner, and A. Schwenk, Phys. Rev. C **70**, 061002(R) (2004).

[196] V. R. Pandharipande, D. R. Phillips, and U. v. Kolck, Phys. Rev. C **71**, 064002 (2005).

[197] E. Epelbaum, H. Krebs, and U.-G. Meißner, Nucl. Phys. A **806**, 65 (2008).

[198] S. Ishikawa and M. R. Robilotta, Phys. Rev. C **76**, 014006 (2007).

[199] E. Epelbaum, A. M. Gasparyan, H. Krebs, and C. Schat, Eur. Phys. J. A **51**, 26 (2015).

[200] L. Girlanda, A. Kievsky, and M. Viviani, Phys. Rev. C **84**, 014001 (2011).

[201] S. A. Abbas, *Group Theory in Particle, Nuclear, and Hadron Physics*, 1st ed. (CRC Press, 2016).

[202] P. Navrátil, Few Body Syst. **41**, 117 (2007).

[203] A. Dyhdalo, S. K. Bogner, and R. J. Furnstahl, Phys. Rev. C **95**, 054314 (2017).

[204] M. Piarulli, A. Baroni, L. Girlanda, A. Kievsky, A. Lovato, E. Lusk, L. E. Marcucci, S. C. Pieper, R. Schiavilla, M. Viviani, and R. B. Wiringa, arXiv:1707.02883 .

[205] K. Hebeler, H. Krebs, E. Epelbaum, J. Golak, and R. Skibinski, Phys. Rev. C **91**, 044001 (2015).

[206] J. Golak, D. Rozpędzik, R. Skibiński, K. Topolnicki, H. Witała, W. Glöckle, A. Nogga, E. Epelbaum, H. Kamada, C. Elster, and I. Fachruddin, Eur. Phys. J. A **43**, 241 (2010).

[207] R. Skibinski, J. Golak, K. Topolnicki, H. Witała, H. Kamada, W. Glöckle, and A. Nogga, Eur. Phys. J. A **47**, 48 (2011).

[208] E. Epelbaum, Phys. Lett. B **639**, 456 (2006).

[209] E. Epelbaum, Eur. Phys. J. A **34**, 197 (2007).

[210] H. McManus and D. Riska, Phys. Lett. B **92**, 29 (1980).

[211] M. R. Robilotta, Phys. Rev. C **31**, 974 (1985).

[212] N. Kaiser, Eur. Phys. J. A **48**, 135 (2012).

[213] S. Weinberg, Phys. Rev. **131**, 440 (1963).

[214] R. Jost and A. Pais, Phys. Rev. **82**, 840 (1951).

[215] W. Kohn, Rev. Mod. Phys. **26**, 292 (1954).

[216] K. Meetz, J. Math. Phys. **3**, 690 (1962).

[217] S. Weinberg, Phys. Rev. **130**, 776 (1963).

[218] M. Scadron and S. Weinberg, Phys. Rev. **133** (1964).

[219] S. K. Bogner, A. Schwenk, R. J. Furnstahl, and A. Nogga, Nucl. Phys. A **763**, 59 (2005).

[220] S. K. Bogner, R. J. Furnstahl, S. Ramanan, and A. Schwenk, Nucl. Phys. A **773**, 203 (2006).

[221] R. Navarro Pérez, J. E. Amaro, and E. Ruiz Arriola, Phys. Rev. C **91**, 054002 (2015).

[222] J. Hoppe, *Weinberg eigenvalue analysis based on chiral interactions*, Bachelor's thesis, Technische Universität Darmstadt (2016), (supervised by A. Schwenk and C. Drischler).

[223] S. Ramanan, S. Bogner, and R. J. Furnstahl, Nucl. Phys. A **797**, 81 (2007).

[224] S. Ramanan and M. Urban, Phys. Rev. C **88**, 054315 (2013).

[225] S. Srinivas and S. Ramanan, Phys. Rev. C **94**, 064303 (2016).

[226] G. E. Brown and A. D. Jackson, *The nucleon-nucleon interaction* (Elsevier Science Publishing Co Inc., U.S., 1976).

[227] W. Glöckle, *The Quantum Mechanical Few-Body Problem* (Springer, Berlin, Heidelberg, 1983).

[228] R. Machleidt, private communication, (2017).

[229] R. Machleidt, F. Sammarruca, and Y. Song, Phys. Rev. C **53**, R1483 (1996).

[230] C. Drischler, *Towards Full N^{3}LO Calculations of Asymmetric Nuclear Matter*, Master's thesis, Technische Universität Darmstadt (2014), (supervised by A. Schwenk and K. Hebeler).

[231] J. W. Holt, N. Kaiser, and W. Weise, Phys. Rev. C **79**, 054331 (2009).

[232] A. Schwenk and B. Friman, Phys. Rev. Lett. **92**, 082501 (2004).

[233] R. Skibiński, J. Golak, K. Topolnicki, H. Witała, E. Epelbaum, W. Glöckle, H. Krebs, A. Nogga, and H. Kamada, Phys. Rev. C **84**, 054005 (2011).

[234] J. Golak, R. Skibiński, K. Topolnicki, H. Witała, E. Epelbaum, H. Krebs, H. Kamada, U.-G. Meißner, V. Bernard, P. Maris, J. Vary, S. Binder, A. Calci, K. Hebeler, J. Langhammer, R. Roth, A. Nogga, S. Liebig, and D. Minossi, Eur. Phys. J. A **50**, 177 (2014).

[235] L. Tolos, B. Friman, and A. Schwenk, Nucl. Phys. A **806**, 105 (2008).

[236] W. H. Dickhoff and C. Barbieri, Prog. Part. Nucl. Phys. **52**, 377 (2004).

[237] V. Somà and P. Bozek, Phys. Rev. C **80**, 025803 (2009).

[238] D. Ding, A. Rios, H. Dussan, W. H. Dickhoff, S. J. Witte, A. Carbone, and A. Polls, Phys. Rev. C **94**, 025802 (2016).

[239] C. Barbieri and A. Carbone, "Self-consistent green's function approaches," in *An Advanced Course in Computational Nuclear Physics: Bridging the Scales from Quarks to Neutron Stars*, edited by M. Hjorth-Jensen, M. P. Lombardo, and U. van Kolck (Springer International Publishing, Cham, 2017) pp. 571–644.

[240] S. Fritsch, N. Kaiser, and W. Weise, Phys. Lett. B **545**, 73 (2002).

[241] S. Fiorilla, N. Kaiser, and W. Weise, Nucl. Phys. A **880**, 65 (2012).

[242] R. Furnstahl, H.-W. Hammer, and S. Puglia, Ann. Phys **322**, 2703 (2007).

[243] W. Kohn and J. M. Luttinger, Phys. Rev. **118**, 41 (1960).

[244] J. M. Luttinger and J. C. Ward, Phys. Rev. **118**, 1417 (1960).

[245] N. Kaiser, Eur. Phys. J. A **48**, 58 (2012).

[246] H.-W. Hammer and R. J. Furnstahl, Nucl. Phys. A **678**, 277 (2000).

[247] G. P. Lepage, J. Comput. Phys. **27**, 192 (1978).

[248] T. Hahn, Comput. Phys. Commun. **168**, 78 (2005).

[249] W. H. Press, S. A. Teukolsky, W. T. Vetterling, and B. P. Flannery, *Numerical Recipes: The Art of Scientific Computing*, 3rd ed. (Cambridge University Press, New York, NY, USA, 2007).

[250] A. R. Krommer and C. W. Überhuber, *Computational Integration* (Society for Industrial and Applied Mathematics, 1987).

[251] C. W. Überhuber, *Numerical Computation 2: Methods, Software, and Analysis*, 1st ed. (Springer, 1997).

[252] T. Hahn, Comput. Phys. Commun. **207**, 341 (2016).

[253] J. Simonis, K. Hebeler, J. D. Holt, J. Menéndez, and A. Schwenk, Phys. Rev. C **93**, 011302(R) (2016).

[254] F. Coester, Nucl. Phys. **7**, 421 (1958).

[255] F. Sarazin, J. S. Al-Khalili, G. C. Ball, G. Hackman, P. M. Walker, R. A. E. Austin, B. Eshpeter, P. Finlay, P. E. Garrett, G. F. Grinyer, K. A. Koopmans, W. D. Kulp, J. R. Leslie, D. Melconian, C. J. Osborne, M. A. Schumaker, H. C. Scraggs, J. Schwarzenberg, M. B. Smith, C. E. Svensson, J. C. Waddington, and J. L. Wood, Phys. Rev. C **70**, 031302 (2004).

[256] Y. A. Litvinov, T. J. Bürvenich, H. Geissel, Y. N. Novikov, Z. Patyk, C. Scheidenberger, F. Attallah, G. Audi, K. Beckert, F. Bosch, M. Falch, B. Franzke, M. Hausmann, T. Kerscher, O. Klepper, H.-J. Kluge, C. Kozhuharov, K. E. G. Löbner, D. G. Madland, J. A. Maruhn, G. Münzenberg, F. Nolden, T. Radon, M. Steck, S. Typel, and H. Wollnik, Phys. Rev. Lett. **95**, 042501 (2005).

[257] D. M. Brink and R. A. Broglia, *Nuclear Superfluidity: Pairing in Finite Systems*, Cambridge Monographs on Particle Physics, Nuclear Physics and Cosmology, Vol. 24 (Cambridge University Press, 2005).

[258] D. J. Dean and M. Hjorth-Jensen, Rev. Mod. Phys. **75**, 607 (2003).

[259] D. G. Yakovlev and C. J. Pethick, Ann. Rev. Astron. Astrophys. **42**, 169 (2004).

[260] D. Page, J. M. Lattimer, M. Prakash, and A. W. Steiner, Astrophys. J. Suppl. Ser. **155**, 623 (2004).

[261] D. Page, J. M. Lattimer, M. Prakash, and A. W. Steiner, Astrophys. J **707**, 1131 (2009).

[262] D. Page, M. Prakash, J. M. Lattimer, and A. W. Steiner, Phys. Rev. Lett. **106**, 081101 (2011).

[263] D. D. Johnson, Phys. Rev. B **38**, 12807 (1988).

[264] V. V. Khodel, V. A. Khodel, and J. W. Clark, Nucl. Phys. A **679**, 827 (2001).

[265] M. Tinkham, *Introduction to Superconductivity*, 2nd ed. (Dover Publications, 1996).

[266] J. Schrieffer, *Theory of Superconductivity* (Perseus Books, 1999).

[267] J. Bardeen, L. N. Cooper, and J. R. Schrieffer, Phys. Rev. **106**, 162 (1957).

[268] J. Bardeen, L. N. Cooper, and J. R. Schrieffer, Phys. Rev. **108**, 1175 (1957).

[269] M. Baldo, U. Lombardo, and P. Schuck, Phys. Rev. C **52**, 975 (1995).

[270] A. Altland and B. Simons, *Condensed Matter Field Theory* (Cambridge University Press, 2006).

[271] S. Maurizio, J. W. Holt, and P. Finelli, Phys. Rev. C **90**, 044003 (2014).

[272] U. Lombardo and H.-J. Schulze, "Superfluidity in neutron star matter," in *Physics of Neutron Star Interiors*, edited by D. Blaschke, A. Sedrakian, and N. K. Glendenning (Springer Berlin Heidelberg, Berlin, Heidelberg, 2001) pp. 30–53.

[273] A. Gezerlis and J. Carlson, Phys. Rev. C **77**, 032801 (2008).

[274] K. Hebeler, A. Schwenk, and B. Friman, Phys. Lett. B **648**, 176 (2007).

[275] J. Clark, C.-G. Källman, and C.-H. Y. D. Chakkalakal, Phys. Lett. B **61**, 331 (1976).

[276] T. Ainsworth, J. Wambach, and D. Pines, Phys. Lett. B **222**, 173 (1989).

[277] J. Wambach, T. Ainsworth, and D. Pines, Nucl. Phys. A **555**, 128 (1993).

[278] H. Heiselberg, C. J. Pethick, H. Smith, and L. Viverit, Phys. Rev. Lett. **85**, 2418 (2000).

[279] H.-J. Schulze, A. Polls, and A. Ramos, Phys. Rev. C **63**, 044310 (2001).

[280] A. Schwenk, B. Friman, and G. E. Brown, Nucl. Phys. A **713**, 191 (2003).

[281] A. Gezerlis, C. J. Pethick, and A. Schwenk, in *Novel Superfluids: Volume 2*, International Series of Monographs on Physics, Vol. 157, edited by K.-H. Bennemann and J. B. Ketterson (Oxford University Press, Oxford, 2014) Chap. 22, p. 580.

[282] S. Gandolfi, A. Y. Illarionov, S. Fantoni, F. Pederiva, and K. E. Schmidt, Phys. Rev. Lett. **101**, 132501 (2008).

[283] L. P. Gor'kov and T. K. Melik-Barkhudarov, Sov. Phys. JETP **13**, 1018 (1961).

[284] A. Rios, A. Polls, and W. H. Dickhoff, J. Low Temp. Phys. **189**, 234 (2017).

[285] M. Baldo, J. Cugnon, A. Lejeune, and U. Lombardo, Nucl. Phys. A **536**, 349 (1992).

[286] P. Papakonstantinou and J. W. Clark, J. Low Temp. Phys. **189**, 361 (2017).

[287] T. Takatsuka and R. Tamagaki, Prog. Theor. Phys. Suppl. **112**, 27 (1993).

[288] A. Baran, A. Bulgac, M. M. Forbes, G. Hagen, W. Nazarewicz, N. Schunck, and M. V. Stoitsov, Phys. Rev. C **78**, 014318 (2008).

[289] M. Baldo, Ø. Elgarøy, L. Engvik, M. Hjorth-Jensen, and H.-J. Schulze, Phys. Rev. C **58**, 1921 (1998).

[290] E. Krotscheck, Z. Phys. **251**, 135 (1972).

[291] O. A. Rubtsova, V. I. Kukulin, V. N. Pomerantsev, and H. Müther, Phys. Rev. C **96**, 034327 (2017).

[292] V. A. Khodel, V. V. Khodel, and J. W. Clark, Nucl. Phys. A **598**, 390 (1996).

[293] J. M. Dong, U. Lombardo, and W. Zuo, Phys. Rev. C **87**, 062801 (2013).

[294] J. W. Clark, V. A. Khodel, and M. V. Zverev, in *Condensed Matter Theories*, Vol. 17, edited by M. P. Das and F. Green (Nova Science Publishers, New York, 2003) Chap. 2, p. 23.

[295] T. Takatsuka, Prog. Theor. Phys. **44**, 905 (1970).

Acknowledgments

First of all, I express my deepest gratitude to my adviser Achim Schwenk for his continuous excellent support since my early days in 2012. His open-minded character and his profound “taste” of physics created a fruitful environment to work on my own skills. Thanks for giving me the opportunity to attend to conferences, summer schools, and internships. With same strength, I am grateful to Kai Hebeler. His office door was literally never closed and there seems to be no question that could not have been answered.

My special thanks go to Arianna Carbone, Dick Furnstahl, Kai Hebeler, Jan Hoppe, Thomas Krüger, Jim Lattimer, Achim Schwenk, and Vittorio Somà for strong collaborations.

I appreciated being part of the theory center and, especially, within the *strongint* group. I thank the many current and former group members, among others, Alexander Bartl, Victoria Durant, Jason Holt, Thomas Krüger, Javier Menéndez, Johannes Simonis, Ingo Tews, and Kyle Wendt. Thank you very much!

During the writing of this manuscript I got welcome feedback and useful comments from Kai Hebeler, Jan Hoppe, Joel Lynn, Achim Schwenk, Ingo Tews, and Corbinian Wellenhofer.

The presented Monte-Carlo framework is an extensive project. I am grateful to Andreas Ekström, Boris Carlsson, and Christian Forssén for important insights into chiral NN forces and for providing us with the matrix elements of N^{2}LOsim (and its N^{3}LO version) for internal benchmarks. The computations were carried out on the Lichtenberg high-performance cluster (HHLR) of the TU Darmstadt. A key step for applications was runtime-optimization, where Christian Iwainsky from the HHLR was a professional help. Thomas Hahn provided us with the Monte-Carlo library “CUBA” and valuable advice for numerical integration in general. Thanks to all of you for making this possible.

For fruitful discussions related to the project on pairing gaps I thank Evgeny Epelbaum, Jeremy Holt, and Vittorio Somà. Together with Sunethra Ramanan and Sarath Srinivas, we jointly benchmarked our results to overcome the numerical intricacies of the gap equation.

Moreover, I enjoyed the interesting discussions with Corbinian Wellenhofer who I met regularly over the years at conferences, workshops, and DPG spring meetings.

From both, a scientific and a personal point of view, the TALENT summer school 2017 at the INT in Seattle influenced me a lot. I thank the organizers, Chuck Horowitz and Sanjay Reddy, and all the participants for creating such a lovely working atmosphere.

Awarded a theory internship of the SFB 1245 I was lucky to be able to spend three weeks at OSU in Columbus to work with Dick Furnstahl on Weinberg eigenvalues. The warm hospitality in the OSU theory group is inexpressible and beyond compare, especially, I mention Alex Dyhdalo, Dick Furnstahl, Gojko Vujanovic, and Sarah Wesolowski.

This work was supported by the ERC Grant No. 307986 STRONGINT and the Deutsche Forschungsgemeinschaft through Grant SFB 1245.

I am also grateful to the Stiftung Jugend forscht e.V. as well as the Deutsches Zentrum für Luft- und Raumfahrt (DLR) e.V., particularly, the DLR_Graduate_Program for state-of-the-art training of hard and soft skills, well-suited for life, research, and all the rest. Working in interdisciplinary teams with different scientific backgrounds was great. This would not have been possible without the professional support by Ute Friedrichs and Denise Fechner.

Last but not least, I thank the person who guided my appreciation for physics, Olaf Tech, and my parents for so many things, too much to mention explicitly.

Curriculum Vitae

Person

Name:	Christian Drischler
Date of birth:	March 5, 1990
Place of birth:	Rüsselsheim
Citizenship:	German

Education

2000 – 2009	Immanuel-Kant Gymnasium Rüsselsheim, Germany
June 10, 2009	Abitur (general qualification for university entrance)
2009 – 2012	Bachelor studies, TU Darmstadt, Germany
September 19, 2012	Bachelor's degree, B.Sc., thesis: *Asymmetric nuclear matter based on chiral effective field theory interactions* supervisor: Prof. Ph.D. Achim Schwenk and Dr. Vittorio Somà
2012 – 2014	Master studies, TU Darmstadt, Germany
October 10, 2014	Master's degree, M.Sc., thesis: *Towards Full N^{3}LO Calculations of Asymmetric Nuclear Matter* supervisor: Prof. Ph.D. Achim Schwenk and Dr. Kai Hebeler
2014 – 2017	Doctoral studies and scientific researcher, TU Darmstadt, Germany advisers: Prof. Ph.D. Achim Schwenk and Dr. Kai Hebeler

Miscellaneous

2015	TALENT summer school: "Nuclear physics of neutron stars and supernovae" at the Institute of Nuclear Theory (INT), University of Washington, WA, USA, organized by Prof. Ph.D. Sanjay Reddy and Prof. Ph.D. Charles J. Horowitz
January 2017	Research internship in Prof. Ph.D. Richard J. Furnstahl's group at The Ohio State University, Columbus, OH, USA (supported by the SFB 1245)
2015 – 2017	Fellowship of the DLR_Graduate_Program, Deutsches Zentrum für Luft- und Raumfahrt (DLR) e.V.

Erklärung zur Dissertation

Hiermit versichere ich, die vorliegende Dissertation ohne Hilfe Dritter nur mit den angegebenen Quellen und Hilfsmitteln angefertigt zu haben. Alle Stellen, die aus Quellen entnommen wurden, sind als solche kenntlich gemacht. Diese Arbeit hat in gleicher oder ähnlicher Form noch keiner Prüfungsbehörde vorgelegen.

Darmstadt, den 27. November 2017

(Christian Drischler)